

---

# Spatially-Resolved Age and Metallicity of Galaxies and Their Stellar Shells and Streams in the *Magneticum* Simulation

Johannes Stoiber

---



Munich 2024



---

**Räumlich aufgelöste Alter und  
Metallizitäten von Galaxien und deren  
Sternenschalen und -ströme in der  
*Magneticum* Simulation**

Johannes Stoiber

---



München 2024



---

# **Spatially-Resolved Age and Metallicity of Galaxies and Their Stellar Shells and Streams in the *Magneticum* Simulation**

**Johannes Stoiber**

---

**Master's Thesis**

at the University Observatory Munich  
Ludwig Maximilian University

Submitted by

**Johannes Stoiber**

born in Furth im Wald

Supervised by

Prof. Dr. Klaus Dolag, Dr. Rhea-Silvia Remus

M.Sc. Lucas Valenzuela, M.Sc. Lucas Kimmig

Munich, 27.11.2024



*We don't need your education,  
We just need more simulation . . .*

*Starset (in their song "Dystopia")*



# Contents

<b>1</b>	<b>Introduction</b>	<b>1</b>
1.1	Galaxies . . . . .	1
1.1.1	Morphology . . . . .	2
1.1.2	Kinematics . . . . .	7
1.1.3	Ages and Metallicities . . . . .	10
1.2	Tidal Stellar Shells and Streams . . . . .	14
<b>2</b>	<b>Methodology</b>	<b>17</b>
2.1	The Magneticum Pathfinder Simulation . . . . .	17
2.2	Simulation Merger Trees . . . . .	18
2.3	Centering and Rotation of Galaxies . . . . .	19
2.4	Luminosity Calculations . . . . .	20
2.5	Definitions of Galaxy Properties . . . . .	21
2.6	Voronoi-binned Maps . . . . .	23
<b>3</b>	<b>Age and Metallicity of Galaxies</b>	<b>27</b>
3.1	Global Properties of Galaxies . . . . .	31
3.2	Spatially Resolved Properties of Galaxies . . . . .	41
3.2.1	Radial Profiles . . . . .	43
3.2.2	Metallicity Gradients . . . . .	47
3.3	Other Galaxy Classifications . . . . .	54
3.4	Summary and Conclusion . . . . .	60
<b>4</b>	<b>Prolate Rotators</b>	<b>65</b>
4.1	Formation and Stability of Prolate Rotators . . . . .	65
4.2	Global Properties of Prolate Rotators . . . . .	70
4.3	Summary and Conclusion . . . . .	73
<b>5</b>	<b>Properties and Progenitors of Shells and Streams</b>	<b>75</b>
5.1	Identification of Shells and Streams . . . . .	76
5.2	Properties of Shells and Streams . . . . .	81
5.2.1	Properties of Shells . . . . .	83
5.2.2	Properties of Streams . . . . .	84

5.2.3	Summary: Properties of Shells and Streams . . . . .	88
5.3	Connecting Shells and Streams to Their Progenitor Satellite Galaxies . . . .	89
5.3.1	Identification of Progenitors . . . . .	89
5.3.2	Evolution of Progenitors . . . . .	94
5.3.3	Decomposition of Shell and Stream Galaxies . . . . .	95
5.3.4	Comparing Progenitors to $z = 0$ Features . . . . .	97
5.3.5	Properties of the Progenitors . . . . .	100
5.3.6	Summary: Connecting Shells and Streams to Their Progenitors . .	102
<b>6</b>	<b>Summary and Conclusion</b>	<b>105</b>
<b>A</b>	<b>Different Options to Calculate Ages</b>	<b>110</b>
<b>B</b>	<b><math>\Phi_{ZR}</math></b>	<b>111</b>
<b>C</b>	<b>Stacked Metallicity Profiles and Resulting Gradients</b>	<b>112</b>
<b>D</b>	<b>Diagnostics Plots for Shells and Streams</b>	<b>121</b>
	<b>References</b>	<b>179</b>

# Chapter 1

## Introduction

In recent years, the advances in the exploration of space have fascinated mankind. Within the last 10 years, three physics Nobel Prizes were awarded to astrophysicists: In 2017 it was awarded to Rainer Weiss, Barry C. Barish, and Kip S. Thorne “for decisive contributions to the LIGO detector and the observation of gravitational waves”, in 2019 to James Peebles “for theoretical discoveries in physical cosmology” and to Michel Mayor and Didier Queloz “for the discovery of an exoplanet orbiting a solar-type star”, and in 2020 to Roger Penrose “for the discovery that black hole formation is a robust prediction of the general theory of relativity” and to Reinhard Genzel and Andrea Ghez “for the discovery of a supermassive compact object at the centre of our galaxy”<sup>1</sup>. Lately, the images taken by the James Webb Space Telescope (JWST) released by NASA<sup>2</sup> added to the astronomy excitement. Figure 1.1 displays a galaxy observed by the JWST. It is this fascinating type of object this thesis deals with. The following chapter introduces relevant concepts of our current knowledge about galaxies, ranging from their morphology and kinematics, over their ages and the content of elements heavier than helium (called *metallicity* in the astrophysics community), ending with intriguing features visible in the outer regions of galaxies called stellar shells and streams. Chapter 2 presents the simulation from which the analyzed galaxies are taken, and the methods used to investigate them. The ages and metallicities of galaxies and the question of how they are distributed along a galaxy’s radius is investigated in Chapter 3. This is done for different groups of galaxies. For a specific group of galaxies called *prolate rotators*, Chapter 4 investigates their formation, stability, and properties. Finally, Chapter 5 focuses on the ages and metallicity of stellar shells and streams in the outskirts of galaxies. The progenitor galaxies of these features are identified, and their properties analyzed and compared to the features’ properties.

### 1.1 Galaxies

Galaxies are the accumulations of stars that have long fascinated humans. Our very own galaxy is the “milky way” that is visible as a patch of diffuse light stretching over our night-sky. The Sun orbits the Milky Way’s center at about 8 kpc (Francis & Anderson, 2014).

---

<sup>1</sup><https://www.nobelprize.org/>

<sup>2</sup><https://science.nasa.gov/mission/webb/>



**Figure 1.1:** The galaxy LEDA 2046648 observed by the James Web Space Telescope. Image Credit: ESA/Webb, NASA & CSA, A. Martel

Its name originates from Greek mythology, where it was thought to be a river of Hera’s milk. In fact, the word “galaxy” derives from the Greek word for milk. The investigation of these “nebulae” in the night-sky over the past millennia, centuries, and decades involved many renowned scientists such as Galileo Galilei, who discovered that the Milky Way is not a diffuse band of light but consists of individual stars, Immanuel Kant, who speculated that the “nebulae” are “island universes” similar to the Milky Way, Charles Messier, who compiled a catalog of “nebulae” during his search for comets, William Herschel, who made the distinction between *gaseous nebulae*<sup>3</sup> and unresolved stellar systems, Johan Ludvig Emil Dreyer, who added to William and Caroline Herschel’s catalog and released it as the *New General Catalog* (NGC), and many more scientists (Binney & Merrifield, 1998). One of the most important cornerstones of galactic astronomy is Edwin Hubble’s measurement – and confirmation of Kant – that some of the observed “nebulae” are stellar systems of their own and not part of the Milky Way (Hubble, 1925). This was followed by the even more interesting result that the radial velocities of these galaxies increase with their distance from the Milky Way, which is now known as the *Hubble law*  $v_r = H_0 \times D$ , where  $v_r$  is the galaxy’s radial velocity,  $D$  the distance to the galaxy, and  $H_0$  the famous *Hubble constant* (Hubble, 1926; Hogg, 1999). This discovery is what led to the establishment of the *expanding universe* and modern cosmology and astrophysics. One field investigated since then is the study of the formation and evolution of galaxies.

### 1.1.1 Morphology

#### Hubble Fork

Hubble and his predecessors already noticed that the “nebulae” come in varying shapes and morphologies. A very early classification according to their shape was presented in Hubble’s

---

<sup>3</sup>Examples of gaseous nebulae are planetary nebulae that consist of gas ejected from red giant stars or supernova remnants that are the remains of a star’s outer hull after it exploded during a supernova.

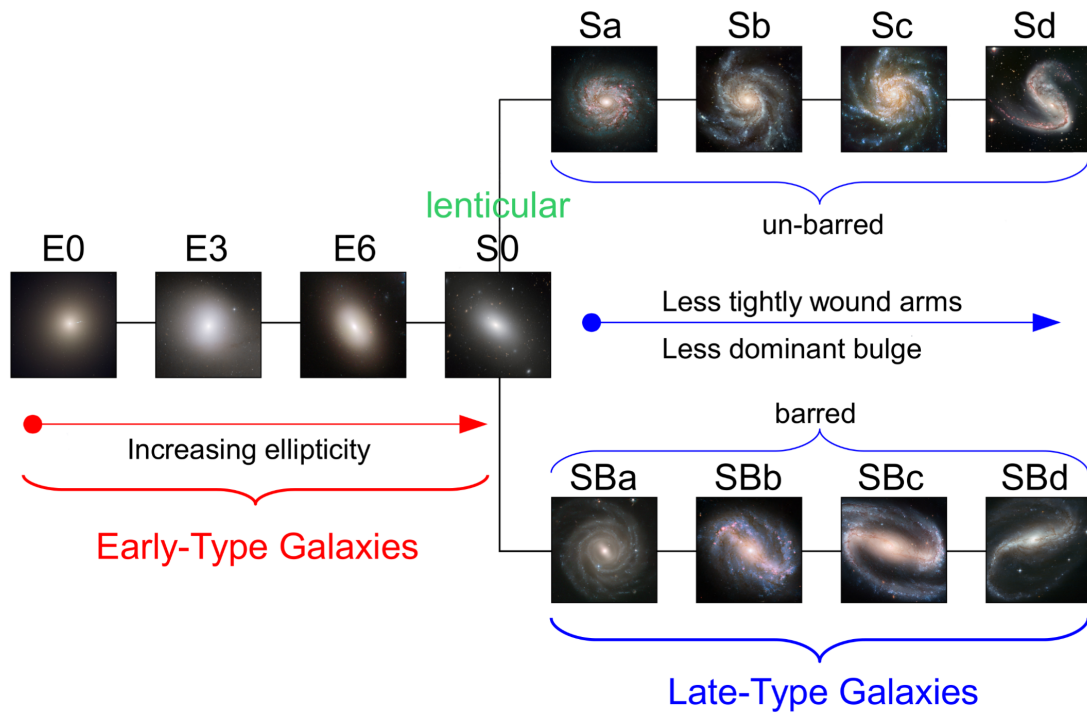


**Figure 1.2:** The “Hubble tuning-fork” illustrating the classification of galaxies due to their morphology, first introduced by Hubble (1936). Image credit: NASA, ESA, M. Kornmesser, annotated and presented by Remus (2015).

book *The Realm of the Nebulae* (Hubble, 1936). His classification, which is known as the *Hubble tuning fork*, is illustrated in Figure 1.2.

Hubble thought that galaxies evolved from the left to the right in this diagram. This scenario is now refuted, but the galaxies on the left-hand side are still referred to as *early-type* galaxies (ETGs) and the galaxies on the right-hand side as *late-type* galaxies (LTGs) (Binney & Merrifield, 1998). The shape of ETGs is smooth and structureless, which is why they are called *elliptical galaxies* (E). They are labeled by  $E_n$  and vary from very round (E0) to elongated (E7) where the number  $n$  specifies the ellipticity  $e$

$$n = 10 \times e = 10 \times \left(1 - \frac{b}{a}\right), \quad (1.1)$$

where  $b/a$  is the apparent axial ratio (Binney & Merrifield, 1998). Before the tuning fork bifurcates into two branches of “normal” (S) and “barred” (SB) *spiral galaxies*, the *lenticular galaxies* build a transitional class designated by S0. They were established by Sandage (1961) as armless disk galaxies. The “normal” spiral galaxies host an elliptical central bulge of brightness surrounded by luminous spirals, the *spiral arms*. The *barred* spiral galaxies exhibit a *bar* within which the bright bulge is located and which is connected to the spiral arms. The subtypes (a, b, c, and d) of spirals are characterized according to the influence of the bulge, the tightness of the spiral arms and the degree to which the arms are resolved into stars or emission nebulae. Often these three criteria are tightly correlated and therefore galaxies with very distinct bulges, which have tightly wound, diffuse shining spiral arms are situated to the left-hand side of the *Hubble tuning fork* (Sa, SBa), while galaxies

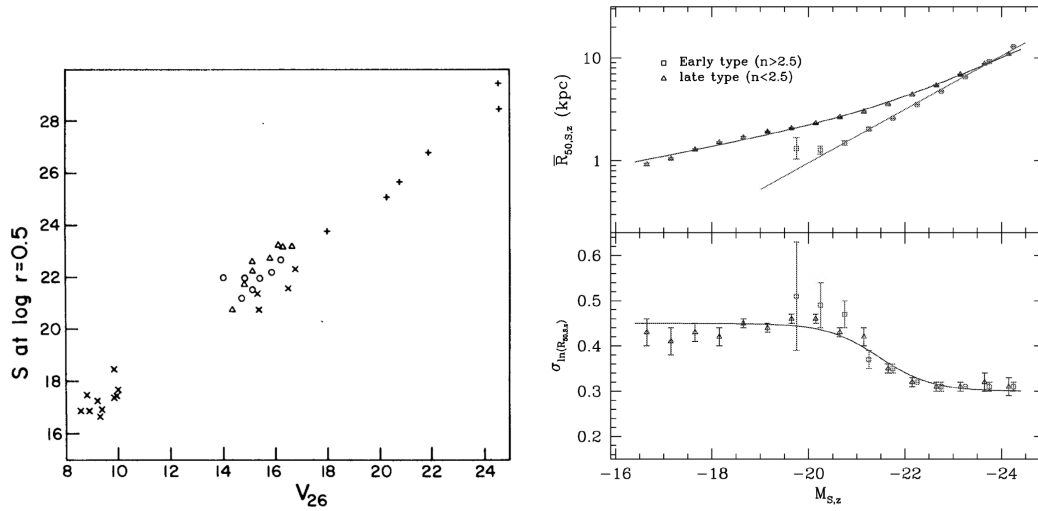


**Figure 1.3:** *Left panel:* The surface brightness-luminosity relation as presented by Caldwell (1983) *Right panel:* The stellar mass-half-light radius relation as presented by Shen et al. (2003), specifically the median (*top panel*) and dispersion (*bottom panel*) of the distribution of the r-band Sérsic half-light radius. The squares represent ETGs and the triangles represent LTGs.

with faint bulges, which have loosely wound, eminently resolved spiral arms, are situated to the right-hand side of the Hubble fork (Sd, SBd). Intermediate classes are designated by Sb and SBb, and Sc and SBc. For even finer classification, stages between these levels can be assigned, for example Sab in between Sa and Sb (Binney & Merrifield, 1998). Finally, there are many more finer classifications for irregular galaxies (I/Irr) (de Vaucouleurs, 1963), peculiar galaxies (P) (Arp, 1966), ring galaxies (Sandage, 1961; de Vaucouleurs, 1963), and many more.

### Mass-Size Relation

Apart from a visual classification, a galaxy’s structural properties, such as its size, combined with their stellar mass can be used to infer their morphology. Related to its stellar mass is a galaxy’s luminosity, while the surface brightness is related to its size (Lange et al., 2015). The first observation of a linear relation between luminosity and surface brightness was achieved by Caldwell (1983) (see left panel of Figure 1.3), suggesting that a scaling relation between a galaxy’s size, and its stellar mass exists. In fact, this mass-size relation is for example observed by Shen et al. (2003) and Lange et al. (2015) (see right panel of Figure 1.3) for the stellar half-light radius and stellar mass.

More recently, Lange et al. (2015) investigated the mass-size relation using 8399 galaxies from the GAMA survey regarding its dependence on various divisions into early- and late-type galaxies and on the choice of filter bands. They conclude that the choice of division is not critical, but one should rather focus on the mass limits and sample selection. Assuming a constant mass-to-light ratio, the half-light radius  $r_e$  is the same as a galaxy’s stellar half-mass radius  $r_{1/2}$ , which is the radius at which half the stellar mass of a galaxy is enclosed:

$$M_{\star}(r < r_{1/2}) = \frac{1}{2} M_{\star,\text{tot}} \quad (1.2)$$

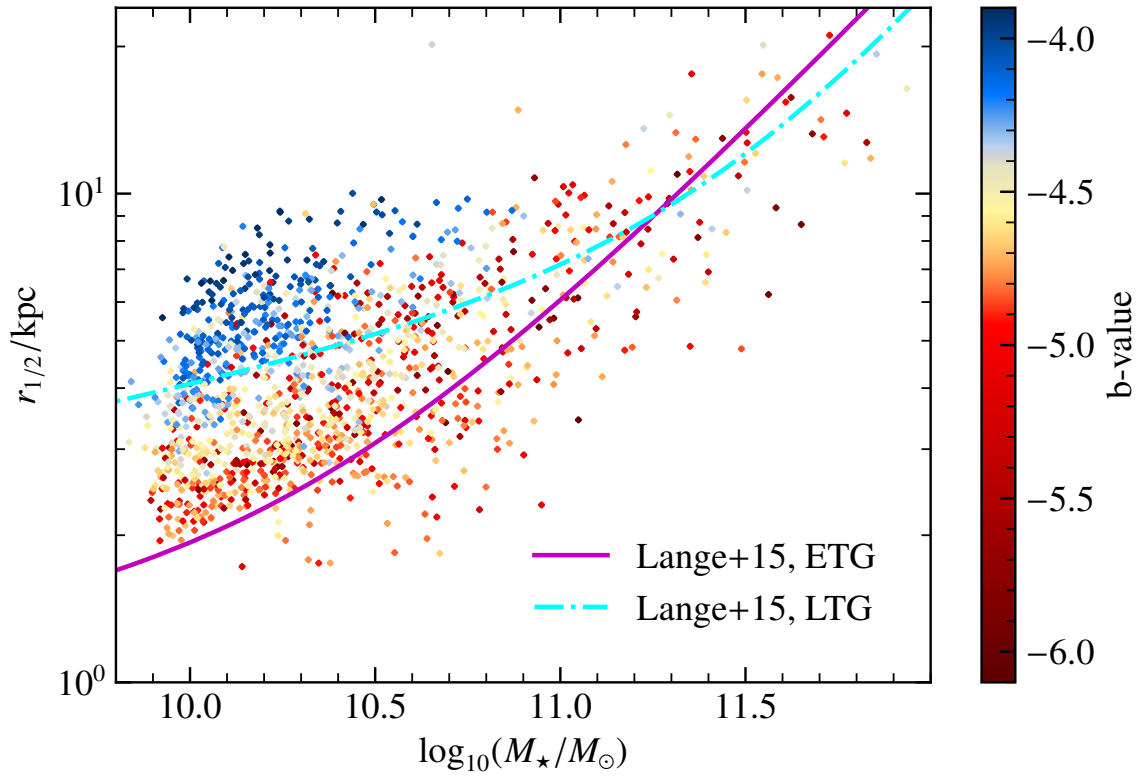


**Figure 1.4:** The mass-size relation: The stellar half-mass radius as a function of stellar mass  $M_*$ , colored according to their  $b$ -value, which is a tracer for the galaxy’s morphology. Red represents spheroidal (i.e., elliptical) galaxies, blue represents disk (i.e., spiral) galaxies and intermediate galaxies are yellow. Overplotted are the fits of this relation in ETGs (magenta) and LTGs (cyan) to a combination of two power-law functions  $r_{1/2} = \gamma(M_*/M_\odot)^\alpha(1 + M_*/M_\odot)^{\beta-\alpha}$  by Lange et al. (2015). The fitting parameters are taken from their population definition according to morphology in the r-band.

The morphology of simulated galaxies can be quantified by the so-called  $b$ -value that will be introduced below. Here, it is demonstrated that the size of a galaxy is related to its morphology. Shown in Figure 1.4 is the stellar half-mass radius  $r_{1/2}$  as a function of stellar mass  $M_*$ , colored by the  $b$ -value for *Magneticum* galaxies, which will be introduced in Chapter 3. Overplotted are the fits to ETGs and LTGs by Lange et al. (2015). It is very evident that disk galaxies (blue) have larger sizes at fixed stellar mass compared to spheroids (red). The latter can reach larger radii than any disk at high enough stellar masses. The observational results for ETGs and LTGs match the shown simulated spheroids and disks, respectively.

### Sérsic Profile

A possibility to measure a galaxy’s half-light radius is given by fitting a galaxy’s surface brightness profile to a fitting function, whose fitting parameters include the half-light radius (or effective radius)  $r_e$  or it can be derived from one of the fitting parameters. Several such functions were put forward, including

$$\frac{\log_{10}(I_{R^{1/4}}(r))}{\log_{10}(I_e)} = -3.33 \left( \left( \frac{r}{r_e} \right)^{1/4} - 1 \right), \quad (1.3)$$

which is called the *de Vaucouleurs  $R^{1/4}$  profile* (de Vaucouleurs, 1948), where the numerical factor 3.33 is chosen such that the definition of the half-light radius  $r_e$  is satisfied (Binney & Merrifield, 1998):

$$\int_0^{r_e} I(r) 2\pi r dr = \frac{1}{2} \int_0^{\infty} I(r) 2\pi r dr \quad (1.4)$$

However, some early-type galaxies deviate significantly from the best-fit  $R^{1/4}$ -profile. A three-parameter fitting function is required to capture their behavior. The *Sérsic profile* is one such formula, sometimes also called the *generalized de Vaucouleurs profile*, and given by

$$\frac{\log_{10}(I_S(r))}{\log_{10}(I_e)} = -b_n \left( \left( \frac{r}{r_e} \right)^{1/n} - 1 \right), \quad (1.5)$$

where  $b_n$  is again chosen so that  $r_e$  is the half-light radius, and  $n$  is called the *Sérsic index*. This index correlates with the half-light radius of a galaxy, such that extended galaxies have large Sérsic indices, while concentrated galaxies have small indices (Caon et al., 1993). Elliptical galaxies typically have Sérsic indices between 2 and 6 (Remus, 2015).

Finally, the surface brightness profile of a spiral galaxy's disk is described by an exponential function (Binney & Merrifield, 1998),

$$I_{\text{exp}}(r) = I'_e \exp\left(-b \frac{r}{r_e}\right), \quad (1.6)$$

which is a Sérsic profile with index  $n = 1$ . A spiral galaxy's bulge, on the other hand, appears similar to an elliptical galaxy having a Sérsic index between 2 and 4 (Remus, 2015).

## b-value

Now the classification method already mentioned above can be introduced. Simulated galaxies can be classified into *disks*, *intermediates* and *spheroids* by using the *b-value*,

$$b = \log_{10}\left(\frac{j}{\text{kpc km/s}}\right) - \frac{2}{3} \log_{10}\left(\frac{M_{\star}}{M_{\odot}}\right), \quad (1.7)$$

which is a proxy for a galaxy's position in the stellar mass-stellar specific angular momentum plane (Teklu et al., 2015). Teklu et al. (2017) state that a criterion based on this parameter is not the most robust due to the existence of fast rotators among spheroidal galaxies (Emsellem et al., 2007). The main advantage of this method – over the commonly used circularity parameter  $\epsilon_{\text{circ}}$ <sup>4</sup> – is that all galaxies in a sample can be classified. Teklu et al. (2015) can not classify a significant number of the galaxies in their sample using a criterion based on circularity  $\epsilon_{\text{circ}}$  and the cold gas fraction. Romanowsky & Fall (2012) expect disk galaxies for  $b \approx -4$  and spheroids for  $b \approx -5$ . Teklu et al. (2017) introduce the classification that galaxies with  $b > -4.35$  are disks, while galaxies with  $b < -4.73$  are spheroids. All

<sup>4</sup>The circularity parameter can be expressed as follows:  $\epsilon_{\text{circ}} = \frac{j_z}{j_{\text{circ}}} = \frac{j_z}{r V_{\text{circ}}}$ , where  $j_{\text{circ}}$  is the predicted specific angular momentum assuming a circular orbit with radius  $r$  around a halo center of mass, with an orbital velocity of  $V_{\text{circ}}(r) = \sqrt{GM(r)/r}$ , and  $j_z$  is the  $z$ -component of the particular angular momentum of a single particle (Teklu et al., 2015).

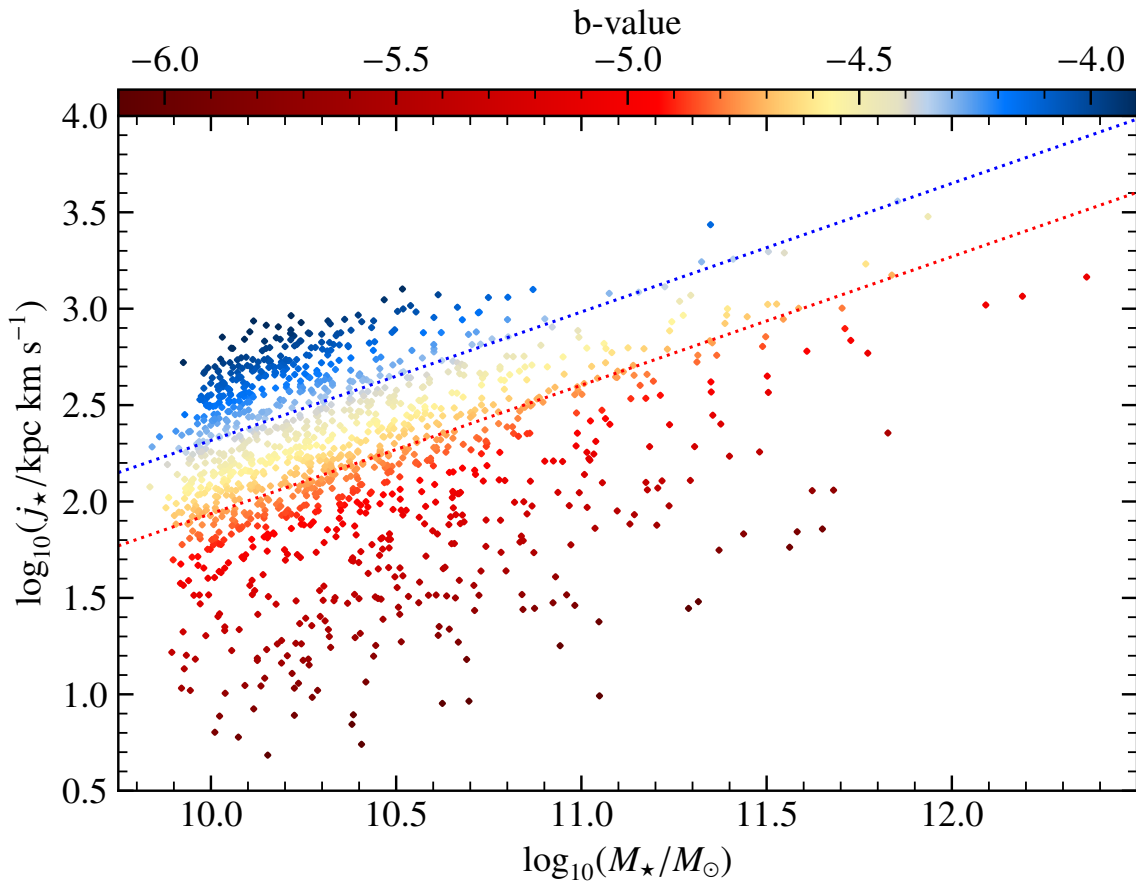


**Figure 1.5:** Stellar mass  $\log_{10}(M_{\star}/M_{\odot})$  as a function of stellar specific angular momentum  $\log_{10}(j_{\star}/\text{kpc km s}^{-1})$ , colored by the  $b$ -value. The red dots are spheroidal, the blue dots are spiral, and the yellow galaxies are intermediate galaxies.

galaxies in between are intermediates. This classification is illustrated in Figure 1.5, which is the stellar mass-stellar specific angular momentum plane colored by the  $b$ -value. The red dots are spheroidal galaxies, the blue dots are spirals and the yellow dots are intermediate galaxies. One can see that they are separated by the blue and red dotted lines, which represent the above-mentioned boundaries between disks, intermediates and spheroids.

### 1.1.2 Kinematics

The other side of the same coin of describing galaxies are their kinematics that describe the motions of stars with respect to each other and regarding the center-of-velocity of their galaxy. The most accessible velocity component is the one parallel to the line-of-sight of an observer, called the line-of-sight velocity ( $losv$ ) and its standard deviation or dispersion, called the line-of-sight velocity dispersion ( $losv\sigma$ ). These are measured by observing the spectrum of a collection of stars and inferring their velocity via the relativistic Doppler effect<sup>5</sup>. An illustrative example of the importance of galaxy kinematics is the emergence of “dark matter”. Extensive measurements of the  $losv$  profile of spiral galaxies (Oort, 1940; Rubin

<sup>5</sup>The observed wavelength of  $\lambda_{\text{obs}}$  is shifted from its emitted wavelength  $\lambda_{\text{em}}$  by  $\lambda_{\text{obs}} - \lambda_{\text{em}} = \lambda_{\text{em}} \times v/c$  where  $v$  is the  $losv$  and  $c$  the speed of light (Binney & Merrifield, 1998, Chap. 2.2).

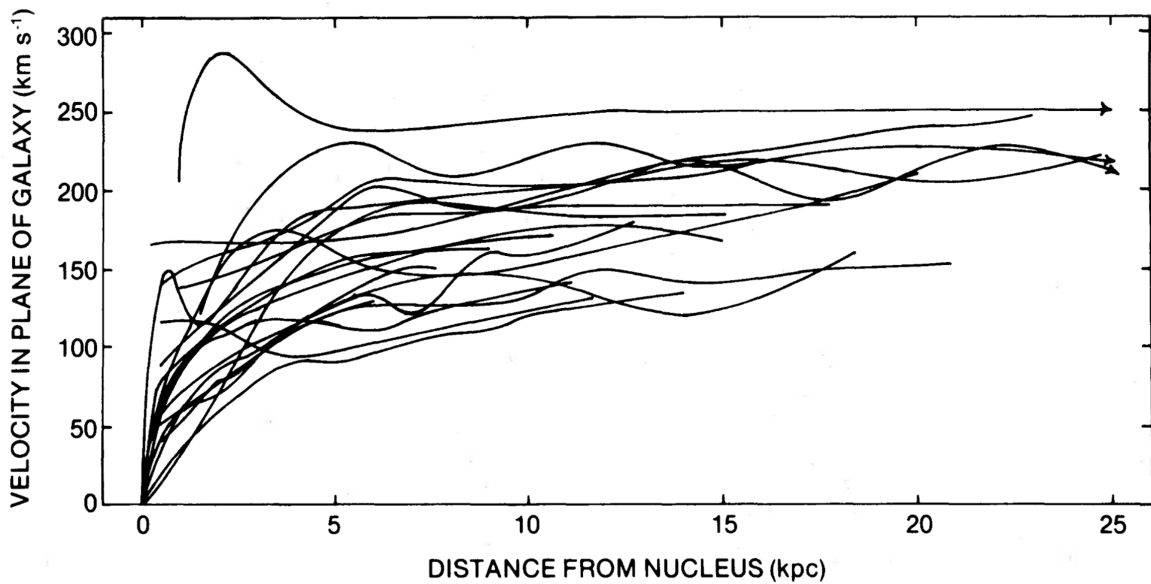


**Figure 1.6:** Multiple velocity profiles of different galaxies taken from Rubin et al. (1980). The velocity profile is the velocity as a function of the distance to the center of the galaxy.

et al., 1965; Rubin & Ford, 1970; Rubin et al., 1978, 1980) revealed that the stars’ velocity increases with the radius in the center but stays constant at high radii (See Figure 1.6). This is not expected for a mass distribution where most of the mass is concentrated at the center, which is observed from the luminous matter. The expectation is a decrease in the velocity  $\propto 1/r$ . This means that there must be a vast amount of non-luminous matter at large radii in the halo of galaxies. This non-luminous mass was termed “dark matter” by Zwicky (1937), who investigated the velocity dispersion of galaxies within the Coma Cluster and concluded that the mass within the system needs to be at least 400 times larger than the luminous matter suggests.

### Kinematic Groups

A spiral galaxy’s rotation pattern is easily understood, as it exhibits a simple regular rotation around its minor axis. For a long time, it was thought that elliptical galaxies are dispersion dominated and their stars are on triaxial orbits. The IFU<sup>6</sup> survey ATLAS<sup>3D</sup> revealed that the kinematic variety of elliptical galaxies is much larger than previously thought. Krajnović et al. (2011) investigated the 260 ATLAS<sup>3D</sup> ETGs and produced  $losv$  and  $losv\sigma$  maps that can be used to classify the galaxies according to their kinematic features into five groups: regular rotators, non-rotators, complex but non-specific velocity maps, kinematically distinct cores, and double peaks in the velocity dispersion map. A similar classification for the simulated galaxies used in this work are the *kinematic classes of early-type galaxies* introduced by Schulze et al. (2018) for the Magneticum Box4 galaxies. The classes are

<sup>6</sup>The term IFU stands for “Integral field unit”, which describes a type of observation where an array of fibers is used to measure the spectrum within individual parts of a galaxy and which yields spatially resolved maps of spectra. Examples are SAURON (Bacon et al., 2001; de Zeeuw et al., 2002), ATLAS<sup>3D</sup> (Cappellari et al., 2011), SAMI (Croom et al., 2012), CALIFA (Sánchez et al., 2012), and MaNGA (Bundy et al., 2015).

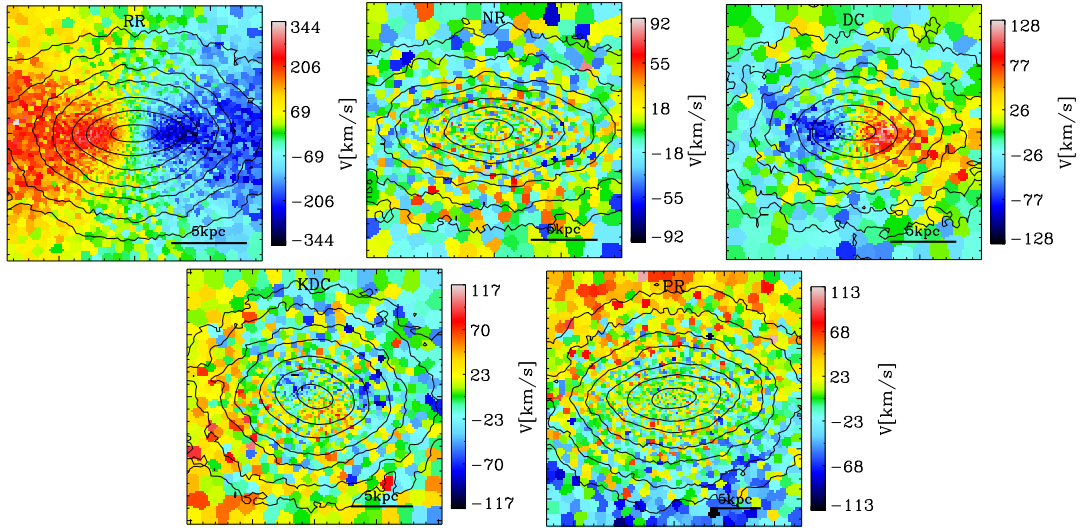


**Figure 1.7:** The five kinematic groups defined by Schulze et al. (2017): Regular rotator (RR), non-rotators (NR), distinct core (DC), kinematically distinct core (KDC), and prolate rotators (PR). The solid black lines represent contours of constant density. Image taken from Schulze et al. (2017).

regular rotators (620/900), non rotators (129/900), distinct cores (25/900), kinematically distinct cores (5/900), and prolate rotators (20/900). 91 galaxies could not be classified. A detailed description can be found in Section 3.3. An example for each group (except for the unclassified galaxies) is shown in Figure 1.7. The group with the smallest sample are prolate rotators, which will have a particular focus in this thesis. They are described in more detail in Chapter 4.

### $V/\sigma$ -Parameter and $\lambda_R$

Parts of this thesis focus more on the internal kinematics of galaxies where a major concern is whether a galaxy is rotating or is dominated by velocity dispersion. In the following, two parameters that encapsulate this information are introduced. The first is the  $V/\sigma$ -parameter. It is used as an indicator of rotational support, expressed as the ratio of ordered to random motion (Illingworth, 1977). It can be calculated as the combined mass-weighted root-mean-square of the velocities and velocity dispersion calculated from a Voronoi-binned (see Section 2.6) 2D kinematic map.

$$\frac{V}{\sigma} = \sqrt{\frac{\sum_i M_i \bar{V}_i^2}{\sum_i M_i \sigma_i^2}}, \quad (1.8)$$

where  $V_i$ ,  $\sigma_i$ , and  $M_i$  are the mean  $losv$ , mean  $losv\sigma$ , and the stellar mass within the  $i$ th Voronoi-bin.

One of the first large integral-field spectroscopy surveys, SAURON (Bacon et al., 2001; de Zeeuw et al., 2002), revealed that early type galaxies appear in two general classes, *fast* and *slow rotators* (Emsellem et al., 2007). They introduced the  $\lambda_R$  parameter

$$\lambda_R \equiv \frac{\langle R|V| \rangle}{R\sqrt{V^2 + \sigma^2}}, \quad (1.9)$$

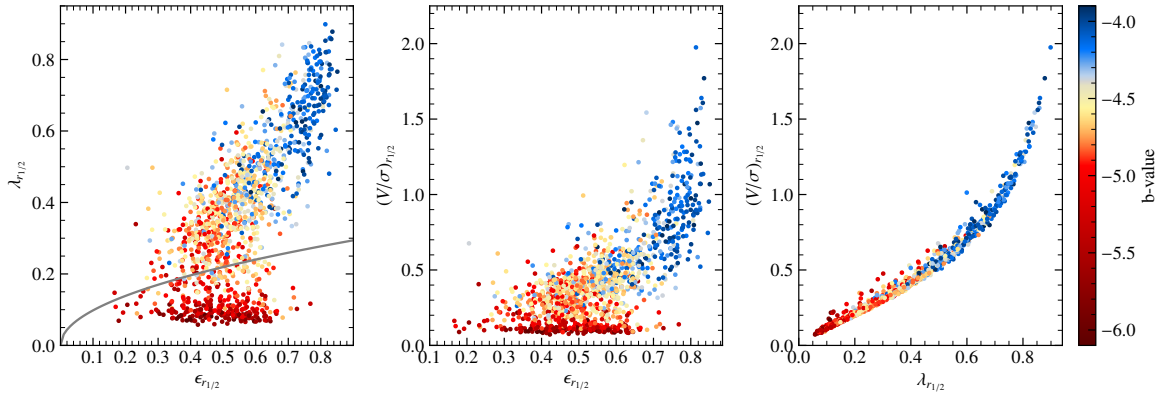


**Figure 1.8:**  $\lambda_{r_{1/2}}$  (left panel) and  $(V/\sigma)_{r_{1/2}}$  (middle panel) as a function of the ellipticity  $\epsilon$ , and  $(V/\sigma)_{r_{1/2}}$  as a function of  $\lambda_{r_{1/2}}$ . The color depicts the  $b$ -value. The gray line in the first panel represents the  $\lambda_{r_{1/2}} = 0.31\epsilon$  boundary between fast and slow rotators, which was defined by Emsellem et al. (2007).

where  $R$  is the 2D distance to the galactic center,  $V$  is  $losv$ ,  $\sigma$  the  $losv\sigma$ , and the brackets  $\langle \cdot \rangle$  represent the luminosity weighted mean value. The main motivation to introduce  $\lambda_{r_{1/2}}$  was that  $V/\sigma$  does not differentiate between small-scale and large-scale rotation (Emsellem et al., 2007). Measured by integral-field spectroscopy in individual Voronoi-bins (See Section 2.6), this can be calculated as

$$\lambda_R = \frac{\sum_{i=1}^N F_i R_i |V_i|}{\sum_{i=1}^N F_i R_i \sqrt{V_i^2 + \sigma_i^2}}, \quad (1.10)$$

where  $F_i$  is the flux within the  $i$ th Voronoi bin,  $R_i$  the bin's distance to the center and  $V_i$  and  $\sigma_i$  the mean stellar  $losv$  and  $losv\sigma$ . Emsellem et al. (2007) found that there is a general split at  $\lambda_{R_e} = 0.1$ . The large integral-field spectroscopy survey ATLAS3D (Cappellari et al., 2011) defined the boundary between *fast* and *slow rotators* to be at  $\lambda_{R_e} = 0.31\epsilon$  (Emsellem et al., 2011). van de Sande et al. (2021) prefer the  $\lambda_{R_e} = 0.08 + \epsilon/4$  with  $\epsilon < 0.4$  (Cappellari, 2016) over the former criterion. More details on the calculation of quantities from a Voronoi grid can be found in Section 2.6.

Finally, Figure 1.8 shows the parameters  $\lambda_{r_{1/2}}$  (left panel) and  $(V/\sigma)_{r_{1/2}}$  (middle panel) as a function of the ellipticity  $\epsilon$ , and  $(V/\sigma)_{r_{1/2}}$  as a function of  $\lambda_{r_{1/2}}$  (right panel). As expected, the disk (blue) galaxies occupy the region of fast rotators in the  $\lambda_{r_{1/2}}-\epsilon$  plane, while most spheroidal galaxies are slow rotators. A similar, but skewed distribution can be seen in the  $V/\sigma-\epsilon$  plane. The  $V/\sigma-\lambda_{r_{1/2}}$  relation is relatively tight, as expected for two parameters designed to capture similar information.

### 1.1.3 Ages and Metallicities

#### Mass-Metallicity Relation

One of a galaxy's most fundamental characteristics is its metallicity. Stellar metallicities are a direct tracer of the star formation and chemical enrichment history (e.g. Guérou

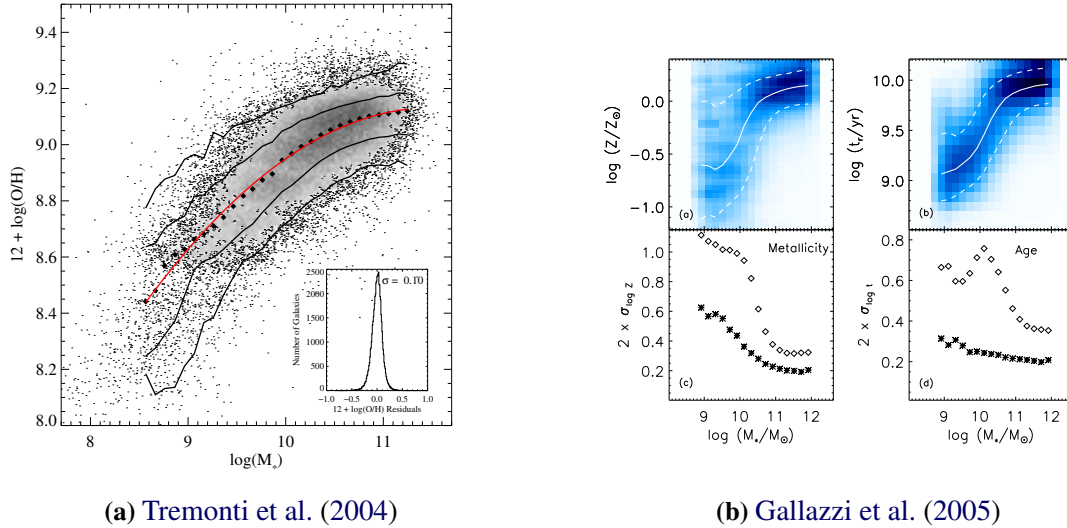


**Figure 1.9:** *Left panel:* The stellar mass-gas phase metallicity relation observed by Tremonti et al. (2004). *Right panel:* The stellar mass-stellar metallicity relation (*left*) and stellar mass-stellar age relation (*right*) observed by Gallazzi et al. (2005). The bottom panels show the uncertainty of the metallicity/age as a function of stellar mass.

et al., 2015). First detected by Lequeux et al. (1979), using a small sample of spectrophotometric observations of HII regions in irregular and blue compact galaxies, the gas-phase metallicity of star-forming galaxies rises with increasing  $M_{\text{gas}}/M_{\text{tot}}$ . This is the so called *Mass-Metallicity Relation* (MZR). Increasing the sample to  $\sim 53000$  star-forming galaxies observed by the Sloan Digital Sky Survey (SDSS), Tremonti et al. (2004) established a tight ( $\pm 0.1$  dex) correlation between stellar mass and the gas-phase metallicity, which flattens above  $10^{10.5} M_\odot$  (See Figure 1.9a). This is interpreted as galactic winds being effective at removing metals from the potential wells of low-mass galaxies. Comparing nine strong-line emission metallicity calibrations, Kewley & Ellison (2008) demonstrated that the choice of metallicity calibration strongly affects the y-intercept of the MZR. This tendency is seen in star-forming galaxies at least up to  $z \sim 3$ , indicating a transition toward greater metallicities throughout cosmic time, particularly in low mass galaxies (Maiolino et al., 2008). Regarding stellar metallicities, a similar relation was found by Gallazzi et al. (2005) using the spectra of a large sample of SDSS galaxies, which is shown in Figure 1.9b. Population synthesis models in combination with stacked spectra (Zahid et al., 2017; Sextl et al., 2023) or even observations of individual blue and red supergiants (Kudritzki et al., 2016; Davies et al., 2017; Bresolin et al., 2022; Urbaneja et al., 2023; Sextl et al., 2024) solidified the existence of the stellar mass-stellar metallicity relation.

Recently, the importance of a galaxy’s size when studying stellar population properties was restated by Vaughan et al. (2022), showing that the offset between star-forming and passive galaxies in the MZR can be significantly reduced by replacing  $M_\star$  with  $\Phi = \log_{10}(M_\star/M_\odot) - \log_{10}(r_{1/2}/\text{kpc})$ , a proxy for the baryonic gravitational potential. This is closely related to the fact that ETGs are more compact than LTGs at fixed stellar mass (Lange et al., 2015) and therefore show shallower gravitational potentials (Vaughan et al., 2022). At fixed mass,

galaxies that are more compact are older and more metal-rich (Scott et al., 2017). Previously, D’Eugenio et al. (2018) found  $\Phi$  to be more tightly correlated to the gas-phase metallicity than to the stellar mass. Sánchez-Menguiano et al. (2024) used a machine-learning approach to argue that  $\Phi = \log_{10}(M_{\star}/M_{\odot}) - 0.6 \log_{10}(r_{1/2}/\text{kpc})$  is an even better predictor for the gas-phase metallicity.

### Mass-Age Relation

The age of stars in galaxies is a direct measurement of when the last star formation episode took place, which again is directly related to the formation history of galaxies. Therefore, another important relation is that between a galaxy’s age and its stellar mass. Mean ages typically increase with stellar mass (Gallazzi et al., 2005; González Delgado et al., 2015; San Roman et al., 2018; Nanni et al., 2024). The stellar mass-stellar age relation is shown in Figure 1.9b. This trend is referred to as “downsizing”, that is, more massive galaxies are formed at earlier times. Therefore, older galaxies have more mass (Cowie et al., 1996). González Delgado et al. (2015) demonstrate that this “downsizing” holds true at all radii. Furthermore, ETGs are older than LTGs at fixed stellar mass.

### Metallicity Gradients

Spectroscopic galaxy surveys utilizing IFUs (Integral Field Units) like ATLAS<sup>3D</sup> (Cappellari et al., 2011), CALIFA (Sánchez et al., 2012), SAMI (Croom et al., 2012; Bryant et al., 2015), and MaNGA (Bundy et al., 2015) have become invaluable in the study of galaxy evolution because of their capabilities to spatially resolve stellar population properties and kinematics. The distribution of stellar populations at different ages bears the stamp of the formation processes, and this can be utilized as a tracer of the history of star formation and assembly (Guérou et al., 2015). These spatially resolved surveys have also been used to investigate the gas-phase MZR (Sánchez et al., 2019). Many observational campaigns have investigated radial age and metallicity profiles: González Delgado et al. (2015) report on CALIFA galaxies having declining age profiles, that is older stars are found in the core, whereas younger stars are found in the outer regions. Sbc type galaxies exhibit the steepest negative age gradients, flattening towards S0 and E type galaxies and towards Sd galaxies, while Sd type galaxies gradients are flatter than in the S0 and E cases. They also observe the gradient to become more negative with increasing stellar mass up to  $\sim 1 \times 10^{11} M_{\odot}$ . However, this is a secondary dependence, while the primary dependence is with the Hubble type. They find that metallicity profiles are slightly decreasing, but Sd type galaxies’ metallicity has almost no dependence on radius, while Sbc type galaxies’ metallicity has the strongest dependence. The metallicity gradients also become more negative with increasing mass up to  $1 \times 10^{11} M_{\odot}$ . These results, regarding the negative age and metallicity gradients, favor the “inside-out” growth of galaxies. Goddard et al. (2017) and Neumann et al. (2021) analyze the MaNGA galaxies and confirm the declining age profiles for LTGs. For ETGs, however, both find (mildly) positive age gradients (stronger in the mass-weighted case) over all masses,

that is the stars get younger toward the center. This may indicate that star formation in ETGs proceeds in an “outside-in” fashion. The metallicity profiles deduced from the MaNGA survey are generally declining for all morphologies, but the gradient is significantly steeper in late-type galaxies (Goddard et al., 2017). The ALHAMBRA survey, a survey based on photometric multi-filter measurements (San Roman et al., 2018), finds flat radial age and declining radial [Fe/H] profiles for early-type galaxies. The iMaNGA project’s sample of simulated galaxies is drawn from the cosmological hydrodynamic simulation Illustris TNG50 (Pillepich et al., 2019; Nelson et al., 2018), which was chosen expressly to imitate MaNGA galaxies (Nanni et al., 2024). Mock MaNGA data cubes are created and examined in the same manner as MaNGA galaxies (Nanni et al., 2024). The simulation predicts higher light-weighted stellar ages at all radii. However, the gradients are consistent, except for an increasing age profile for low-mass lenticular galaxies and a significantly shallower decline of the age profile in high mass spiral galaxies in the iMaNGA sample compared to MaNGA. In general, iMaNGA exhibits steeper metallicity gradients and lower stellar metallicities than observations. Again, the simulation departs stronger for spirals, where the gradient is steeper than found in observations over all masses.

It is interesting to analyze the metallicity profiles for stars in different stellar populations according to their age. This can give insightful details on the chemical enrichment history. Investigating stellar proxies, like planetary nebulae (PNe) and HII regions, in a small sample of local galaxies, Peña & Flores-Durán (2019) found that young objects (Peimbert Type I PNe, HII regions) show steeper negative metallicity gradients than old objects (non-Type I PNe). Applying a population synthesis technique, Sextl et al. (2024) confirm the negative metallicity gradient of the young component, while the old population exhibits no gradient, in the spiral galaxy NGC 1365. Both studies argue that one mechanism for the gradient in the old population being flatter might be stellar radial migration, that is stars wander from their initial position to different radii, diffusing the metallicity-radius relation (Roškar et al., 2008).

To find out what causes the metallicity to decline with radius, several studies investigated if the steepness of the metallicity gradient correlates with global galactic parameters. Metallicity gradients become steeper with stellar mass up to  $1 \times 10^{10} M_{\odot}$  for CALIFA galaxies (González Delgado et al., 2015). This dependence is also prominent in MaNGA galaxies, where LTGs show an even stronger negative correlation between metallicity gradient and stellar mass than ETGs (Goddard et al., 2017). The sample of simulated ETGs in iMaNGA does not reproduce the metallicity gradients’ dependence on stellar mass, but the iMaNGA LTGs have steeper negative gradients as their stellar mass increases (Nanni et al., 2024).

Jones et al. (2013) measured the redshift evolution of metallicity gradients in four gravitationally lensed galaxies at  $z = 2.0 - 2.4$ , compared them to the literature, and found that the steep negative metallicity gradients flatten with time. Therefore, an older galaxy should have flatter metallicity gradients. A correlation of gas-phase metallicity gradients with mass-weighted age is not observed by Cheng et al. (2024), but they find an anti-correlation with an evolutionary time parameter that is related to the specific star formation history. This



**Figure 1.10:** The galaxy NGC 747 exhibiting stellar shells and streams. Image credit: Duc et al. (2013)

means more evolved galaxies have steeper metallicity gradients. A similar trend is found by Mercado et al. (2021) in zoom-in simulated dwarf galaxies. Their median stellar age is anti-correlated with the stellar metallicity gradients. The gradients are flatter in galaxies with a younger stellar population.

Rotationally dominated galaxies are found to have mostly steep negative gas-phase metallicity gradients, while dispersion-dominated galaxies mostly show flat or positive gradients (Jones et al., 2013; Sharda et al., 2021). This is confirmed by the cosmological simulation Illustris TNG50, where steep negative gas-phase metallicity gradients are only found in rotationally dominated galaxies, while almost all dispersion-dominated galaxies have flat or positive gas-phase metallicity gradients (Hemler et al., 2021). On the contrary, the steepest stellar metallicity gradients are found in dispersion dominated, early-type galaxies in the CALIFA survey (Zhuang et al., 2019).

## 1.2 Tidal Stellar Shells and Streams

Tidal shells and streams are features made up of stars which are found in the outskirts of galaxies. An impressive example of a galaxy which exhibits both types of features is NGC 474, which is seen in Figure 1.10. It was observed and processed to highlight the low surface brightness features by Duc et al. (2013).

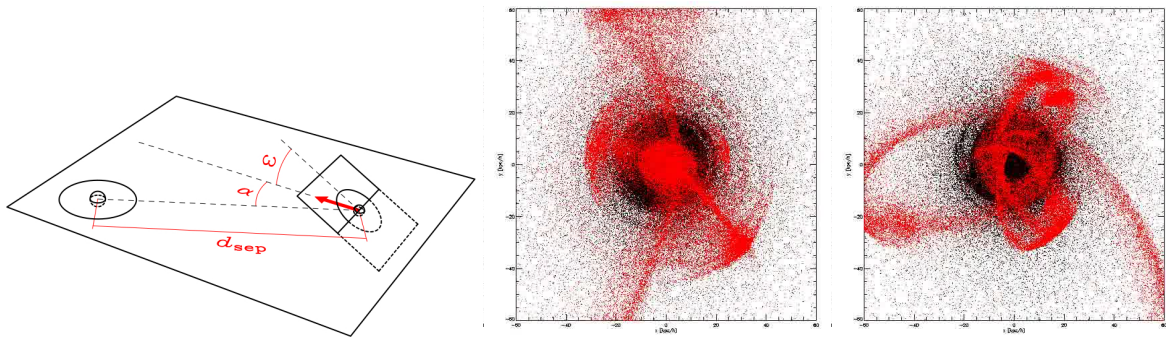


**Figure 1.11:** The simulation results by Karademir et al. (2019). *Left panel:* Illustration of the setup. The tilt between the merging satellite and the host galaxy is kept at  $\omega = 30^\circ$ . The merger occurs within the disk plane of the host galaxy, with an impact parameter of  $\alpha$ . *Middle panel:* Snapshot of the  $\alpha = 10^\circ$  simulation at a merger ratio of 1:50. *Right panel:* Snapshot of the  $\alpha = 40^\circ$  simulation at a merger ratio of 1:50. The host galaxy’s particles are shown in back, the satellite galaxy’s particles in red. Image source: <https://www.usm.uni-muenchen.de/~halos/database/family1.php>.

These tidal features hold information about their host galaxy’s formation history because they are remnants of satellite galaxies that once fell into the host galaxy. Therefore, they are particularly interesting for our understanding of galaxy formation. They have been studied and classified in galaxy surveys such as MATLAS (Duc et al., 2015; Bílek et al., 2020; Sola et al., 2022) and the Stellar Streams Legacy Survey (Martínez-Delgado et al., 2023a). Sola et al. (2022) created and used the online annotation tool JAFAR<sup>7</sup> to classify LSB features, such as tidal tails, streams, and shells, around 352 nearby galaxies from the MATLAS and CFIS survey. Among others, they calculated the widths of streams and radii of shells. Not only observational progress is being made, but simulations try to predict the formation scenario of shells and streams. Karademir et al. (2019) use isolated disk merger simulations and conclude that shells result from an infalling satellite galaxy on a radial orbit (small impact parameter, e.g.,  $\alpha = 10^\circ$ ), while streams are formed on orbits with a higher angular momentum (large impact parameter, e.g.,  $\alpha = 40^\circ$ ), as illustrated by Figure 1.11. Additionally, they find that if the satellite passes through the host galaxy’s disk, the features are more pronounced. A peculiar class of “umbrella”-like tidal features, which appear as a shell with a stream connected to their concave side, is sometimes observed and was studied in an isolated merger scenario by Martínez-Delgado et al. (2023b) for the tidal ring galaxy NGC 922. They estimated a total stellar mass for the umbrella of between  $6.9$  and  $8.5 \times 10^8 M_\odot$  and suggest a formation scenario of the tidal ring and “umbrella” structure from the infall of a gas-rich satellite around 150 Myr ago.

Shells and Streams were also studied in cosmological simulations such as Illustris (Pop et al., 2018; Amorisco, 2015) who find the same formation trends regarding their orbit. Pop et al. (2018) find that shells are preferentially formed by major mergers ( $M_\star^{\text{host}}/M_\star^{\text{satellite}} \gtrsim 1 : 10$ ) in a time-window of  $\sim 4$  to 8 Gyr. Large satellites can fall in on more circular orbits and still produce shells compared to less massive satellites, due to dynamical friction.

<sup>7</sup><https://jafar.astro.unistra.fr/>

Simulations are also used to predict the detection rate and identification possibilities of upcoming galaxy surveys (Martin et al., 2022; Khalid et al., 2024; Miro-Carretero et al., 2024). Martin et al. (2022) produce realistic mock images using the NewHorizon cosmological simulation at the 10-yr depth of the Legacy Survey of Space and Time (LSST) of the Vera C. Rubin Observatory  $\mu_{\text{limit}} \sim 30 - 31 \text{ mag arcsec}^{-2}$ . 80% of the flux from tidal features is detected at this limit. Khalid et al. (2024) also produce mock images from the NewHorizon, Eagle, IllustrisTNG, and Magneticum simulation at a similar surface brightness limit and detect a tidal feature fraction of  $f_{\text{tidalfeature}} \sim (36 \pm 4)\%$  for all of them. The simulations also agree regarding the trends of  $f_{\text{tidalfeature}}$  with halo and stellar mass, suggesting that the different implementations of subgrid physics and hydrodynamics do not significantly impact the physics of tidal shells and streams, which are driven by gravity.

Regarding the metallicities of stellar shells, Pop et al. (2017) identified 39 shell galaxies from a sample of 220 massive ellipticals from the Illustris simulation and found that stellar shells are more metal-rich than their surrounding host galaxy and formed through merger with high mass ratios. They measure that shell galaxies have higher metallicities at  $2 - 4r_{\text{eff}}$  compared to galaxies without shells. Regarding the age of streams, observations of the individual stream around M83 by Barnes et al. (2014) determine it to be at least older than  $\sim 100 \text{ Myr}$  from flux measured in the FUV band.

Finally, Valenzuela & Remus (2024) connect the tidal features in the outskirts to the inner kinematics of galaxies (see Section 1.1.2). Host galaxies are much more often elliptical galaxies, as opposed to disk galaxies. Shells are preferentially found around slow rotating galaxies and most often around prolate rotators. The highest likelihood of exhibiting a tidal feature have kinematically distinct cores, namely, 20% are accompanied by streams. A similar trend is also observed in the SAMI galaxy survey by Rutherford et al. (2024), who use the detection of low surface brightness tidal features to study the role mergers play in the creation of slow rotators. The average  $\lambda_{r_e}$  is significantly lower for galaxies with shell features. Shell features are related to a radial major merger (e.g., Karademir et al., 2019).

# Chapter 2

## Methodology

### 2.1 The Magneticum Pathfinder Simulation

The galaxies analyzed in this work are selected from the *Magneticum Pathfinder Simulations*<sup>1</sup> (Hirschmann et al., 2014; Ragagnin et al., 2017, Dolag et al. in prep.), which is a suite of cosmological hydrodynamical simulations performed with the Tree/SPH code GADGET-3, the successor of GADGET-2 (Springel et al., 2001b), including various improvements, for example the used kernels (Dehnen & Aly, 2012; Beck et al., 2016), artificial viscosity (Dolag et al., 2005b), and passive magnetic fields (Dolag et al., 2009). The underlying cosmology is standard  $\Lambda$ CDM using parameters adopted from the seven-year results of the Wilkinson Microwave Anisotropy Probe (WMAP7, Komatsu et al. (2011)). The density parameters are  $\Omega_b = 0.0451$ ,  $\Omega_M = 0.272$ , and  $\Omega_\Lambda = 0.728$ , for baryons, matter, and dark energy. The reduced Hubble parameter is  $h = 0.704$  and the normalization of the fluctuation amplitude at 8 Mpc is  $\sigma_8 = 0.809$ .

Additionally, the simulations consider a collection of subgrid models responsible for physics important for the enrichment of the ISM with metals, such as cooling, star formation and winds (Springel & Hernquist, 2003), black holes and AGN feedback (Springel et al., 2005; Fabjan et al., 2010; Hirschmann et al., 2014). Thermal conduction is implemented as 1/20th of the classical Spitzer value (Spitzer, 1962; Dolag et al., 2004). The models focusing on stellar evolution and metal enrichment are described by Tornatore et al. (2004, 2007) and Dolag et al. (2017). Up to four stellar particles can be formed from one gas particle (Springel & Hernquist, 2003). Each star particle represents a simple stellar population following the initial mass function by Chabrier (2003).

For this work, I use Box4 (uhr), which has a side length of 48 Mpc/h. The masses of particles are  $m_{\text{DM}} = 3.6 \times 10^7 M_\odot h^{-1}$ ,  $m_{\text{gas}} = 7.3 \times 10^6 M_\odot h^{-1}$ , and on average  $\langle m_\star \rangle = 1.4 \times 10^6 M_\odot h^{-1}$ , for dark matter, gas, and stars, respectively. The softening lengths are  $\epsilon_{\text{dm}} = \epsilon_{\text{gas}} = 1.4 \text{ kpc } h^{-1}$ , and  $\epsilon_\star = 0.7 \text{ kpc } h^{-1}$ . The galaxies in this box have been found to match well with observations regarding angular momentum (Teklu et al., 2015), kinematics (Schulze et al., 2018; van de Sande et al., 2019; Schulze et al., 2020), dynamics (Remus et al.,

---

<sup>1</sup>[www.magneticum.org](http://www.magneticum.org)

2017; Teklu et al., 2017; Harris et al., 2020), and the in-situ components’ fractions (Remus & Forbes, 2022). The stellar metallicity gradients have been studied and compared with those of globular clusters in ETGs (Forbes & Remus, 2018).

Main halos and subhalos are identified by SUBFIND (Springel et al., 2001a), which applies a standard friends-of-friends (FOF) algorithm (Davis et al., 1985) and is modified to include the baryonic component (Dolag et al., 2009). SUBFIND identifies *halos* as the FOF group. In a second step, this FOF group is taken as an input to find *substructures* within it. A *substructure candidate* is a region enclosed by an isodensity contour that crosses a saddle point. One can imagine this algorithm as the gradual lowering of a global density threshold, where two separate regions will first only grow in size, until they join at a saddle point. Additionally, enforcing the particles within such a region to be self-bound and several other modifications, for example ensuring that one particle is only attributed to one *substructure candidate*, leads to the definition of a *subhalo*. Its position is set to that of the most bound particle, and its velocity center to the mean velocity of all particles within it. This approach always leads to a *main subhalo*, the most massive one within the FOF group, the remaining *subhalos*, and particles that are not yet bound to any of these structures, representing “fuzz” (Springel et al., 2001a).

## 2.2 Simulation Merger Trees

Merger trees are a way to find the merger history of a selected *subhalo*, for example, two separate subhalos in a previous snapshot merge to form a single subhalo in the final snapshot. The merger tree provides the information to find the two former subhalos for a given final subhalo. A very basic algorithm to construct the merger tree of dark matter halos is given as follows: Imagine a halo  $H_A$  at redshift  $z_A$  ( $t_{\text{sim},A}$ ) and a halo  $H_B$  at  $z_B > z_A$  ( $t_{\text{sim},B} < t_{\text{sim},A}$ ). If at least half of the  $H_B$  particles are contained within  $H_A$  and the most bound particle of  $H_B$  is also contained within  $H_A$ , then the halo  $H_B$  is considered a *progenitor* of a halo  $H_A$  (Springel et al., 2001a). With a few additions, this simple algorithm can also be used to construct merger trees for *subhalos*. The structure of such a merger tree is presented in 2.1. The term *progenitor* is already described above. A halo  $H_A$  (middle circle in bottom row) can have multiple *progenitors* (sometimes called *direct progenitors*)  $H_B^1, H_B^2, H_B^3$  (middle three circles in 2nd row from the bottom). In the opposite direction,  $H_A$  is the *descendant* of  $H_B^1, H_B^2, H_B^3$ . The most massive among  $H_B^1, H_B^2, H_B^3$  is the *first progenitor*  $\hat{H}_B$  (3d from the left in the 2nd row from the bottom) of  $H_A$ . The remaining *progenitors* are sometimes called the *progenitor siblings* of  $\hat{H}_B$ . Because halos aren’t always recognized in every snapshot, it is likely that not all *direct progenitors* are from the same snapshot (see the direct progenitors of the middle halo in the 2nd row from the bottom). This includes the *first progenitor*.

Using such merger trees, the mass assembly history (e.g. bottom row of Figure 3.2) can be calculated, or a certain halo can be traced back in time while creating maps of their mass, velocity, etc. so that their full evolution is visually available, as done in Chapter 4.

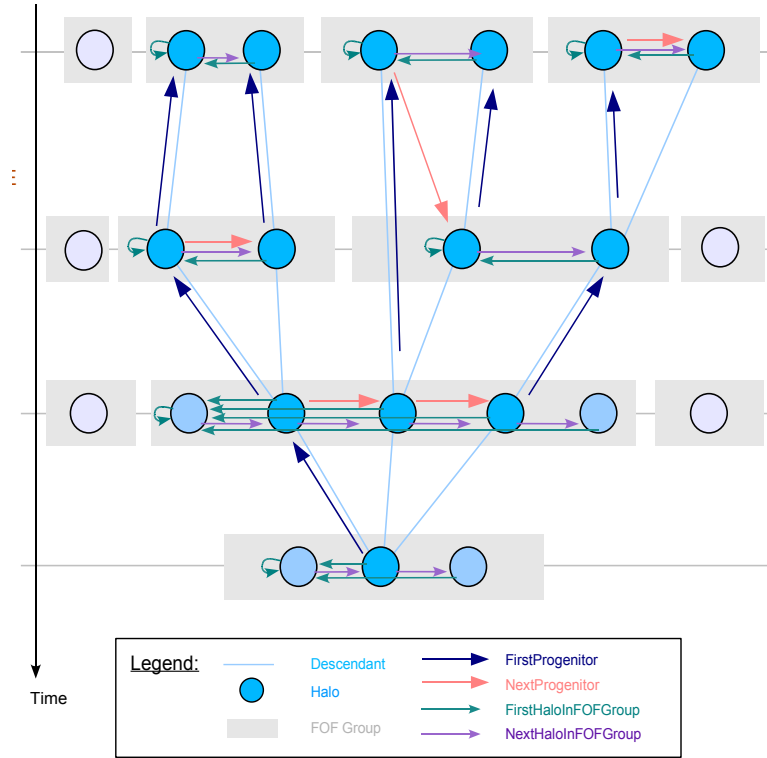


**Figure 2.1:** The structure of a halo merger history tree.

## 2.3 Centering and Rotation of Galaxies

This thesis mostly deals with galaxies or structures found within and around them. Therefore, it needs to be defined what “galaxy” means in the context of cosmological simulations. In Section 2.1 the definitions of *halo*, *main subhalo*, and *subhalo* were introduced. Unless stated otherwise, I will refer to a *main subhalo* as *galaxy* or *central galaxy* or *host galaxy*, in the context where a *subhalo* falls into the *main subhalo*, and to the infalling subhalo as *satellite galaxy*. Most often, a mass cut is applied to ensure that a galaxy contains enough particles to be sufficiently resolved. Another measure to ensure consistent conditions is a robust centering of each galaxy. The method used here follows that of Valenzuela et al. (2024).

First, the initial half-mass radius  $r_{1/2}^{\text{ini}}$  is calculated from all particles within  $10\%r_{\text{vir}}$ . Next, the stellar center-of-mass is iteratively determined using a shrinking-sphere method (Power et al., 2003). Initially, the center-of-mass within a sphere of radius  $4r_{1/2}^{\text{ini}}$  is calculated, then the particles shifted accordingly, and finally the sphere is shrunk by 2.5%. This is done repeatedly until the sphere reaches a radius of  $1r_{1/2}^{\text{ini}}$ , it includes only 1% of the initial stellar particles or 1000 stellar particles. The whole galaxy is translated into the center-of-mass frame of the final iteration. The actual half-mass radius  $r_{1/2}$  is calculated in this frame in the same manner as the initial one. Finally, the center-of-velocity is calculated as the mass-weighted mean velocity from the stellar particles that are within  $1r_{1/2}$  and are not the fastest 10% according to the absolute velocity. Again, a transformation is applied to the galaxy particles’ velocities. If the gas content of the galaxy is considered, the same translation using

the stellar center-of-mass and velocity are applied. This approach provides a robust centering of the galaxies.

The calculation of the shape of each galaxy and the corresponding rotation matrix can be calculated from the mass distribution tensor (Zemp et al., 2011) (also called the inertia or shape tensor)

$$M_{ij} = \sum_k m_k r_{k,i} r_{k,j}, \quad (2.1)$$

where  $m_k$  is the particle mass,  $\mathbf{r}_k$  the particle position relative to the host galaxy’s center, and  $k$  runs over all particles within  $3r_{1/2}$ . Valenzuela et al. (2024) discusses several different methods to determine the most accurate shape, and conclude an iterative unweighted method at constant volume produces the best results. “Unweighted”, in this case, refers to not using an additional weight  $w(\mathbf{r}_k)$ . In the iterative approach, an initial tensor  $\mathbf{M}$  is first calculated from all considered particles, the rotation matrix  $\mathbf{M}^{-1}$  is determined as its inverse, the particles are rotated accordingly and the axis ratios are determined. This is repeated until the axis ratios  $q = b/a$  and  $s = c/a$  do not change much anymore ( $\Delta = 1 \times 10^{-4}$ ) or a maximum of 50 iterations is reached. These axis ratios, where  $a \geq b \geq c$  are the half-axis lengths of the corresponding ellipsoid, can be calculated from the eigenvalues ( $\lambda_1 \geq \lambda_2 \geq \lambda_3$ ) of  $\mathbf{M}$  as  $q = \sqrt{\lambda_2/\lambda_1}$ ,  $s = \sqrt{\lambda_3/\lambda_1}$ , and  $p = \sqrt{\lambda_3/\lambda_2} = c/b$ . The particles are rotated with the rotation matrix  $\mathbf{M}^{-1}$ . The *edge-on* projection is found by plotting  $\mathbf{r}_1$  against  $\mathbf{r}_3$ , the *face-on*, and *side-on* projections are visible by considering  $\mathbf{r}_1$  against  $\mathbf{r}_2$ , and  $\mathbf{r}_2$  against  $\mathbf{r}_3$ , respectively. The algorithms used in this work are implemented in the JuliaCosmoSims package and GadgetIO.jl (Böss & Valenzuela, 2024).

## 2.4 Luminosity Calculations

The luminosity of stellar particles is an important quantity that is not intrinsic to N-body/SPH particles, but needs to be calculated additionally. It is very useful to be able to compare simulations to observations because a star’s luminosity obviously heavily effects our observation of its spectrum and any other quantity. The GALAXEV code (Bruzual & Charlot, 2003) was used to construct tables that encompass metallicities (metal mass fraction of total mass) between 0.0001 and 0.05, from which the stars’ luminosities are calculated. Additionally, the star particle’s age and initial mass are included in the computation, so that the final value is obtained by a trilinear interpolation. The AB magnitude for a single stellar particle is calculated as  $m_{AB} = -2.5 \log_{10}(\frac{L}{L_\odot}) + 8.90$ . This calculation is implemented in the JuliaCosmoSims package. Figure 2.2 shows the color-magnitude diagram (*left panel*), and the color-stellar mass diagram (*right panel*). Here, color is defined as the difference between the **u**- and **r**-band, and the **r**-band magnitude is used. As expected, the galaxies separate into the so-called *red sequence*, made up of spheroidal (low *b-value*) galaxies, and the *blue cloud*, made up of disk galaxies (high *b-value*). Between the two, a gap called the *green valley* is expected. Observational results of which are displayed by the green lines in the *right panel*

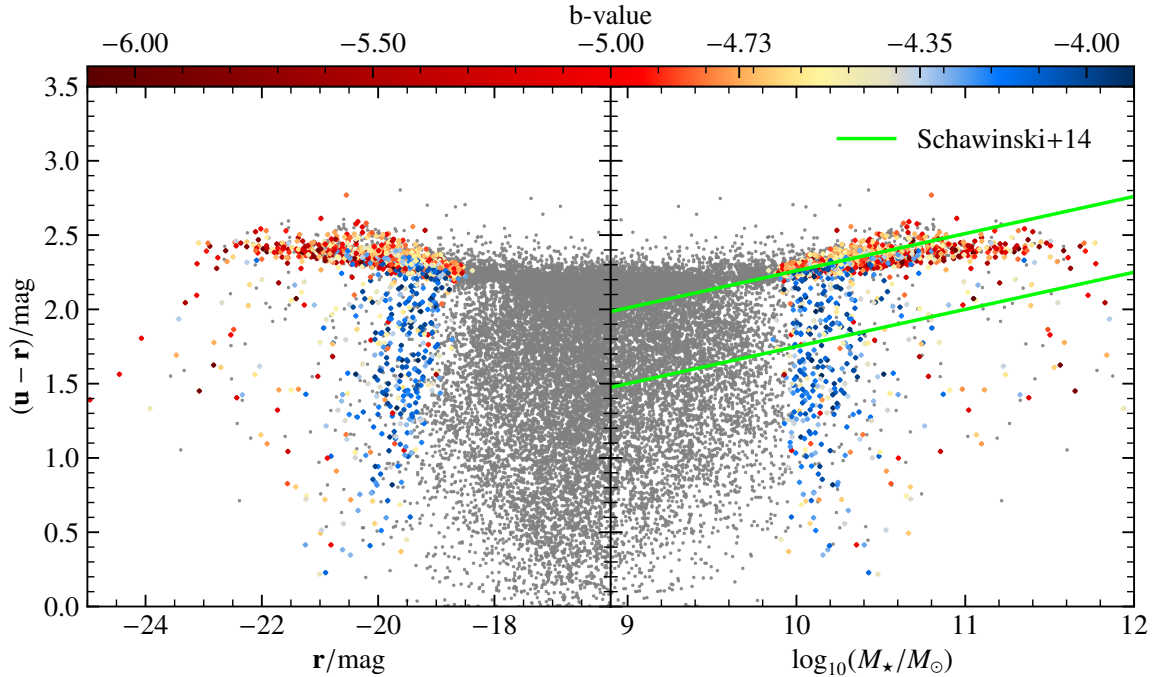


**Figure 2.2:** *Left panel:* Color( $u - r$ )-magnitude( $r$ ) digram of the *Magneticum* galaxies. *Right panel:* Color( $u - r$ )-stellar mass  $M_*$  diagram of the *Magneticum* galaxies. In both panels, the galaxies are colored by their  $b$ -value. Subhalos with masses  $< 1 \times 10^{10} M_\odot$  are shown as gray dots. The right panel also shows results by Schawinski et al. (2014) depicting the boundaries of the so called “green valley” as green lines.

(Schawinski et al., 2014). The slope of the *green valley* as measured by Schawinski et al. (2014) is not exactly reproduced, but a slight slope in the color-stellar mass diagram is present for spheroidal galaxies. The *blue cloud* is extended by the  $< 1 \times 10^{10} M_\odot$  subhalos to lower stellar masses (higher magnitudes/lower luminosity). Overall, the simulation combined with the above luminosity calculation produces luminosities that agree well with observations.

## 2.5 Definitions of Galaxy Properties

Several global and spatially resolved properties of galaxies will be considered in this work. I will introduce general parameters in this section. Some more specialized parameters will be defined in subsequent sections. Following the calculation of the galaxies’ shape tensors described in Section 2.3 the intrinsic ellipticity of each galaxy is calculated from the ellipsoid’s 3D axis ratio  $s$ , as

$$\epsilon = 1 - s, \quad (2.2)$$

which is tightly correlated with the 2D determined edge-on ellipticity (Valenzuela et al., 2024).

One of the most important parameters in extragalactic astrophysics is the stellar mass of a galaxy. In this work, *stellar mass* will refer to the sum of the masses of all stellar particles within a sphere of a certain radius:

$$M_{\star} = \sum_i m_i^{\text{star}}(r_i < \tilde{r}) \quad (2.3)$$

Two different radii will be used, either  $\tilde{r} = 3r_{1/2}$  or  $\tilde{r} = 0.1r_{\text{vir}}$ . It will be stated where necessary which radius is used. This is done to be better comparable to observations, as many current observations cannot resolve a galaxy to large radii. Another important property is the age of a galaxy. The simulation output provides the scale factor  $a_{\text{form}}^2$  of the universe at which each stellar particle formed. A galaxy's age is calculated by first transforming  $a_{\text{form}}$  into the star's age (lookback time) and averaging over all stars within a sphere of radius  $3r_{1/2}$ , resulting in the mean stellar age

$$\langle t_{\star} \rangle_{\text{lw/mw}} = \frac{\sum_i w_i t_{\text{lookback}}(a_{\text{form}}^i)}{\sum_i w_i}, \quad (2.4)$$

where  $w_i$  can be the r-band luminosity or the stellar mass for the considered particle in the luminosity weighted (lw) or mass weighted (mw) case, respectively. Averaging  $a_{\text{form}}$  first and transforming the mean formation scale factor into an age strongly correlates with the first method (see Appendix A).

Closely related to the age of a galaxy is the metallicity of a galaxy. There are several definitions of this term within the discipline of astrophysics. The ones used in this work are

$$[Z] = \log_{10}(Z/Z_{\odot}), \quad (2.5)$$

where  $Z$  is the sum of the mass fractions of all elements heavier than helium and  $Z_{\odot} = 0.0140$  (Kudritzki et al., 2016). The second one is

$$[Z/H] = \log_{10}(Z/H) - \log_{10}(Z/H)_{\odot}, \quad (2.6)$$

where  $Z$  is the same as before,  $H$  is the mass fraction of hydrogen and  $(Z/H)_{\odot} = 0.0181$  (Asplund et al., 2009). If this quantity is to be weighted similarly to how the age is weighted, one needs to be careful. The weighted mean of, for example Equation 2.5, is

$$\langle [Z] \rangle_{\text{lw/mw}} = \frac{\sum_i w_i [Z]_i}{\sum_i w_i} = \frac{\sum_i w_i \log_{10}(Z_i/Z_{\odot})}{\sum_i w_i}. \quad (2.7)$$

A more direct approach would be to calculate the weighted mean before applying the logarithm

$$\log_{10}(\langle Z/Z_{\odot} \rangle_{\text{lw/mw}}) = \log_{10}\left(\frac{\sum_i w_i Z_i/Z_{\odot}}{\sum_i w_i}\right). \quad (2.8)$$

Because  $Z_i$  are mass fractions, summing over them yields the total mass of all metals within a galaxy divided by the total mass. The logarithm is often applied afterward. But one

---

<sup>2</sup>The scale factor is defined in a FLRW (Friedmann-Lemaître-Robertson-Walker) universe. At an arbitrary reference time  $t_0$ , the scale factor is  $a(t_0) = 1$  and the comoving distance  $d_0$  is equal to the proper distance  $d(t_0) = d_0$  between two objects. The proper distance between these two objects at a different time  $t$  is then given by  $d(t) = a(t)d_0$ , where  $a(t)$  is the scale factor at  $t$ . It is related to the cosmological redshift as  $a(t) = 1/(1+z)$ .

still needs to be careful when comparing this result to observations because observational methods are rather different. Gas phase metallicities are often derived from individual spectral lines ratios, for example from the ratio [O III] ( $\lambda = 4363 \text{ \AA}$ ) to a lower excitation state [O III] ( $\lambda = 5007 \text{ \AA}$ ) from which the electron temperature  $T_e$  can be estimated and further a metallicity can be inferred using several models (Kewley & Ellison, 2008). These approaches are highly dependent on the chosen metallicity calibration (Kewley & Ellison, 2008). An approach to measuring stellar metallicities of galaxies is *stellar population synthesis* (Zahid et al., 2017; Sestl et al., 2023, 2024), where the spectrum of a whole galaxy is modeled as the linear combination of the spectra of  $n_{\text{SSB}}$  *single stellar bursts* (SSBs), which depend on age  $t_i$  and the logarithmic metallicity  $[Z]_i$ . The fit of the linear combination to the observed spectrum yields the coefficients  $b_i$ , which describe the contribution of burst  $i$ . Typically, the average metallicity of a galaxy is then calculated as  $[Z] = \sum_i^{n_{\text{SSB}}} b_i [Z]_i$  (Sestl et al., 2023). These very different approaches cannot be directly compared to the simulations. A direct comparison requires a more refined modeling, including mock spectra of each simulation particle being convoluted with noise, instrumental resolution characteristics and applying the same analysis pipeline used for observations (e.g., Nelson et al., 2018). On the flip side, this dramatically reduces the quality of the simulation data, for example higher uncertainties are introduced by adding artificial noise, applying a certain telescope’s point-spread function and many more alterations, which are inherent to observational techniques. Due to all these differences, the interpretation of a comparison with observations needs to be done carefully. Nevertheless, for reasons stated above, Equation 2.8 and its counterpart regarding  $[Z/H]$  will be used in this work.

Moving to spatially resolved quantities, metallicity gradients will be considered. They are quantified by radially binning the stellar particles within a sphere of  $3r_{1/2}$  in equal-number bins that each contain 50 particles and fitting a straight line

$$[Z/H](r) = \nabla[Z/H] \times r/r_{1/2} + [Z/H]_0, \quad (2.9)$$

similar to equation (1) in Kudritzki et al. (2016). An exemplary spheroidal, intermediate, and disk galaxy are shown in Figure 3.20. Finally, I introduce the definitions of different age population of stars. In this work, star particles younger than 2 Gyr will be called *young* stars, particles between 2 Gyr and 8 Gyr are *middle-aged*, and *old* stellar particles are older than 8 Gyr.

## 2.6 Voronoi-binned Maps

The Voronoi-binning technique is based on the *Voronoi Tessellation*, named after the Russian mathematician Georgy Voronoy. Given a set of points (or seeds/generators) it is a partition of a plane into regions according to the *nearest-neighbor-rule*: “Each point (seed/generator) is associated with the region of the plane closest to it” (Aurenhammer, 1991) (see Figure 2.3). The resulting cells are called *Voronoi cells* and are convex polygons. This type of tessellation

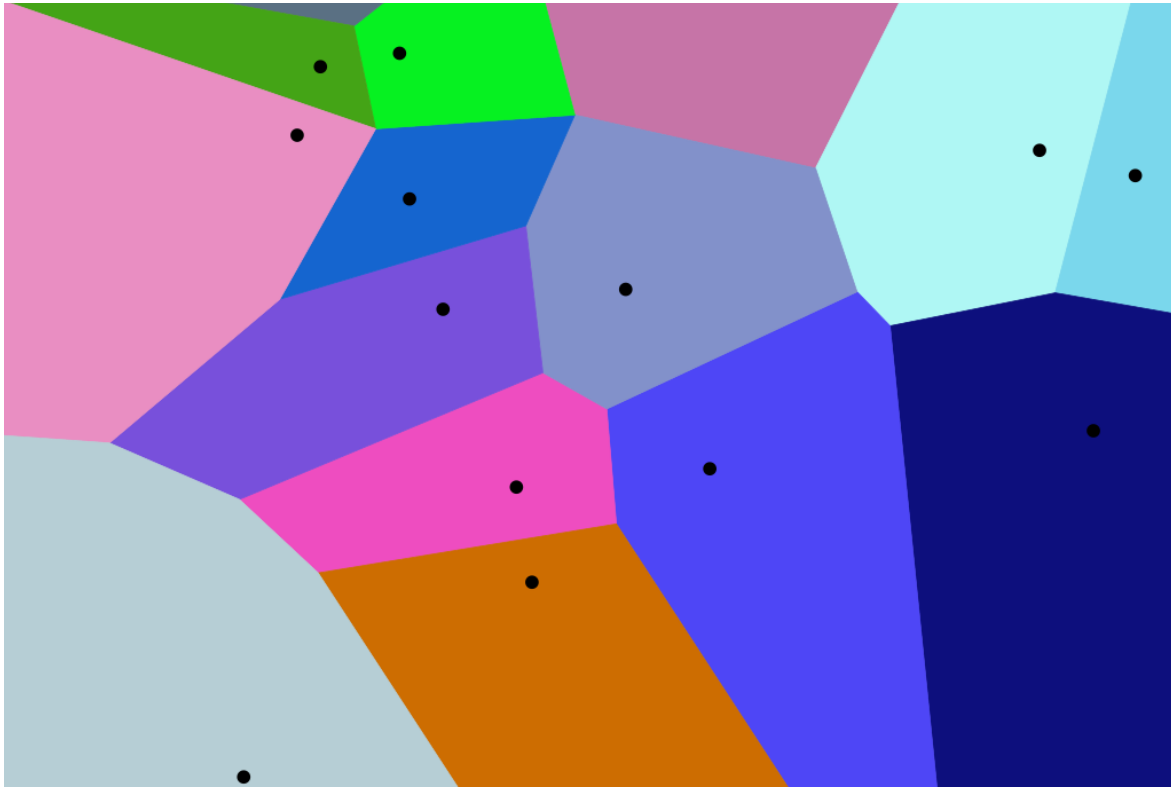


**Figure 2.3:** Voronoi Tessellation of the plane given a set of seeds. Image credit: Balu Ertl (Pseudonym), Image Source: [https://en.wikipedia.org/wiki/Voronoi\\_diagram](https://en.wikipedia.org/wiki/Voronoi_diagram)

has a large variety of applications in the natural sciences, for example in solid-state physics, the Voronoi cell around a crystal lattice point is called a *Wigner-Seitz* cell which is used to investigate all sorts of crystal structures, or in biology, where they model cells. In astrophysics, they can be used to increase the signal-to-noise (S/N) ratio, which is typically done when using IFU spectroscopy. The original pixels from the bundle of fibers observing a galaxy are binned together within Voronoi-cells. When using this approach on simulation output, the only difference is, that instead of pixels the simulation particles are used.

A popular method is an adaptive spatial binning technique using centroidal Voronoi tessellations (Cappellari & Copin, 2003) because it satisfies three convenient requirements.

1. It properly tessellates the whole plane without overlapping or holes.
2. The bins are fairly “round” or “compact” so that each pixel is still closely associated with its original position.
3. The scatter in the S/N of the bins is small so that spatial resolution is not sacrificed over a required minimal S/N.

The second requirement is only satisfied by the *centroidal* Voronoi tessellation, where a uniquely tailored choice of seeds is used. The seeds  $z_i$  need to coincide with the mass centroids

$$z_i = \frac{\int_{V_i} \mathbf{r} \rho(\mathbf{r}) d\mathbf{r}}{\int_{V_i} \rho(\mathbf{r}) d\mathbf{r}} \quad (2.10)$$

of the corresponding Voronoi cells  $V_i$ . This can be achieved using the following algorithm presented by Cappellari & Copin (2003):

1. Select an random initial set  $z_i$  of seeds drawn from a probability distribution proportional to  $\rho(\mathbf{r})$ .
2. Perform a Voronoi tessellation of the considered plane with the seeds  $z_i$ .
3. Compute the mass centroids of the Voronoi cells  $V_i$  according to the density  $\rho' = \rho^2$ . Make the mass centroids the new seeds.
4. Iterate from step 2. over step 3. until the coordinates of the Voronoi tessellation do not change anymore.

Voronoi-binned maps are created from the mean values of the desired property within each Voronoi cell. In this work, the above algorithm – with a few modifications – is used as implemented in the JuliaCosmoSims package.

Because the density of stellar particles is higher in the center of a galaxy, the Voronoi-cells will be smaller there (e.g. see Figure 3.2).  $(V/\sigma)_{r_{1/2}}$  and  $\lambda_{r_{1/2}}$  are calculated from such a Voronoi-binned map using the mean line-of-sight velocity and mean line-of-sight velocity dispersion within each cell according to Equation 1.8 and 1.9. The used Voronoi cells' seeds/mass centroids lie within the galaxy's shape ellipse, calculated at  $1r_{1/2}$ .



# Chapter 3

## Age and Metallicity of Galaxies

Stellar ages and metallicities are a direct tracer of a galaxy's star formation and chemical enrichment history. There are two scaling relations connecting the galaxy's metallicity and age to its stellar mass, the mass-metallicity relation and mass-age relation. Massive galaxies are typically more metal-rich and older than low-mass galaxies (e.g., Tremonti et al., 2004, Gallazzi et al., 2005). A more detailed insight into the star formation history give spatially resolved ages and metallicities. If stars are first formed in the center and star formation is progressing outward (*inside-out growth*), the galaxy will have a negative age gradient. If the opposite is true – stars first forming in the outskirts and star formation progressing inward (*inside-out growth*) – the age gradient will be positive (e.g., González Delgado et al., 2015). In the first scenario, stars had more time to enrich their surroundings with metals, which is why the interstellar medium and newly formed stars are more metal rich in the center, again leading to a negative metallicity gradient (e.g. Venturi et al., 2024). Again, the opposite scenario would build up a positive metallicity gradient. The spatial distribution of metals and ages can be studied by IFU surveys, which record a spectrum in multiple different parts of a galaxy, from which the ages and metallicities can be calculated via stellar population synthesis methods (Goddard et al., 2017; Neumann et al., 2021; Nanni et al., 2024). Studying relations between the metallicity gradient and global properties of a galaxy can give a hint towards what shapes this metallicity gradient, in addition to the progression of star formation. One known possible relation is the increase in the negative metallicity gradient's absolute value with increasing stellar mass (e.g., González Delgado et al., 2015; Goddard et al., 2017; Nanni et al., 2024). Several other properties related to the galaxy's age or rotational support have also been investigated, but no conclusive results have been established so far (e.g. Jones et al., 2013; Zhuang et al., 2019; Mercado et al., 2021; Sharda et al., 2021; Hemler et al., 2021; Cheng et al., 2024).

In the following chapter, the global properties regarding stellar ages and metallicities of galaxies and their connection to stellar masses and their sizes is studied. Followed by an analysis of age and metallicity profiles and metallicity gradients. The contribution and distribution of stars of different ages gives valuable insights into the formation and assembly history of a galaxy. Therefore, a classification of stellar populations will be used. We split the stellar content of the galaxies into a *young*, *middle-aged*, and *old* population, as defined

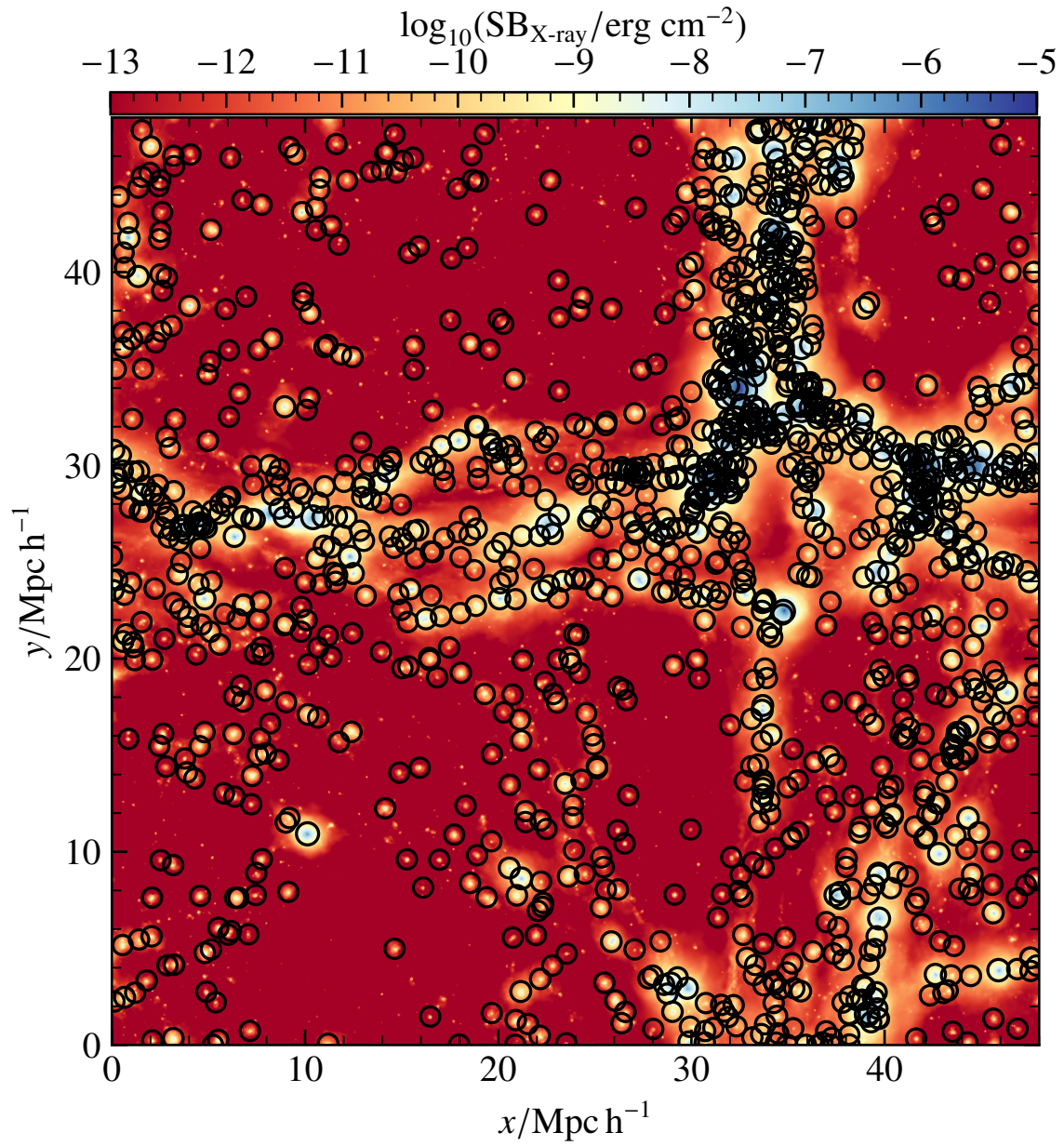


**Figure 3.1:** X-ray surface brightness map of Magneticum Box 4. Each galaxy considered in Chapter 3 is enclosed by a circle, whose radius is scaled by its stellar mass. This map was produced using *smac* (Dolag et al., 2005a) and data extracted from the Cosmological Webportal (Ragagnin et al., 2017).

in Section 2.5. Finally, the age and metallicity profiles are investigated for different groups of galaxies.

I extract all main subhalos identified by SUBFIND with stellar masses  $M_{\star} \geq 10^{10} M_{\odot}$  at  $z = 0$ . After selection, the stellar mass is calculated within a sphere of radius  $3r_{1/2}$  resulting in  $9.83 < \log_{10}(M_{\star}/M_{\odot}) < 12.36$ , while 90% of the galaxies lie within  $9.96 < \log_{10}(M_{\star}/M_{\odot}) < 11.18$ . This limit was chosen to ensure a sufficient resolution of the stellar component, resulting in 1319 galaxies, whose positions are circled in the X-ray surface brightness map of Box4 in Figure 3.1. They are centered robustly as described in Section 2.3. The classification into *disks*, *intermediates* and *spheroids* is done using the *b-value* considering only particles within  $3r_{1/2}$ , as described in Section 1.1. This method labels 334 galaxies as disks, 463 as intermediates and 522 as spheroids.

To get a first insight into the of ages and metals in galaxies, Figure 3.2 shows Voronoi-binned edge-on maps for an exemplary spheroidal (*left column*) and disk (*right column*) galaxy together with their stellar mass assembly and star formation history. The stellar mass within  $3r_{1/2}$  of the spheroidal and disk galaxy are  $4.2 \times 10^{11} M_{\odot}$  and  $2.57 \times 10^{11} M_{\odot}$ . Their mean luminosity-weighted stellar ages  $\langle t_{\star} \rangle_{\text{lw}}$  are 9.63 Gyr and 8.65 Gyr and they have a luminosity-weighted metallicity  $\log_{10}(\langle Z/Z_{\odot} \rangle_{\text{lw}})$  of 1.39 and 1.66. These global properties are already representative of the trends, that spheroidal galaxies are on average more massive and older than disk galaxies. In the *first row* of Figure 3.2, the color represents the mean stellar age, in the *second row* the color encodes the luminosity-weighted mean stellar metallicity  $\log_{10}(\langle Z/Z_{\odot} \rangle_{\text{lw}})$ . The *third to fifth rows* are the same as the second row, only for the young, middle-aged, and old stars, respectively. In the *sixth row*, the black line shows the stellar mass assembly history, that is how the stellar mass of the galaxy's progenitors changed over time and the blue histogram shows the star formation history, that is the distribution of ages among the galaxy's stars. The spheroidal galaxy appears to be rather homogeneously populated by mostly old stars, while the disk galaxy's disk consists of young stars. The center of the spheroidal is slightly more metal-rich, while the disk galaxy's disk is clearly more metal-rich than the outskirts. As expected, the young stars in the disk are the most metal-rich population, followed by the middle-aged stars, while the old stars are metal-poor. But in all three populations, the metal-rich stars are still located in the disk. Surprisingly, the young stars in the center of the spheroidal galaxy are metal-poor compared to middle-aged stars in the center of the spheroidal galaxy. This can be explained by the mass accretion and star formation history. The stellar mass of the spheroidal galaxy sharply doubled roughly 6 Gyr ago, which indicates a major merger, while the disk galaxy had a shallow but steady increase in its stellar mass. Both galaxies formed the majority of their stars more than 10 Gyr ago, but the disk galaxy produced more of its stars in the last 5 Gyr than the spheroidal galaxy. The metal enrichment of the disk galaxy therefore is dominated by gradual star formation, during which each generation of stars produces metals that enrich the next generation of stars. It can be hypothesized that the merger disturbed this gradual star formation in the spheroidal galaxy, which lead to the young stars being less metal-rich than the middle-aged stars. These two examples already provide insight into how metallicity, ages, and their distributions among a

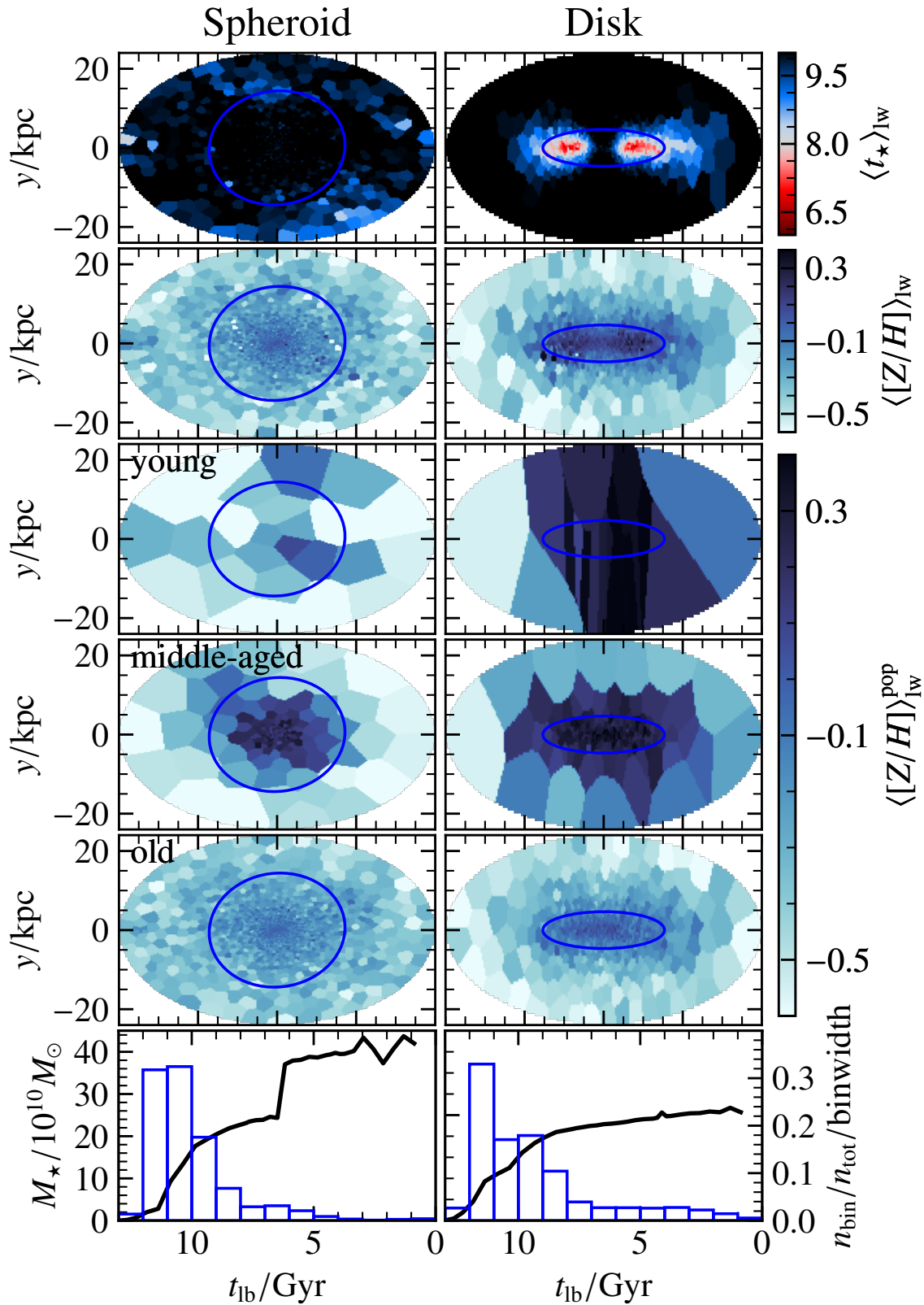


**Figure 3.2:** Voronoi-binned edge-on age and metallicity maps for an exemplary spheroidal (*left column*) and disk (*right column*) galaxy, together with their stellar mass assembly and star formation history. The blue ellipse represents the 2D ellipse at one (3D) half-mass radius  $r_{1/2}$ . *First Row:* The color represents the luminosity-weighted mean stellar age  $\langle t_{\star} \rangle_{\text{lw}}$  of each bin. *Second Row:* The color encodes the luminosity-weighted mean stellar metallicity  $\langle [Z/H] \rangle_{\text{lw}}$  of the bin. *Third Row:* Same as the second row, only for young stars ( $t < 2$  Gyr). *Fourth Row:* Same as second row, only for middle-aged stars ( $2 \text{ Gyr} < t < 8$  Gyr). *Fifth Row:* Same as second row, only for old stars ( $t > 8$  Gyr). *Sixth Row:* The black line shows the stellar mass assembly history, that is how the stellar mass of the galaxy’s progenitors changed over time and the blue histogram shows the star formation history, that is the distribution of ages among the galaxy’s stars.

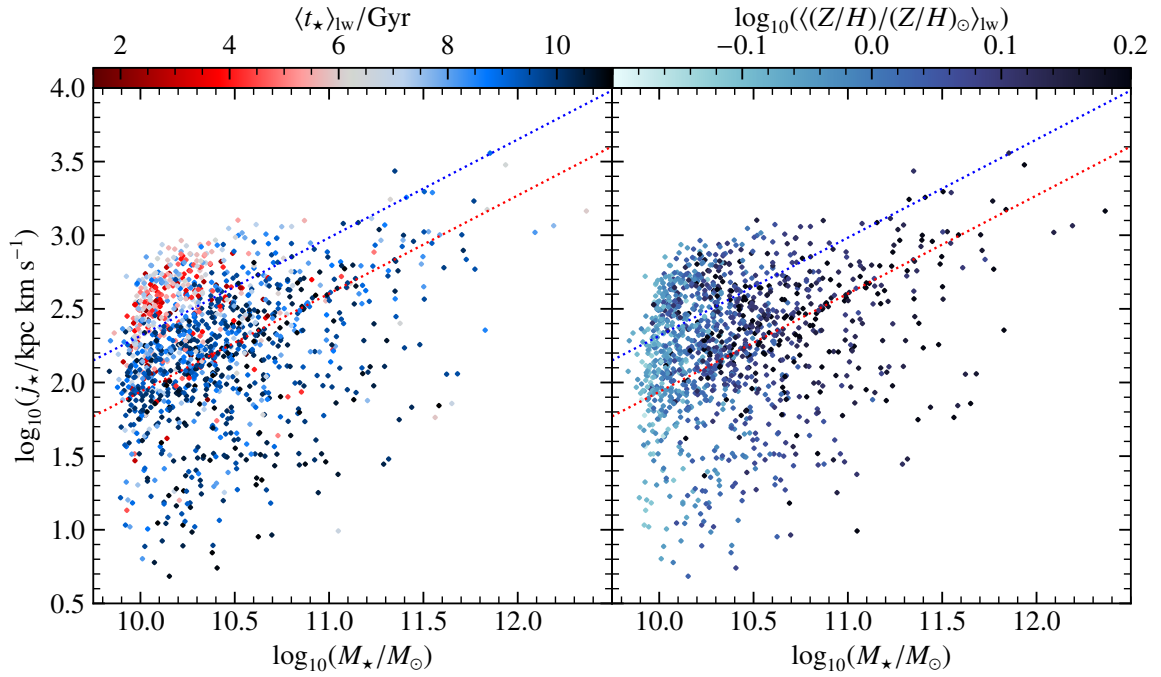


**Figure 3.3:** *Left:* Stellar specific angular momentum  $j_\star$  as a function of stellar mass  $M_\star$ , which are color coded by the luminosity (r-band) weighted stellar age  $\langle t_\star \rangle_{lw}$ . *Right:* The same as left, but the galaxies are color coded by the luminosity (r-band) weighted stellar metallicity  $\log_{10}(\langle Z/Z_\odot \rangle_{lw})$ , where  $Z$  is the sum of the mass fractions of all elements heavier than helium and  $Z_\odot = 0.0140$  (Kudritzki et al., 2016). The blue and red dotted lines are the boundaries in the  $b$ -value that divide the galaxies into disks ( $b > -4.35$ ), intermediates ( $-4.73 < b < -4.35$ ) and spheroids ( $b < -4.73$ ) (Teklu et al., 2015).

galaxy are connected to its formation history and why it is interesting to further analyze these connections.

### 3.1 Global Properties of Galaxies

Now I am investigating the global properties of the galaxy sample and how they compare to observations. Figure 3.3 shows the stellar specific angular momentum  $j = \sum_i m_i \mathbf{r}_i \times \mathbf{v}_i / \sum_i m_i$  as a function of the stellar mass  $M_\star$ , that is the stellar mass-stellar specific angular momentum plane. The left panel is colored by the luminosity-weighted stellar age  $\langle t_\star \rangle_{lw}$ , while the right panel is colored by the luminosity-weighted stellar metallicity  $\log_{10}(\langle Z/Z_\odot \rangle_{lw})$ . The blue and red dotted lines are the boundaries in the  $b$ -value that divide the galaxies into disks ( $b > -4.35$ ), intermediates ( $-4.73 < b < -4.35$ ) and spheroids ( $b < -4.73$ ) (Teklu et al., 2017). In the left panel, one can clearly see that disk galaxies (above the blue dotted line) are generally younger than spheroids (below the red dotted line). In the right panel, the metal-poorest galaxies are located at the lower end of the mass range, while the metallicity increases towards the higher end of the mass range. This suggests that age correlates with morphology, while metallicity correlates more with mass.

It is expected that luminosity-weighted ages  $\langle t_\star \rangle_{lw}$  are biased towards younger ages compared to mass-weighted ages  $\langle t_\star \rangle_{mw}$ , as young stars are typically brighter than old stars (Binney & Tremaine, 1987, Chap. 9). The luminosity-weighted metallicity  $\log_{10}(\langle Z/Z_\odot \rangle_{lw})$

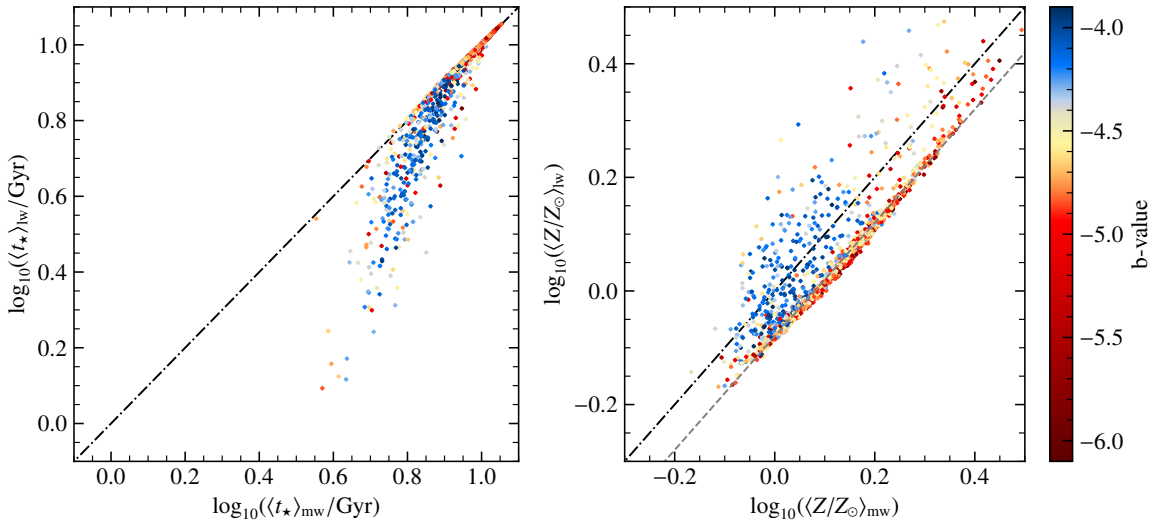


**Figure 3.4:** *Left:* Luminosity-weighted mean stellar age  $\langle t_{\star} \rangle_{lw}$  as a function of mass-weighted mean stellar age  $\langle t_{\star} \rangle_{mw}$ . *Right:* Luminosity-weighted mean stellar metallicity  $\log_{10}(\langle Z/Z_{\odot} \rangle_{lw})$  as a function of mass-weighted mean stellar metallicity  $\log_{10}(\langle Z/Z_{\odot} \rangle_{mw})$ . Both panels are colored by the  $b$ -value. The black dash-dotted line is the one-to-one relation. The gray dash-dotted line in the right panel is the one-to-one relation shifted down by 0.08 dex.

is also expected to be higher than the mass-weighted case, as young stars also are more metal-rich because they form out of gas which was already enriched (Binney & Tremaine, 1987, Chap. 9). Figure 3.4 shows the luminosity-weighted age  $\langle t_{\star} \rangle_{lw}$  as a function of mass-weighted age  $\langle t_{\star} \rangle_{mw}$  in the left panel and luminosity-weighted metallicity  $\log_{10}(\langle Z/Z_{\odot} \rangle_{lw})$  as a function of mass-weighted metallicity  $\log_{10}(\langle Z/Z_{\odot} \rangle_{mw})$  in the right panel. In both panels, the galaxies are colored by their  $b$ -value and the gray dash-dotted line represents the one-to-one relation. It is clear that luminosity-weighted ages are smaller than mass-weighted ages. Younger galaxies have greater discrepancies between mass-weighted and luminosity-weighted ages. This is especially the case, for disk galaxies (blue), while most spheroidal galaxies (red) lie on the one-to-one relation. This can be explained by the fact that disk galaxies are younger than spheroidal galaxies as can be seen in Figure 3.3 (*left panel*). Contrary to the naive expectation, luminosity-weighted metallicity is lower than mass-weighted metallicity for almost all spheroidal galaxies. As indicated by the gray dashed line, this difference is approximately 0.08 dex. It is only for some disk galaxies, that the luminosity-weighted metallicity is higher. In the following, I will mostly deal with luminosity-weighted quantities because this is what is more directly obtained from observations.

Now I split the galaxy sample into *disks*, *intermediates* and *spheroids*, as described in Section 1.1. As the stellar mass, together with angular momentum, is one of the most important quantities of a galaxy (Romanowsky & Fall, 2012), I study the relation of stellar age and stellar mass, divided into morphological classes. Figure 3.5 shows the luminosity- (*left panel*) and mass-weighted (*right panel*) stellar age as a function of stellar mass where the galaxies are split according to their  $b$ -value into spheroids (red circles), intermediates (orange crosses), and disks (blue diamonds). The black pentagons represent the mean values for all galaxies within the same mass bins. For comparison, I add results by SAMI

(Scott et al., 2017, open circles), CALIFA (González Delgado et al., 2015, filled crosses), MaNGA/iMaNGA (Nanni et al., 2024, open diamonds/filled diamonds) and SDSS (Gallazzi et al., 2005, black upside-down triangles) to the luminosity-weighted results (*left panel*) and only MaNGA/iMaNGA to the mass-weighted results (*right panel*). While there is a clear split up at low masses between the three morphological types, they seem to have similar ages at high masses, though there are (almost) no disks at the highest masses. At a fixed mass, spheroids are the oldest, while disks are the youngest, over (almost) the whole mass range, which is in general agreement with Scott et al. (2017), Goddard et al. (2017), and Nanni et al. (2024). The relation for spheroids is almost flat. González Delgado et al. (2015) note their almost flat age-mass relations for (early-type) spirals (Sa), S0s, and ellipticals as evidence for morphology playing a more important role than mass for these galaxy types. There is a general trend that more massive galaxies are on average older. This “downsizing” (Cowie et al., 1996) is also found in observational studies (e.g. Gallazzi et al., 2005, González Delgado et al. (2015), Scott et al. (2017), San Roman et al. (2018), and Nanni et al. (2024)). It describes the assumption that at higher redshift more massive galaxies were formed (Cowie et al., 1996), subsequently indicating that low-mass galaxies did not yet have enough time to produce a large abundance of metals (Gallazzi et al., 2005). The trends are the same in the luminosity-weighted case as well as in the mass-weighted case, except for the fact that the second method produces on average older galaxies. A similar trend was found for spatially resolved ages by Goddard et al. (2017).

This establishes the relation between a galaxy’s age and its mass. Another well-known galaxy scaling relation is the mass-size relation, that is the stellar half-mass radius  $r_{1/2}$  as a function of stellar mass  $M_*$ . Wondering whether a galaxy’s age is also related to its size, Figure 3.6 presents the mass-size relation for all galaxies, spheroids, intermediates and disks (from the left to the right). The color encodes the luminosity-weighted stellar age  $\langle t_* \rangle_{lw}$  of each individual galaxy. Over-plotted are the fits to a combination of two power-law functions  $r_{1/2} = \gamma(M_*/M_\odot)^\alpha (1 + M_*/M_\odot)^{\beta-\alpha}$  by Lange et al. (2015). The fitting parameters are taken from their population definition according to morphology in the r-band. The general trend is that more massive galaxies are larger and at fixed mass young galaxies have larger radii, as also seen by Scott et al. (2017). This split up is more evident when comparing spheroids to disks. Consistent with observations (Lange et al., 2015), spheroids on average have smaller radii than disks at  $\lesssim 10^{11.25} M_\odot$ . As most young galaxies are disks, this is the same dichotomy as seen in the ages. There are no disks at the high-mass end, while the spheroids reach the largest (larger than most disks) radii in this section.

Apart from its size or radius, the appearance of a galaxy can also be described by its intrinsic ellipticity (calculated as described in Section 2.3). Additionally, how the stars within a galaxy move can have an effect on its shape, for example, rotating disk galaxies typically have spiral arms. To analyze a possible connection between these aspects, Figure 3.7 shows the luminosity-weighted stellar age  $\langle t_* \rangle_{lw}$  in dependence on the intrinsic ellipticity  $\epsilon$  (*left panel*) and the  $v/\sigma$ -parameter (*right panel*) for individual galaxies. The color encodes the  $b$ -value of the galaxies. The left panel illustrates that galaxies with low ellipticities are older

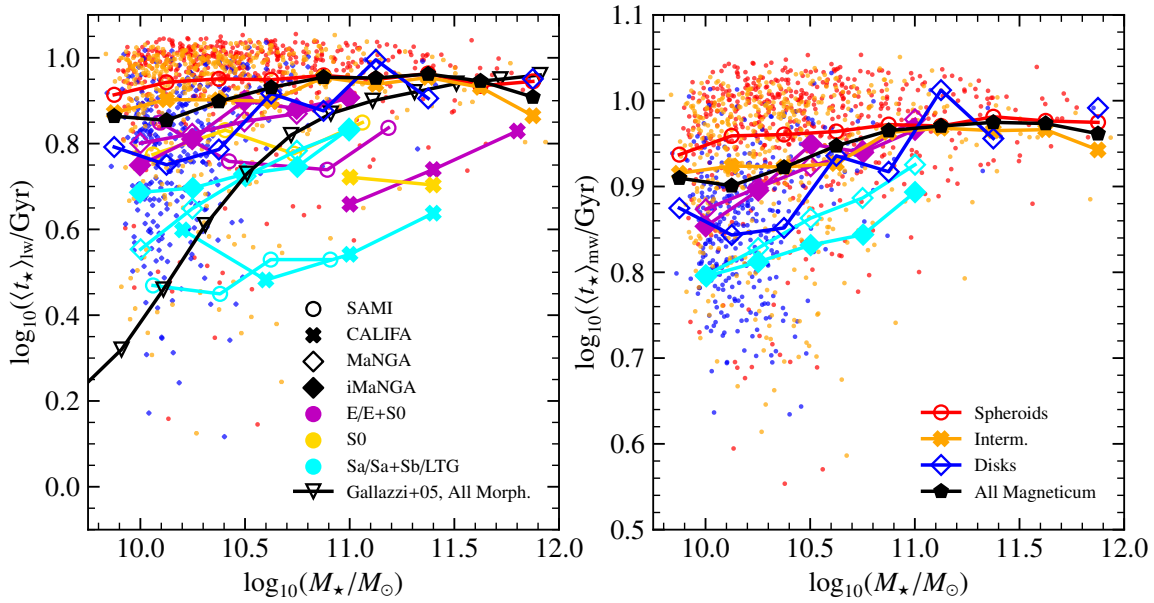


**Figure 3.5:** *Left Panel:* luminosity-weighted mean stellar age as a function of stellar mass within three half-mass radii  $r_{1/2}$ . *Right Panel:* mass-weighted mean stellar age as a function of stellar mass within three half-mass radii  $r_{1/2}$ . The galaxies are split into their morphological types and mean ages within mass bins are calculated. Red empty circles represent spheroids, orange filled crosses intermediates, and blue diamonds disks. The respective small filled symbols are the individual Magneticum galaxies. The black pentagons show the mean of each mass bin for all galaxies. In the left panel, results by SAMI (Scott et al., 2017), CALIFA (González Delgado et al., 2015), MaNGA/iMaNGA (Nanni et al., 2024), and SDSS (Gallazzi et al., 2005) are overplotted. In the right panel, only MaNGA/iMaNGA (Nanni et al., 2024) are shown. The SAMI and CALIFA E type, and MaNGA/iMaNGA E and S0 type galaxies are colored magenta, the SAMI and CALIFA S0 type are colored gold, and the SAMI Sa and Sb type, the CALIFA Sa type, and MaNGA/iMaNGA LTGs are colored cyan.

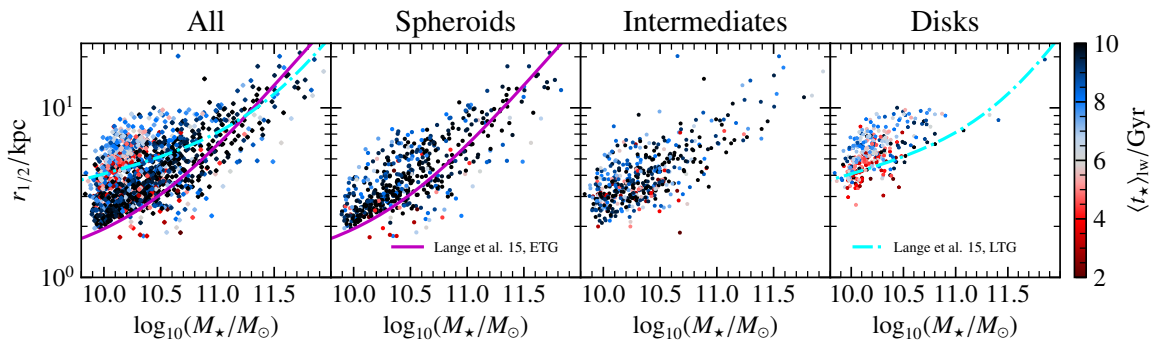


**Figure 3.6:** Stellar half-mass radius  $r_{1/2}$  as a function of stellar mass within a sphere of radius  $3r_{1/2}$  for all galaxies (left), spheroids (second from left), intermediates (second from right), and disks (right). The color encodes the luminosity-weighted stellar age of each individual galaxy. For comparison, the fits to a combination of two power-law functions by (Lange et al., 2015) the ETGs (purple line) and LTGs (cyan dash-dotted line) are shown for spheroids and disks, respectively.

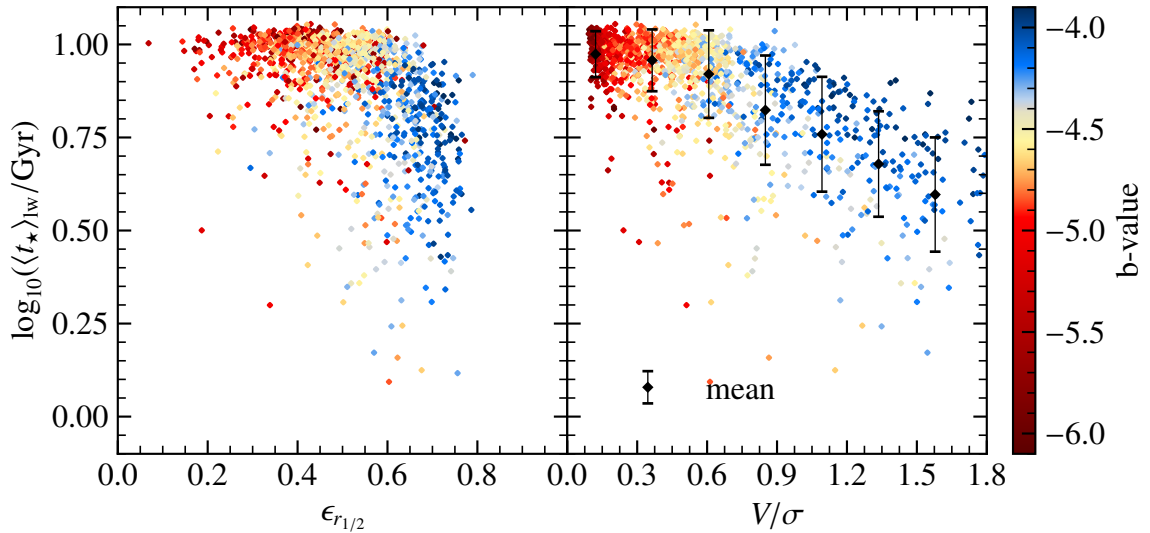


**Figure 3.7:** *Left:* Intrinsic ellipticity  $\epsilon$  vs. luminosity-weighted stellar age  $\langle t_{\star} \rangle_{\text{lw}}$ . *Right:*  $V/\sigma$ -parameter vs. luminosity-weighted stellar age. The black dots and the error bars are the mean values and the standard-deviations within the bins. In all panels, the galaxies are color-coded by the  $b$ -value.

and have lower  $b$ -values (spheroids) than galaxies with high ellipticities, which have higher  $b$ -values (disks). In the right panel, it is evident that low  $b$ -value galaxies (i.e. spheroids), are old and have low rotational support while high  $b$ -value galaxies (i.e. disks), become gradually younger as their rotational support increases.

Another measure of rotational support is the  $\lambda_R$ -parameter, introduced in Section 1.1.2. Figure 3.8 shows the  $\lambda_{r_{1/2}}-\epsilon$  plane colored by the luminosity-weighted mean stellar age  $\langle t_{\star} \rangle_{\text{lw}}$ . As already discussed for Figure 1.8, the galaxies above the gray line ( $\lambda_{R_e} = 0.31\epsilon$ ) are fast rotators and below there are slow rotators. Generally, there is the trend that slow rotators are old, while the most rotationally supported fast rotators are very young. Fast rotators with lower rotational support can also be old.

In addition to stellar mass and age, the stellar metallicity is also an important property for studying galaxy formation and evolution, as the abundance of heavy elements reflects the star formation history. For this reason, I analyze the mass-weighted stellar metallicity  $\log_{10}(\langle Z/Z_{\odot} \rangle_{\text{mw}})$  in the following. One of the most important scaling relations between metallicity with a global galaxy property is the mass-metallicity relation (MZR), first found for the gas-phase metallicity (Tremonti et al., 2004; Kewley & Ellison, 2008), but later confirmed for the stellar metallicity as well (Gallazzi et al., 2005; Kudritzki et al., 2016; Zahid et al., 2017; Davies et al., 2017; Bresolin et al., 2022; Urbaneja et al., 2023). Figure 3.9 shows the mass-weighted metallicity  $\log_{10}(\langle Z/Z_{\odot} \rangle_{\text{mw}})$  as a function of the mass-weighted age  $\langle t_{\star} \rangle_{\text{mw}}$  (age-metallicity relation, AMR, *left panel*), and as a function of the stellar mass within a sphere of radius  $3r_{1/2}$  (mass-metallicity relation, MZR, *middle panel*). The color encodes the  $b$ -value of the galaxies. The right panel shows the distribution of  $\log_{10}(\langle Z/Z_{\odot} \rangle_{\text{mw}})$  within disk, intermediate and spheroidal galaxies. The middle panel includes an orthogonal distance regression<sup>1</sup> fit to a quadratic function (cyan straight line). The fitting parameters are given

<sup>1</sup><https://docs.scipy.org/doc/scipy/reference/odr.html>

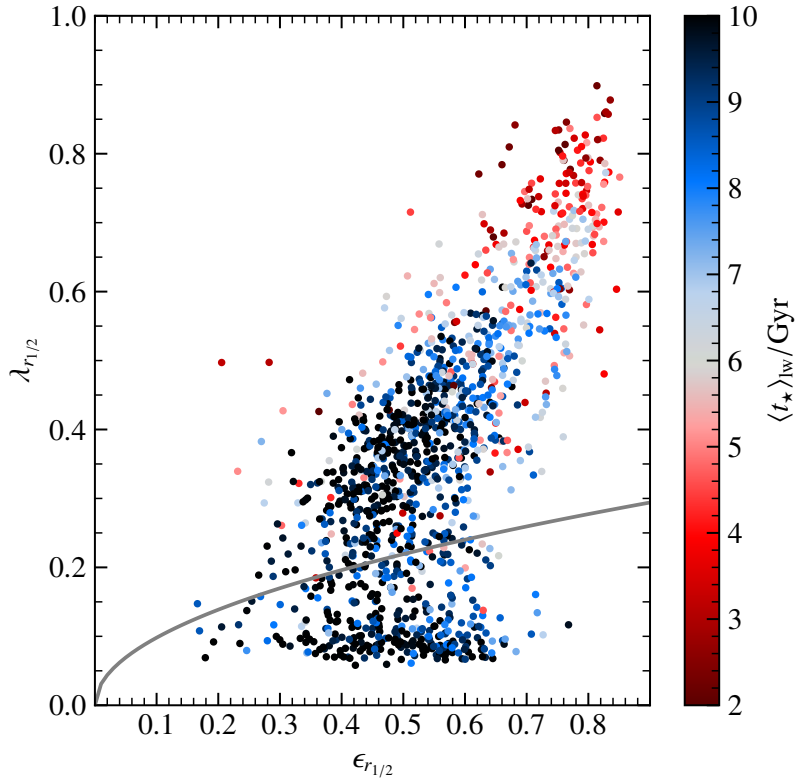


**Figure 3.8:**  $\lambda_{r_{1/2}}-\epsilon$  plane colored by the luminosity-weighted mean stellar age  $\langle t_{\star} \rangle_{lw}$ . The gray line shows the  $\lambda_{r_{1/2}} = 0.31\epsilon_{r_{1/2}}$  boundary between fast (above) and slow (below) rotators introduced by Emsellem et al. (2011).

in Table 3.1. To quantify the scatter of the relation, the Pearson correlation coefficient  $p$  and the mean orthogonal distance  $\langle OD \rangle$  are shown. For comparison, the middle panel includes the observational MZR for the gas phase from Tremonti et al. (2004) (black diamonds), Pettini & Pagel (2004) (black circles) and Pilyugin & Thuan (2005) (black triangles) as presented by Kewley & Ellison (2008), and the fitted curve presented by Maiolino et al. (2008) for  $z = 0.07$ . These measurements used strong line emissions that were transformed into  $[Z]$  by using  $[Z] = [O/H] - [O/H]_{\odot}$  with  $[O/H] = 12 + \log_{10}(N(O)/N(H))$  and  $[O/H]_{\odot} = 8.69$  (Asplund et al., 2009). Also added are relations obtained using stellar spectra: Sextl et al. (2023) fitted stacked spectra of star-forming galaxies in the SDSS and applied population synthesis models (open squares) and multiple other studies analyzed individual blue supergiants (BSG) (Kudritzki et al., 2016; Davies et al., 2017; Bresolin et al., 2022; Urbaneja et al., 2023, large open circles). Also shown is the prediction of a galaxy evolution lookback model by Kudritzki et al. (2021) (magenta dash-dotted line). In the AMR of the Magenticum galaxies (*first panel*) the disks and spheroids seem to occupy distinct regions, where the disk-like galaxies are young and metal-poor, while spheroidal galaxies are older and metal-rich. The MZR shows that metallicity increases with mass. The disk-like galaxies and spheroidal galaxies occupy a similar region. There is a general agreement with Pettini & Pagel (2004), Sextl et al. (2023), the data measured from Blue Supergiants (BSG) (Kudritzki et al., 2016; Davies et al., 2017; Bresolin et al., 2022; Urbaneja et al., 2023), and the lookback model (Kudritzki et al., 2021). Finally, on average disk galaxies have the

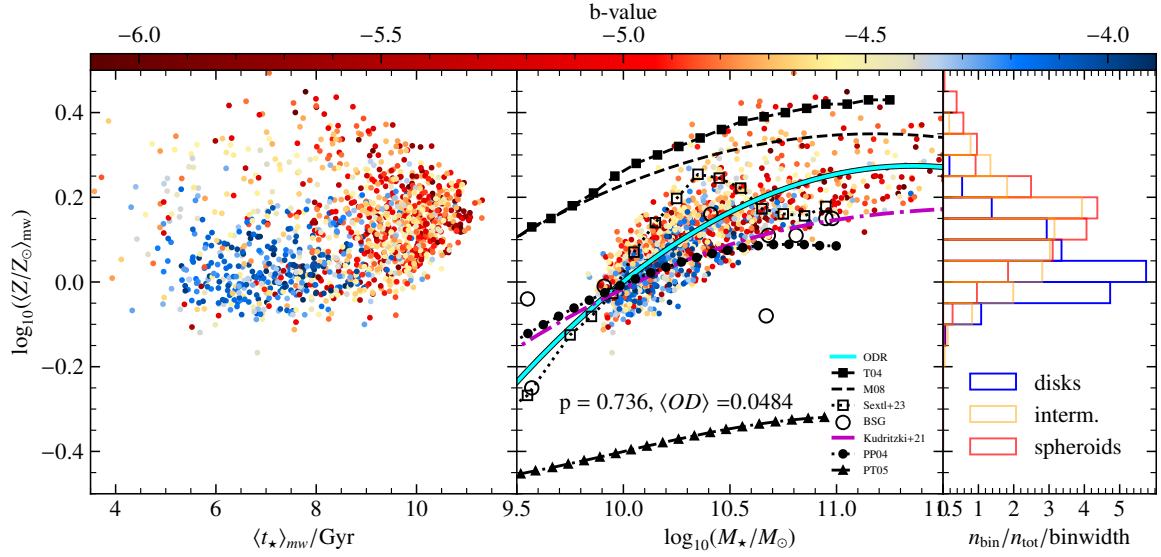


**Figure 3.9:** *First Panel:* Mass-weighted stellar metallicity  $\log_{10}(\langle Z/Z_{\odot} \rangle_{\text{mw}})$  as a function of mass-weighted stellar age  $\langle t_{\star} \rangle_{\text{mw}}$ . *Second Panel:* Mass-weighted stellar metallicity  $\log_{10}(\langle Z/Z_{\odot} \rangle_{\text{mw}})$  as a function of stellar mass  $M_{\star}$  within three half-mass radii  $r_{1/2}$ . The cyan line presents an orthogonal distance regression fit to the data. To quantify the scatter of the relation, the Pearson correlation coefficient  $p$ , and the mean orthogonal distance  $\langle OD \rangle$  are shown. Over-plotted are the observed gas-phase MZR from Tremonti et al. (2004) (T04, black filled squares), Pettini & Pagel (2004) (PP04, black filled circles) and Pilyugin & Thuan (2005) (PT05, black filled triangles) as presented by Kewley & Ellison (2008), and Eq. 2 from Maiolino et al. (2008) (M08, black dashed lines) with fitting parameters for  $z = 0.07$ . The stellar MZR from Blue Supergiants (BSG) (Kudritzki et al., 2016; Davies et al., 2017; Bresolin et al., 2022; Urbaneja et al., 2023; Sextl et al., 2024) (black open circles), stacked SDSS spectra (Sextl et al., 2023) (black open squares), and the prediction from the galaxy evolution lookback model by Kudritzki et al. (2021) (magenta dash-dotted line) is shown as well. *Third Panel:* Distribution of metallicity  $\log_{10}(\langle Z/Z_{\odot} \rangle_{\text{mw}})$  among the different morphological types.

$\alpha$	$\beta_0$	$\beta_1$	$\beta_2$
0	-0.147	3.348	-18.746
0.6	-0.180	3.930	-21.214
0.8	-0.150	3.307	-17.858
1.0	-0.089	2.058	-11.480

**Table 3.1:** Fitting parameters to the function  $y = \beta_0 x^2 + \beta_1 x + \beta_2$  for the MZR ( $\alpha = 0$ ) and  $\Phi$ ZR, where  $\Phi = \log_{10}(M_{\star}/M_{\odot}) - \alpha \log_{10}(r_{1/2}/\text{kpc})$ .

lowest metallicity by  $\sim 0.2$  dex as seen in the histogram (*right panel*), while intermediate and spheroidal galaxies have a similar metallicity.

Two very early explanations for the existence of the mass-metallicity relation are either more massive galaxies form fractionally more stars and therefore experience more metal enrichment or less massive galaxies loose more of their enriched gas due to feedback processes because it is easier to escape their potential well (Tremonti et al., 2004). The baryonic gravitational potential does not only depend on the mass, but also on a galaxies' radius. Therefore, it is interesting to investigate, whether a galaxy's metallicity is related to its position in the mass-size relation. Similar to how Figure 3.6 shows the galaxies' luminosity-weighted age  $\langle t_{\star} \rangle_{\text{lw}}$  in the mass-size relation, Figure 3.10 shows the galaxies' luminosity-weighted

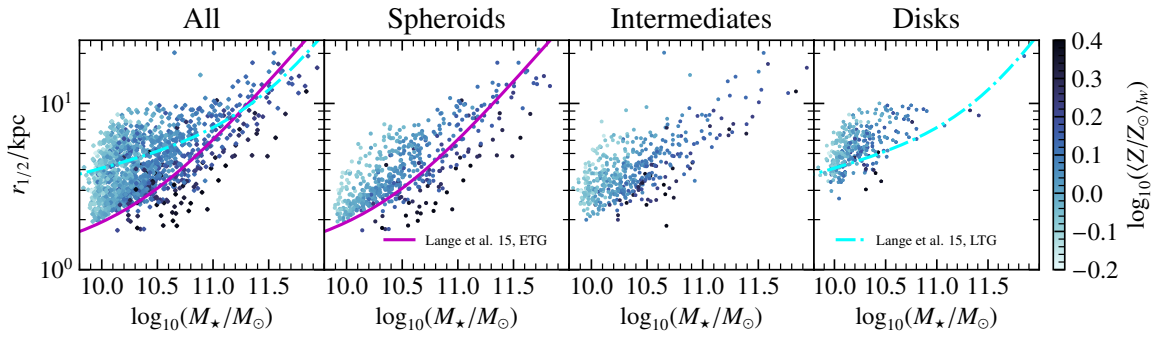


**Figure 3.10:** Stellar half-mass radius  $r_{1/2}$  as a function of stellar mass within a sphere of radius  $3r_{1/2}$  for all galaxies (left), spheroids (second from left), intermediates (second from right), and disks (right). The color encodes the luminosity-weighted mean stellar metallicity  $\log_{10}(\langle Z/Z_{\odot} \rangle_{lw})$  of each individual galaxy. For comparison, the fits to a combination of two power-law functions by (Lange et al., 2015) to ETGs (purple dotted line) and LTGs (cyan dash-dotted line) is shown for spheroids and disks respectively.

metallicity  $\log_{10}(\langle Z/Z_{\odot} \rangle_{lw})$  in the mass-size relation. While the ages of galaxies are split into old (spheroids and intermediates) and young (disks) galaxies by the morphology, both metal-rich and metal-poor galaxies can be found for each morphology. Instead, it can be seen that the metallicity increases with stellar mass, which reflects of the mass-metallicity relation (Figure 3.9) and is also seen in Figure 3.3.

Again, one can ask whether a galaxy’s shape or rotation has an effect on its metallicity. Figure 3.11 shows the luminosity-weighted stellar metallicity as a function of the intrinsic ellipticity  $\epsilon$  (*left panel*) and the  $V/\sigma$ -parameter (*right panel*) for individual galaxies. The color encodes the  $b$ -value of the galaxies. Compared to Figure 3.7, which shows the age as a function of the same quantities, the trends are not as clear here. The left panel shows no dependence at all, while the mean metallicity within seven equally spaced bins appears to slightly increase with  $V/\sigma$ , but this is not significant as all values lie within the standard deviations of each other.

Finally, Figure 3.12 is similar to Figure 3.8, but colored by luminosity-weighted stellar metallicity. Again, the color gradient is not as clear as before, but there still is a concentration of metal-rich galaxies in the top-right corner, among the most pronounced fast rotators. Most slow rotators are metal-poor. This might be surprising as slow rotators are thought to be more massive than fast rotators (Emsellem et al., 2011) and therefore also more metal-rich according to the MZR. A very likely formation scenario for slow rotators are multiple sequential minor mergers (Moody et al., 2014), rather than through a gas-rich major merger. Therefore, they have very little ongoing star formation, making them old and metal-poor.

Recently, it was restated that the size of a galaxy needs to be considered when analyzing the MZR (Vaughan et al., 2022; Sánchez-Menguiano et al., 2024). It was reported that  $\Phi = M_{\star}/r_{1/2}^{\alpha}$  is the best predictor for a galaxy’s gas-phase metallicity  $Z_g$  for  $\alpha = 0.6$  (Sánchez-Menguiano et al., 2024). The best predictor should have a strong correlation and a low scatter with the metallicity. I calculate  $\Phi = \log(M_{\star}/M_{\odot}) - \alpha \log(r_{1/2}/\text{kpc})$ , characterize the correlation via the Pearson correlation coefficient, and characterize the scatter via an

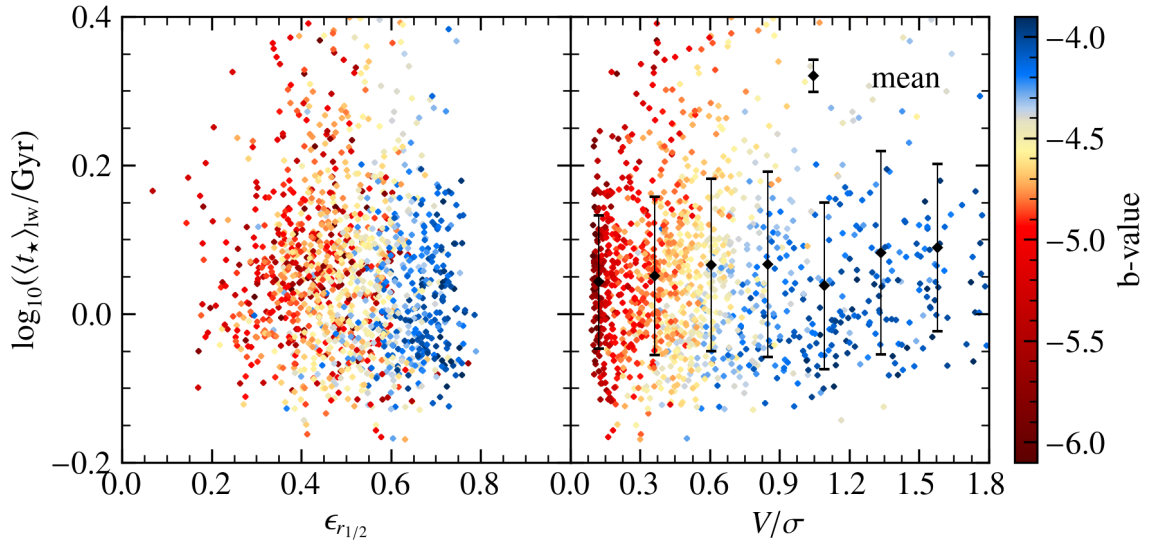


**Figure 3.11:** *Left:* Intrinsic ellipticity  $\epsilon$  vs. luminosity-weighted stellar age. *Right:*  $V/\sigma$ -parameter vs. luminosity-weighted stellar age. The black dots and the error bars are the mean values and the standard-deviation within each bin. In all panels, the galaxies are color coded by the luminosity-weighted mean stellar metallicity  $\log_{10}(\langle Z/Z_{\odot} \rangle_{lw})$ .

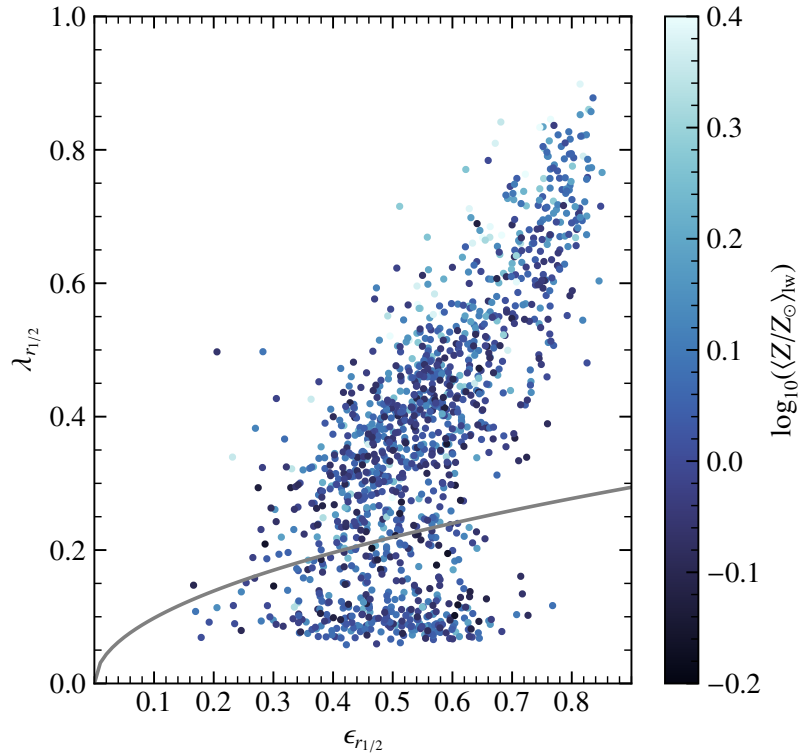


**Figure 3.12:**  $\lambda_{r_{1/2}}-\epsilon$  plane colored by the luminosity-weighted mean stellar metallicity  $\log_{10}(\langle Z/Z_{\odot} \rangle_{lw})$ . The gray line shows the  $\lambda_{r_{1/2}} = 0.31\epsilon_{r_{1/2}}$  boundary between fast (above) and slow (below) rotators introduced by Emsellem et al. (2011).

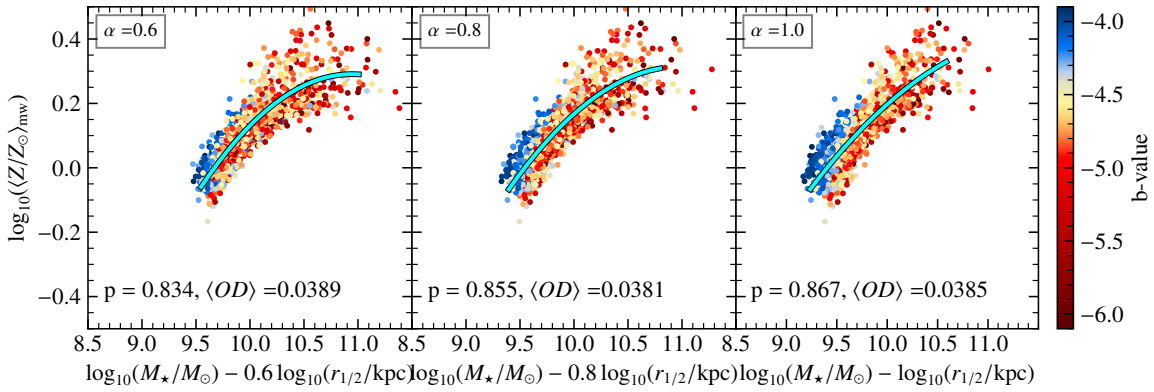


**Figure 3.13:**  $\Phi$ ZR: Mass-weighted mean metallicity  $\log_{10}(\langle Z/Z_{\odot} \rangle_{\text{mw}})$  as a function of  $\Phi = \log_{10}(M_{\star}/M_{\odot}) - \alpha \log_{10}(r_{1/2}/\text{kpc})$  for  $\alpha = 0.6$  (left panel),  $\alpha = 0.8$  (middle panel), and  $\alpha = 1.0$  (right panel). The cyan lines represent an orthogonal distance regression fit to a quadratic function. Shown in each panel is the Pearson correlation coefficient  $p$  and the mean orthogonal distance  $\langle OD \rangle$  as a measure for the scatter of the relation.

orthogonal distance regression fit to a quadratic function and the mean orthogonal distance  $\langle OD \rangle$ . I checked whether  $\Phi$  and  $\alpha = 0.6$  are also the best predictors for the mass-weighted stellar metallicity  $\log_{10}(\langle Z/Z_{\odot} \rangle_{\text{mw}})$ . An excerpt of the whole parameter study (Appendix B) is shown in Figure 3.13, specifically the mass-weighted mean metallicity  $\log_{10}(\langle Z/Z_{\odot} \rangle_{\text{mw}})$  as a function of  $\Phi = \log_{10}(M_{\star}/M_{\odot}) - \alpha \log_{10}(r_{1/2}/\text{kpc})$  for  $\alpha = 0.6$  (left panel),  $\alpha = 0.8$  (middle panel), and  $\alpha = 1.0$  (right panel). The strongest correlation ( $p = 0.867$ ) is found for  $\alpha \sim 1$ , whereas the relation is tightest for  $\alpha \sim 0.8$  as indicated by the lowest mean orthogonal distance  $\langle OD \rangle = 0.0381$ . All combinations are more tightly correlated and have a lower scatter than the MZR ( $p = 0.736$ ,  $\langle OD \rangle = 0.0484$ ). Interestingly, increasing  $\alpha$  separates the disk and spheroidal galaxies further. This is an imprint of the mass-size relation (Figure 3.6, Figure 3.10), where disk galaxies are larger at a fixed stellar mass. Subtracting an increasingly larger value that depends on the size yields a smaller  $\Phi$  for a larger galaxy.

Finally, I apply the definition of different stellar age populations (see, Section 2.5, *young*:  $t_{\star} < 2$  Gyr, *middle-aged*:  $2$  Gyr  $< t_{\star} < 8$  Gyr, *old*:  $t_{\star} > 8$  Gyr). To investigate how the different stellar populations contribute to the galaxies' classification according to the  $b$ -value. Figure 3.14 shows the  $b$ -value distribution of the galaxies calculated by only using their *young* (purple), *middle-aged* (cyan), or *old* (orange) stellar particles, for spheroids (left panel), intermediate galaxies (middle panel), and disks (right panel). The distributions are shown as violin plots, where the horizontal blue line within each violin represents the median of each distribution and the continuous black lines represent the  $b$ -value border between spheroids and intermediates ( $b = -4.73$ ) and between intermediates and disks ( $b = -4.35$ ). Within each morphology, the young population's median  $b$ -value is the highest, the old population's median  $b$ -value is the lowest, while the middle-aged population's median  $b$ -value is in between. The young population's median  $b$ -value is roughly the same for each morphology ( $\sim -3$ ), but stretches from very high to very low values for spheroids and lies completely above the  $-4.35$  mark for disk galaxies. The old population's distribution is the most compact and its median always follows perfectly the total  $b$ -value, that is for spheroids

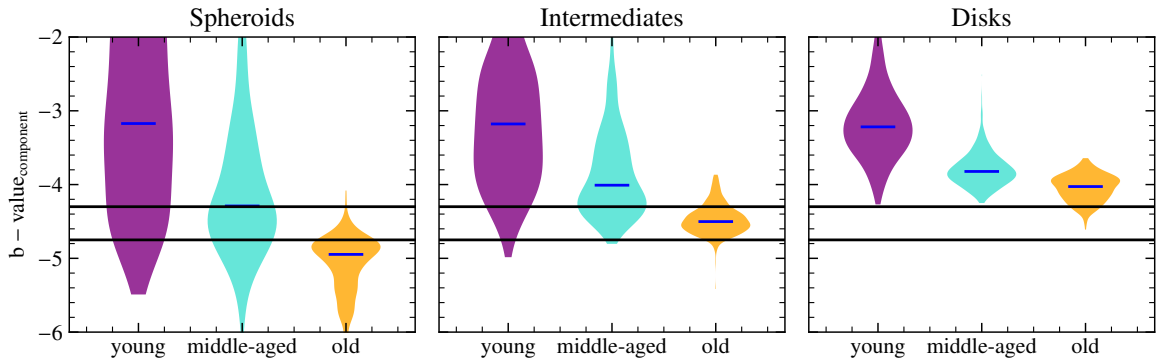


**Figure 3.14:** The  $b$ -value distribution for the young (purple), middle-aged (cyan) and old (orange) stellar population for spheroids (*left panel*), intermediate galaxies (*middle panel*), and disks (*right panel*). The median  $b$ -value for each distribution is shown in blue. The black horizontal lines indicate the boundaries between spheroids and intermediates ( $-4.73$ ) and between intermediates and disks ( $-4.35$ ).

the old population’s median is below the  $-4.73$  mark, for intermediates is between the two marks and for disks it is above the  $-4.35$  mark. This indicates that the overall dynamically based morphology, that is the  $b$ -value, is dominated by the old populations. This was expected because most stellar particles within the galaxies are old. Interestingly, the young populations have the largest range of  $b$ -values in spheroidal galaxies, with the median even showing disk-like behavior. This might hint at the existence of young disk-like kinematically distinct cores (Krajnović et al., 2011; Schulze et al., 2017, 2018) within the spheroidal galaxies.

Because the mass-metallicity relation (see, Figure 3.9) is one of the most important relations for galaxy evolution, Figure 3.15 shows again the mass-weighted mean stellar metallicity  $\log_{10}(\langle Z/Z_{\odot} \rangle_{\text{mw}})$  as a function of stellar mass  $M_{\star}$ , but this time split into the three morphologies, that is spheroids (*left column*), intermediate galaxies (*middle column*), and disk galaxies (*right column*) and into the three age populations, that is old (*top row*), middle-aged (*middle row*), and young (*bottom row*). Additionally, the relation for the MZR  $f(x) = a(x - M_0)^2 + K_0 - 12 - 8.69$ , adopted from Maiolino et al. (2008), was fit to each relation. The fitting parameters can be found in Table 3.2. While spheroids show a similar metallicity within old and young stars, the disk galaxies clearly show a split up, where old stars are more metal-poor than young stars. This also leads to old stars being more metal-rich in spheroids than in disks. In young and middle-aged stars, the difference between spheroids and disks is small.

## 3.2 Spatially Resolved Properties of Galaxies

In this section, I will analyze the radial distribution of age and metallicity in general and individually for each stellar age population. The contribution of the different populations to the distribution of mass and metallicity is also investigated. I also focus on the metallicity gradient and how it is correlated to global properties of the galaxy. Finally, the difference in the distribution of metals in young and old stars is investigated.

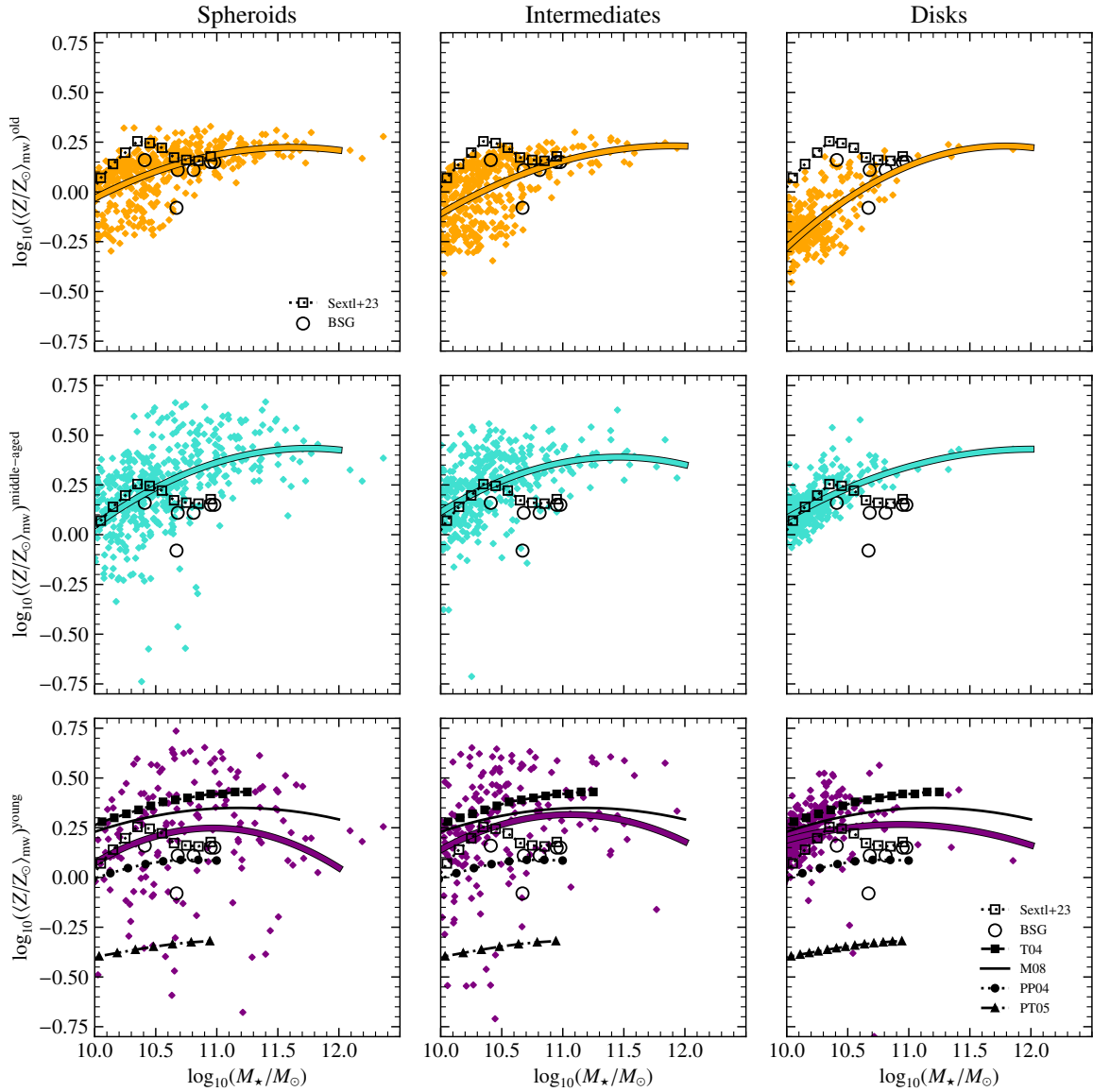


**Figure 3.15:** The mass-metallicity relation split into the different morphologies and different stellar age populations. The same observed relations also shown in Figure 3.9 are over-plotted, but only stellar measurements are shown for old and middle-aged stars, while the gas-phase measurements are also shown for young stars, whose metallicity is thought to still resemble the gas-phase because it traces recent star formation. Each panel shows a fit to the function  $f(x) = a(x - M_0)^2 + K_0 - 12 - 8.69$  adopted from Maiolino et al. (2008), whose fitting parameters are listed in Table 3.2.

Parameter	old	middle-aged	young
Spheroids			
$a$	-0.09794	-0.12648	-0.18737
$M_0$	11.61595	11.75182	10.96792
$K_0$	20.91395	21.12394	20.93815
Intermediates			
$a$	-0.09454	-0.13021	-0.15577
$M_0$	11.89864	11.45683	11.06512
$K_0$	20.92120	21.07983	21.00619
Disks			
$a$	-0.15912	-0.08526	-0.09097
$M_0$	11.78953	12.01621	10.93128
$K_0$	20.92032	21.11983	20.95639

**Table 3.2:** Fitting parameters to the function  $f(x) = a(x - M_0)^2 + K_0 - 12 - 8.69$  for the MZR in Figure 3.15 for different stellar populations and morphologies.

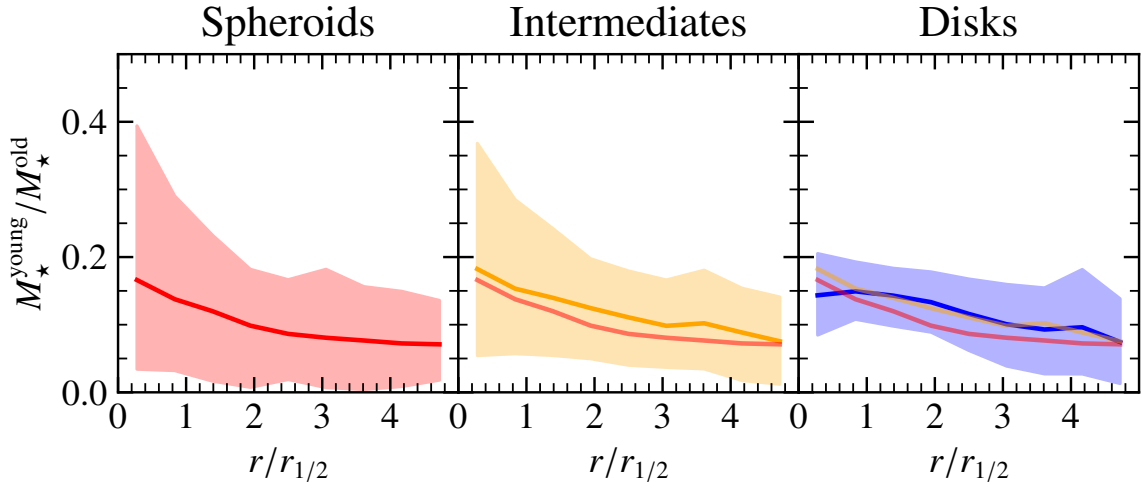


**Figure 3.16:** Radius in units of the half-mass radius  $r_{1/2}$  vs. mean of the ratio of mass in young and old stars  $M_{\star}^{\text{young}}/M_{\star}^{\text{old}}$  in each radial bin subdivided into spheroids, intermediates and disks.

### 3.2.1 Radial Profiles

To get a general sense of which region is influenced by what population of stars, the radial distribution of the ratio of the mass in young stars and the mass in old stars  $M_{\star}^{\text{young}}/M_{\star}^{\text{old}}$  is shown in Figure 3.16. Said ratio is presented as a function of radius  $r/r_{1/2}$ . From left to right, spheroids (red), intermediates (orange) and disks (blue) are shown respectively. The lines represent the mean ratio in nine radial bins and the shaded region is the range between the 0.9 and 0.1 percentiles, including 80% of the galaxies. In general, there is more mass in the old stars. Therefore, the ratio is always less than 0.4. The overall trend is that young stars have the largest significance in the center.  $M_{\star}^{\text{young}}/M_{\star}^{\text{old}}$  continually decreases for spheroidal and intermediate galaxies. It is slightly larger in intermediates over the whole radial range, but is largest in disks galaxies. In the center of disks  $M_{\star}^{\text{young}}/M_{\star}^{\text{old}}$  decreases towards the inside because it is largest at about one half-mass radius  $1r_{1/2}$ .

This gives an impression of what to expect for the radial distribution of ages. Figure 3.17 shows the mass-weighted mean stellar age  $\langle t_{\star} \rangle_{\text{mw}}$  (*top row*) and luminosity-weighted mean stellar age  $\langle t_{\star} \rangle_{\text{lw}}$  (*bottom row*) as a function of radius  $r/r_{1/2}$ , again for spheroidal (*left column*), intermediate (*middle column*) and disk-like (*right column*) galaxies. The shaded region contains 80% of the galaxies. For comparison, results by González Delgado et al. (2015), San Roman et al. (2018), Goddard et al. (2017), and Nanni et al. (2024) are overplotted. For comparisons with Goddard et al. (2017) and Nanni et al. (2024) I use their  $9.935 < \log_{10}(M_{\star}/M_{\odot}) < 10.552$ , and  $10 < \log_{10}(M_{\star}/M_{\odot}) < 10.5$  mass bin, respectively, as most of our galaxies lie in this mass range. The radial profiles of spheroidal and intermediate galaxies are rather flat, while the disk-like galaxies have a minimum age at a radius around one to two half-mass radii, as expected from considering Figure 3.16. Figure 3.16 also suggests a central dip in ages for spheroidal galaxies and intermediates, and indeed such a slightly positive age gradient is seen in the inner part of the shaded region. This gradient is steeper for the spheroids compared to intermediates. This positive gradient in ETGs is also seen in the results by Goddard et al. (2017) (magenta dash-dotted line with errorbars) in the mass-weighted case, and also by San Roman et al. (2018) (magenta dotted line with circles and errorbars) and Neumann et al. (2021) (not shown), indicating an “outside-in” progression of star formation in spheroids, where stars in the outskirts formed earlier than in the center. Nanni et al. (2024) find this positive age gradient in iMaNGA galaxies (mass-weighted, magenta solid line with squares), but not in the observed galaxies. Contrary to that, disk-like galaxies have a central ( $r < 2r_{1/2}$ ) negative age gradient, as already suggested by the dip in the center of the ratio  $M_{\star}^{\text{young}}/M_{\star}^{\text{old}}$  in disk galaxies. This indicates an “inside-out” formation of disk galaxies, wherein central stars originated prior to those in the outskirts, aligning with observations (González Delgado et al., 2015, cyan dashed line, Goddard et al., 2017, cyan dashed line with errorbars, Neumann et al., 2021, not shown, Nanni et al., 2024, cyan dashed line with circles). Overall, disk galaxies are younger than spheroids at all radii. All these trends are more pronounced in the luminosity-weighted case because it leads to younger obtained mean ages.

Previously, for example, Figure 3.2 showed that the distribution of stellar ages is closely related to the distribution of stellar metallicity. Figure 3.18 shows the mass-weighted mean stellar metallicity  $\langle [Z/H] \rangle_{\text{mw}}$  (*top row*) and luminosity-weighted mean stellar metallicity  $\langle [Z/H] \rangle_{\text{lw}}$  (*bottom Row*) as a function of radius  $r/r_{1/2}$ . The galaxies are also split into spheroidal (red line, *left column*), intermediate (orange line, *middle column*) and disk-like (blue line, *right column*) galaxies. The contours represent the 0.1 and 0.9 quantiles, including 80% of the galaxies. Over-plotted are results by Nanni et al. (2024) as circles (MaNGA) and squares (iMaNGA) for elliptical (magenta), lenticular (dark orange) and spiral (cyan) galaxies. I only show their  $10 \leq \log(M_{\star}/M_{\odot}) \leq 10.5$  mass bin, as most of our galaxies lie in this range. All profiles are declining, that is the center is always more metal-rich than the outskirts. This is indicative of an inside-out growth. In contrast to the age profiles, where the spheroids show a slight hint of outside-in growth, the metallicity profiles hint at an inside-out growth for all morphologies. Intermediates and spheroids almost exactly

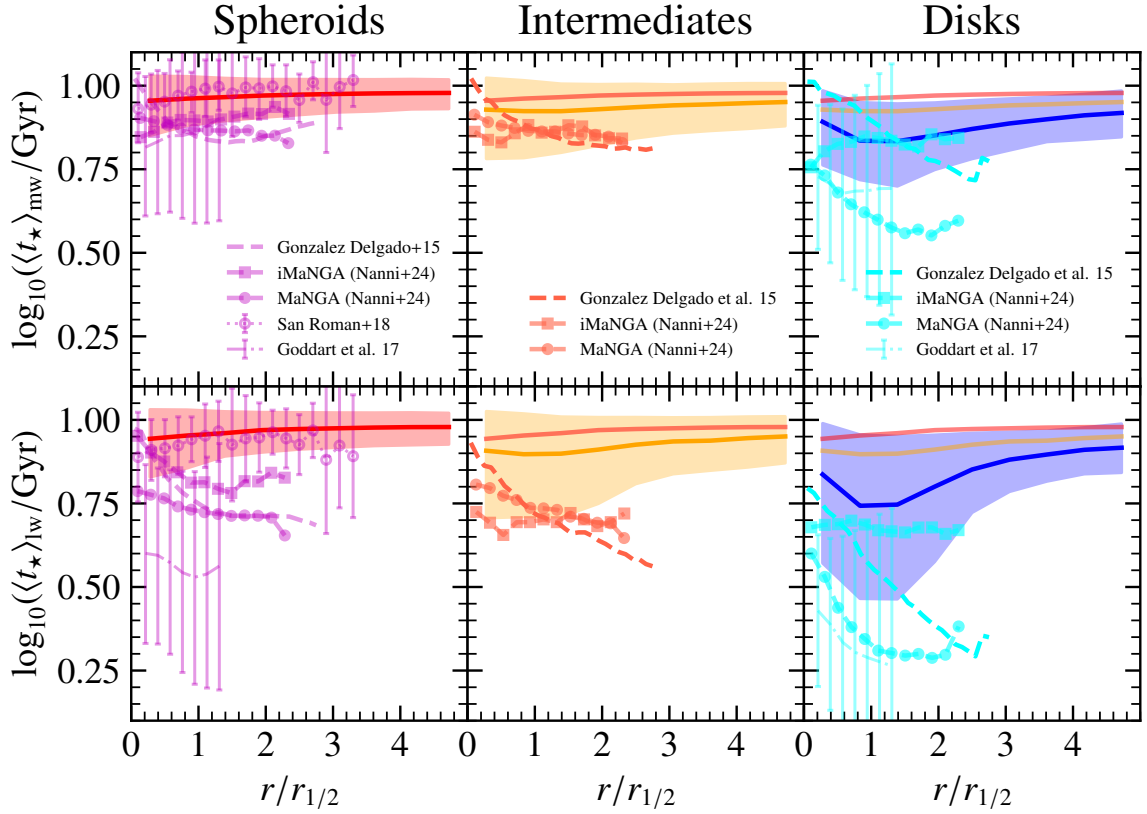


**Figure 3.17:** *Top Row:* Radius vs. mass-weighted mean stellar age  $\langle t_{\star} \rangle_{mw}$  in each radial bin. *Bottom Row:* Radius vs. luminosity-weighted mean stellar age  $\langle t_{\star} \rangle_{lw}$  in each radial bin. Spheroids are shown as red circles, intermediates are orange crosses and disks as blue diamonds. The contours represent the 0.1 and 0.9 quantiles. For comparison, magenta lines in the left column show the results for ETGs by González Delgado et al. (2015) (dashed), San Roman et al. (2018) (dotted with circles and errorbars), Goddard et al. (2017) (dash-dotted with errorbars), and Nanni et al. (2024) (MaNGA as solid with circles, iMaNGA as solid with squares). The orange dashed line in the middle panel represents S0s as observed by González Delgado et al. (2015), the solid lines with circles and squares again represent MaNGA and iMaNGA lenticular galaxies, respectively (Nanni et al., 2024), as comparison to intermediate galaxies. Cyan lines in the right panel are observed LTGs by González Delgado et al. (2015) (dashed), Goddard et al. (2017) (dash-dotted with errorbars), and Nanni et al. (2024) (MaNGA as solid with circles, iMaNGA as solid with squares). For comparisons with Goddard et al. (2017) and Nanni et al. (2024) I use their  $9.935 < \log_{10}(M_{\star}/M_{\odot}) < 10.552$ , and  $10 < \log_{10}(M_{\star}/M_{\odot}) < 10.5$  mass bin, respectively, as most of our galaxies lie in this mass range.

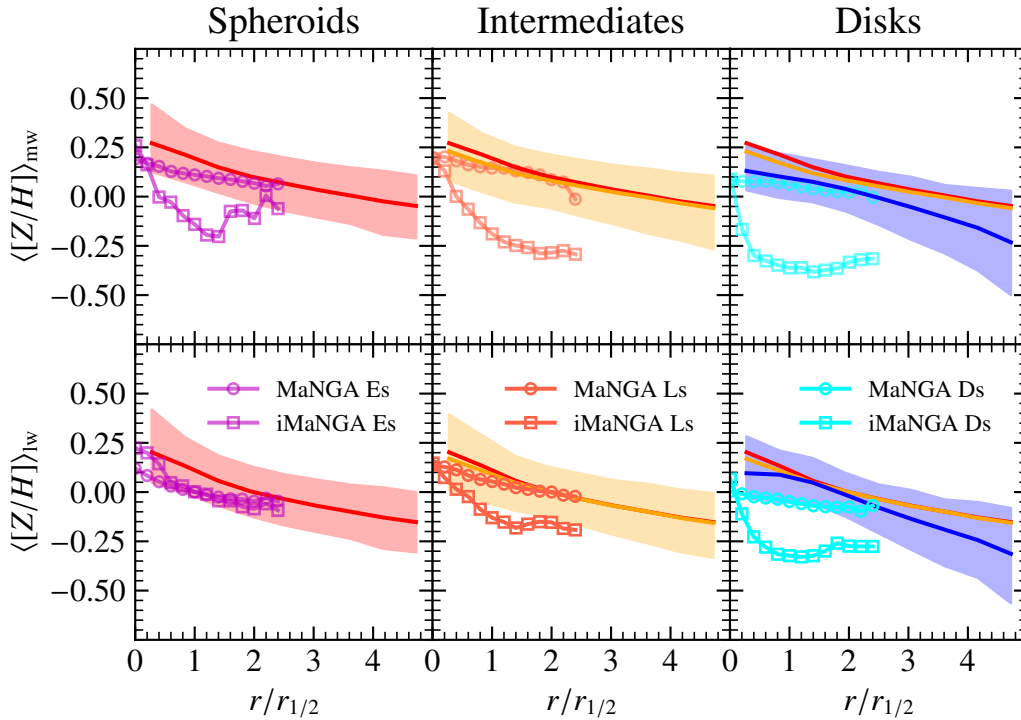


**Figure 3.18:** *Top Row:* Mass-weighted mean stellar metallicity  $\langle [Z/H] \rangle_{mw}$  as a function of radius  $r/r_{1/2}$ . *Bottom Row:* Same as *top Row* but luminosity-weighted  $\langle [Z/H] \rangle_{lw}$ . The contours represent the 0.1 and 0.9 quantiles. Over-plotted is observed data by Nanni et al. (2024) as circles (MaNGA) and squares (iMaNGA) for elliptical (magenta), lenticular (dark orange), and spiral (cyan) galaxies. We only show their  $10 \leq \log(M_{\star}/M_{\odot}) \leq 10.5$  mass bin, as most of our galaxies lie in this range.

coincide, while disks are slightly less metal-rich than the former two over all radii, but have a slightly steeper gradient. This is true for both the luminosity and mass-weighted case, and is consistent with all considered observations. In the luminosity-weighted case, the distribution of metallicity  $\langle [Z/H] \rangle_{lw}$  in spheroids is consistent with MaNGA and iMaNGA galaxies (Nanni et al., 2024). Intermediate galaxies in Magneticum almost agree perfectly with the MaNGA galaxies, while iMaNGA underpredicts the metallicity over all radii. The Magneticum disk galaxies are slightly more metal-rich than MaNGA disks, as presented by Nanni et al. (2024). iMaNGA disks are even less metal-rich than MaNGA galaxies over all radii.

The mass-metallicity relation can differ for different age populations (Figure 3.15). Therefore, I now investigate the radial metallicity distribution split into different stellar ages. Figure 3.19 shows the luminosity-weighted mean stellar metallicity  $\langle [Z/H] \rangle_{lw}$  for young (purple), middle-aged (cyan), old (orange) and all stars (black) as a function of radius  $r/r_{1/2}$ . All age populations lie within or very close to the contours for spheroids and intermediates, but not for disk galaxies where especially old stars are very metal-poor compared to the total mean. Over almost the whole radial range, middle-aged stars are the most metal-rich in spheroids. In disks, however, the young stars are the most metal-rich up to around three half-mass radii. This difference in the metallicity of middle-aged stars was already hinted at in Figure 3.2. Old stars are the most metal-poor over all radii in all morphological types. The old and middle-aged stars’ metallicity roughly decreases at the same rate as the mean

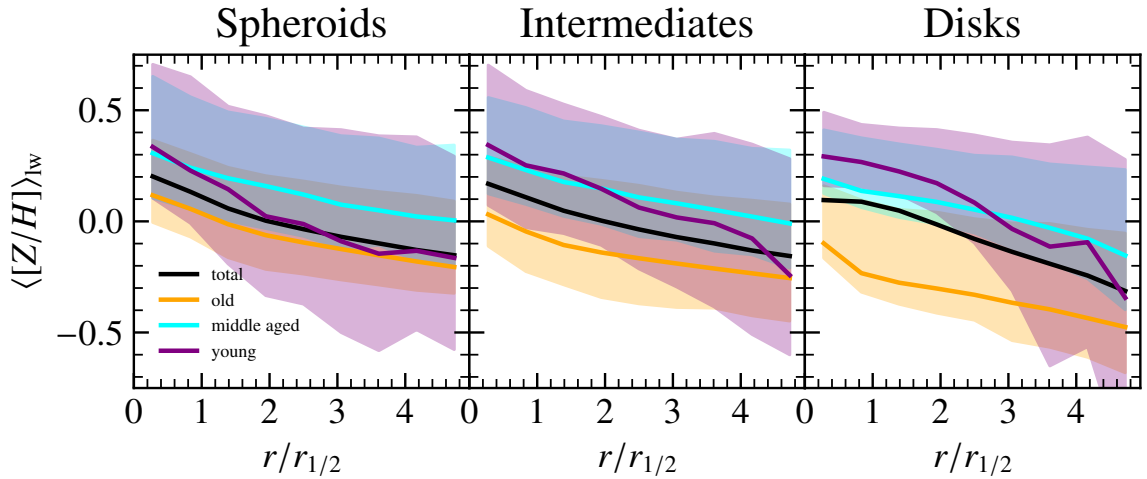


**Figure 3.19:** Luminosity-weighted mean stellar metallicity  $\langle [Z/H] \rangle_{\text{lw}}$  for young (purple), middle-aged (cyan), old (orange) and all stars (black) as a function of radius in units of the stellar half-mass radius  $r_{1/2}$ .

metallicity of all stars. The young stars have metallicities as high as middle-aged stars in the center (or higher in case of the disks), and as low as old stars in the outskirts. The young star’s metallicity therefore declines the steepest. Observations of the abundance of O, Ne, and Ar in PNe and HII-regions in selected disk galaxies (M31, M33, NGC300, and the Milky Way) (Peña & Flores-Durán, 2019) confirm that younger objects (Peimbert type I PNe and HII-regions) show steeper metallicity gradients than the older objects (Peimbert type II PNe). They speculate that stellar radial migration plays an important role in shaping these gradients. This agrees with observations of the inner region ( $r < r_{1/2}$ ) of the spiral NGC 1365 by Sextl et al. (2024). In this specific spiral, the old stars have no clear metallicity gradient, while young stars exhibit a negative metallicity gradient. While these five example galaxies are not statistically profound, this discrepancy nevertheless highlights the need to further investigate the different behavior of metallicity gradients in the young and old stellar population.

### 3.2.2 Metallicity Gradients

In this subsection, I study the differences in the metallicity gradients of the young and old stellar population, but prior to that, the overall metallicity gradients need to be analyzed to draw meaningful conclusions. Therefore, metallicity gradients are quantified and investigated whether there is a correlation with global properties. A correlation of metallicity gradients with stellar mass is well established in the literature (González Delgado et al., 2015; Goddard et al., 2017; Neumann et al., 2021; Nanni et al., 2024). Jones et al. (2013) find that steep negative gas-phase metallicity gradients flatten with time, that is young galaxies have more negative metallicity gradients than old galaxies. Mercado et al. (2021) find a negative correlation of stellar metallicity gradients with the median stellar age in simulated dwarf galaxies, that is young galaxies have flatter gradients than old galaxies. Cheng et al. (2024) find no correlation with mass-weighted mean stellar age, but a negative correlation of gas-phase metallicity gradients with evolutionary time in galaxies at cosmic noon ( $0.6 < z <$

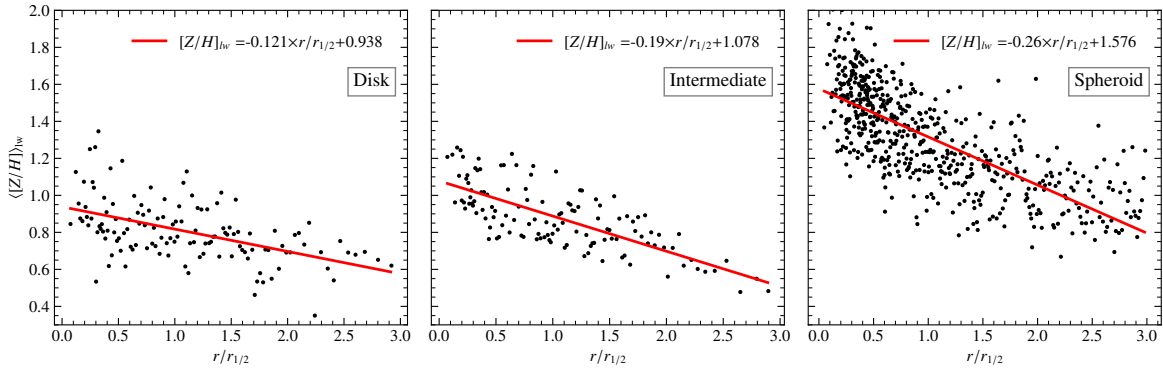


**Figure 3.20:** Luminosity-weighted stellar metallicity  $\langle [Z/H] \rangle_{lw}$  as a function of radius in units of the stellar half-mass radius  $r_{1/2}$  for an exemplary spheroidal (*top panel*), intermediate (*middle panel*), and disk galaxy (*bottom panel*) (the spheroid and disk are the same as in Fig. 3.2). The slope of a straight line fit is called the metallicity gradient  $\nabla[Z/H]$  in this work.

2.6), which is not the redshift range of the studies Magneticum galaxies ( $z = 0.07$ ). In the gas phase, steep negative metallicity gradient are primarily observed in rotation dominated galaxies (Jones et al., 2013; Sharda et al., 2021). Illustris TNG50 galaxies exhibit steep negative gas phase metallicity gradients almost exclusively in rotation dominated galaxies, while shallow gradients can be found in dispersion and rotation dominated galaxies (Hemler et al., 2021). Simulations of dwarf galaxies show no correlation between stellar metallicity gradient strength and the  $v/\sigma$ -parameter (Mercado et al., 2021). Opposed to the results in the gas-phase (Hemler et al., 2021; Sharda et al., 2021), dispersion dominated early-type galaxies observed by CALIFA are found to have steep negative stellar metallicity gradients, while dispersion dominated late-type galaxies have shallow gradients (Zhuang et al., 2019).

I investigate correlations with the global properties of galaxies in Magneticum: Stellar mass  $M_\star$  within a sphere of radius  $3r_{1/2}$ , luminosity-weighted mean stellar age  $\langle t_\star \rangle_{lw}$ , and the  $v/\sigma$ -parameter. The metallicity gradient is calculated as outlined in Section 2.5. The metallicity gradients of an exemplary spheroidal, intermediate, and disk galaxy are shown in Figure 3.20.

The stellar metallicity gradient  $\nabla\langle [Z/H] \rangle_{lw}$  of galaxies is shown in Figure 3.21 for disk (blue, *first row*), intermediate (orange, *second row*) and spheroidal galaxies (red, *third row*) as a function of stellar mass  $M_\star$  (*first column*), luminosity-weighted mean stellar age  $\langle t_\star \rangle_{lw}$  (*second column*), and the  $v/\sigma$ -parameter (*third column*). The fourth column shows the distribution of  $\nabla\langle [Z/H] \rangle_{lw}$  and the median. Each panel shows a straight line fit to the shown properties that takes the standard deviation of each metallicity gradient into account. The resulting slopes and respective Pearson correlation coefficients  $p$  are given in Table 3.3. Several observational results are overplotted as gray dots (Nanni et al., 2024) and dark gray pentagons (Zhuang et al., 2019). Finally, it also shows the luminosity-weighted metallicity gradients measured within  $3r_{1/2}$  from stacked metallicity profiles as empty circles with errorbars. These are discussed in Appendix C. All metallicity gradients are negative. This is another hint at the inside-out growth of galaxies (Venturi et al., 2024). The distribution of metallicity gradients in disk galaxies (blue) is confined between 0 and -0.5, while intermediate

(orange) and spheroidal galaxies (red) can have much steeper metallicity gradients (0 to -0.8). On average, disk galaxies, with a median metallicity gradient of  $\mu = -0.12$ , have shallower gradients than spheroids ( $\mu = -0.26$ ), with intermediates representing a transition between them ( $\mu = -0.19$ ). This is consistent with CALIFA (dark gray pentagons) (Zhuang et al., 2019)<sup>2</sup>, where type Sa-Sd have a median metallicity gradient of  $\mu = -0.16$ , type S0 of  $\mu = -0.23$  and type E galaxies  $\mu = -0.26$ , and iMaNGA (Nanni et al., 2024) where  $\mu = -0.32$  for LTGs and  $\mu = -0.46$  for ETGs. MaNGA galaxies (gray dots) (Nanni et al., 2024) show a different trend in this regard, that is  $\mu = -0.14$  for LTGs and  $\mu = -0.09$  for ETGs. A negative correlation of the metallicity gradients with stellar mass is expected (González Delgado et al., 2015; Goddard et al., 2017; Neumann et al., 2021; Nanni et al., 2024) and confirmed in Magneticum galaxies (*first column*). The magnitude of the Pearson correlation coefficient of metallicity gradients with stellar mass is low ( $p = -0.13$  for disks and  $p = -0.25$  for spheroids). Therefore, a straight line fit might not be justified, but because the correlation is seen in the literature and Magneticum galaxies lie within the cloud of MaNGA galaxies, a fit is performed nevertheless. The slopes of these straight line fits are  $-0.078$  and  $-0.022$ , respectively, that is disk galaxy's metallicity gradients are more strongly correlated with mass than spheroidal galaxies, which is consistent with observations (Goddard et al., 2017; Nanni et al., 2024). This is also confirmed by a straight line fit to the galaxies in MaNGA and iMaNGA in the same mass range ( $9.8 < \log(M_\star/M_\odot) < 11.5$ ) as Magneticum galaxies (*first column*).

Disk galaxies (blue) show a slight positive correlation ( $p = 0.34$ ) between metallicity gradient and the luminosity-weighted mean stellar age  $\log_{10}(\langle t_\star \rangle_{\text{lw}}/\text{Gyr})$  (*second column*). Intermediate (orange) and spheroidal (red) galaxies show no clear correlation, but clearly occupy a different region in the metallicity gradient-mean stellar age plane because spheroidal galaxies are mainly at the high age end and spread over the whole gradient range, while disk galaxies have shallower metallicity gradients and spread over the whole age range. Even though it is small, the slope of the  $\nabla\langle [Z/H] \rangle_{\text{lw}} - \log_{10}(\langle t_\star \rangle_{\text{lw}})$  relation is positive. This flattening of the metallicity gradient with time can be a consequence of radial migration of stars over time, that is high metallicity stars from the center wander outwards, while low metallicity stars wander towards the center, diluting the gradient (Roškar et al., 2008). Size growth of galaxies can also account for the change in metallicity gradients (Jones et al., 2013). By comparing four lensed high-redshift galaxies with galaxies from the literature, Jones et al. (2013) find that steep negative gas-phase metallicity gradients flatten with time. As opposed to my result in stars, a negative correlation of the gas-phase metallicity gradient with an evolutionary time parameter<sup>3</sup> is found by Cheng et al. (2024), but no correlation with mass-weighted age, while Mercado et al. (2021) also find a negative correlation of median

<sup>2</sup>Zhuang et al. (2019) measure gradients as  $\nabla[Z]$  instead of  $\nabla[Z/H]$ , which is used in this work. The difference of the median  $\nabla[Z] - \nabla[Z/H]$  is about 0.02 in our simulations, and therefore does not impact our conclusions.

<sup>3</sup> $t_E = \int_{t_i}^{t_{\text{obs}}} \frac{1}{(t-t_i)} \times \frac{1}{\text{sSFR}(t-t_i)} \times dt$  (Cheng et al., 2024)

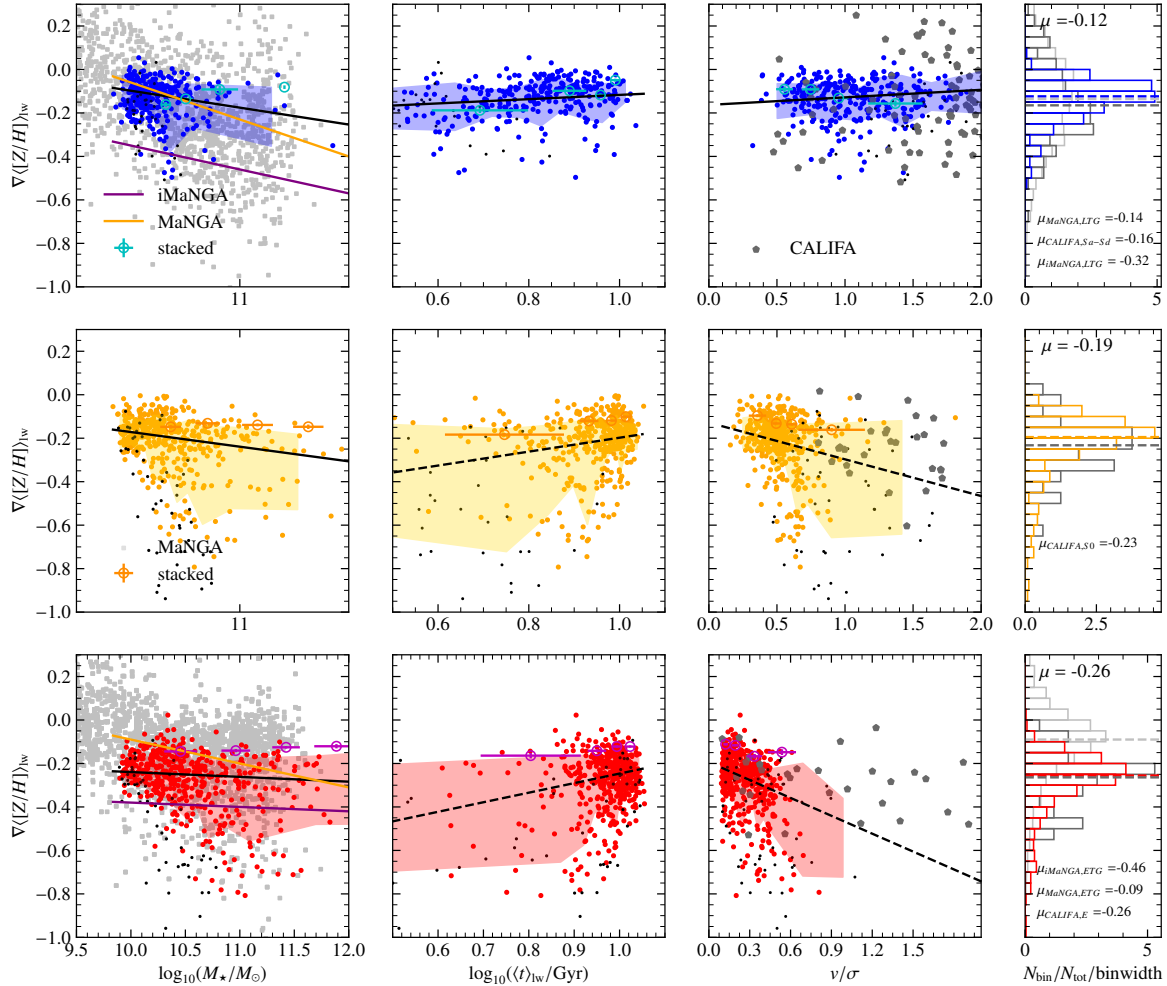


**Figure 3.21:** The luminosity-weighted metallicity gradients  $\nabla\langle[Z/H]\rangle_{lw}$  as a function of the stellar mass  $M_{\star}$  within a sphere of radius  $3r_{1/2}$  (*first column*), the luminosity-weighted mean stellar age  $\langle t_{\star} \rangle_{lw}$  (*second column*), the  $v/\sigma$  parameter (*third column*), and the distribution of  $\nabla\langle[Z/H]\rangle_{lw}$  (*fourth column*) for disks (*top row*), intermediate galaxies (*middle row*), and spheroidal galaxies (*bottom row*). The black line is a straight line fit to the data. If a straight line fit is not representative of the cloud of dots, the line is dashed. The Pearson correlation coefficient  $p$  for the axes of each panel and the slope are given in Table 3.3. The colored area represents the  $1\sigma$  deviation around the straight line. For comparison, the purple and orange lines represent fits to the data from iMaNGA and MaNGA as extracted from Nanni et al. (2024) and cut to have the same mass range as the Magenticum galaxies ( $9.8 < \log(M_{\star}/M_{\odot}) < 11.5$ ). The gray squares in the background of the top and bottom left panel represent the unaltered dataset of MaNGA LTGs (*first row*) and ETGs (*third row*). The gray pentagons in the right column represent CALIFA type Sa-Sd, type S0 and type E galaxies, from top to bottom, as taken from Zhuang et al. (2019). The median of each distribution of metallicity gradients is given as  $\mu$  in the histograms panels.

**Table 3.3:** Slopes and Pearson correlation coefficients from Figure 3.21.

Parameter	$\log_{10}(M_{\star}/M_{\odot})$	$\log_{10}(\langle t_{\star} \rangle_{\text{lw}}/\text{Gyr})$	$v/\sigma$
Disks			
Slope	-0.078	0.098	0.035
Pearson $p$	-0.13	0.34	-0.12
Intermediates			
Slope	-0.067	0.32	-0.169
Pearson $p$	-0.27	0.34	-0.36
Spheroids			
Slope	-0.067	0.44	-0.274
Pearson	-0.27	0.32	-0.47

stellar age with metallicity gradients in dwarf galaxies, which are not part of the Magneticum galaxy sample.

I find a negative correlation of  $V/\sigma$  (*third column*) with the stellar metallicity gradient within intermediate (orange) and spheroidal (red) galaxies. This trend is not observed among stars by (Zhuang et al., 2019), but rotationally dominated galaxies exhibit steeper negative gas phase metallicity gradients (Sharda et al., 2021; Hemler et al., 2021). The slope is slightly positive for disk galaxies and becomes increasingly more negative over intermediates to spheroidal galaxies. The disagreement of the negative correlation coefficient  $p$  and the positive slope for disks might be due to the high uncertainties of the metallicity gradients of a few high  $V/\sigma$  galaxies. In general, most disk galaxies are rotation dominated ( $V/\sigma > 0.6$ ) and have slightly negative metallicity gradients, consistent with CALIFA galaxies (Zhuang et al., 2019). Most spheroidal galaxies are dispersion dominated ( $V/\sigma < 0.3$ ), while the steepest gradients are found in spheroids around  $V/\sigma \sim 0.6$ . CALIFA E type galaxies include galaxies with a higher  $V/\sigma$ -parameter than Magneticum spheroids, but their median metallicity gradient matches the Magneticum spheroids. Comparing all galaxies, I find that there are many dispersion dominated galaxies that have steep stellar metallicity gradients, which are not found in the gas phase (Sharda et al., 2021; Hemler et al., 2021). Investigating the gas phase in Magneticum is left for future work. However, Magneticum galaxies are consistent with CALIFA galaxies as presented by Zhuang et al. (2019), who find many dispersion dominated early-type galaxies that exhibit steep negative stellar metallicity gradients. Gradient steepening with  $V/\sigma$  is only observed from Sd to Sb type galaxies by Zhuang et al. (2019) and reverses from Sb to E type galaxies, that is gradients become steeper with decreasing  $V/\sigma$ . Overall the correlation of metallicity gradients with stellar mass is found in Magneticum, stellar metallicity gradients seem to become shallow with increasing galactic age, while the opposite is true for gas-phase metallicity gradients, and the complicated connection between metallicity gradients and kinematic features will be the subject of future work.

Fig. 3.19 already revealed that there is a difference in the metallicity distribution in the young ( $t_{\star} < 2$  Gyr) and old ( $t_{\star} > 8$  Gyr) stellar population. Therefore, it is interesting to investigate how the metallicity of these stellar populations is correlated with radius to see

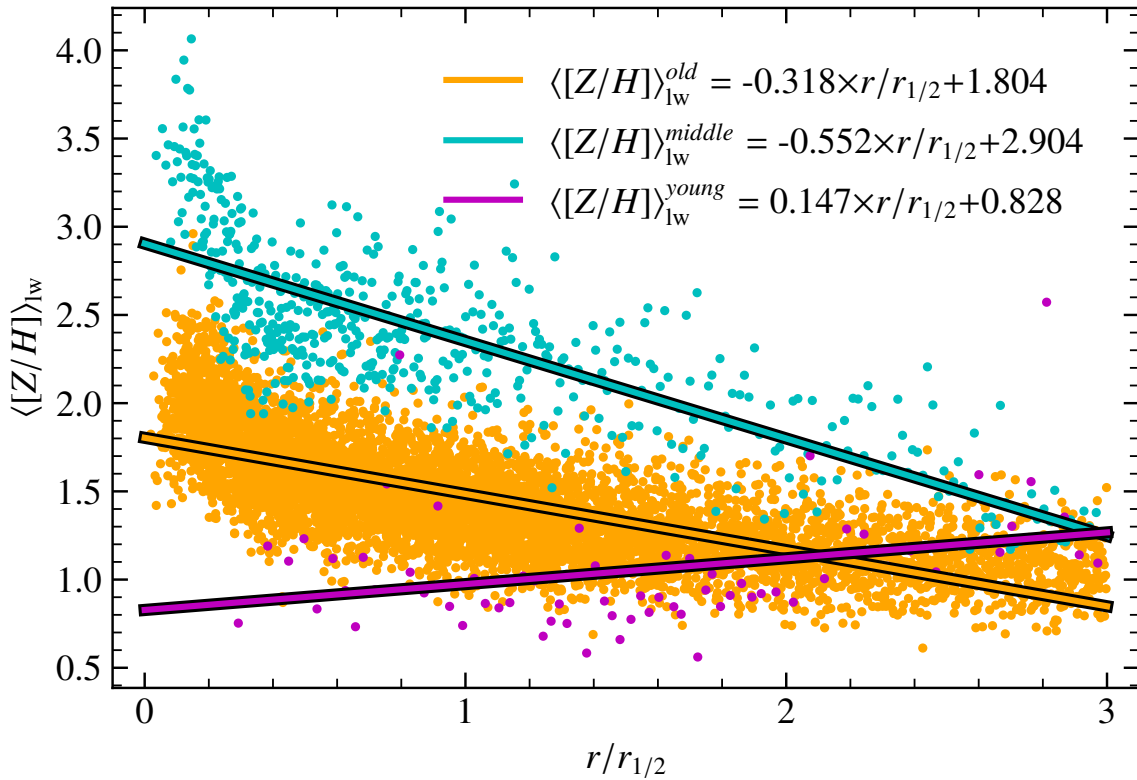


**Figure 3.22:** Luminosity-weighted stellar metallicity  $\langle [Z/H] \rangle_{\text{lw}}$  as a function of radius in units of the stellar half-mass radius  $r_{1/2}$  for an exemplary galaxy. The slope of a straight line fit to the stellar particles in the respective stellar population (young, middle-aged, old) is the respective metallicity gradient  $\nabla \langle [Z/H] \rangle_{\text{lw}}^{\text{young, middle-aged, old}}$  of said stellar population.

the spatially resolved details of the distribution. This is done in two approaches: ① By calculating the metallicity gradient  $\nabla \langle [Z/H] \rangle_{\text{lw}}$  but only for stellar particles that fall into each age population:  $\nabla \langle [Z/H] \rangle_{\text{lw}}^i$ , where  $i \in [\text{young, middle-aged, old}]$ . ② By calculating the Pearson correlation coefficient  $p$  of the star particles radius with their metallicity in the respective stellar population:  $p_i = p((r/r_{1/2})^i | (Z/H)^i / (Z/H)_\odot)$ , where  $i \in [\text{young, middle-aged, old}]$ . This value has a similar information content as the metallicity gradient, and parametrizes whether the gradient is negative ( $p < 0$ ) or positive ( $p > 0$ ), but also includes information about how much the data points scatter, that is  $|p| \sim 0$  is a circular cloud while  $|p| \sim 1$  indicates a straight line. This is only done for galaxies that have more than 200 young star particles, to ensure proper statistical robustness, which reduces the sample to 396 galaxies. An example of the three different gradients within one galaxy is shown in Figure 3.22. Again, a straight line is fit to radial bins containing 50 stellar particles within the respective age category. The dots represent individual radial bins. Old stars are orange, middle-aged stars are cyan, and young stars are purple. In this specific case, the old and middle-aged gradient is negative (-0.318 and -0.552), while the young gradient surprisingly is positive (0.147).

Figure 3.23a reveals the variety of possible combinations of young and old metallicity gradients. It shows the young metallicity gradient  $\nabla \langle [Z/H] \rangle_{\text{lw}}^{\text{young}}$  on the y-axis and the old metallicity gradient  $\nabla \langle [Z/H] \rangle_{\text{lw}}^{\text{old}}$  on the x-axis. The dots are colored by the  $b$ -value, with

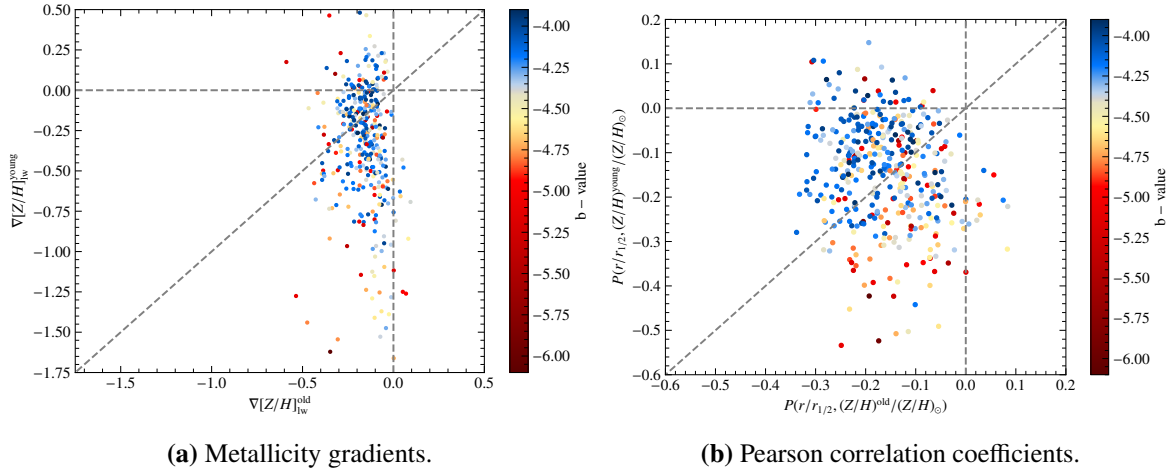


**Figure 3.23:** *Left panel:* Young metallicity gradient  $\nabla\langle[Z/H]\rangle_{\text{lw}}^{\text{young}}$  vs old metallicity gradient  $\nabla\langle[Z/H]\rangle_{\text{lw}}^{\text{old}}$ . *Right panel:* Pearson correlation coefficient  $p$  of  $(r/r_{1/2})^{\text{young}}$  and  $(Z/H)^{\text{young}}/(Z/H)_{\odot}$  vs  $p$  of  $(r/r_{1/2})^{\text{old}}$  and  $(Z/H)^{\text{old}}/(Z/H)_{\odot}$ . In both panels, the color encodes the  $b$ -value of the galaxy and the gray dashed lines mark zero on each axis and the one-to-one relation.

which there is no direct correlation. This plane can be divided into four groups: ① The old and young gradients are positive, ② The old and young gradients are negative, ③ The old gradient is positive, the young gradient is negative, ④ The old gradient is negative, the young gradient is positive. Galaxies in group ① grow completely from the outside-in (Venturi et al., 2024), but no galaxies exist in this section. This case can therefore be ruled out. Galaxies in group ②, which is the majority of galaxies (322 out of 396), grow in the typical inside-out growth scenario (Venturi et al., 2024). The more interesting groups are ③ and ④. Group ③ only includes 13 galaxies and is a very peculiar case, where the old stars have a positive metallicity gradient, while the young stars have the negative metallicity gradient. My focus will lie on group ④, which includes 61 galaxies, where the old metallicity gradient is negative, while the young metallicity gradient is positive. This configuration can be explained by the following scenario: A galaxy grows in a typical inside-out growth, building up a negative metallicity gradient. Then its star formation is stopped, and later it rejuvenates, meaning that it starts forming stars again. If this process is stronger in the outskirts, the newly formed stars will have a higher metallicity there compared to the center, which leads to a positive metallicity gradient among these younger stars. Fortuné et al. (in prep.) introduce a *star formation history classification* for the same galaxies that are investigated in this work. Two of these classes are so-called *rejuvenators* and *hoppers*. They initially lie on the star formation main sequence of galaxies, until they are quenched and later rejuvenate, and hop back onto the main sequence. Six of the 61 galaxies in group ③ are rejuvenators and 31 are hoppers, that is 60% of the galaxies that exhibit a positive young metallicity gradient have been quenched and later rejuvenate their star formation. Another instance of rejuvenation in the Magneticum simulation is presented by Remus & Kimmig (2023), in their case, in Box3. They investigate galaxies that were quenched at high redshift. Some restarted star formation afterward, which primarily occurs in the outskirts between  $1r_{1/2}$  and  $3r_{1/2}$ , also agreeing with this scenario.

A similar plane can be covered by calculating the Pearson correlation coefficient  $p_{\text{old}}$  and plotting it against the Pearson correlation coefficient  $p_{\text{young}}$ . This should show a similar population of the four groups, except the values on the x- and y-axis do not represent the strength of the gradient but rather the strength of the correlation and therefore the statistical robustness of the metallicity gradient. This is shown in Figure 3.23b. The correlation coefficient reaches values between  $\sim -0.5$  and  $\sim 0.1$  for  $p_{\text{young}}$  showing that the positive young metallicities gradients are fit to distributions that are not as tightly correlated as the negative young metallicity gradients. The correlation coefficients  $p_{\text{old}}$  range from  $\sim -0.3$  to 0. This suggests that one has to be careful when interpreting the significance of the young positive metallicity gradients.

Finally, I checked whether various global properties of the galaxies are correlated with the young or old metallicity gradient. Figure 3.24 presents the same figure as Figure 3.23a colored by ① the luminosity-weighted mean stellar age  $\langle t_{\star} \rangle_{\text{lw}}$ , ② the luminosity-weighted mean stellar metallicity  $\log_{10}(\langle Z/Z_{\odot} \rangle_{\text{lw}})$ , ③ the star formation rate (SFR), ④ the cold gas to star ratio  $M_{\text{coldgas}}/M_{\star}$ , ⑤ the stellar mass  $\log_{10}(M_{\star}/M_{\odot})$ , and ⑥ the black hole to star ratio  $M_{\text{BH}}/M_{\star}$ . There are the slight trends that the bulk of galaxies with a negative young metallicity gradient are younger, more metal-rich and have a higher star formation rate than galaxies that have a positive or almost flat young metallicity gradient. There are no clear trends with stellar mass, the cold gas mass or the mass of the galaxies central black hole. This shows that galaxies that intrinsically form stars build up a negative metallicity gradient. The correlation with age only reflects that currently formed stars are young and metal-rich.

### 3.3 Other Galaxy Classifications

In the previous section, the classification according to the star formation history was already mentioned and their connection to metallicity gradients discussed. To gain a more profound insight, the radial metallicity and age distribution of the galaxies in this classification will be analyzed. The metallicity gradients' relation with the  $V/\sigma$ -parameter, which is related to the galaxies' kinematics, was also investigated in the last section. For that reason, kinematic classes will also be studied regarding the age and metallicity profiles. The two classifications used here are:

① The *star formation history classes* introduced by Fortuné et al. (in prep.) for the 1307 Magneticum Box4 galaxies. By comparing each galaxy's evolution of the star formation rate over time to the star formation rate main sequence  $\log_{10}(\text{SFR}(M_{\star}, t)) = (A - B \times t/\text{Gyr}) \times \log_{10}(M_{\star}/M_{\odot}) - (C - D \times t/\text{Gyr})^4$  (Speagle et al., 2014; Pearson et al., 2018). This analysis reveals five different types:

- Main Sequence (MS): Galaxies that stay on the “main sequence” for their entire evolution (22/1307).

<sup>4</sup>Speagle et al. (2014) find the fitting parameters to be  $A = 0.4 \pm 0.02$ ,  $B = 0.026 \pm 0.003$ ,  $C = 6.51 \pm 0.24$ , and  $D = 0.11 \pm 0.03$ .

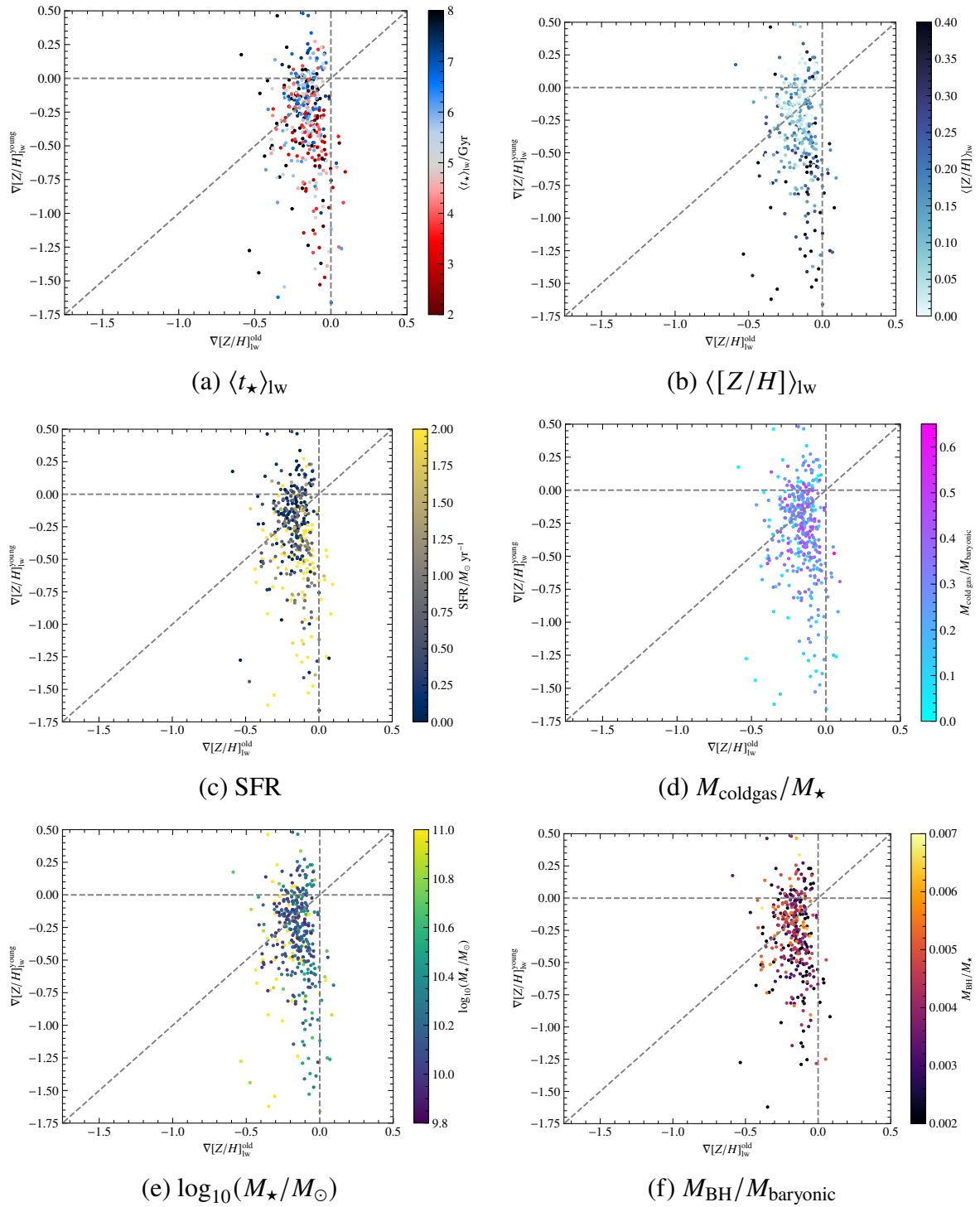


**Figure 3.24:** Same as Figure 3.23a, colored by the individually captioned properties.

- Caught (Ct): Galaxies that drop below the main sequence at some point in time but retain some star formation and later get “caught” by the main sequence, as it drops to lower star formation rates at later times (20/1307).
- Quenched Late (QL) and Quenched Early (QE): The bulk of galaxies in this sample are, “quenched” and their SFR drops below the main sequence permanently. These can be split into galaxies that do so “early” ( $z > 1$ , 660/1307) in their evolution and those that do so “late” ( $z < 1$ , 188/1307).
- Rejuvenators and Hoppers (Rj): The last class consists of galaxies that drop below the main sequence once (or multiple times) and later raise their star formation again, called “rejuvenators” (and “hoppers”) (417/1307).

② The *kinematic classes of early-type galaxies* (ETGs) introduced by Schulze et al. (2018) for the Magneticum Box4 galaxies based on observed types of galaxies from IFU surveys (e.g., Krajnović et al., 2011). This classification is based on the 2D velocity and velocity dispersion map based on a Voronoi tessellation (Cappellari & Copin, 2003) and was performed for all ETGs. They classify ETGs as all subhalos determined by SUBFIND that satisfy the following conditions: ①  $M_{\star} > 2 \times 10^{10} M_{\odot}$ , ②  $r_{1/2} > \frac{1.4 \text{ kpc}}{h(z+1)}$ , ③  $f_{\text{gas}} = M_{\text{coldgas}}/M_{\star} \leq 0.1$ , where  $M_{\text{coldgas}}$  is the total mass of all gas particles at temperatures below  $1 \times 10^5$  K within  $3r_{1/2}$ . This results in 900 “Magneticum ETGs” in Box4. Schulze et al. (2018) describe the classes as follows:

- Regular rotators (RR): The velocity map shows a well-defined, ordered rotation around the minor axis, with no kinematic features (620/900).
- Non rotators (NR): The velocity map exhibits no distinct kinematic feature and low-level velocities (129/900).
- Distinct core (DC): The velocity map features a central rotating component surrounded by a low-level or non-rotating component (35/900).
- Kinematically distinct core (KDC): The velocity map shows a central rotating component surrounded by a region with inclined rotation with respect to the central component (5/900). This explicitly includes counter-rotating cores.
- Prolate rotator (PR): The velocity map shows ordered rotation around the major axis of the galaxy (20/900).
- Unclass (U): The galaxy cannot be assigned to any of the previous groups (91/900).

In the following, the kinematically distinct cores will be excluded due to their very limited number.

First, I will focus on the *star formation history classes*. Figure 3.25 is the same as Figure 3.16, that shows the mass ratio of young stars compared to old stars  $M_{\star}^{\text{young}}/M_{\star}^{\text{old}}$  as a function of the radius  $r/r_{1/2}$ , but grouped into (from left to right) quenched early, quenched late, main sequence, caught and rejuvenator galaxies instead of spheroids, intermediates and disks. The galaxies that are quenched early have almost no mass in young stars compared to the mass in old stars ( $M_{\star}^{\text{young}}/M_{\star}^{\text{old}} \sim 0.1$ ), which is the case over the whole radial range. The stellar mass in the center of galaxies that stay on the main sequence has a high amount of

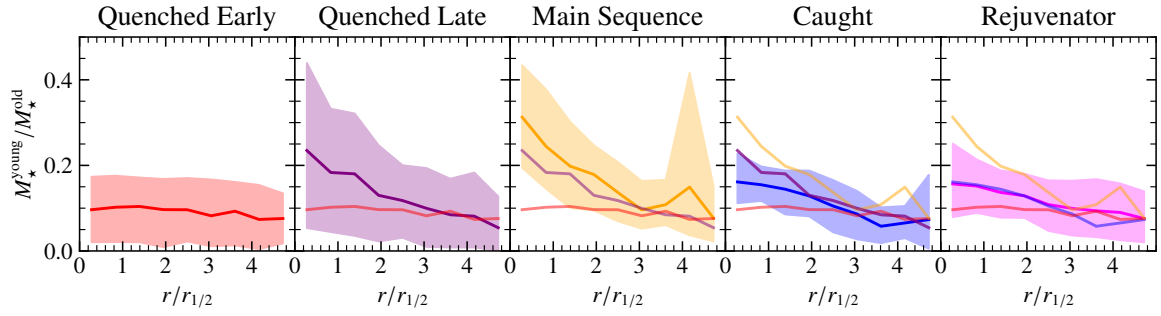


**Figure 3.25:** Radius in units of the half-mass radius  $r_{1/2}$  vs. mean of the ratio of mass in young and old stars in each radial bin subdivided into quenched late, quenched early, main sequence, caught and rejuvenator galaxies as presented by Fortuné et al. (in prep.). The boundaries of the shaded regions are the 0.1 and 0.9 quantiles within each bin.

young stars ( $M_*^{\text{young}}/M_*^{\text{old}} \sim 0.3$ ), which drops towards the outskirts to values comparable to the early quenched galaxies. This shows that star formation on the main sequence primarily happens in the center. Galaxies that are quenched late exhibit a similar distribution as main sequence galaxies, only shifted to smaller values. These are galaxies that lived on the main sequence for a long time, but because their star formation stopped before reaching  $z = 0$ , they have less mass in young stars. Finally, the last two classes behave almost identical. In the outskirts, both have a ratio  $M_*^{\text{young}}/M_*^{\text{old}}$  which is comparable to the other classes, while the ratio in the center lies between the one for quenched early and quenched late galaxies. However, the shape of the distribution is flatter than the more spiked shape of the center of the quenched late and main sequence galaxies. The maximum still lies in the center.

A more direct view on the distribution of ages among the star formation history classes is presented in Figure 3.26, which is similar to Figure 3.17. It shows the mass-weighted (*top row*) and luminosity-weighted (*bottom row*) age profiles for the different *star formation classes*. The behavior of the mass and luminosity-weighted cases are the same, but the latter representation is more pronounced. There, the same trends are present: The quenched late galaxies are old over the whole radial range up to  $5r_{1/2}$ . Compared to spheroids, there is also no dip in the 0.1 quantile contour, making it the oldest group of galaxies. The main sequence galaxies have the youngest centers, while the quenched late galaxies lie in between, as expected from Figure 3.25. The remaining two classes are youngest at  $\sim 1r_{1/2}$ , similar to disk galaxies (see, Figure 3.17), while the galaxies that are caught are slightly shifted to even younger values than the rejuvenators. The fact that the rejuvenated galaxies are youngest in a radial range distinct from the core supports the scenario for the formation scenario of galaxies with a positive young metallicity gradient presented in the last section: There is a large overlap with rejuvenating galaxies, where young metal-rich stars form outside  $\geq 1r_{1/2}$ .

Finally, I analyze the radial metallicity distribution of these classes, similar to Figure 3.18 and Figure 3.19. Figure 3.27 shows the luminosity-weighted mean metallicity  $\langle [Z/H] \rangle_{\text{lw}}$  as a function of radius  $r/r_{1/2}$  for (from left to right) quenched early, quenched late, main sequence, caught and rejuvenator galaxies (*top row*). The *bottom row* shows the metallicity distribution calculated in the same fashion, but split into the three stellar age populations,

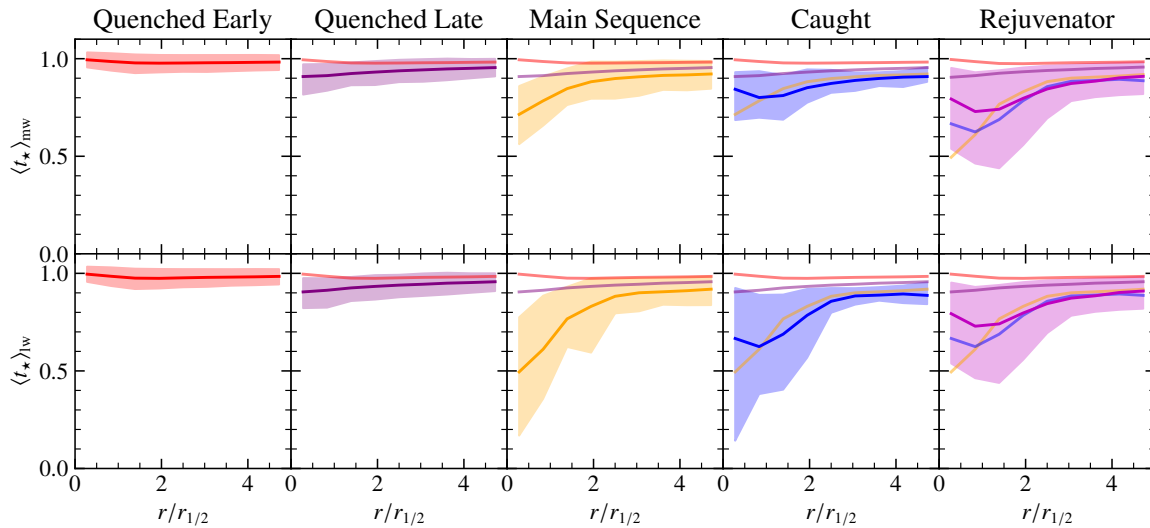


**Figure 3.26:** Same as Figure 3.17, but for the star formation history classes presented by Fortuné et al. (in prep.).

young, middle-aged, and old stars. The black line represents the total distribution, that is also shown in the top row. All total metallicity profiles are declining. The quenched early galaxies are metal-poor over almost all radii ( $\langle [Z/H] \rangle_{lw} \sim 0$ ), the main sequence galaxies have the most metal-rich core ( $\langle [Z/H] \rangle_{lw} \sim 0.5$ ) and are declining the most. Again, the quenched late galaxies are an intermediary class between the quenched early and main sequence galaxies. The caught galaxies have a shallow profile in the core at a value similar to the quenched late galaxies, but are the most metal-poor in their outskirts. The rejuvenator galaxies’ radial metallicity profile is very similar to the caught galaxies’ profile but is slightly shifted to metal-poor values. The *bottom row* reveals that within the quenched early galaxies, all stellar populations have similar values that mimic the total profile. The steep decline in the main sequence galaxies’ profile is driven by the young and middle-aged stars, while the old stars are metal-poor over all radii. This is also the case for the caught and rejuvenator galaxies’ profile, with a similar shape to the total profile in the young and middle-aged stars. Following the formation scenario for positive young metallicity gradients, one expects that the young stars in rejuvenator galaxies have an increasing metallicity profile. This is not confirmed here. This is the case because only 60% of galaxies with a positive young metallicity gradient are rejuvenators. The remaining galaxies can still have a different star formation history. There are also many more rejuvenators, which do not have a positive metallicity gradient. This underlines that the presented formation scenario is only one of many possible formation scenarios for positive young metallicity gradients.

Now, I want to focus on the *kinematic classes* presented by Schulze et al. (2018). These distinguish between rotating and non-rotating galaxies and galaxies which rotate in a peculiar way. This rotation pattern might be caused by different stellar population. Therefore, Figure 3.28 presents the distribution of the *b-value* split into the different stellar populations, as it was done for Figure 3.14. The young stars’ median *b-value* is highest and within the “disks” range for all classes, while the old stars’ median *b-value* is lowest and within the

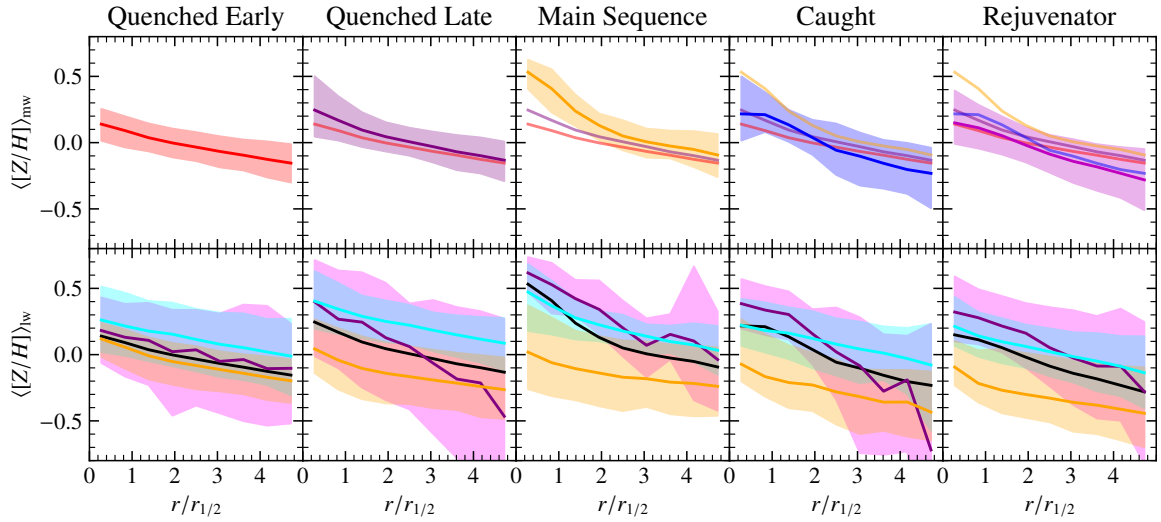


**Figure 3.27:** Same as Figure 3.18 and Figure 3.19, but for the star formation history classes presented by Fortuné et al. (in prep.).

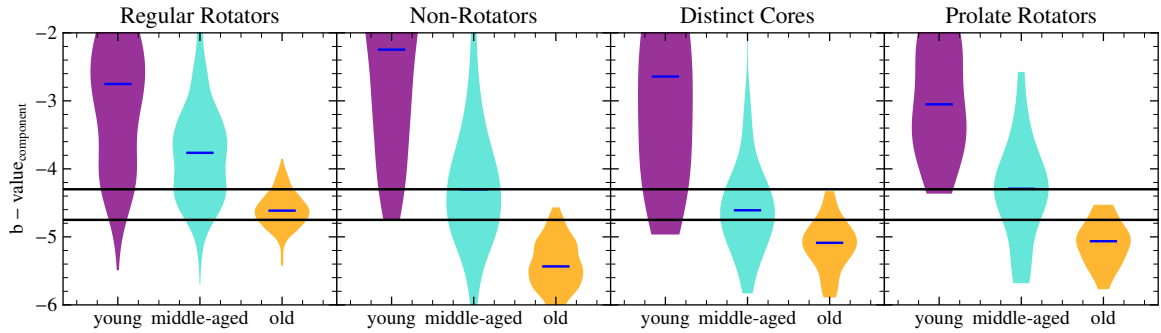


**Figure 3.28:** Same as Figure 3.14 for the kinematic classes presented by Schulze et al. (2018).

“spheroids” range, except for the regular rotators, where it is within the “intermediates” range. The middle-aged stars’ median  $b$ -value typically also lies within this range, but is disk-like for regular rotators. The lowest median value for the old population is found for non-rotators. This shows that within regular rotators, both young and middle-aged stars shape the total  $b$ -value to be “intermediate”-like. In non-rotators the old component is the most spheroidal-like and a significant amount of middle-aged stars seem to be spheroidal-like. Interestingly, the prolate rotators’ young component’s  $b$ -value distribution lies entirely in the disk-like range, which might suggest that their rotating stars are young. The distinct cores’ rotating component is also thought to be young (Schulze et al., 2017). The  $b$ -value does not only encode the angular momentum, but also the stellar mass of the galaxies. As most of the mass is within old stars (see, Figure 3.16, Figure 3.25, Figure 3.29), the low  $b$ -value of the old stars is partly due to their mass compared to the younger stars.

Finally, the equivalent figures to Figure 3.25, Figure 3.26 and Figure 3.27 were produced for the kinematic classes as well, which are presented in Figure 3.29, Figure 3.30, and Figure 3.31. Figure 3.29 and Figure 3.30 show that the oldest class over all radii is the non-rotator class, followed by the prolate rotators. The regular rotators and distinct core galaxies are old as they are ETGs, but they exhibit a higher mass ratio  $M_{\star}^{\text{young}}/M_{\star}^{\text{old}}$  in the core. The

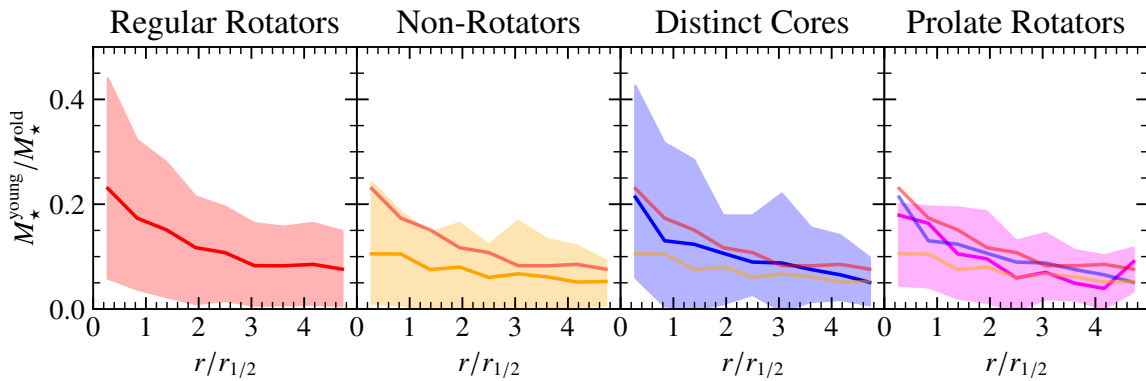


**Figure 3.29:** Same as Figure 3.25 for the kinematic classes presented by Schulze et al. (2018).

distinct core galaxies are younger in the center. The 0.1-quantile region for regular rotators also shows a decrease in age in the center. The distinct core galaxies have the youngest core, which further solidifies the suspicion that the rotating component in the core is built up by young stars. Schulze et al. (2017) have found that a 1:1 binary disk galaxy merger, where each spiral galaxy has an initial gas fraction of 20% and hosts a stellar bulge and a central black hole, produces a KDC if merged in a specific orbital configuration. This KDC is then dominated by the newly formed stars. The same result was obtained by Hoffman et al. (2010). McDermid et al. (2006) suggested that there are two types of KDCs: The first one is composed of young KDCs formed by major mergers, which was already mentioned. The second type occurs when a KDC consisting of old stars is formed by sequential minor mergers (Moody et al., 2014; Schulze et al., 2017), which deposit their stellar material in the outskirts around a central rotating disk. This second type could also be part of the stacked profile in Figure 3.30, diluting the young signal from the center. Finally, all metallicity profiles in Figure 3.31 are declining. The central metallicity is highest for distinct core galaxies, but the profile declines to the same values as the others in the outskirts. When split into the three stellar age populations, also shown in Figure 3.31, still all metallicity profiles are declining with no notable difference between the four groups because all of them are ETGs (or spheroids).

### 3.4 Summary and Conclusion

In this chapter, I analyzed galaxies taken from Box 4 (uhr) of the hydrodynamical cosmological *Magneticum Pathfinder simulations* to study their ages and metallicities and the distribution of said parameters as radial profiles and as metallicity gradients. It is investigated how these gradients are related to global properties of the galaxies. This is done for all stellar particles and for different stellar age populations. Finally, the age and metallicity profiles for galaxies of different specific classes are studied. All selected galaxies have stellar masses larger than  $\log_{10}(M_{\star}/M_{\odot}) = 9.83$ . I used the *b-value* (Teklu et al., 2015) to classify them into spheroidal, intermediate, and disk-like galaxies. I first analyze some global properties, connecting mass, age, metallicity, size, and rotational support  $V/\sigma$ . The following conclusions could be drawn:

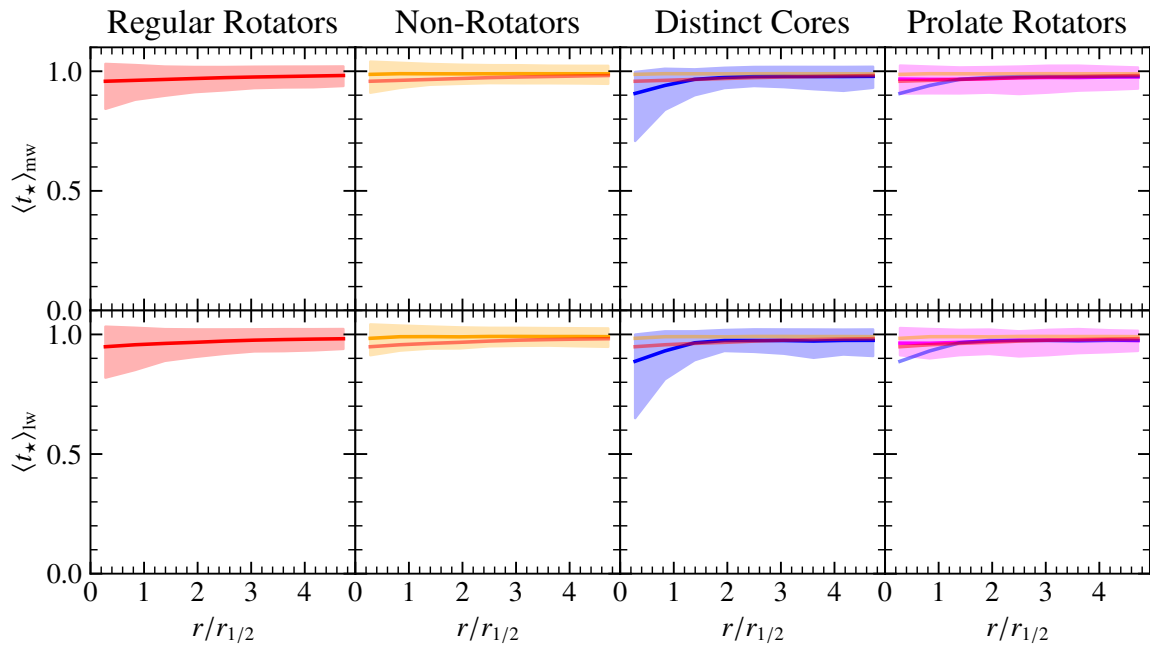


**Figure 3.30:** Same as Figure 3.26 for the kinematic classes presented by Schulze et al. (2018).

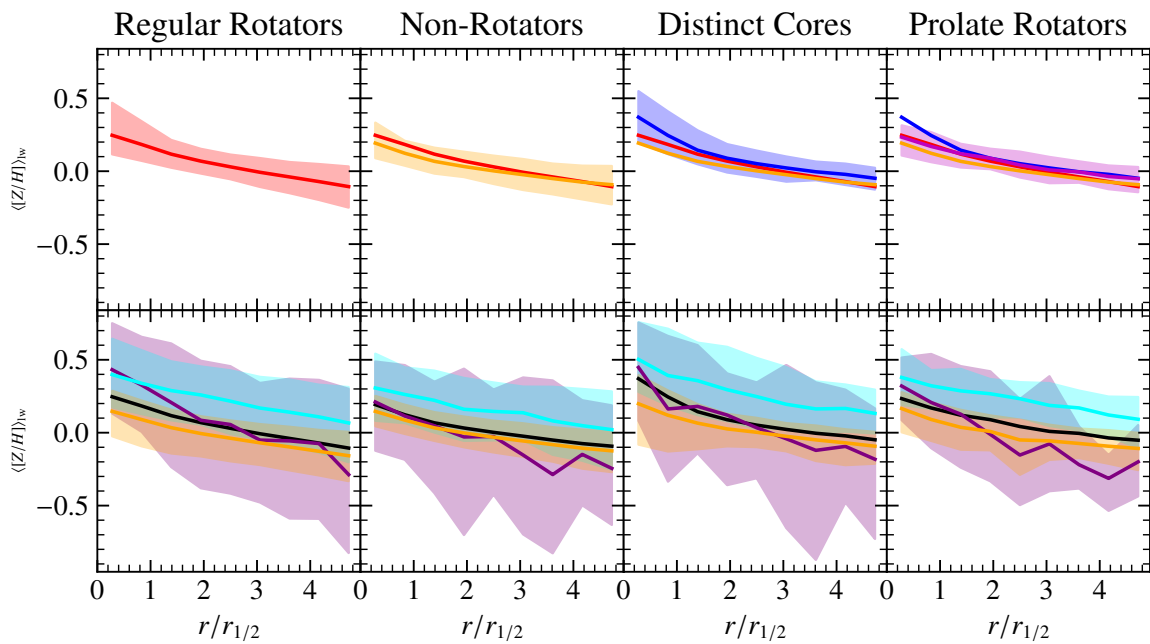


**Figure 3.31:** Same as Figure 3.27 for the kinematic classes presented by Schulze et al. (2018).

- The difference between luminosity-weighted (lw) and mass-weighted (mw) ages and metallicities was investigated, where the luminosity-weighted age lies below the mass-weighted age, especially for disks, and the luminosity-weighted metallicity also lies below the mass-weighted metallicity, almost at a constant rate (of 0.08 dex), for spheroids, while many disks have a higher luminosity-weighted metallicity than mass-weighted metallicity.
- It was recovered that a galaxy's age  $\langle t_{\star} \rangle_{lw}$  is correlated with its morphology, while its metallicity  $\log_{10}(\langle Z/Z_{\odot} \rangle_{lw})$  is correlated with its stellar mass  $M_{\star}$ .
- At fixed mass, spheroidal galaxies are older than disk galaxies and overall the age slightly increases with mass, consistent with Gallazzi et al. (2005); González Delgado et al. (2015); Scott et al. (2017); Nanni et al. (2024).
- At fixed mass, larger galaxies are younger, in agreement with Scott et al. (2017) and Lange et al. (2015). This is explained by the fact that disk galaxies are larger and younger than spheroids at a fixed mass. In contrast, the metallicity is not correlated with size or morphology but increases with stellar mass.
- Young galaxies, which generally are disks, are on average more rotationally supported, measured by  $V/\sigma$  and  $\lambda_{r_{1/2}}$ , and have higher ellipticities  $\epsilon$  than old galaxies, which generally are spheroids.
- Magneticum galaxies reproduce the observed mass-metallicity relation (MZR) well, where more massive galaxies are more metal-rich. On average, disk galaxies have lower metallicities  $[Z]_{mw}$  compared to spheroids.
- The  $\Phi$ ZR ( $\Phi = \log(M_{\star}/M_{\odot}) - \alpha \log(r_{1/2}/\text{kpc})$ ) for the stellar component of Magneticum galaxies is tightest for  $\alpha \sim 0.8$ , opposed to  $\alpha \approx 0.6$  as found for gas by Sánchez-Menguiano et al. (2024).
- The contributions of the three different stellar age populations (*young*:  $t_{\star} < 2$  Gyr, *middle-aged*:  $2 \text{ Gyr} < t_{\star} < 8$  Gyr, *old*:  $t_{\star} > 8$  Gyr) to the *b-value* were tested: Young stars are mostly in the disk-like range ( $b > -4.35$ ) for all morphologies, while the old stars always lie in the range of the respective actual morphology of the galaxy, which leads to the conclusion that the *b-value* is dominated by the behavior of old stars.
- The mass-metallicity relation is still in place when the galaxies' stars are separated into these stellar populations, but in disks old stars are more metal-poor than young stars and old stars in spheroids.

Then I analyzed spatially resolved properties, that is age and metallicity profiles, and metallicity gradients. This is done for all stars and for stars separated into young, middle-aged and old stars. Their relation to global parameters of galaxies is also investigated.

- The distribution of the ratio  $M_{\star}^{\text{young}}/M_{\star}^{\text{old}}$  suggests, that the center of spheroidal and intermediate galaxies is influenced more strongly by young stars than the centers of disk galaxies.
- Spheroids have a slightly increasing age profile, that is the center is younger than the outskirts, which favors an “outside-in” progression of star formation, where the age increases with galactic radius, consistent with González Delgado et al. (2015);

Goddard et al. (2017). Disk galaxies, on the other hand, show decreasing age profiles in their center, supporting the "inside-out" formation scenario, that is less star formation activity in the bulge and a younger stellar population at large radii.

- All morphologies have declining metallicity  $\langle [Z/H] \rangle_{lw}$  profiles, consistent with Nanni et al. (2024). Splitting the stars into the three populations reveals that over (almost) all radii the middle-aged stars have the highest metallicity  $\langle [Z/H] \rangle_{lw}$  in spheroids and intermediates, while the young population is the most metal-rich in disks up to  $\sim 2.5r_{1/2}$ . The difference in metallicity  $\langle [Z/H] \rangle_{lw}$  within the populations is also largest in disks.
- The young stellar population has the steepest decline in the metallicity  $\log_{10}(\langle Z/Z_{\odot} \rangle_{lw})$  profile over  $5r_{1/2}$  in all morphologies, but in the center of disks ( $r < r_{1/2}$ ) the metallicity in old stars seems to decline faster.

The difference in the metallicity profiles of young stars between spheroids and disk galaxies seems to be related to the mass assembly and star formation history of a galaxy (see Figure 3.2). Disk galaxies mostly can evolve undisturbed and therefore continuously form stars, always enriching the next generation of stars. Therefore, young stars are the most metal-rich. In contrast, spheroidal galaxies live in denser regions and experience various minor and major mergers, which disturb their star formation. Their young stars can be directly accreted as part of dwarf galaxies or are formed from newly accreted pristine gas, both of which generally are less metal-rich. Dwarf galaxies – in line with the mass-metallicity relation – are less metal-rich. It is speculated that in less massive galaxies metal-rich gas can more easily escape the gravitational potential before it can be formed into stars, and they therefore are less metal-rich (Tremonti et al., 2004).

I then calculated the metallicity gradient  $\nabla \langle [Z/H] \rangle_{lw}$  within  $3r_{1/2}$  and investigated their correlation with global properties.

- The median metallicity gradient  $\nabla \langle [Z/H] \rangle_{lw}$  in spheroidal galaxies is the most negative, followed by intermediates, while disk galaxies have the flattest gradients, consistent with Zhuang et al. (2019).
- I confirm that there is a trend to steeper negative metallicity gradients  $\nabla \langle [Z/H] \rangle_{lw}$  with increasing stellar mass, which is most pronounced in disk galaxies, consistent with González Delgado et al. (2015); Goddard et al. (2017); Neumann et al. (2021); Nanni et al. (2024).
- Within disks galaxies the slope of the metallicity profile does not significantly change with increasing  $V/\sigma$ , while within spheroids and intermediates the metallicity gradients steepen with increasing  $V/\sigma$ .

Goddard et al. (2017) suggest that the steepening of metallicity gradients with mass is a result of the deeper potential wells of massive galaxies that shape the metallicity gradient during the formation. This contrasts with massive systems experiencing more major mergers, which lead to a flatter metallicity gradient due to the redistribution of stars during such an event. On the other hand, a system experiencing a merger event is generally less rotationally supported. Merger events are therefore a possible explanation for the trend of steepening

metallicity gradients with increasing  $V/\sigma$ . Furthermore, I investigated the relation between the metallicity gradients within the young and old stellar populations. The majority of galaxies have both a negative young and old metallicity gradient, representative of an “inside-out” progression of star formation (322 out of 396). Interestingly, 61 galaxies have a negative old but a positive young metallicity gradient. Some of these galaxies might be galaxies whose star formation was quenched once and later restarted in their outskirts (Remus & Kimmig, 2023). Although the Pearson correlation coefficient between the metallicity and the radius of the young stars of these galaxies is also negative, its absolute value is low, advising to treat this interpretation with caution. The star formation rate seems to increase with decreasing (steepening) young metallicity gradient. Finally, the age and metallicity profiles of other galaxy classifications were investigated: ① For the *star formation history classes* defined by Fortuné et al. (in prep.) the following can be stated:

- Main sequence galaxies have the youngest stars in the center, while quenched early galaxies are overall old, with quenched late galaxies being an intermediary class between the former two.
- Caught and rejuvenator galaxies have a minimum in their age profiles at  $\sim 1r_{1/2}$ , while overall being younger than quenched late galaxies but older than main sequence galaxies, most significantly in the center.
- The metallicity profiles are all declining. The galaxies that are the most metal-rich in the center are main sequence galaxies, the most metal-poor are quenched early galaxies and rejuvenators, with quenched late and caught galaxies again being intermediary classes, respectively. The difference between caught and rejuvenator galaxies and the quenched galaxies is that the former classes’ metallicity profiles are flatter in the center than those of the latter classes.

The last classification to be analyzed was the ② The *kinematic classes* defined by Schulze et al. (2018) and the following can be concluded:

- All classes are old over all radii because they are all ETGs.
- The distinct core galaxies exhibit a decline of age in the center, which is representative of a type of distinct core, which formed in a major merger from newly formed stars.
- The regular rotators 0.1-quantile line in the age profile also exhibits a decline in age towards the center.
- Again, all metallicity profiles are declining. The highest metallicity is found in the center of distinct core galaxies.

# Chapter 4

## Prolate Rotators

In this chapter, I further study the early type galaxies (ETGs), whose stars primarily rotate around the major axis, called *prolate rotators*. They are part of the *kinematic classes of early-type galaxies* presented in the last chapter (see Section 3.3) and introduced by Schulze et al. (2018) for the *Magneticum* Box4 galaxies. They are thought to have formed from a major merger of two galaxies (Ebrova & Lokas, 2017; Tsatsi et al., 2017; Ebrova et al., 2021), where the final infall of a satellite galaxy is approximately aligned with the angular momentum vector of the central galaxy’s progenitor. This causes the descendant to be elongated in the direction of the angular momentum vector, that is the major axis is roughly parallel to it (e.g. Hegde et al., 2022). This radial merger often leads to the build up of stellar shells around the prolate rotator (Ebrova et al., 2021; Valenzuela & Remus, 2024). Because they are the result of a major merger, one expects a high stellar mass (Tsatsi et al., 2017; Ebrova & Lokas, 2017). These are a very rare and peculiar class of galaxies with a number of 6 out of 81 in the CALIFA Kinematic Subsample (Tsatsi et al., 2017) and only 2% (20 galaxies) in the *Magneticum* ETGs sample. In the previous chapter, the radial age profile for prolate rotators was presented (see Section 3.3), showing that they are old over their whole radial range (up to  $5r_{1/2}$ ). This raises the question if the rotation pattern is also stable for a long time. A conflicting fact is that they are very rare, which could be explained by the scenario that prolate rotation is only visible for a very short amount of time. Another possibility is that the prolate rotation is stable for a long time, but the configuration is truly very rare. In this chapter, I analyze the stability of this prolate rotation and whether this rotation pattern is stable over a long time, or whether it is washed out or rearranged back to regular rotation. Additionally, the proposed formation scenario will be investigated and their merger ratio calculated. Finally, the stellar ages and whether the rotation is dominated by young or old stars is identified.

### 4.1 Formation and Stability of Prolate Rotators

First, the *stability* of this prolate rotation is tested, that is how long after the first establishment of prolate rotation the galaxy is continuously prolately rotating. This can be probed by running an isolated disk galaxy merger simulation, which is set up to form an elliptical galaxy that

exhibits prolate rotation. For the study of this, I use one such simulation out of a set of 10 simulations of disk-disk and disk-spheroid mergers, which were run with the cosmological hydrodynamical TreeSPH Code GADGET-2 (Springel, 2005). Schauer et al. (2014) and Schulze et al. (2017) provide further details about the simulation. This specific simulation is a 1:1 disk-disk merger with a gas fraction of  $f_{\text{gas}} = 0.2$ , that also produces a KDC. Here, I focus on the rotation pattern outside the very center ( $> 1r_{1/2}$ ). Figure 4.1 shows four snapshots (from top to bottom) of said simulation at  $t_1 = 1.08$  Gyr,  $t_2 = 1.292$  Gyr,  $t_3 = 1.576$  Gyr, and  $t_4 = 6.106$  Gyr after the start of the simulation. To compute luminosities for the stellar particles, their age  $t_{\star}$ , metallicity  $Z$  (i.e., the sum of the mass fractions of all elements heavier than helium) and their initial mass  $m_{\star}^{\text{ini}}$  are required (see Section 2.4). Each isolated disk galaxy initially consists of “disk” particles and “bulge” particles, which do not have age information. Newly formed star particles are given the information about the simulation time when they were formed  $t_{\text{form}}^{\text{new,sim}}$ . The ages are now computed using the following scheme: I assume that the start of the simulation is at an age of the universe of  $t_{\text{start}} = 9.8$  Gyr and that all disk and bulge particles were formed at the same time and initially have an age of  $t_{\star}^{\text{disk,ini}} = 6$  Gyr and  $t_{\star}^{\text{bulge,ini}} = 8$  Gyr. The formation times of bulge and disk particles are then equal to  $t_{\text{form}}^{\text{disk/bulge}} = t_{\text{start}} - t_{\star}^{\text{disk/bulge,ini}}$ , while the formation time of newly formed stars needs to be shifted into the new time frame  $t_{\text{form}}^{\text{new}} = t_{\text{form}}^{\text{new,sim}} + t_{\text{start}}$ . Finally, the age of all stars in a snapshot at  $t_{\text{sim}}$  is given by  $t_{\star} = (t_{\text{start}} + t_{\text{sim}}) - t_{\text{form}}$ . The metallicity of all particles is considered to be the same, at solar metallicity  $Z_{\odot} = 0.0134$  (Asplund et al., 2009). Instead of the initial mass of a stellar particle, its current mass  $m_{\star}^{\text{ini}} = m_{\star}$  is used in the calculation of its luminosities. In Figure 4.2, the left column shows a 2D-binned stellar mass map, the middle column a Voronoi-binned luminosity-weighted stellar line-of-sight velocity ( $losv$ ) map, and the right column a Voronoi-binned luminosity-weighted stellar velocity dispersion ( $losv\sigma$ ) map. The blue ellipses in each panel represent the galaxy’s shape at  $1r_{1/2}$  and at  $3r_{1/2}$ . The snapshot at  $t_1$  depicts the galaxies after their first core passage and before the second and final one, after which the system settles into an elliptical galaxy. At  $t_2$  the relaxation process through dynamical friction and violent relaxation is still ongoing, but a developing KDC can already be spotted in the center of the  $losv$  map. At  $t_3$  the general rotation pattern is settled, with the KDC in the center. The surrounding rotation pattern is very regular, but not oblate, meaning a rotation around the short axis. The rotation is also not perfectly prolate, meaning a rotation around the long axis, but rather a tilted rotation between the two axes. Nevertheless, this rotation is taken as an approximation to prolate rotation and its stability is assumed to be similar to a prolate rotations’ stability. At  $t_4$ , this tilted rotation is still in place at the same angle, while the KDC vanished due to dynamical friction (Schulze et al., 2017). This leads to the conclusion that prolate rotation is stable over at least  $t_{\text{stability}} = t_4 - t_3 \approx 4.5$  Gyr. Due to the absence of any significant changes of the velocity map between  $t_3$  and  $t_4$ , it is plausible that prolate rotation is stable for much longer than this. Of course, this is only the case within an isolated framework where there are no disruptions due to in-falling satellite galaxies, major mergers or tidal forces by neighboring galaxies.

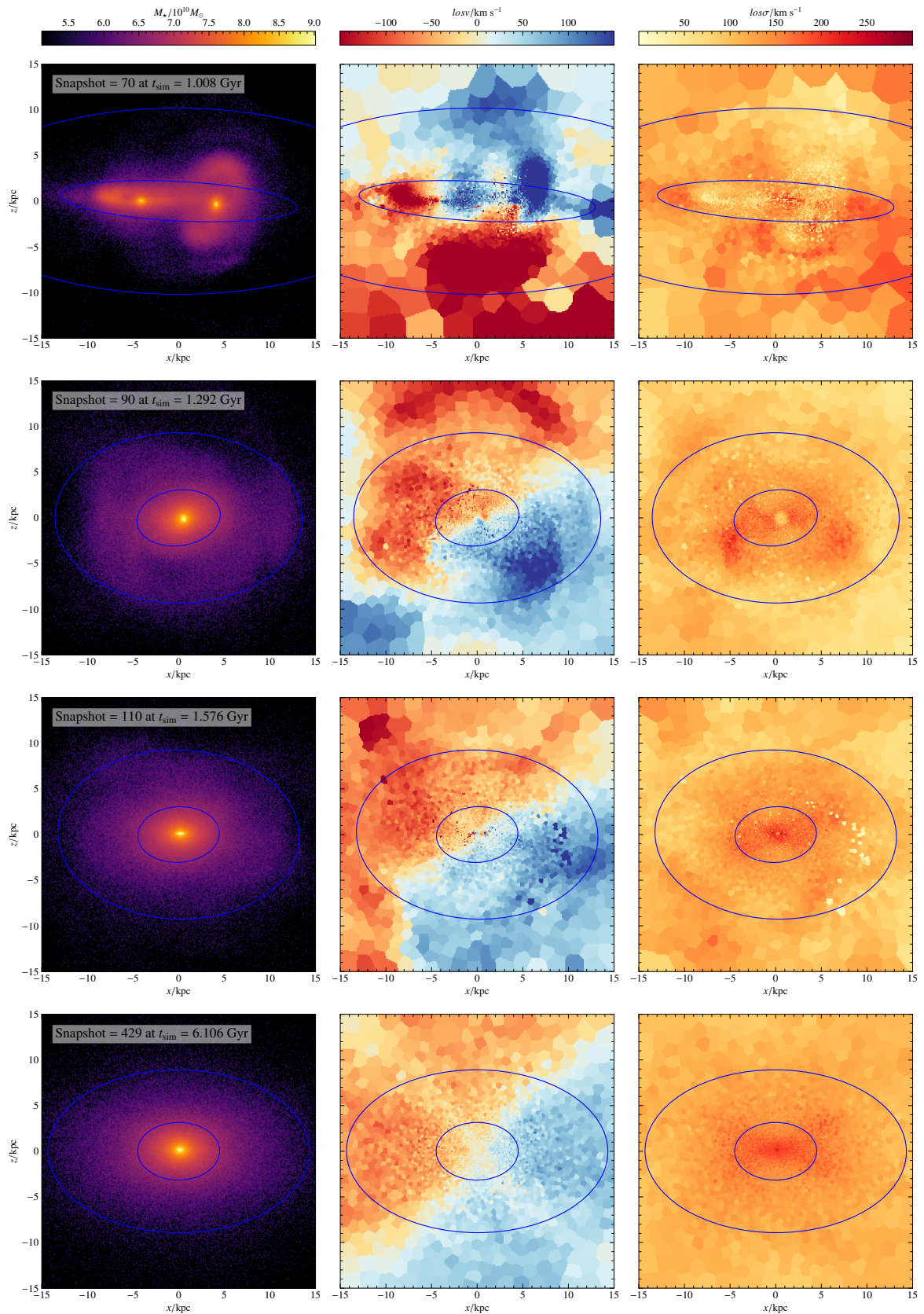


**Figure 4.1:** Snapshots at  $t_1 = 1.08$  Gyr,  $t_2 = 1.292$  Gyr,  $t_3 = 1.576$  Gyr, and  $t_4 = 6.106$  Gyr after the start of an isolated disk-disk merger simulation from a set of simulations performed by Schauer et al. (2014). *Left column:* 2D-binned stellar mass map, *Middle column:* Voronoi-binned luminosity-weighted stellar line-of-sight velocity ( $losv$ ) map, *Right column:* Voronoi-binned luminosity-weighted stellar velocity dispersion map. The blue ellipses in each panel represent the galaxy's shape at  $1r_{1/2}$  and  $3r_{1/2}$ .

An approach that takes more aspects of realistic galaxy formation into account, including the full cosmological framework of merging galaxies, gas in- and outflows, the expansion of the universe, and many more details, are cosmological simulations. As already mentioned in Section 3.3, Schulze et al. (2018) compiled a list of 22 prolate rotators found at  $z = 0$  in Box4 (uhr) of the Magneticum Pathfinder Simulations. The formation of an example galaxy, from now on referred to as P1 (“Prolate Rotator 1”) is illustrated in Figure 4.2. The top three rows show the first progenitors of the central galaxy P1. The 1st row shows the 2D-binned stellar mass maps, the 2nd row the Voronoi-binned luminosity-weighted  $losv$  map and the 3rd row shows the age of the universe at the stars’ formation also in a Voronoi-binned luminosity-weighted map. The blue ellipses in each panel represent the galaxy’s shape at  $1r_{1/2}$  and at  $3r_{1/2}$ . All panels are rotated into the edge-on frame at  $3r_{1/2}$  of the central galaxy in the second column ( $z = 0.52$ ).

The morphology, kinematics and the age of the two galaxies are not enough to completely describe their collision. A crucial aspect is the orbit on which the satellite galaxy P2 falls into the central galaxy P1. This was already hinted at with the red (direction to the satellite/central galaxy) and white (relative velocity of the satellite) arrows in Figure 4.2, but this figure is based on the particles output of the simulation, which has a very limited time resolution. A higher time resolution is available from the SUBFIND output, which includes the galaxies’ positions and velocities. With this information and the shape information from Figure 4.2 the orbit can be constructed. Figure 4.3 shows the edge-on (*left panel*), face-on (*middle panel*), and side-on (*right panel*) projection of the central galaxy P1 at  $z = 0.52$ . The orange ellipses in the center of each panel are the shapes of P1 at  $1r_{1/2}$  and  $3r_{1/2}$ , and the orange arrow points in the direction of the minor axis in each projection. The satellite’s positions at  $z = 0.57$  to  $z = 0.47$  are over-plotted as 8 black crosses, which includes 3 positions with particle/shape information and 5 positions where only SUBFIND data is available. The shapes indicated by ellipses at the  $1r_{1/2}$ ,  $3r_{1/2}$ , and the minor axis direction of the satellite galaxy are shown in blue where particle/shape information is available. The red arrow points towards the central galaxy, and the black arrow indicates the direction towards which the satellite galaxy is moving.

At  $z = 0.57$  and  $z = 0.52$  the central galaxy P1 is a clear regular rotator with  $\lambda_{1r_{1/2}} = 0.41$  and its minor axis (blue arrow) and angular momentum vector (cyan arrow) are almost perfectly aligned. There is also a ring of young stars, which is aligned with the rotation pattern. At  $z = 0.57$  the satellite galaxy P2 also exhibits a regular rotation pattern, although the main rotation is further outside at  $3r_{1/2}$ , which is why  $\lambda_{1r_{1/2}}$  is lower at a value of 0.1 and the specific angular momentum vector is not as closely aligned with the minor axis. The young stars are also concentrated around  $3r_{1/2}$ . At  $z = 0.52$  it is even more kinematically disrupted, but still rather regular. This is the case because at that point it already passed by close to the central galaxy. Looking at the red arrow, at  $z = 0.57$  the satellite was to the left and slightly below the central galaxy and at  $z = 0.52$  it is to the top right. This passage is also seen in the orbit in Figure 4.3. Finally, P2 crashes into P1 at  $z = 0.47$  from the top right, almost parallel to the minor axis of P1 in  $z = 0.52$  in the edge-on projection. That

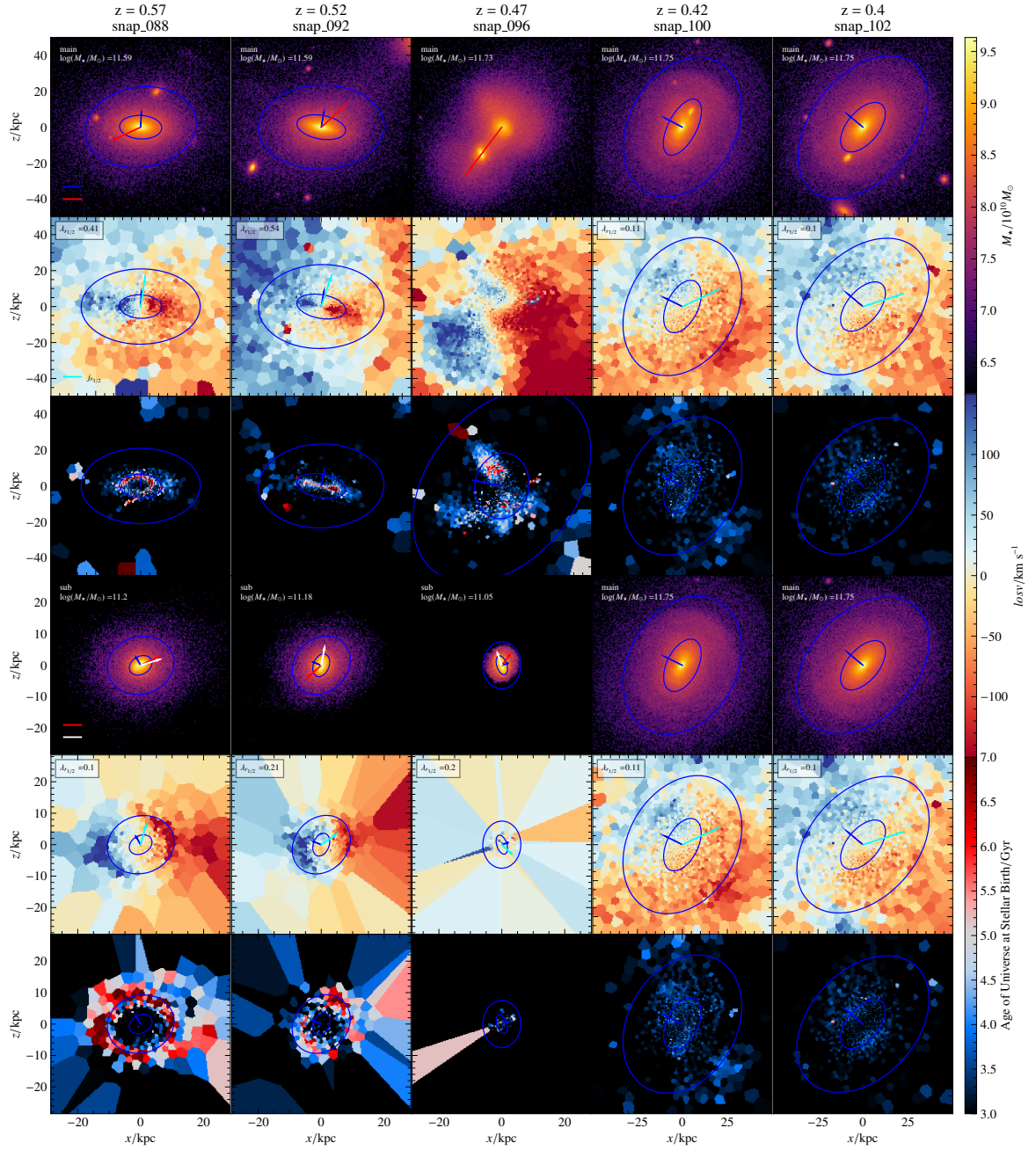


**Figure 4.2:** Detailed view on the merger causing the prolate rotation of P1. The first three rows depict the progenitors of P1, while the last three rows depict the progenitors and descendants of P2, the satellite galaxy which falls into P1 at  $z = 0.47$  (*center column*). The 1st and 4th row show the 2D-binned stellar mass maps, the 2nd and 5th row the Voronoi-binned luminosity-weighted  $losv$  map, and the 3rd and 6th row show the age of the universe at the stars’ formation also in a Voronoi-binned luminosity-weighted map. The blue ellipses in each panel represent the galaxy’s shape at  $1r_{1/2}$  and at  $3r_{1/2}$ . All panels are rotated into the edge-on frame at  $3r_{1/2}$  of the central galaxy in the second column ( $z = 0.52$ ). Blue arrows depict the direction of the minor axis of the calculated 2D shape ellipsoid, cyan arrows depict the direction of the stellar specific angular momentum vector for all stars within a sphere of  $3r_{1/2}$ , red arrows point towards the position of the satellite galaxy (or central galaxy), white arrows point in the direction of the current velocity of the satellite galaxy. In the top-left corner of row 1 and 4, the status of each galaxy (central  $\hat{=}$  “main”), satellite  $\hat{=}$  “sub”) together with its stellar mass within  $3r_{1/2}$  is shown, while row 2 and 5 depict  $\lambda_{l1/2}$  for each galaxy in its current projection.

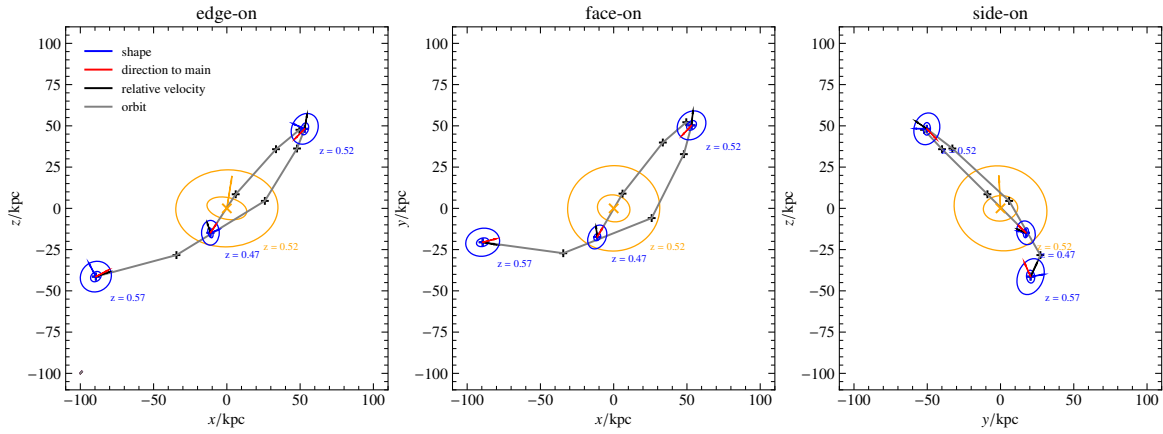


**Figure 4.3:** The orbit of P2 before falling into P1 in the edge-on (*left panel*), face-on (*middle panel*), side-on (*right panel*) in gray. The shape ellipses at  $1r_{1/2}$  and  $3r_{1/2}$  of P1 in the snapshot at  $z = 0.52$  is shown in each projection in orange. The blue ellipses show the same shape ellipses for P2 at  $z = 0.57, 0.52, 0.47$  in blue. Finally, the red arrows are the direction from P2 to P1 and the black arrow indicates the direction in which P2 is moving.

means that the collision is a very central hit onto the disk of the central galaxy, similar to the configuration found by Tsatsi et al. (2017), Ebrova & Lokas (2017), and Hegde et al. (2022). The *losv* map of P1 is irregular during the merger, while the P2 maps are not very meaningful because it already lost a lot of its stars to P1. At  $z = 0.42$  the shape is now elongated in the direction of the infall of P2 into P2 (red arrow in the top middle panel). The rotation pattern now is aligned around the major axis of the edge-on projection of P1. In projection, the specific angular momentum vector is not aligned with the minor axis anymore, but rather  $\geq 90^\circ$  rotated. P1 is not yet relaxed after the merger; a surviving substructure is still visible to the top right of the center within the  $1r_{1/2}$  ellipse. Finally, the rotation pattern settles into a prolate rotation at  $z = 0.40$ , similar to  $z = 0.42$ , but now also the age map settled into an interesting pattern: The center is old and most young stars are found at the  $1r_{1/2}$  ellipse, but not in the direction of the major axis, that is it appears that the young stars are part of the prolate rotation. Another interesting feature observed in the snapshots after the merger is a shell-like over-density in the mass map between the  $1r_{1/2}$  and  $3r_{1/2}$  ellipses to the bottom left. In conclusion, this prolate rotator was formed at  $z = 0.47$  during a galaxy merger, where a satellite galaxy hit its central galaxy centrally face-on on a radial orbit, consistent with Tsatsi et al. (2017), Ebrova & Lokas (2017), and Hegde et al. (2022). This prolate rotation is then sustained until  $z = 0$  for  $\sim 4.8$  Gyr. The merger ratio is  $r_{\text{merger}} = M_{\star}^{\text{central}}/M_{\star}^{\text{satellite}} = 2.13$  (see Section 4.2).

## 4.2 Global Properties of Prolate Rotators

As already mentioned, the P1 prolate rotator is one of 22 prolate rotators found in Box4 (uhr) of the Magneticum Pathfinder simulations. The classification was presented by Schulze et al. (2018) and described in Section 3.3 where their radial profile of stellar ages and stellar metallicity is investigated. Generally, the prolate rotator class is old (see Section 3.3). First, I

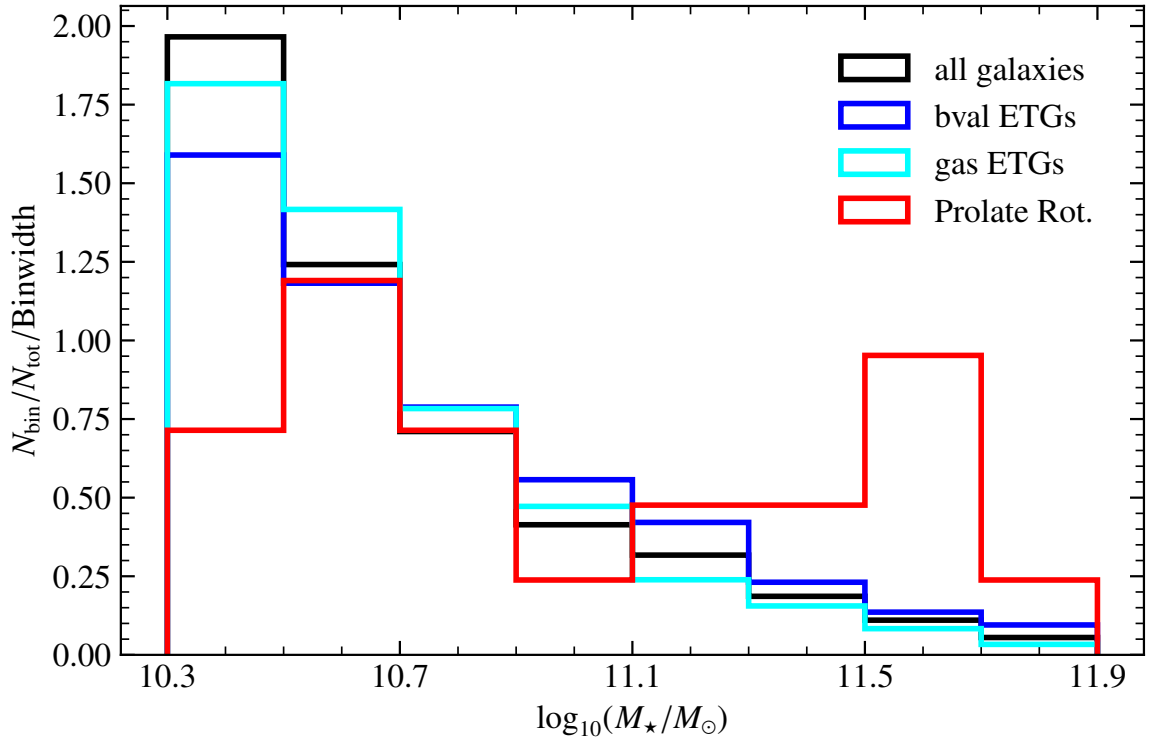


**Figure 4.4:** Distribution of stellar mass within a sphere of radius  $10\% r_{\text{vir}}$  for prolate rotators (red), ETGs or spheroids as classified by the  $b$ -value (blue), ETGs as classified by Schulze et al. (2018) using a cold gas criterion (cyan), and all galaxies (black).

present the mass distribution of these prolate rotators in Figure 4.4, which can also be found in the appendix of Schulze et al. (2018). The red histogram represents the prolate rotators, the blue histogram all ETGs or spheroids as classified by the  $b$ -value, the cyan histogram all ETGs as classified by Schulze et al. (2018) using the cold gas fraction criterion, and the black histogram all 1316 galaxies found in Box4 with stellar masses  $M_{\star} \geq 1 \times 10^{10} M_{\odot}$  (as defined in Chapter 3). The mass shown in Figure 4.4 is the stellar mass within  $10\% r_{\text{vir}}$ . Both classifications of ETGs contain fewer low-mass galaxies relative to all galaxies.  $b$ -value selected ETGs have relatively more high-mass galaxies, while cold gas-selected ETGs have relatively more intermediate-mass galaxies. The mass distribution of prolate rotators is bimodal, with a peak at intermediate and high masses. The intermediate mass peak’s value is similar to that of ETGs and all galaxies, while the prolate rotators are clearly over-represented in the peak at high masses. Prolate rotators are therefore more likely to be found at higher masses ( $\log_{10}(M_{\star}/M_{\odot}) \geq 11$ ), consistent with other simulations (Ebrova & Lokas, 2017) and observations (Tsatsi et al., 2017).

Because I am interested in the stability of prolate rotation (see Figure 4.1), another interesting property is the lifetime of prolate rotators. As already mentioned, the 22 prolate rotators in the Magneticum sample (Schulze et al., 2018) were identified at  $z = 0$ . The lifetime of their prolate rotation was determined by producing 2D-binned stellar mass maps, Voronoi-binned luminosity-weighted  $losv$ ,  $losv\sigma$ , age  $\langle t_{\star} \rangle_{\text{lw}}$ , and metallicity  $\log_{10}(\langle Z/Z_{\odot} \rangle_{\text{lw}})$  maps for all main progenitors of each prolate rotator in an edge-on, face-on, and side-on projection, and visually identifying the snapshot of first prolate rotation (FPR). This was possible for all

22 prolate rotators. Additionally, the merger ratio  $r_{\text{merger}} = M_{\star}^{\text{central}} / M_{\star}^{\text{satellite}}$  is determined, by walking the merger tree (see Section 2.2). First, the galaxy’s snapshot of FPR is visually identified. Its first progenitors in the next several snapshots are then selected and the subhalos, which merge into the same descendants, called *progenitor siblings*, collected. This process always uses the stellar mass as calculated by SUBFIND. For each snapshot, the most massive *progenitor sibling* is taken as a *potential progenitor* of the satellite galaxy which merged with the galaxy, producing the prolate rotation. For each *potential progenitor*, the snapshot of *peak stellar mass* (PSM), that is the snapshot at which the first progenitors of the *potential progenitor* have the most stellar mass  $M_{\star}^{\text{satellite}}$ , is identified. During this process, its assembly history is plotted, which shows an exemplary galaxy’s stellar mass as a function of the universe’s age. A suitable in-falling satellite progenitor’s assembly history looks similar to Figure 4.5. Its stellar mass initially grows until it hits its PSM and later suddenly drops. This happens because during its approach to the central galaxy (or main subhalo), SUBFIND already attributes the outermost stars of the subhalo to the main subhalo. The dip before the final decline in Figure 4.5 might be due to the passage through the main subhalo before the final in-fall. After visually inspecting the assembly histories of all *potential progenitors*, I then decided which one will be the satellite galaxy progenitor. If this approach fails, the satellite galaxy progenitor is identified by selecting the stellar particles which make up the perceived progenitor in the 2D-binned stellar mass map and matching it with the 25 subhalos closest to the central galaxy that are more massive than  $1 \times 10^8 M_{\odot}$ . The subhalo whose stellar particles have the most matching IDs with the selected stellar particles is chosen as the satellite galaxy progenitor. The merger ratio  $r_{\text{merger}}$  is determined, by identifying the stellar mass of the central galaxy’s first progenitor  $M_{\star}^{\text{central}}$  at the satellite galaxy progenitor’s snapshot of PSM. Using these two approaches,  $r_{\text{merger}} = M_{\star}^{\text{central}} / M_{\star}^{\text{satellite}}$  was determined for 19 out of the 22 prolate rotators. For the remaining 3 galaxies, both approaches failed, potentially due to the low time resolution, which makes it difficult to visually identify potential progenitors. The snapshot of FPR can be transformed into a redshift  $z^{\text{FPR}}$  and lookback time  $t_{\text{lb}}^{\text{FPR}}$  using the simulation’s cosmological parameters.

Both these parameters’ (i.e.,  $z^{\text{FPR}}$  or  $t_{\text{lb}}^{\text{FPR}}$ , and  $r_{\text{merger}}$ ) distributions are shown in Figure 4.6. Keep in mind that these prolate rotators were identified at  $z = 0$ . Therefore, the first appearance of prolate rotation is concentrated at times between 0 Gyr and 3 Gyr ago, which is the same range as found by Ebrova & Lokas (2017) for prolate rotators taken from the Illustris simulation. Some already formed at earlier times, up to  $\sim 9$  Gyr ago. There might be more prolate rotators that formed early, but their prolate rotation might be destroyed before they reach  $z = 0$ , which is why they were not identified. Currently, there is work in progress to identify prolate rotators at earlier times, which enables a more complete analysis of the stability of prolate rotation (Remus et al. (in prep.)). But I can note, that – without disruptions – a lifetime of up to  $\sim 9$  Gyr is possible for prolate rotation. The merger mass ratio  $r_{\text{merger}}$  distribution (*right panel* of Figure 4.6) reveals that most prolate rotators are formed by major mergers (1:1 to 1:4). Only two are minor mergers ( $> 1:5$ ). Ebrova & Lokas (2017) define the merger mass ratio reciprocally to my definition, that is  $r_{\text{merger}}^{\text{EL17}} = M_{\star}^{\text{satellite}} / M_{\star}^{\text{central}} = r_{\text{merger}}^{-1}$ .

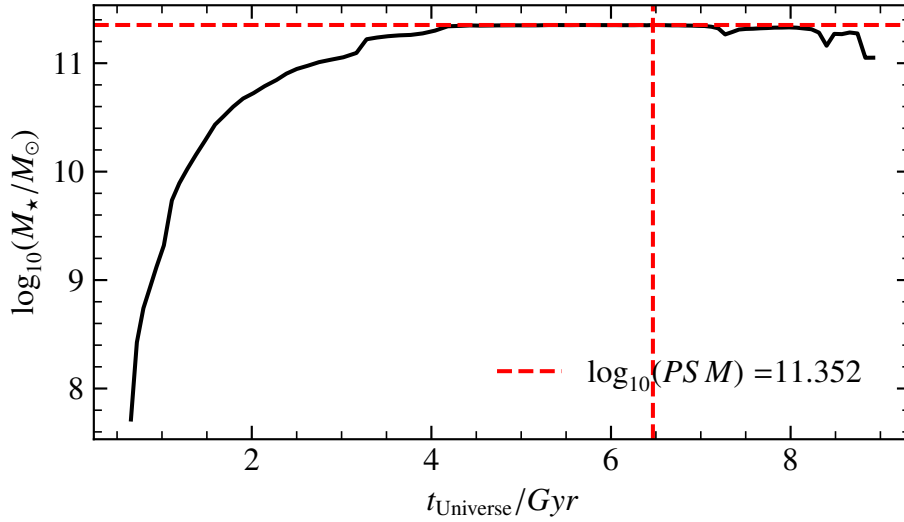


**Figure 4.5:** Assembly history (black line), that is stellar mass as a function of the Universe’s Age for the prolate rotator progenitor P2. The vertical dashed red line marks the age of the Universe at PSM, which is marked by the horizontal dashed red line.

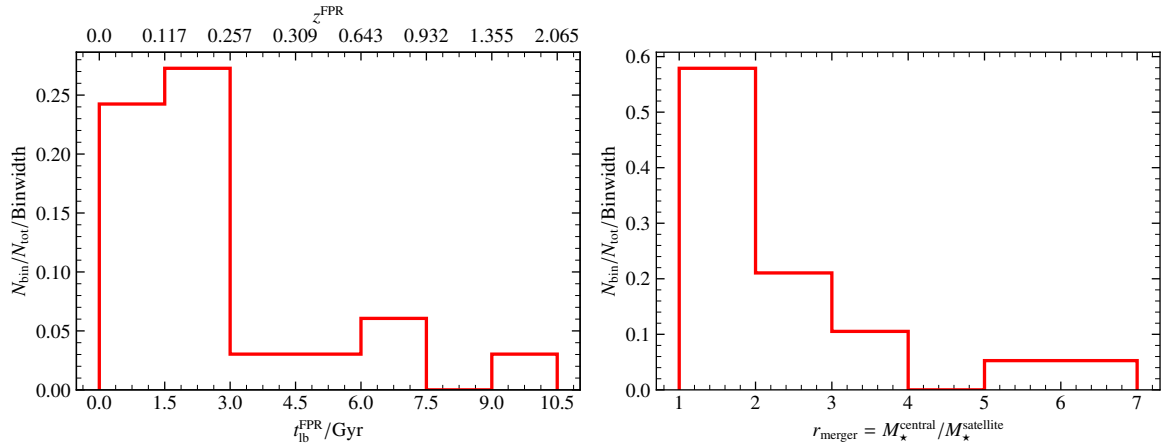


**Figure 4.6:** *Left panel:* Histogram of lookback-time  $t_{lb}$  (bottom x-axis) or redshift (top x-axis) of the prolate rotators’ first prolate rotation (FPR). *Right panel:* Histogram of the merger ratio  $r_{merger} = M_{\star}^{central} / M_{\star}^{satellite}$ .

They identify a “golden sample”, which merger ratio is  $r_{merger}^{EL17} \geq 0.3$ , or  $r_{merger} \leq 3.3$ , which is similar to my result.

### 4.3 Summary and Conclusion

In this chapter, I analyzed the stability and formation of prolate rotators. First, I used an isolated disk galaxy merger simulation performed and used by Schauer et al. (2014) and Schulze et al. (2017), and then I analyzed the sample of prolate rotators identified at  $z = 0$  in Box4 of the *Magneticum Pathfinder simulations*.

- The isolated disk galaxy merger simulation produces a spheroidal galaxy with a tilted rotation, which is similar to prolate rotation. This rotation pattern is stable over the whole simulation, that is at least up to 4.5 Gyr.

- An exemplary prolate rotator from the Magneticum sample (Schulze et al., 2018) is formed at  $z = 0.47$  during a radial merger, where the satellite galaxy hits the central galaxy centrally face-on, similar to analyses by Tsatsi et al. (2017), Ebrova & Lokas (2017), and Hegde et al. (2022). The merger ratio is  $r_{\text{merger}} = M_{\star}^{\text{central}} / M_{\star}^{\text{galaxy}} = 2.13$  and the prolate rotation is stable for  $\sim 4.8$  Gyr. The central galaxy initially had a regular rotation pattern with  $\lambda_{1r_{1/2}} = 0.54$ , which becomes  $\lambda_{1r_{1/2}} = 0.11$  for the prolate rotation. The major axis of the prolate rotator is almost parallel to the direction of the final in-fall of the satellite, that is the central galaxy is elongated by the merger, but retains its initial rotation. Interestingly, a shell-like discontinuity within the 2D-binned stellar mass map, interpreted as a stellar shell, is seen after the merger.
- The age of the stars associated with the prolate rotation in the exemplary galaxy is slightly younger than, for example, the center of the galaxy.
- Prolate rotators appear to be more common in higher mass galaxies, consistent with Tsatsi et al. (2017) and Ebrova & Lokas (2017).
- Most galaxies that exhibit prolate rotation at  $z = 0$  developed their prolate rotation (FPR) within the last 3 Gyr. The longest living prolate rotation encountered is stable for  $\geq 9$  Gyr.
- The merger causing the prolate rotation typically has a merger ratio of  $r_{\text{merger}} = M_{\star}^{\text{central}} / M_{\star}^{\text{satellite}} \leq 4$ , consistent with Ebrova & Lokas (2017), which suggests the formation by a major merger.

# Chapter 5

## Properties and Progenitors of Shells and Streams

Galaxy evolution is vastly affected by galaxy mergers. There can be major mergers ( $r_{\text{merger}} = M_{\star}^{\text{central}}/M_{\star}^{\text{satellite}} \leq 4$ ) which completely transform the morphology, kinematics and star formation activity, as seen in Chapter 4. Minor mergers ( $r_{\text{merger}} \geq 4$ ) do not have such dramatic effects but are still relevant, especially for the outskirts of galaxies (Karademir et al., 2019), and multiple minor mergers can amount to the same level of changes as major mergers (Moody et al., 2014). A minor merger results from a satellite galaxy falling into its host galaxy. During this orbit, the satellite experiences strong tidal forces in the gravitational potential of the host galaxy and gets torn apart. The remaining stars of the disrupted galaxies form so-called *tidal features*. Because of their low surface brightness, these are often also called *low surface brightness features*. Depending on the nature of the orbit, the morphology of these features can take various forms (Karademir et al., 2019). In this chapter, I will focus on tidal stellar *shells* and *streams*. *Shells* appear as segments of a concentric circle or ellipse around its host galaxy. A satellite galaxy, which falls in on a very radial orbit (i.e. small impact parameter) forms shells. It is disrupted, and its stars start to oscillate in the potential of the host galaxy. The stars are slowest in the apocenter and stay longer at positions close to it. For this reason, their density is higher at that radius, forming a shell. This leads to shells forming interleaved, first on one side, then on the opposite side, and so on, increasing their radius and separation between them with time (e.g., Bílek et al., 2020). *Streams* are formed from satellite galaxies on orbits with a higher angular momentum (i.e., large impact parameter). Their stars spiral around a galaxy while being disrupted (Karademir et al., 2019).

With the advent of galaxy surveys which can observe up to a very low surface brightness, such as MATLAS (Duc et al., 2015; Bílek et al., 2015) or the upcoming Vera C. Rubin telescope’s Legacy Survey of Space and Time (LSST) there will be a lot of new information available for these features. It is therefore crucial to predict their formation scenario and properties from their observed morphology. For this, the *Magneticum* simulation will be used in the next chapter. I select the galaxies identified to have shells and streams by Valenzuela & Remus (2024), pinpoint the exact shape and location of the existing features,

and analyze their age, metallicity and  $losv\sigma$ . Finally, the progenitor satellite galaxies are determined and their properties studied.

## 5.1 Identification of Shells and Streams

The sample of *Magneticum* galaxies that exhibit stellar shells or streams, was identified by Valenzuela & Remus (2024). Above  $\log_{10}(M_{\star}/M_{\odot}) > 10$  and at  $z = 0$ , there are 24 galaxies with shells and 66 galaxies with streams. For each galaxy, stellar r-band mock observations using the code presented by Martin et al. (2022) were created in an edge-on, face-on, and side-on projection. This is done because many features are not visible in every projection (Pop et al., 2018). The limiting surface brightness limit was chosen to be  $\mu_{\text{lim}} = 30.3 \text{ mag arcsec}^{-2}$  and a spatial resolution of  $0.2 \text{ arcsec pixel}^{-2}$ . These are supposed to match LSST and were also used by Khalid et al. (2024). No noise is added to the images to better identify the feature. Two different contrast levels are used to better identify features at different radii, similar to Pop et al. (2018) who study shells in the Illustris simulation. At a high contrast, the outskirts are better visible, while at a low contrast, the center is not “over-exposed”. Most LSB features are typically found in the outskirts, but dynamically young shells are still close to the center. Additionally, the galaxy’s radial velocity-radius phase space was produced. Using these mock observations and the phase space, the exact location and extent of each feature was marked in each projection. Table 5.1 summarizes the number of galaxies, which exhibit the respective feature  $N_{\text{galaxies}}$ , which indicates how many galaxies the feature could be identified in at least one projection of the stellar mock observations  $N_{\geq 1}$ , and how many were found in each projection (shells were counted individually)  $N_{\text{proj}}$ . Some features were identified to have an umbrella-like shape, which is a shell with a stream connecting it to the host galaxy. These stayed attributed to the initial classification by Valenzuela & Remus (2024) although a more rigorous analysis would need to classify them as their own class. For all shell galaxies, a shell was found in at least one projection, but for 15 stream galaxies no stream could be identified in any projection. These were galaxies that looked like an ongoing merger or simply no feature was detectable. In agreement with Pop et al. (2018), most shells are identified in 2/3 projections (17/24 ~ 71%). But for only 4/24 (~ 17%) shell galaxies shells were identified in 3/3 projections, whereas Pop et al. (2018) find that to be the case with ~ 40% of their sample. This can be attributed to the fact that their projections are random, which is closer to observations, while my projections have a physical meaning related to the shape and orientation of the galaxy, and to differences in the methodology. Within 3/24 (~ 13%) shell galaxies shells were only visible in 1/3 projection. It is notable that shells are mostly identified in the edge-on (51) and face-on (58) projection, but are barely visible in the side-on (4) projection. This can be explained by the fact that most of the time a shell does not cover the entire sphere, but only a spherical cap propagating outward parallel to the major axis. In the line-of-sight parallel to the major axis, one only sees the top of the cap, while possible remaining shells are hidden behind it. The same trend is true for streams, where most are identified in 2/3 projections (28/51 ~ 55%), second most in 3/3 projections

	$N_{\text{galaxies}}$	$N_{\geq 1}$	$N_{=1}$	$N_{=2}$	$N_{=3}$	$N_{\text{edge-on}}$	$N_{\text{face-on}}$	$N_{\text{side-on}}$
Shells	24	24	3	17	4	51	58	4
Streams	66	51	9	28	13	45	48	39

**Table 5.1:** Feature statistics for shells and streams as identified for different projections.

(13/51  $\sim$  25%), and 9/51 ( $\sim$  18%) in 1/3 projections. For streams, the difference between edge-on (45), face-on (48) and side-on (39) is not as extreme as for shells because they do not affect the morphology of the host galaxy as much. For the remaining analysis, the face-on projection is exclusively chosen because most features are identified in this projection.

Several properties of shells and streams are to be determined in the following. Valenzuela & Remus (2024) note that the shells around their exemplary galaxy appear as regions of comparably low velocity dispersion  $losv\sigma$ . This observation is statistically analyzed and extended to streams in this work. As an extension of Chapter 3, the stellar ages and metallicities of shells and streams are also determined. For this purpose, Voronoi-binned (Cappellari & Copin, 2003) maps of said properties are utilized. They are aided by 2D-binned stellar mass maps, the aforementioned stellar mocks, and the radial velocity-radius phase space. Two different approaches will be used for shells and streams, respectively. Both depend on the visual inspection of the aforementioned stellar mock observations.

### Shell Methodology: Radial Profiles in Slices

Only the stellar particles attributed to the specific subhalo by SUBFIND are used because at the time of analysis the shells are already attributed to the host galaxy. Including not yet merged subhalos would skew radial profiles and make it difficult to identify low-contrast features. To minimize biases, only the stellar mocks are presented at the beginning of the analysis. Four mouse clicks are required to identify a shell: ① A position with the angular coordinate of the beginning of the shell  $\theta_1$ . ② A position with the angular coordinate of the end of the shell  $\theta_2$ . ③ A position on the circle with the inner radius of the shell  $r_{\text{in}}$ . ④ A position on the circle with the outer radius of the shell  $r_{\text{out}}$ . Using ① and ② a slice is drawn from the center of the host galaxy to infinity (cyan linear lines in the top row of Figure 5.1). Using ③ and ④ an annulus with the inner and outer radius of the shell is drawn within the slice (round cyan lines in the top row of Figure 5.1). This resulting section of the annulus will be called the *shell area*. Its width is defined as  $w_{\text{shell}} = r_{\text{out}} - r_{\text{in}}$ . The diagnostics plot of an exemplary<sup>1</sup> shell galaxy, Figure 5.1, shows the stellar mock observation and the stellar mass map, together with the luminosity-weighted Voronoi-binned maps of the analyzed properties ( $\langle losv\sigma \rangle$ ,  $\langle t_{\star} \rangle_{\text{lw}}$ ,  $\langle [Z/H] \rangle_{\text{lw}}$ ) in the top row. Overplotted are the contours of the slice and *shell area*. Each panel has an extent of  $14r_{1/2} \times 14r_{1/2}$ . The bottom row displays the radial velocity-radius phase space and several radial profiles with a maximum radius of  $7r_{1/2}$ . The first is the stellar surface density profile  $\Sigma_{\star}(r)$  calculated within 100 equally spaced complete annuli (“global”, magenta dash-dotted line) and 100 equally spaced annuli sections within the slice (“slice”,

<sup>1</sup>The remaining diagnostics plots for all shells are attached in Appendix D.

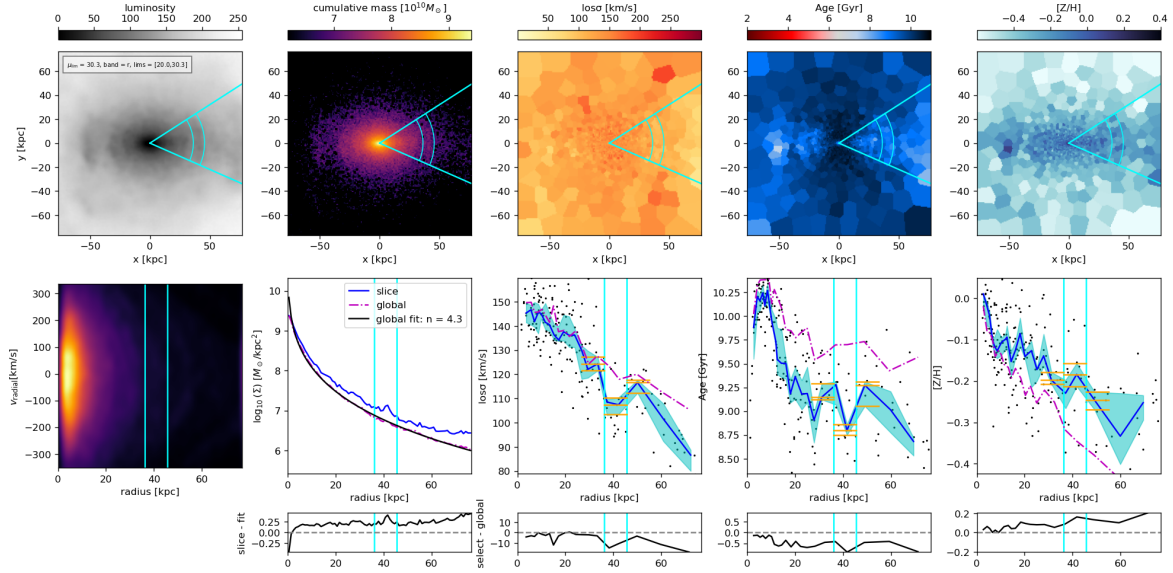


**Figure 5.1:** Diagnostic plot for a stellar shell. The top row consists of (from left to right), a stellar mock map, a 2D-binned stellar mass map, and three luminosity-weighted Voronoi-binned maps of velocity dispersion  $\langle losv\sigma \rangle_{lw}$ , stellar age  $\langle t_{\star} \rangle_{lw}$  and stellar metallicity  $\langle [Z/H] \rangle_{lw}$ . All are in the face-on projection. Overplotted are the contours of the slice and the *shell area* as cyan lines. The bottom left panel shows the radial velocity-radius phase space of stellar particles. The color indicates the Gaussian kernel density estimation. The 2nd panel shows the stellar surface density profile within the slice (blue solid line), for the global galaxy (magenta dash-dotted line) and a fit of Sérsic profile to the global profile (black solid line). The remaining three panels show the radial profiles of the velocity dispersion  $losv\sigma$ , stellar age  $\langle t_{\star} \rangle_{lw}$ , and metallicity  $\langle [Z/H] \rangle_{lw}$ . In each panel the black dots represent individual Voronoi-bins, the blue line represents median values within radial bins which each contain 50 Voronoi-bins, which lie within the slice. The cyan contours stretch from the 0.32 to 0.67-quantile within these radial bins. The magenta dash-dotted line represents the global radial profile, calculated in the radial bins defined by the slice profile. The orange horizontal lines depict the extremum (minimum for  $\langle losv\sigma \rangle$  and age, maximum for metallicity) of the median radial profile (blue line) within the radial range of the shell (cyan vertical lines) and the opposite extremum (maximum for  $\langle losv\sigma \rangle$  and age, minimum for metallicity) within the radial ranges of width  $w_{shell}$  adjacent to the shell, together with their 0.32 and 0.67 quantiles. Below each radial profile, the difference between the profile within the slice and the global profile (or a fit to it in the case of the surface density) is shown.

blue line). A Sérsic-profile (Sérsic, 1963)  $\log_{10}(\Sigma_{\star}(r)/M_{\odot} \text{ kpc}^{-2}) = \log_{10}(\Sigma_0) - k \times r^{1/n}$  (Karademir et al., 2019) is fit to the global stellar surface density profile (black line). The difference between the profile within the slice and the fitted profile is portrayed below the surface density profile. Next to it, there are radial profiles for the stellar  $losv\sigma$ , age and metallicity. They are calculated differently to the surface density profile. The mean values of each Voronoi-bin of the map are used as data points (black dots). Each Voronoi-bin contains roughly 50 stellar particles. They are radially binned so that each radial bin contains 50 Voronoi-bins that lie within the slice (“slice”). The median within each radial bin is used (blue line). The “global” profile is calculated within the bin edges defined by the slice and the median property used (magenta dash-dotted line). Again, the difference between the slice profile and the global profile is shown below each profile. Finally, the properties of the shells are defined as the extremum (minimum for  $\langle losv\sigma \rangle$  and age, maximum for metallicity) of the slice profile within the radial edges of the *shell area* (cyan vertical lines in the bottom row):  $\langle losv\sigma \rangle_{lw}^{\text{shell}}$ ,  $\langle t_{\star} \rangle_{lw}^{\text{shell}}$ ,  $\langle [Z/H] \rangle_{lw}^{\text{shell}}$ . The *surroundings* of a shell are defined as the opposite extremum (maximum for  $losv\sigma$  and age, minimum for metallicity) of the slice profile within the radial ranges  $r_{in} - w_{\text{shell}} < r_{s1} < r_{in}$  and  $r_{out} < r_{s2} < r_{out} + w_{\text{shell}}$  resulting in  $\langle losv\sigma \rangle_{lw}^{s1/s2}$ ,  $\langle t_{\star} \rangle_{lw}^{s1/s2}$ ,  $\langle [Z/H] \rangle_{lw}^{s1/s2}$ . These values are indicated as orange horizontal lines, together with the 0.32 and 0.67 quantiles within the respective radial range. After selecting the stellar particles within the *shell area*, their IDs are saved ( $ID_{\text{shell}}$ ) and their masses summed up to calculate the shells’ stellar mass  $M_{\star}^{\text{shell}}$ .

For this exemplary shell galaxy, the surface density within the slice is always higher compared to the global surface density, indicated by the difference, which is always positive. The major axis is aligned with the shells, which leads to this overdensity in the direction of the shell. There is an additional spike at the position of the shell, which is washed out in the global profile. There is also a clear depression in the velocity-dispersion profile and the age profile at the position of the shell. An increase in metallicity within the shell is not as clearly detectable because of the dominating negative metallicity gradient, but there still is a small spike. In addition, the metallicity profile within the slice, that is within the direction of the shells, also lies above the global metallicity profile. This demonstrates that this approach is suitable to determine the properties of the stars within the shell and its surroundings.

### Stream Methodology: Polygon Selection

Because streams are not confined to concentric circular shells around the center of their host galaxy, a different methodology needs to be defined to capture their shapes and stellar properties. For the same reason, radial profiles are not a suitable tool. Because of their potentially peculiar morphology, the best shape to encompass a stream is a polygon. Again, the stellar mock map is presented, and  $N_{\text{poly}}$  mouse clicks are required to fix the shape. This approach is similar to the annotation tool for LSB features JAFAR<sup>2</sup> presented by Sola et al. (2022), but is far less sophisticated. The area the polygon covers will be called the *stream area*. This

<sup>2</sup><https://jafar.astro.unistra.fr/>

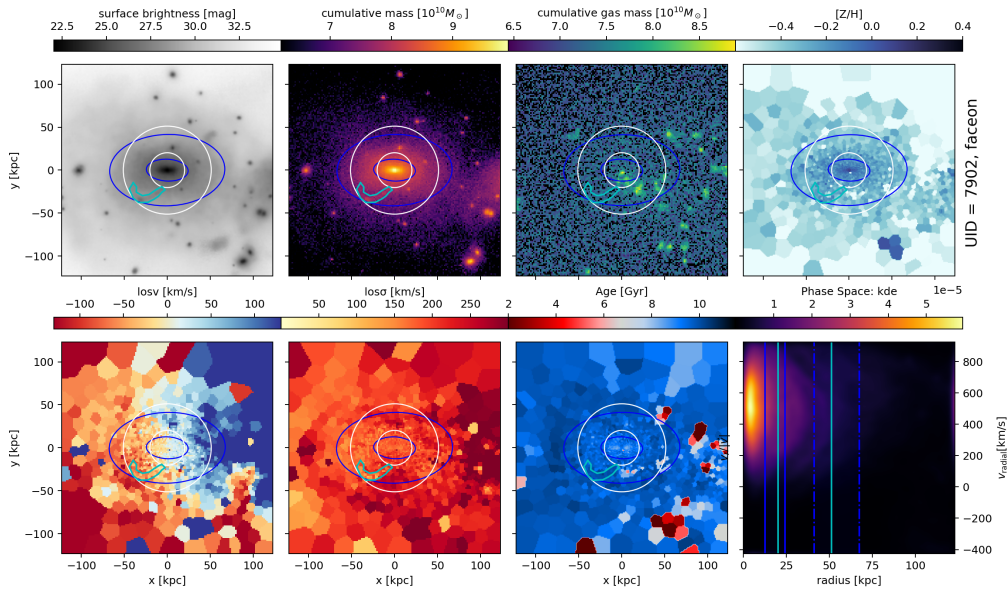


**Figure 5.2:** Diagnostic plot for a stellar stream. The top row consists of (from left to right), a stellar mock map, a 2D-binned stellar mass map, a 2D-binned gas mass map, a luminosity-weighted Voronoi-binned maps of the stellar metallicity  $\langle [Z/H] \rangle_{lw}$ . The bottom row consists of three (from left to right) luminosity-weighted Voronoi-binned maps of the line-of-sight velocity  $losv$ , the velocity dispersion  $losv\sigma$ , and the stellar age  $\langle t_{\star} \rangle_{lw}$ . All are in the face-on projection. Finally, the bottom right panel presents the radial-velocity-radius phase space where the vertical cyan line represents the inner and outer radius of the polygon, and the blue lines represent  $1r_{1/2}$  and  $3r_{1/2}$ . The color indicates the Gaussian kernel density estimation. Overplotted on all maps, the *stream area*/polygon is shown as cyan lines, the inner and outer circle of the *surroundings* annulus are shown in white, and the blue ellipses represent the shape ellipses at  $1r_{1/2}$  and  $3r_{1/2}$ .

projected surface area is calculated using the formula  $A_{\text{poly}} = \frac{1}{2} \sum_{i=1}^{N_{\text{poly}}} \det(x_i, x_{i+1}; y_i, y_{i+1})$ , where  $x_{N_{\text{poly}}+1} = x_1$  and  $y_{N_{\text{poly}}+1} = y_1$ . The length of the polygon  $l_{\text{poly}}$  is estimated as the maximum pairwise distances between two polygon points. This is a good approximation as long as the polygon is a simple convex polygon, that looks like a circle or rectangle. For a simple concave polygon that looks like a banana, this approximation becomes inaccurate, but is the best I can do within the scope of this work. These two parameters are used to estimate the width of the stream  $\hat{w}_{\text{stream}} = A_{\text{poly}}/l_{\text{poly}}$ . Because this estimate can be very inaccurate, a second width is defined.  $w_{\text{stream}}$  is the distance between two points which were highlighted during the identification of the stream (using the right mouse click). This width is purely based on the visual inspection. The stream diagnostic plot<sup>3</sup>, Figure 5.2, only displays maps, namely a stellar mock map, a 2D-binned stellar mass map, a 2D-binned gas mass map, and a luminosity-weighted Voronoi-binned stellar metallicity  $\langle [Z/H] \rangle_{\text{lw}}$  map in the top row. The bottom row includes three luminosity-weighted Voronoi-binned maps of the stellar line-of-sight velocity  $losv$ , velocity dispersion  $losv\sigma$ , and stellar age  $\langle t_{\star} \rangle_{\text{lw}}$ . Finally, the bottom right panel shows the radial velocity-radius phase space. The properties of the stream are defined as the median values of the Voronoi-bins within the *stream area*:  $\langle losv\sigma \rangle_{\text{lw}}^{\text{stream}}$ ,  $\langle t_{\star} \rangle_{\text{lw}}^{\text{stream}}$ ,  $\langle [Z/H] \rangle_{\text{lw}}^{\text{stream}}$ . Each Voronoi-bin contains roughly 50 stellar particles. The *surroundings* of the stream are defined as the annulus with an inner and outer radius that are the same as the minimal and maximal radius of the polygon's points. Again, the median within the annulus is chosen as the property of the *surroundings*, excluding the Voronoi-bins within the polygon:  $\langle losv\sigma \rangle_{\text{lw}}^{\text{s3}}$ ,  $\langle t_{\star} \rangle_{\text{lw}}^{\text{s3}}$ ,  $\langle [Z/H] \rangle_{\text{lw}}^{\text{s3}}$ . The 0.32 and 0.67 quantiles are taken as the uncertainty. Again, the IDs of the stellar particles within the *stream area* are saved ( $\text{ID}_{\text{stream}}$ ) and the particles' mass summed up to calculate the stream's projected stellar mass  $M_{\star}^{\text{stream}}$ .

No quantitative conclusions can be drawn from Figure 5.2 but it illustrates the important areas from which the properties are drawn. Despite this, one can see, that the velocity dispersion within the stream appears to be lower than within its surroundings.

## 5.2 Properties of Shells and Streams

To get an initial overview of the shapes and their location around the host galaxy, Figure 5.3 presents all annotated shapes in the face-on projection. The center of each panel is the center of the host galaxy. The blue polygons represent all individual streams, the orange circle segments represent the inner and outer radial boundaries of individual shells, and the black ellipses represent the shape of the host galaxy at  $1r_{1/2}$  and  $3r_{1/2}$ . Shells mostly appear to the right or left of the center, that is along the major axis, while streams come in a large variety of different locations and shapes, similar to observed streams (Sola et al., 2022). In the following section, the shape and location of shells and streams, together with their stellar population properties, will be analyzed in a more quantitative approach.

<sup>3</sup>The remaining diagnostics plots for all streams are attached in Appendix D.

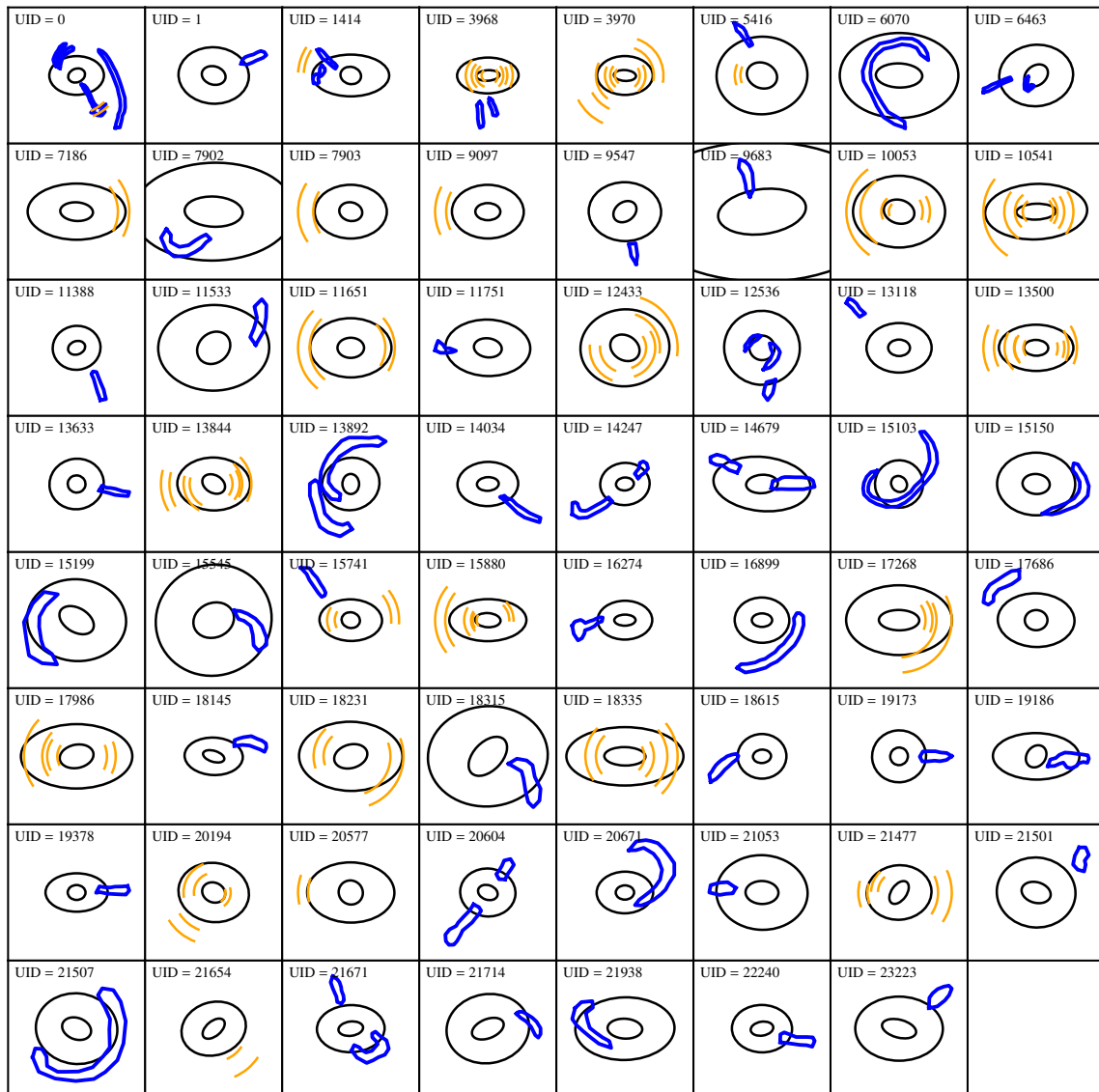


**Figure 5.3:** Annotated shapes of shells and streams. Each panel’s center is the center of the host galaxy. Streams are represented in blue, and shells in orange. The black ellipses represent the shape ellipses at  $1r_{1/2}$  and  $3r_{1/2}$ . Inspired by Sola et al. (2022) (Fig. 7).

### 5.2.1 Properties of Shells

First focusing on the shapes and locations of shells, Figure 5.4 shows the distributions of the average radius of each shell  $\langle r \rangle = (r_{\text{in}} + r_{\text{out}})/2$ , the average angular position  $\langle \theta \rangle = (\theta_1 + \theta_2)/2$ , and the projected stellar mass within the *stream area*  $M_{\star}^{\text{shell}}$ , in the top row. The bottom row presents the distributions of the radial width  $w_{\text{shell}}$ , the angular extent  $\Delta\theta = \theta_2 - \theta_1$ , and the Sérsic-index  $n_{\text{Sersic}}$  of the host galaxy. The majority of shells appear around  $\langle r \rangle \sim 20\text{kpc}$ , with the shell farthest away sitting at  $\langle r \rangle \sim 60\text{kpc}$ , similar to Sola et al. (2022) (black histogram and gray median), who find most shells at  $\leq 40\text{kpc}$ . They also find more shells between 5 kpc and 15 kpc compared to this work. There might be shells in the simulation that are even further away from the host galaxy’s center, but a limited radius was chosen to identify the shells (see Section 5.1). Most shells appear to have a radial width  $w_{\text{shell}}$  between  $\sim 3\text{ kpc}$  to  $\sim 10\text{ kpc}$ . The angular position  $\langle \theta \rangle$  was defined to be zero for a vector fixed to the origin, which is parallel to the positive x-axis and increasing counter-clockwise. Afterward  $\langle \theta \rangle$  was folded onto a range from  $0^\circ$  to  $90^\circ$ , so that shells initially at  $180^\circ$  and  $270^\circ$  coincide with  $0^\circ$  and  $90^\circ$ , respectively. Most shells lie very close to  $0^\circ$ , that is aligned with the major axis, as qualitatively seen in Figure 5.3. No shells are aligned with the minor axis (at  $90^\circ$ ) and very few lie somewhere between. The angular extent (opening angle of the slice) of most shells is close to  $70^\circ$ . The largest extends over  $\sim 130^\circ$ , while all are  $\geq 20^\circ$ . The median shell mass is  $\langle M_{\star}^{\text{shell}} \rangle = 4.39 \times 10^9 M_{\odot}$  ( $\log_{10}(M_{\star}^{\text{shell}}/M_{\odot}) \approx 9.64$ ), while most shells are more massive than  $\sim 1 \times 10^9 M_{\odot}$  (which represents roughly  $\sim 1000$  stellar particles) and less massive than  $\sim 1 \times 10^{10} M_{\odot}$ . These are projected masses which are very likely to include intruder particles, which are particles that originally did not belong to the satellite galaxy which formed the shell, but are part of the host galaxy. Nevertheless, this already suggests that the progenitors of shells can be quite massive. Finally, the median Sérsic-index  $n_{\text{Sersic}}$  is  $\sim 6$ , that is they are likely massive, extended ellipticals (Caon et al., 1993).

As previously mentioned, the velocity dispersion within shells seems to be lower than within their surroundings (Valenzuela & Remus, 2024). It is also interesting to look at the age and metallicity of shells, whether they are old, young or of similar age than their surroundings, or if there is no trend to be found at all. This is what I focus on now. For this purpose, the properties of the surroundings defined as explained in Section 5.1, which gives  $\langle \cdot \rangle_{\text{lw}}^{\text{s1}}$  and  $\langle \cdot \rangle_{\text{lw}}^{\text{s2}}$ . The average of these two values will be used here:  $\langle \cdot \rangle_{\text{lw}}^{\text{s}} = (\langle \cdot \rangle_{\text{lw}}^{\text{s1}} + \langle \cdot \rangle_{\text{lw}}^{\text{s2}})/2$ . Figure 5.5 shows the velocity dispersion, age and metallicity of each shell’s surroundings as a function of the velocity dispersion, age and metallicity within the shell, respectively, in the *top row*. The bottom row displays the ratio of the value within the shell and the value in the surroundings as a function of the value within the shell. The velocity dispersion within the shell is almost always below the velocity dispersion in the surroundings. The ratio  $\langle \text{losv}\sigma \rangle_{\text{lw}}^{\text{shell}} / \langle \text{losv}\sigma \rangle_{\text{lw}}^{\text{surroundings}}$  is below unity for all except for one shell. 68% of shells do so at  $1\sigma$ . The ages of shells are less clear. Almost as many shells are younger than their surroundings than there are shells which are older. Interestingly, the older ( $\langle t_{\star} \rangle_{\text{lw}}^{\text{shell}} \gtrsim 10\text{ Gyr}$ ) the shell is, the less they scatter around the one-to-one relation. Only 42% of shells are younger than their surroundings at  $1\sigma$ .

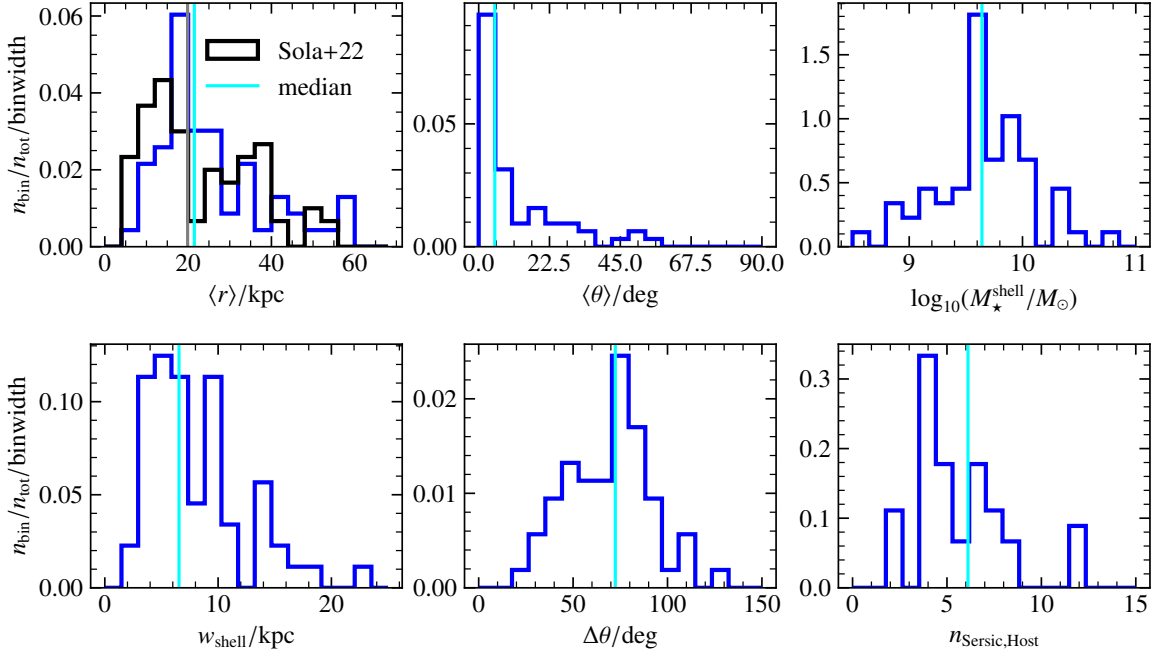


**Figure 5.4:** Distributions of shell properties. *Top row:* mean shell radius  $\langle r \rangle$ , mean angular position  $\langle \theta \rangle$ , and the stellar shell mass  $M_{\star}^{\text{shell}}$ . *Bottom row:* Shell width  $w_{\text{shell}}$ , angular extent (or opening angle of the shell defining slice)  $\Delta\theta$ , and the host galaxy’s Sérsic-index  $n_{\text{Sérsic}}$ . The vertical cyan line is the median of each distribution. The black histogram in the top left panel is the re-binned distribution of the shell radius observed by Sola et al. (2022). Their median is shown as a gray vertical line.

Finally, in agreement with Pop et al. (2017), it appears that most shells are more metal-rich than their surroundings. But their uncertainties are larger: only 32% of shells have a ratio  $\langle [Z/H] \rangle_{\text{lw}}^{\text{shell}} / \langle [Z/H] \rangle_{\text{lw}}^{\text{surroundings}}$  which is greater than unity at  $1\sigma$ .

Another interesting aspect of this is the median difference in velocity dispersion, age and metallicity, especially for observational campaigns trying to use these properties to identify shells. Figure 5.6 shows the difference between the properties within the shell and their surroundings:  $\log v_{\text{lw}}^{\text{shell}} - \log v_{\text{lw}}^{\text{surroundings}}$ ,  $\langle t_{\star} \rangle_{\text{lw}}^{\text{shell}} - \langle t_{\star} \rangle_{\text{lw}}^{\text{surroundings}}$ , and  $\langle [Z/H] \rangle_{\text{lw}}^{\text{shell}} - \langle [Z/H] \rangle_{\text{lw}}^{\text{surroundings}}$ . The median differences are represented by the vertical solid cyan line. The median velocity dispersion difference  $\Delta \langle \log v \sigma \rangle_{\text{lw}}$  is  $\sim -14 \text{ km s}^{-1}$ , the median age difference  $\Delta \langle t_{\star} \rangle_{\text{lw}}$  is  $\sim -0.07 \text{ Gyr}$ , and the median logarithmic metallicity difference  $\Delta \langle [Z/H] \rangle_{\text{lw}}$  is 0.04. The velocity dispersion differences significantly differ from zero, while the age and metallicity differences are very close to zero. The 0.68-quantile for the age difference and the 0.32-quantile for metallicity are very close to zero. The only significant difference between shells and their surroundings is in the velocity dispersion.

## 5.2.2 Properties of Streams

Now the same analysis is done for the selected streams. As mentioned before, Figure 5.3 shows the shapes of the streams as a polygon, which are very diverse. Figure 5.7 quantitatively describes their morphology and positions, as well as the stellar mass and flux. The median average stream radius  $\langle r \rangle = r_{\text{out}} - r_{\text{in}}$  is  $\sim 27 \text{ kpc}$ , slightly larger than for the identified shells. Streams appear singularly, while shells often appear in a whole shell system, which includes

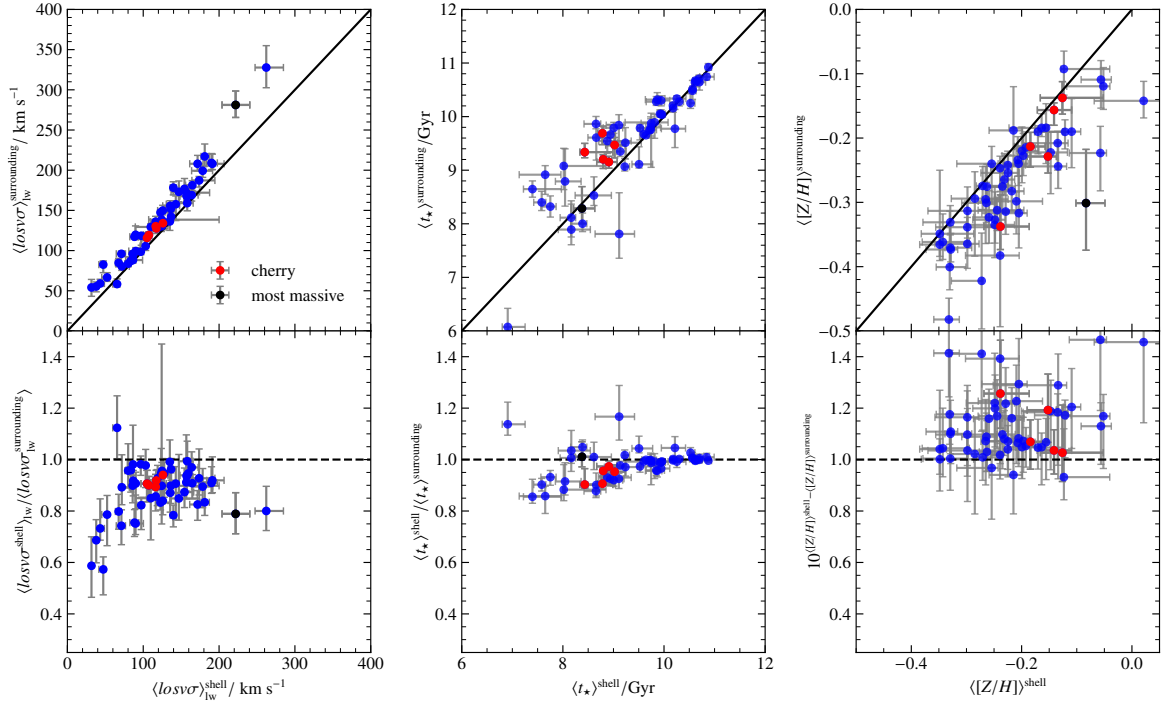


**Figure 5.5:** *Top Row:* Velocity dispersion in the surroundings of each shell  $\langle losv\sigma \rangle_{lw}^{surroundings}$  as a function of the velocity dispersion within the shell  $\langle losv\sigma \rangle_{lw}^{shell}$ , age in the surroundings of each shell  $\langle t_{\star} \rangle_{lw}^{surroundings}$  as a function of the age within the shell  $\langle t_{\star} \rangle_{lw}^{shell}$ , and metallicity in the surroundings of each shell  $\langle [Z/H] \rangle_{surroundings}$  as a function of the metallicity within the shell  $\langle [Z/H] \rangle_{lw}^{shell}$ . The black diagonal line is the one-to-one relation. The errorbars are the distance to the 0.32- and 0.67-quantile. *Bottom Row:* Ratio of  $\langle losv\sigma \rangle_{lw}^{shell}$  and  $\langle losv\sigma \rangle_{lw}^{surroundings}$  as a function of  $\langle losv\sigma \rangle_{lw}^{shell}$ , ratio of  $\langle t_{\star} \rangle_{lw}^{shell}$  and  $\langle t_{\star} \rangle_{lw}^{surroundings}$  as a function of  $\langle t_{\star} \rangle_{lw}^{shell}$ , and  $10^{\langle [Z/H] \rangle_{lw}^{shell} - \langle [Z/H] \rangle_{lw}^{surroundings}}$  as a function of  $\langle [Z/H] \rangle_{lw}^{shell}$ . The last quantity is chosen so that the ratio  $Z^{shell}/Z^{surroundings}$  is represented. The dashed horizontal line is unity.

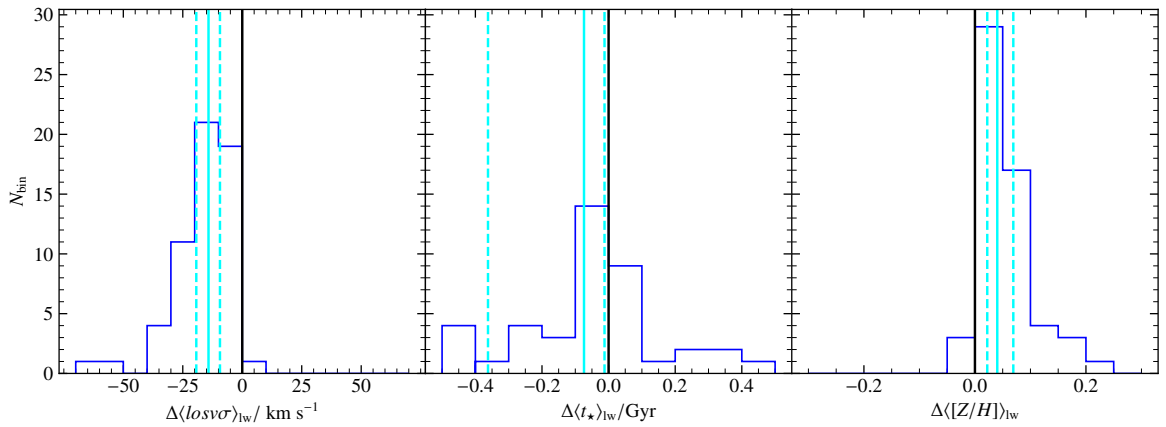


**Figure 5.6:** *Left:* Distribution of  $\Delta \langle losv\sigma \rangle_{lw}$ , *Middle:* Distribution of  $\Delta \langle t_{\star} \rangle_{lw}$ , *Right:* Distribution of  $\Delta \langle [Z/H] \rangle_{lw}$ . The cyan solid vertical lines are the median of each distribution, the dashed lines are the 0.32- and 0.68-quantiles.

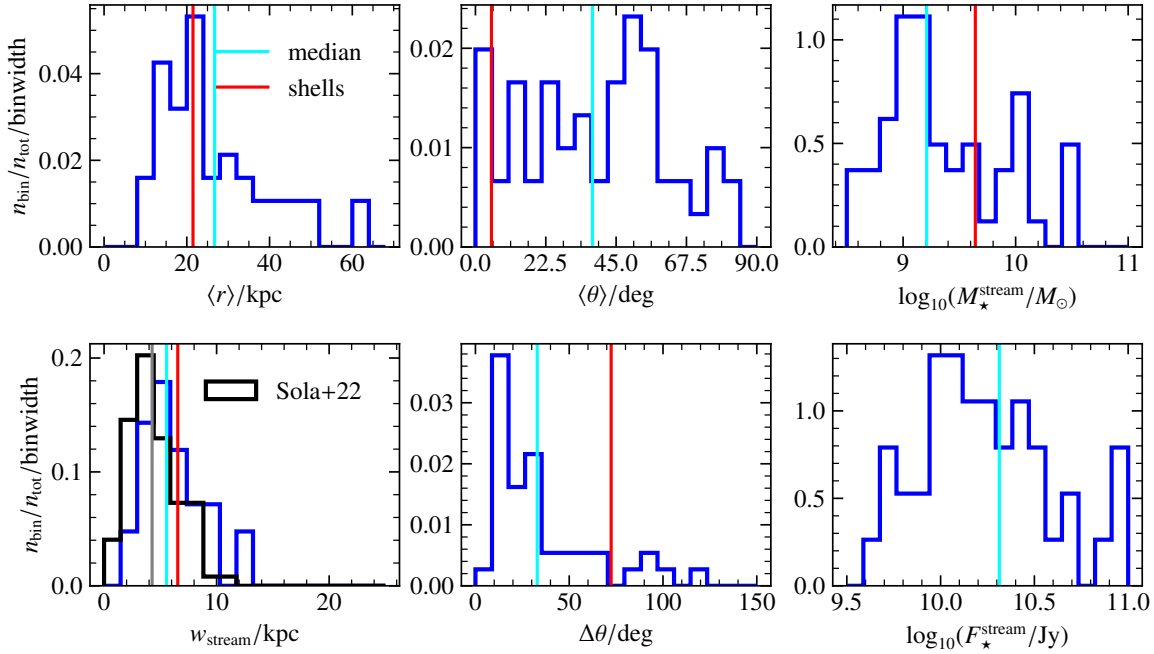


**Figure 5.7:** Distributions of stream properties. *Top row:* mean stream radius  $\langle r \rangle$ , mean angular position  $\langle \theta \rangle$ , and the stellar stream mass  $M_{\star}^{\text{stream}}$ . *Bottom row:* Stream width  $w_{\text{stream}}$ , angular extent  $\Delta\theta$ , and the stream’s flux. The vertical cyan line is the median of each distribution. The black histogram in the bottom left panel is the re-binned distribution of the stream widths observed by Sola et al. (2022). Their median is shown as a gray vertical line.

shells that are further away and shells that are close to the center. This might be the reason why the median shell radius is smaller than the median stream radius. The stream which is furthest away is at a similar radius as the furthest shell ( $\sim 60$  kpc). This limit might be driven by the cut-out radius at which the mock observations were drawn ( $7r_{1/2}$ ). The streams’ width, with a median of  $w_{\text{stream}} \sim 5.6$  kpc, are slightly below the shells’ widths, which is consistent with Sola et al. (2022), who find a median width of  $(4.1 \pm 2.1)$  kpc. As previously speculated from Figure 5.3 the streams angular positions are quite homogeneously distributed and have a median angular extent of  $33^\circ$ . This is smaller than for shells, which can be explained by the fact that they often point towards the center as well as appearing as a section of a spiral or circle around it. Shells, on the other hand, are always sections of a circle. Finally, the projected stellar masses within the *stream area* are lower than within shells at a median of  $\langle M_{\star}^{\text{stream}} \rangle \approx 1.621 \times 10^9 M_{\odot}$  ( $\log_{10}(M_{\star}^{\text{stream}}) \approx 9.21$ ). This supports the scenario where major mergers rather form shells, while minor mergers are associated with streams.

The analyzed stellar population properties can now answer whether the velocity dispersion is also lower within streams and if they are younger/metal rich or older/metal-poor compared to their host galaxy. This is shown in Figure 5.8 in the same fashion as Figure 5.5. Again, the velocity dispersion within streams is smaller than within their surroundings. The ratio  $\langle \text{los}\sigma \rangle_{\text{lw}}^{\text{stream}} / \langle \text{los}\sigma \rangle_{\text{lw}}^{\text{ring}}$  is below unity for 63% of streams at  $1\sigma$ . Overall, the image is very similar to shells. The ages of streams are overall similar to the ages of their surroundings. Only 46% are younger at  $1\sigma$ . Interestingly, there are a few significant young streams, which seem to be different from the remaining sample (in the bottom left of the bottom middle panel).

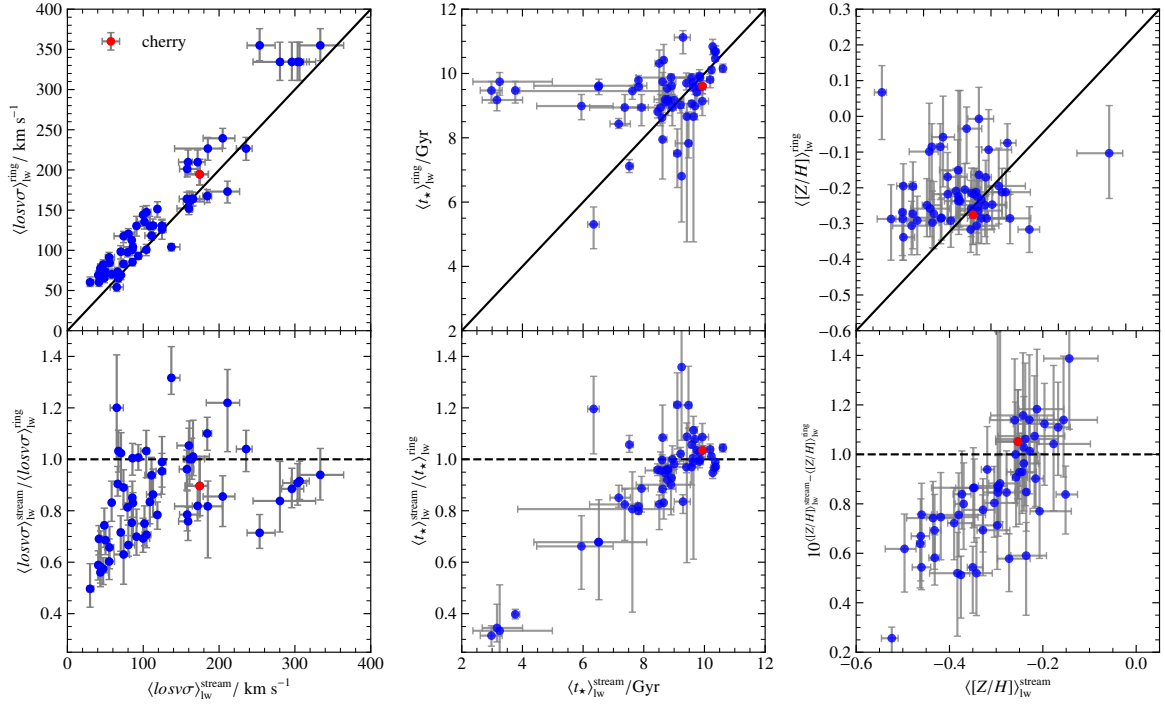


**Figure 5.8:** Same as Figure 5.5, for streams instead of shells.

Also, surprisingly, the metallicity of most streams is lower than their surroundings. 47% are metal-poor compared to their surroundings at  $1\sigma$ . If it is a reliable signal, it might result from the following: The progenitors of shells are possibly more massive than the progenitors of streams, as their stellar masses are larger than within streams (see Figure 5.7). Massive galaxies are more metal-rich than low-mass galaxies, according to the mass-metallicity relation (see Chapter 3). Therefore, shells would be metal-rich compared to streams. Not comparing to shells but simply to their surroundings, this can be explained by a similar effect. The host galaxy is more massive than the progenitors of streams, making it more metal-rich than the streams.

Finally, the differences between the properties within the streams and their surroundings are analyzed. This is shown in Figure 5.9 similar to Figure 5.6. The velocity dispersion within streams is offset to their surroundings. The median is  $\Delta\langle losv\sigma \rangle_{lw} \approx -21 \text{ km s}^{-1}$ , that is they are even more depressed in their velocity dispersion than shells (at  $\Delta\langle losv\sigma \rangle_{lw} \approx -14 \text{ km s}^{-1}$ ). The difference in age is  $\Delta\langle t_{\star} \rangle_{lw}$  is  $\sim -0.31 \text{ Gyr}$ , and the median logarithmic metallicity difference  $\Delta\langle [Z/H] \rangle_{lw}$  is 0.07. For the age, the 0.68-quantile is even positive, while the metallicity off-set is significant at  $1\sigma$ .

The difference between shells being more metal-rich and streams being less metal-rich than their surroundings might also be an imprint of the different methodologies. For streams, simply the median metallicity within the selected Voronoi-bins is taken as the metallicity of streams, whereas for shells, the Voronoi-bins are first radially binned and the metallicity of streams defined as the maximal radial binned metallicity within the shells radial range. The radial binning is supposed to smooth out the effect of taking the maximum, but might still not be physical.

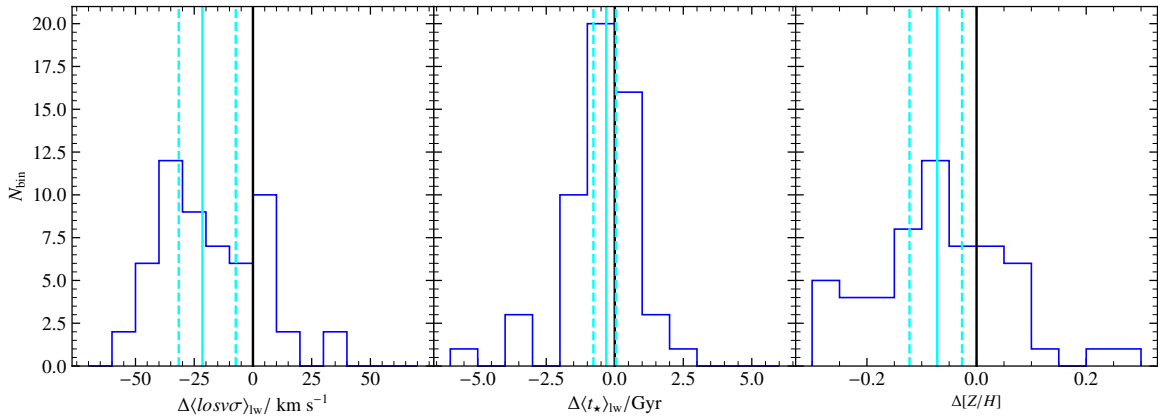


**Figure 5.9:** Same as Figure 5.6 replacing shells with streams.

### 5.2.3 Summary: Properties of Shells and Streams

In this section, the galaxies exhibiting shells and stream in *Magneticum* as identified by Valenzuela & Remus (2024) were studied. Mock observations were created in the edge-on, face-on, and side-on projection. The exact location of each feature in each projection was marked, if possible. Following this, the face-on projection was chosen to be analyzed further and Voronoi-binned maps were produced to extract the velocity-dispersion, age and metallicity of stellar shells and streams. The following conclusions can be drawn:

- Most features are found in the face-on projection, which is why the analysis was done for this projection.
- 71% of shells are found in 2 out of 3 projections, agreeing with Pop et al. (2018). They found shells in 3 out of 3 projections for 40% of their sample, whereas only 17% of galaxies with shells exhibit them in 3/3 projections in this work, which is most likely due to the difference in used projection (random vs. edge-on, face-on, side-on). Almost no shells appear in the side-on projection.
- 55% of streams are found in 2 out of 3 projections, 25% in 3 out of 3 and 18% in 1 out of 3. Most are found in the face-on projection, but at similar rates as in the edge-on and side-on projection.
- Two different methods were used to extract the velocity dispersion, age and metallicity of shells (1st method) and streams (2nd method). For shells, radial profile within slices of the host galaxy were analyzed, while streams were selected using a polygon.

Both shells and streams come in a large variety of different radii, widths, angular positions and extents, shown in Figure 5.3, which were quantitatively analyzed:

- Shells and streams are found at  $\langle r \rangle \sim 20$  kpc and  $\sim 27$  kpc with widths of  $\langle w_{\text{shells}} \rangle = 6$  kpc and  $\langle w_{\text{streams}} \rangle = 5.6$  kpc, agreeing with Sola et al. (2022) in the case of shell radii and stream widths.
- In the studied face-on orientation, the angular position of shells is oriented along the host galaxy’s major-axis, while streams are located all around the host galaxy. The angular extent of shells is larger than for streams.

- The stellar mass of shells ( $\mu = 4.39 \times 10^9 M_{\odot}$ ) is larger than the stellar mass of streams ( $\mu = 1.621 \times 10^9 M_{\odot}$ ).
- Both features' velocity dispersion is lower than the velocity dispersion in their surroundings at  $\Delta\langle l_{\text{osv}}\sigma \rangle_{\text{lw}} \sim -14 \text{ km s}^{-1}$  and  $\sim -21 \text{ km s}^{-1}$ .
- The age of shells and streams is not significantly lower than their surroundings, but there is a noteworthy set of streams which are significantly younger.
- Finally, the shells appear to be more metal-rich than their surroundings, in agreement with Pop et al. (2017). It is speculated that the signal found in this work might be due to an inaccurate analysis method. Streams, on the other hand, appear to be metal-poor compared to their surroundings, which might be because the surroundings belong to the massive host galaxy, which is more metal enriched than the less massive progenitors of streams, according to the mass-metallicity relation.

## 5.3 Connecting Shells and Streams to Their Progenitor Satellite Galaxies

The last section focused on the morphology, kinematics and stellar population properties of the low-surface brightness features around galaxies, stellar tidal shells and streams. A few key differences could be identified, which raised the question whether the properties are related to the properties of the progenitor galaxies of these features. Therefore, in the following section the progenitor galaxies of shells and streams are identified, and their properties analyzed and connected to the properties of the identified shells and streams. Additionally, the true morphologies and masses can be identified, which previously were hidden or permeated by particles belonging to the host galaxy.

### 5.3.1 Identification of Progenitors

In this section, the algorithm used to identify the progenitors of shells and streams is described. It is illustrated in Figure 5.10. The initial ingredients are the IDs of stellar particles within the feature, which were saved during their identification ( $\text{ID}_{\text{shell}}$ ,  $\text{ID}_{\text{stream}}$ ) as mentioned in Section 5.1. The host galaxy's first progenitors are identified in the previous 10 snapshots, which have particle data (up to  $z = 0.42$  Gyr). Then the subhalos within  $3r_{\text{vir}}$  that have a stellar mass more massive than  $1 \times 10^8 M_{\odot}$  are selected, and finally, their stellar IDs are matched with the  $\text{ID}_{\text{shell/stream}}$ . If the number of matching IDs  $N_{\text{match}}$  is larger than 50, the subhalo is taken as a *potential shell/stream progenitor*. Now, starting with the *potential shell/stream progenitor* with the most matching IDs, the reverse process is done until the *true shell/stream progenitor* is found. The stellar IDs of the identified *potential shell/stream progenitor* are saved, and the corresponding stellar particles selected at  $z = 0$ , shifted into the center-of-mass frame of the host galaxy and rotated to the same viewing angle (face-on). The 2D-binned stellar mass map for these particles is plotted and compared to the stellar

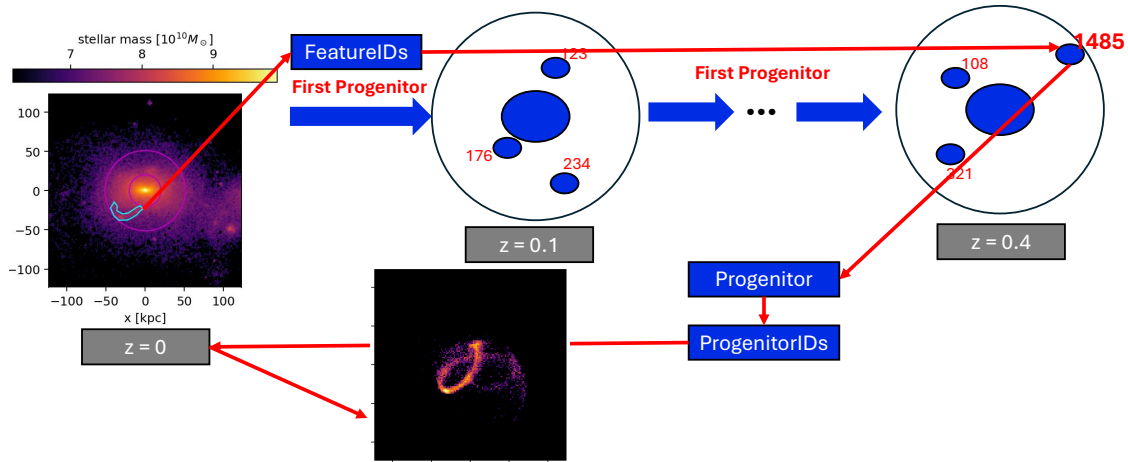


**Figure 5.10:** Illustration of the algorithm used for finding the progenitors of shells and streams.

mass map of the host galaxy. If the plotted stellar particles build up a shell system or stream in the same spot where the initial shell or stream has been selected, it is used as the *true shell/stream progenitor*. Afterward, several properties of the *true progenitor* are calculated at their snapshot of peak stellar mass, as well as the host galaxy’s stellar mass. Their assembly histories are also plotted as verification of the selected system. An expected assembly history is shown in Figure 5.11. The host galaxy’s stellar mass (blue dashed line) increases at the end, while the shell/stream progenitor’s stellar mass (black solid line) decreases and finally vanished before  $z = 0$ . Also, the host galaxy’s mass is expected to always lie above the stream progenitor’s mass, while the shell’s progenitor’s mass might be similar to the host galaxy’s mass. Using this for 60/60 *apparent shells* and 43/57 *apparent streams*, a progenitor could be identified. Because many shells are produced by the same progenitor, there are only 27 shell progenitors. Most streams have different progenitors, but there are three exceptions amounting to 40 stream progenitors. Unfortunately and interestingly, among the streams for which no progenitor could be identified is the group of significantly younger streams, pointed out in Section 5.2.2. It was attempted to not only match the stream’s stellar IDs with the subhalo’s stellar IDs but also include gas particles by bit-masking the part of the particle IDs which indicate the gas particles star formation generation (Springel et al., 2001b). This analysis sparked some interesting speculations about the formation of these young streams, but could not be finished satisfactorily and therefore constitutes future work.

Before analyzing the progenitor’s properties, the true morphology of the shells (streams), that is the distribution of the *true shell/stream progenitor’s* stellar particles traced forward to  $z = 0$ , are shown in Figure 5.12 (Figure 5.13). Several of the *true shells* look like a whole galaxy which has shells (UID 3969, 3970, 7186, 10053, 10541, 12433, 17268). Others appear seemingly as cones, whose spike is in the center of the host galaxy and which are placed parallel to the major axis (x-axis) and transition into shells at large radii (UID 5416,

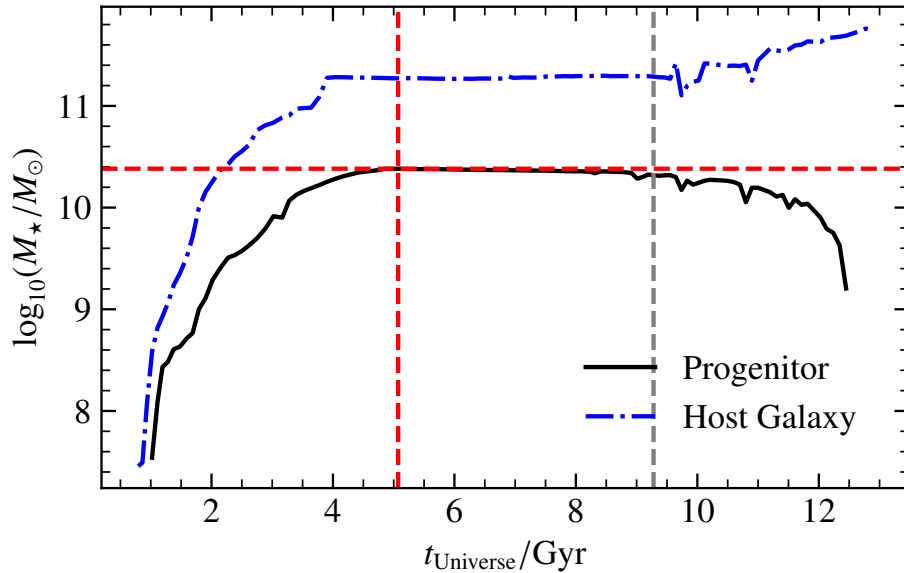


**Figure 5.11:** Assembly History of the host galaxy (blue dash-dotted line) and of the shell/stream progenitor (black solid line). The snapshot in which the progenitor was identified, that is where most of the progenitors stellar IDs match the stellar IDs or the shell/stream, is indicated by the gray dotted vertical line. The snapshot of PSM is indicated by the red dashed vertical line. The PSM is indicated by the red dashed horizontal line.

11651, 13500, 13844, 15741, 15880, 17986, 18231, 18335, 20577, 21477). Some have peculiar shapes that rather look like “umbrella”-like structures (UID 0, 1414, 7903, 9097, 20194). The first group of *true shells* can be explained as already severely phase mixed into its host galaxy, whereas “umbrella”-like shells might still be very early in their evolution. As expected, all shells of the same galaxy also have the same progenitor, with one exception (UID 10541).

The *true streams* (Figure 5.13) come in a similar variety. Several appear as a simple singular straight or arc-like stream (UID 0, 1, 11388, 11533, 14679, 15741, 19173, 22240), most prominent are streams appearing as (multiple) circles or spirals (UID 1414, 7902, 13118, 13892, 14247, 15103, 15545, 16274, 16899, 17686, 18615, 20671, 21503, 21507, 21671, 21714, 21938, 23233), and finally, there are again “umbrella”-like shapes (UID 0, 12536, 13633, 15199, 19186, 19378, 20604). Some cannot be put in any of these groups (UID 11751, 18315). The difference between circles and straight or arc-like streams could simply be a different projection. The prominence of circles might be due to the selected face-on projection. The appearance of *umbrella*-like features among shells and streams proposes that they are an intermediate state between shells and streams. There were some galaxies that have multiple apparent streams (UID 0, 1414, 3968, 6463, 12536, 13892, 14247, 14679, 20604, 21671). Some of these turned out to be part of the same *true stream* (UID 13892, 14247, 20604), while others are truly two different *true streams* (UID 1414, 14679, 21671). For the remaining multiple apparent streams, either both or one of them could not be identified.

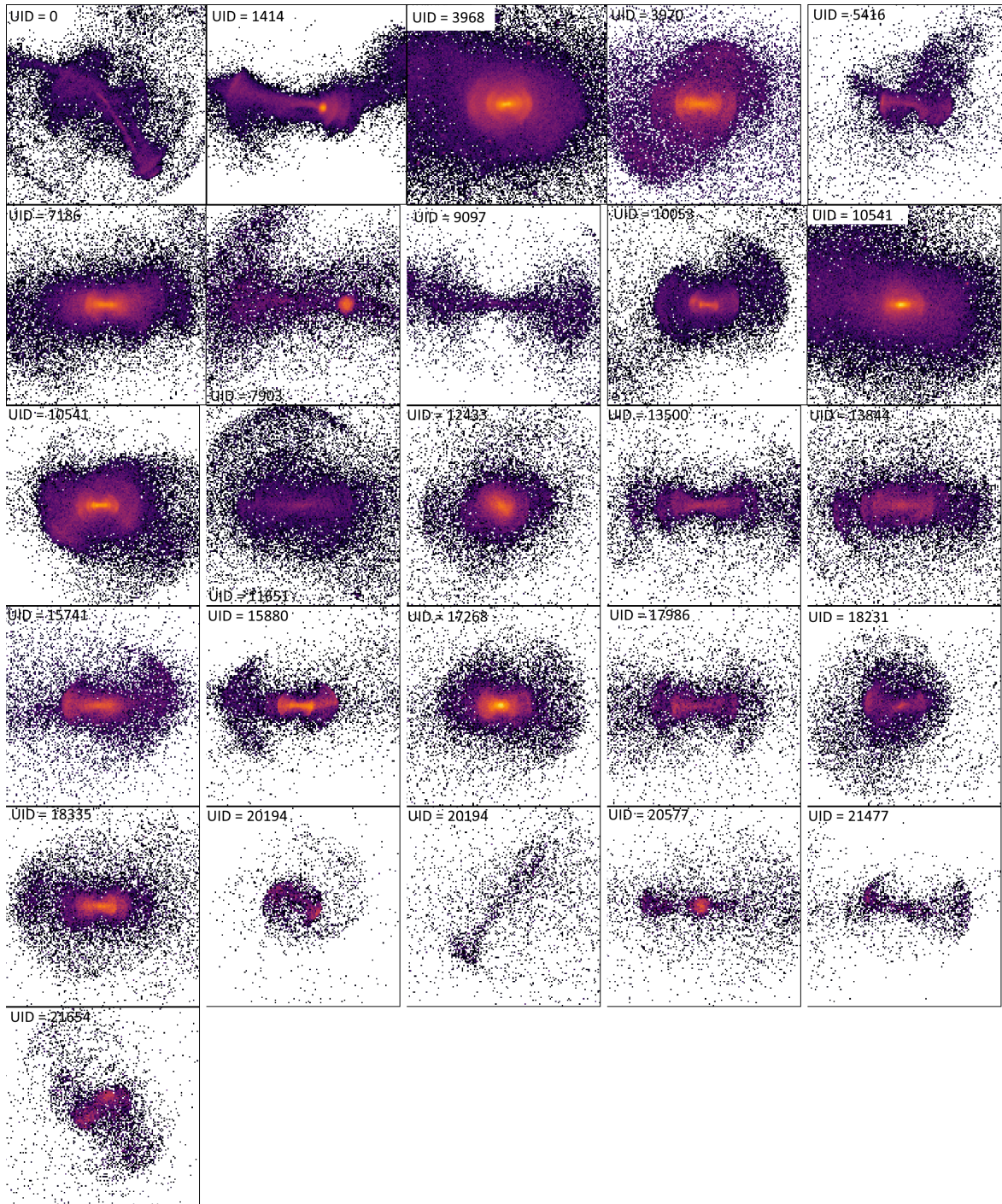


**Figure 5.12:** True morphologies of the shells, that is the distribution of the *true shell progenitor's* particles forward traced to  $z = 0$ .

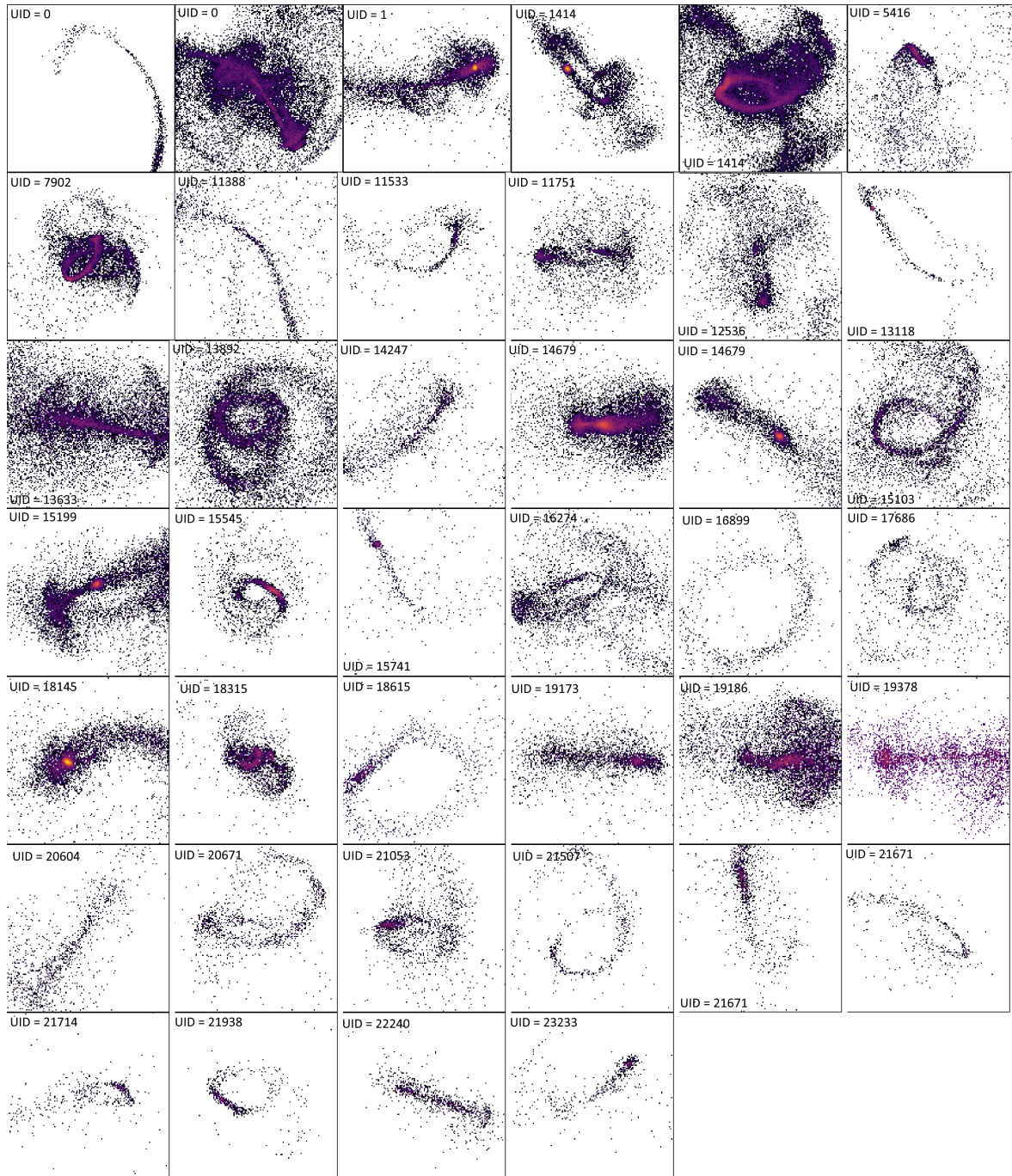


**Figure 5.13:** True morphologies of the streams, that is the distribution of the *true stream progenitor's* particles forward traced to  $z = 0$ .

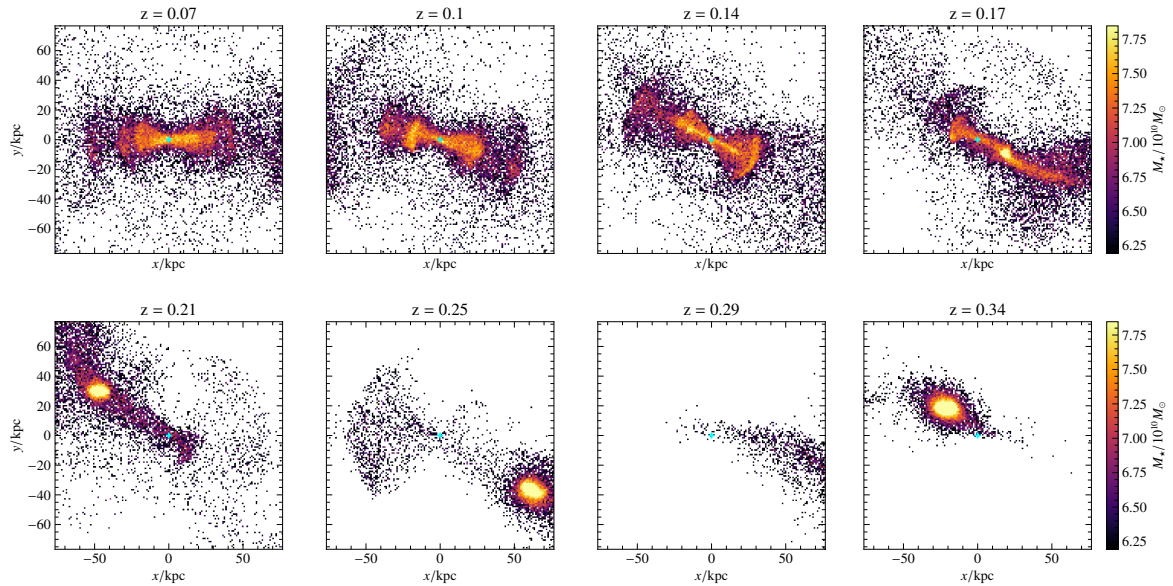


**Figure 5.14:** Evolution of an exemplary *true shell* (UID 13500). Each panel shows the 3D-binned stellar mass maps of the stellar particles belonging to the identified shell progenitor. Time evolved from the bottom right ( $z = 0.34$ ) to the top left ( $z = 0.07$ ). Each particle distribution is centered and rotated into the face-on frame of the host galaxy at  $z = 0$ .

### 5.3.2 Evolution of Progenitors

Having identified the stellar IDs of each *true shell/stream*, maps of these particles can not only be produced at  $z = 0$ , but also in previous snapshots. This allows to illustrate their evolution from being part of an independent satellite galaxy to tidal shells/stream. Figure 5.14 shows the evolution of a *true shell* at  $z = 0$  (top left panel) to the *shell progenitor* at  $z = 0.34$  (bottom right panel). The host galaxy’s UID is 13500, which will also be analyzed in detail further below. The center of each panel is the host galaxy’s center, marked with a cyan plus symbol. At  $z = 0.34$ , the satellite galaxy passes very close by the center of the host galaxy, produces a first shell at  $z = 0.25$ , a second one at  $z = 0.21$  and many more in the remaining snapshots. Interestingly, the double cone-like shell system seems to be slowly rotating as a whole, as it is tilted at  $z = 0.17$  and slowly aligns parallel to the x-axis at  $z = 0$ .

A similar analysis can be done for a *true stream* (UID 7902), as shown in Figure 5.15. Again, the cyan plus at the center of each panel is the center of the host galaxy and the time evolved from the right ( $z = 0.17$ ) to the left ( $z = 0.07$ ). The initial satellite galaxy passes not as close to the center as the shell producing satellite galaxy does at  $z = 0.17$ . It already is stripped off some stars and subsequently is disrupted and curled up around the center ( $z = 0.14, 0.1$ ) until it finally reaches a “pretzel”-like shape ( $z = 0.07$ ).

These examples illustrate the scenario where shells form from radial mergers, while streams are formed by satellite galaxy infalls on orbits with a higher angular momentum (Karademir et al., 2019).

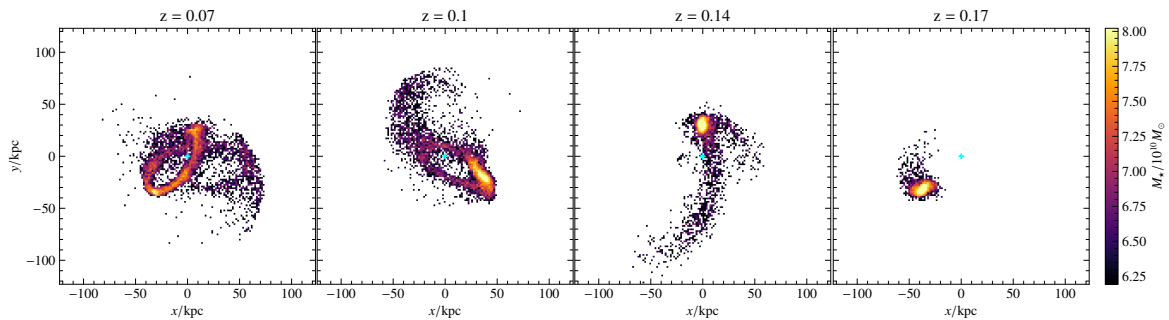


**Figure 5.15:** Evolution of an exemplary *true stream* (UID 7902). Each panel shows the 3D-binned stellar mass maps of the stellar particles belonging to the identified stream progenitor. Time evolved from the right ( $z = 0.17$ ) to the left ( $z = 0.07$ ). Each particle distribution is centered and rotated into the face-on frame of the host galaxy at  $z = 0$ .

### 5.3.3 Decomposition of Shell and Stream Galaxies

Now, these two examples are further analyzed in their decomposition into the host galaxy and the *true shell system/stream*. Figure 5.16 shows the 2D-binned stellar mass map of all particles attributed to the shell galaxy UID 13500 in the left panel. The particles of the *true shell system* are shown in the middle panel, while the right panel shows all particles which are within the galaxy but not within the *true shell system*. The 2D-binned stellar mass map is not the best method to identify the shells, which is why initially the stellar mock observations were used, but it is still possible to identify the shells in the left panel, whereas in the right panel no shells are visible. The same decomposition can be presented for the radial velocity-radius phase space (Figure 5.17). Here the host galaxy (*left panel*), exhibits the usual smooth triangular phase space occupation, where the shells appear as caustics at large radii while the host galaxy appears as an elliptical overdensity at the center (Pop et al., 2017, 2018; Donlon et al., 2024). Looking only at the *true shell system's* phase space (*middle panel*) only the (almost) concentric caustics are seen, while the center at low radial velocities is empty. This means that stars appearing in the *true shell system's* center in Figure 5.16 are all passing through it, and do not remain in the center. Finally, the phase space of the host galaxy without the *true shell system* does not exhibit caustics, meaning it does not have any shells. These results give even more confidence in the correctness of the identification algorithm.

Finally, this decomposition can be done for an exemplary stream galaxy (UID 7902). Figure 5.18 shows the configuration space decomposition as described above for the shell galaxy. The host galaxy (*left panel*) appears in the center, while an arc-like stream peaks out of the bottom left at around  $r = 25$  kpc. The *true stream* (*middle panel*) looks like a “pretzel” which includes the arc in the bottom left. Removing this stream from the host galaxy (*right panel*), leaves the central part of the galaxy, while the arc-like stream is not visible anymore. Figure 5.19 shows the radial velocity-radius phase space decomposition. Again, there is the typical smooth triangular phase space occupation. Interestingly, a caustic appears at larger radii as well. Only looking at the *true stream*, it is revealed that the nature of this caustic is different from the shell caustics. There is the initial caustic and a half one at lower radii and

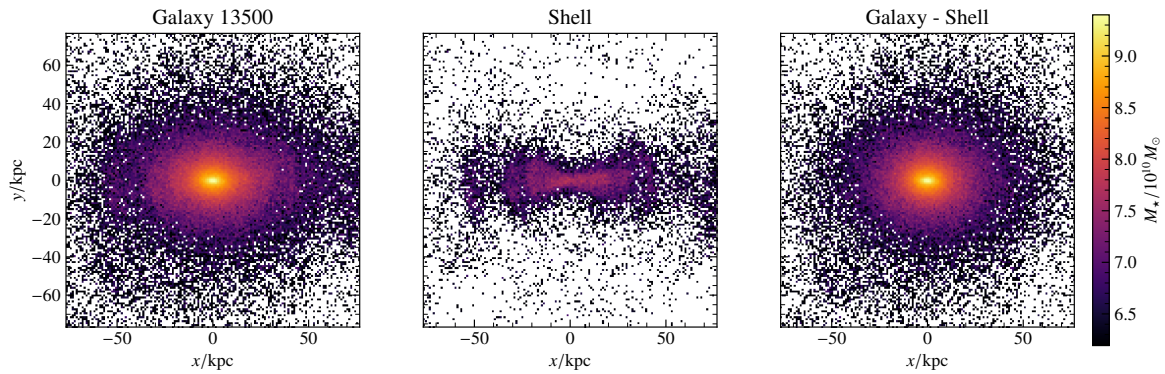


**Figure 5.16:** Decomposition into an exemplary shell system and its host galaxy. *Left:* 2D-binned stellar mass maps of all particles attributed to the galaxy (UID 13500). *Middle:* 2D-binned stellar mass map of all particles attributed to the *true shells* as identified by the algorithm described in Section 5.3.1. *Right:* 2D-binned stellar mass map of all particles in the left panel which are not in the middle panel (relative complement of the left panel with respect to the middle panel).

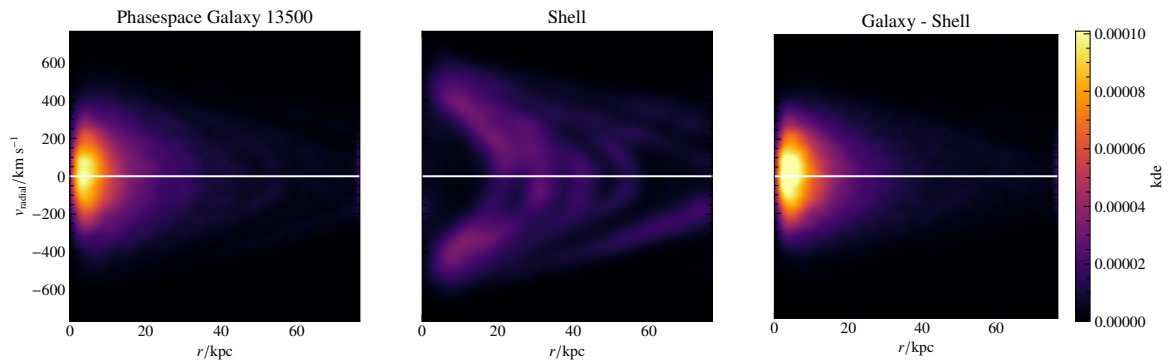


**Figure 5.17:** Phase space decomposition into an exemplary shell and its host galaxy. The same decomposition as Figure 5.16 but presented in the radial velocity-radius phase space of each particle distribution. The color indicates the Gaussian kernel density estimation.

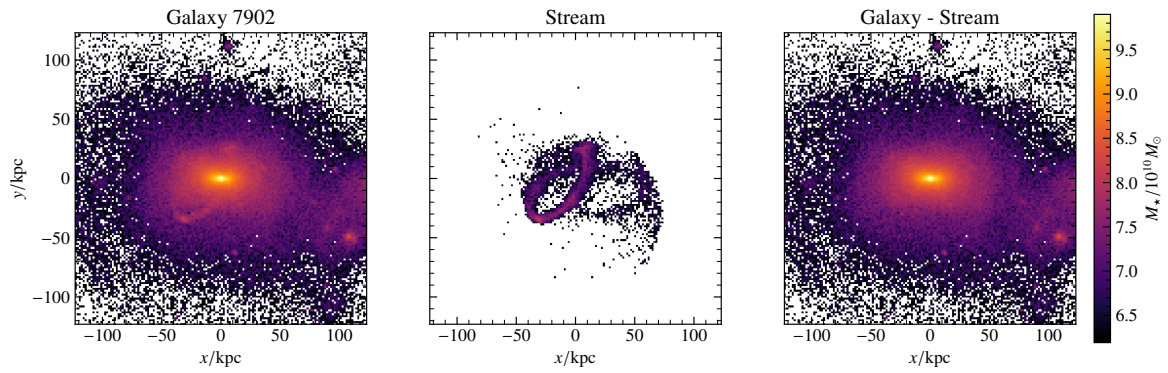


**Figure 5.18:** Decomposition into an exemplary stream and its host galaxy. Same as Figure 5.16 for the galaxy UID 7902.

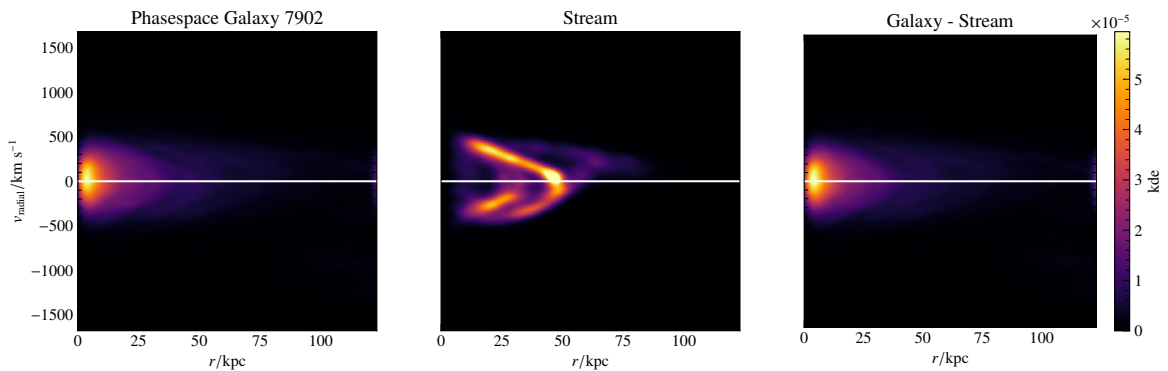


**Figure 5.19:** Phase space decomposition into an exemplary stream and its host galaxy. The same decomposition as Figure 5.16 but presented in the radial velocity-radius phase space of each particle distribution. The color indicates the Gaussian kernel density estimation.

velocities. The galaxy without the stream again does not display this caustic. The highest density section of the stream can be identified in both the configuration space and the phase space, which reveals that it is currently still moving away from the center ( $v_r > 0$ ) but it is right before the turning point ( $v_r = 0$ ).

### 5.3.4 Comparing Progenitors to $z = 0$ Features

It has been demonstrated, by now, that the identification algorithm identified the correct progenitor (excluding the very young streams). Now the properties of the *apparent shell system/stream* can be compared to the properties of the *shell/stream progenitors*, that is the properties calculated at the snapshot of PSM. Figure 5.20 presents the distribution of stellar masses  $M_\star$  within  $10\%r_{\text{vir}}$  within combined shells (red histogram), combined streams (blue histogram), shell progenitors (magenta dashed histogram), and stream progenitors (cyan dashed histogram). Combined means that the masses of all features, which result from the same progenitor, are added together. It is evident that both shells ( $\mu = 9.9$ ) and shell progenitors ( $\mu = 10.7$ ) are more massive than streams ( $\mu = 9.2$ ) and stream progenitors ( $\mu = 9.9$ ). This trend was already hinted at in Figure 5.7 and supports the scenario that shells are formed by more massive progenitors than streams. The peak of the shell distribution

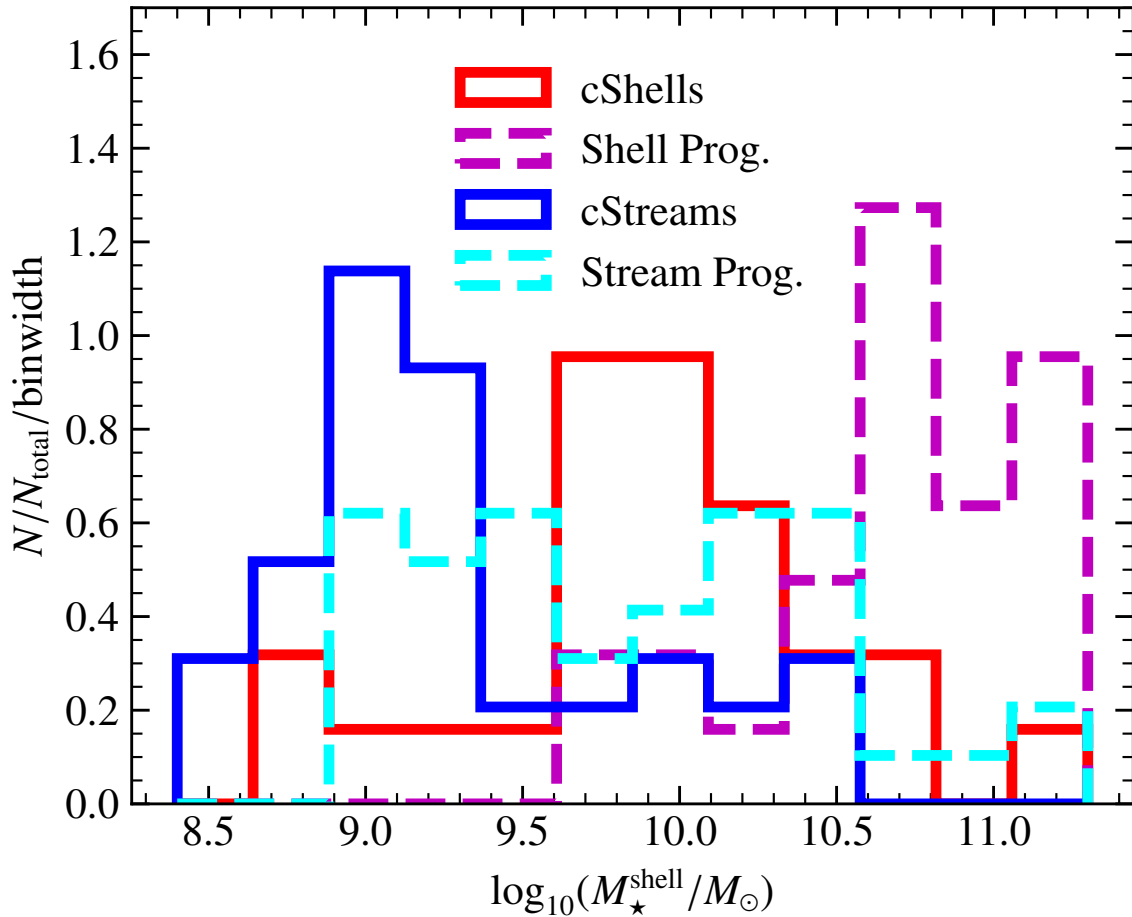
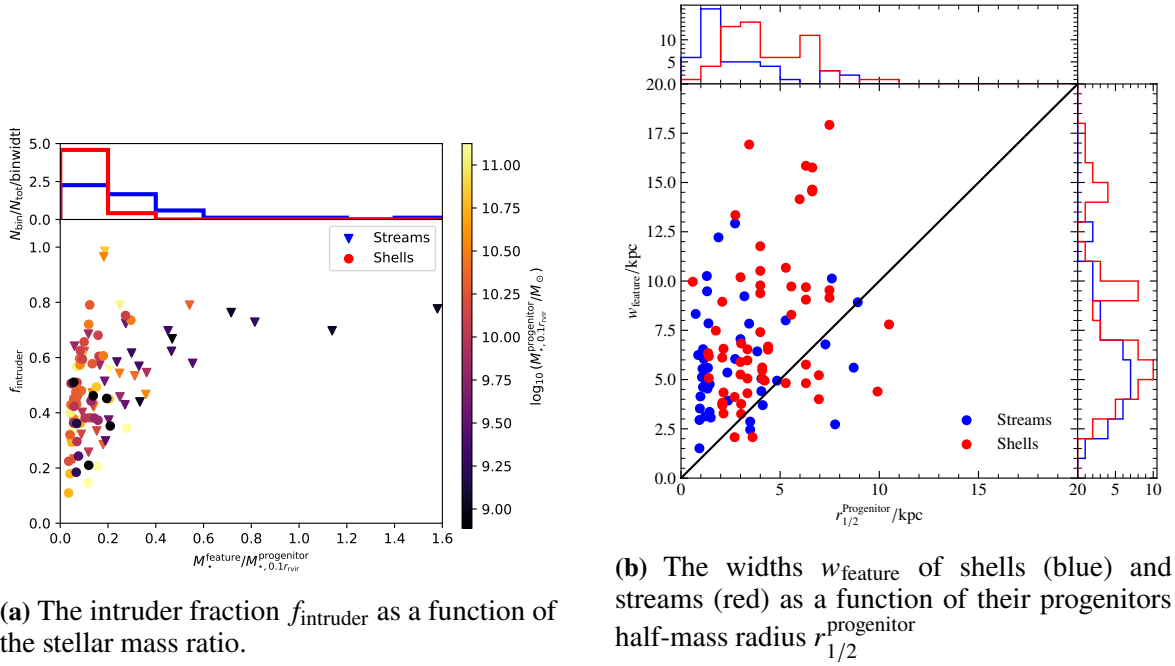


**Figure 5.20:** Comparison of the stellar masses of shells and streams and their progenitors.

is shifted by  $\log_{10}(M_{\star}/M_{\odot}) \sim 0.8$ , while the stream distribution is also shifted to higher masses, but rather smoothed out to be relatively flat.

Related to the stellar masses within the shells or streams  $M_{\star}^{\text{feature}}$  and their progenitors  $M_{\star}^{\text{progenitor}}$  is the ratio between them, which might be related to the fraction of intruders  $f_{\text{intruder}} = |N_{\text{feature}} - N_{\text{match}}|/N_{\text{feature}}$ , where  $N_{\text{feature}}$  is the number of stars within the *shell area* or *stream area* and  $N_{\text{match}}$  the number of stars with this area which stellar IDs match the stellar IDs of particles in the identified progenitor. Therefore, intruders are particles belonging to the host galaxy which got caught within the shell or stream. Ideally, this ratio is zero, but realistically will always be nonzero. A small mass ratio  $M_{\star}^{\text{feature}}/M_{\star}^{\text{progenitor}}$  is expected for shells, as one progenitor produces multiple shells. For streams, a small mass ratio can occur, if only a small part of the stream is covered by the *stream area*. A mass ratio  $M_{\star}^{\text{feature}}/M_{\star}^{\text{progenitor}} \gtrsim 1$  means either the whole stream is covered by the *stream area* and includes some intruders, or only a part of the stream is covered, but the *stream area* includes even more intruders. Figure 5.21a displays the intruder fraction  $f_{\text{intruder}}$  as a function of the stellar mass ratio  $M_{\star}^{\text{feature}}/M_{\star}^{\text{progenitor}}$ . The streams (upside-down triangles) and shells (circles) are colored by the logarithmic stellar progenitor mass. Additionally, the distribution for the mass ratio is shown on top. Overall, both streams (blue histogram) and shells (red histogram) have low mass ratios. As expected, no shells have a mass ratio larger than 0.4,



(a) The intruder fraction  $f_{\text{intruder}}$  as a function of the stellar mass ratio.

(b) The widths  $w_{\text{feature}}$  of shells (blue) and streams (red) as a function of their progenitors half-mass radius  $r_{1/2}^{\text{progenitor}}$ .

**Figure 5.21:** **a)** The intruder fraction  $f_{\text{intruder}}$  as a function of the stellar mass ratio of the respective tidal feature and its progenitor. Shells are shown as upside-down triangles, shells are circles. The symbols are colored by the progenitors stellar mass. On the top, the histogram of the stellar mass ratio is shown, where shells are represented as red and streams as blue. **b)** The widths  $w_{\text{feature}}$  of shells (blue) and streams (red) as a function of their progenitors half-mass radius  $r_{1/2}^{\text{progenitor}}$ . In addition, the histogram distribution of  $w_{\text{feature}}$  and  $r_{1/2}^{\text{progenitor}}$  are shown on top and to the right.

whereas most streams go as far as 0.6 and some even have mass ratios  $> 1$ . The intruder fractions  $f_{\text{intruder}}$  of features at low mass ratios (0.0 to 0.4) covered a range from 0.1 to 0.8, which is acceptable. Only some streams deviate from this, namely two streams at low mass ratios and very high intruder fractions  $\sim 1.0$  which have very massive progenitors. The streams at mass ratios  $\gtrsim 0.8$  have  $f_{\text{intruder}} \sim 0.8$  and low progenitor masses, suggesting it is easy to accidentally select intruders if the stream is not very massive.

Another interesting property to look at is the relation between the features width  $w_{\text{feat}}$  and the progenitors half-mass radius  $r_{1/2}^{\text{progenitor}}$ . Observers studying the width of streams might assume that it corresponds to the size of the progenitor (e.g. Pippert et al., 2024). But other scenarios are also possible. Streams typically are stretched out along their orbit, which might lead to a decrease in their width in the orthogonal direction. It is also imaginable that they puff up during disruption. The shells' size might not be directly connected to the progenitor's size because they are built up from stars which were already stripped from the satellite galaxy. Figure 5.21b displays the features' width as described in Section 5.1 as a function of the progenitor galaxy's half-mass radius  $r_{1/2}$  at PSM. There is no clear correlation, but most widths are much larger than the progenitor's half-mass radius  $r_{1/2}$ . Also, shell progenitors' half-mass radii are on average larger than stream progenitors' half-mass radii. The peaks of the  $w_{\text{feature}}$  distribution are similar, but shells can be wider than streams. This would suggest that streams are puffing up as they fall into the host galaxy. More likely is that the difference arises from the method of calculating the stream width, which is based on a visual

identification of “where the stream ends”, which is more similar to a truncation width/radius (Buitrago & Trujillo, 2024) than to a half-mass radius. A more reliable approach would be to produce stellar mock observations of the streams and measure the light profile perpendicular to their direction of elongation, fitting a Gaussian to it and extracting the FWHM (Pippert et al., 2024). This constitutes future work.

### 5.3.5 Properties of the Progenitors

In this last section, the properties of the shell and stream progenitors are analyzed. By identifying differences between these two groups, it is possible for observers to infer the properties of a progenitor from the observed feature. A first interesting parameter concerns the formation of the feature through a merger, namely the merger ratio  $\mu = M_{\star}^{\text{progenitor}} / M_{\star}^{\text{host}}$ . Here, the masses are stellar masses within  $10\%r_{\text{vir}}$ . As mentioned before, the properties of the progenitor are calculated at their snapshot of PSM (peak stellar mass). To be comparable, the properties of each feature’s host galaxy are calculated at the snapshot of PSM of the feature’s progenitor. Previously, it was speculated multiple times, that the merger ratio of shells might be larger than that of streams. Figure 5.22a shows the distribution of this merger ratio. Indeed, the median merger ratio of shells is 0.4, while the streams’ median is 0.1. The streams’ merger ratio distribution is also much more concentrated and the highest merger ratio is 2:3, while it is fairly flat for shells and includes almost 1:1 mergers.

A property that might be related to the age of the shells and streams presented in Figure 5.5 and, Figure 5.8 is the cold gas fraction  $M_{\text{cold gas}} / (M_{\text{gas}} + M_{\star})$  of their progenitor. A progenitor with a lot of cold gas is more likely to trigger star formation during and after the collision with the host galaxy and produces younger features. Figure 5.22b presents the distribution of the cold gas fraction  $M_{\text{cold gas}} / (M_{\text{gas}} + M_{\star})$  of shell and stream progenitors. The shells’ median is at 0.18 and the streams median at 0.38. Therefore, it is expected that streams are slightly younger than shells. Indeed, the median age of shells presented in Figure 5.5 is 9.5 Gyr, while the median stream age presented in Figure 5.8 is 9.1 Gyr, but these include the group of very young streams, which was not included in the sample of progenitors. This comparison therefore is not reliable.

Another question is whether the progenitors of streams and shells are more likely to be disk galaxies or elliptical galaxies. This question can be answered by calculating the *b-value* of each progenitor. It is the only property that was calculated within  $3r_{1/2}$  instead of  $10\%r_{\text{vir}}$  because that is how it is defined (Teklu et al., 2015). Figure 5.22c presents the distribution of the *b-value* of shells (red) and streams (blue). The vertical dashed gray lines represent the boundaries between spheroids ( $< -4.73$ ), intermediates, and disks ( $> -4.35$ ). Both distributions cover all possible morphologies. There are 11/40  $\sim$  28% stream progenitors and 5/26  $\sim$  19% shell progenitors among disks, 19/40  $\sim$  48% stream progenitors and 12/26  $\sim$  46% shell progenitors among spheroids, and 10/40  $\sim$  25% stream progenitors and 9/26  $\sim$  35% shell progenitors among intermediates. That means slightly more stream progenitors are disks compared to the progenitors of shells.

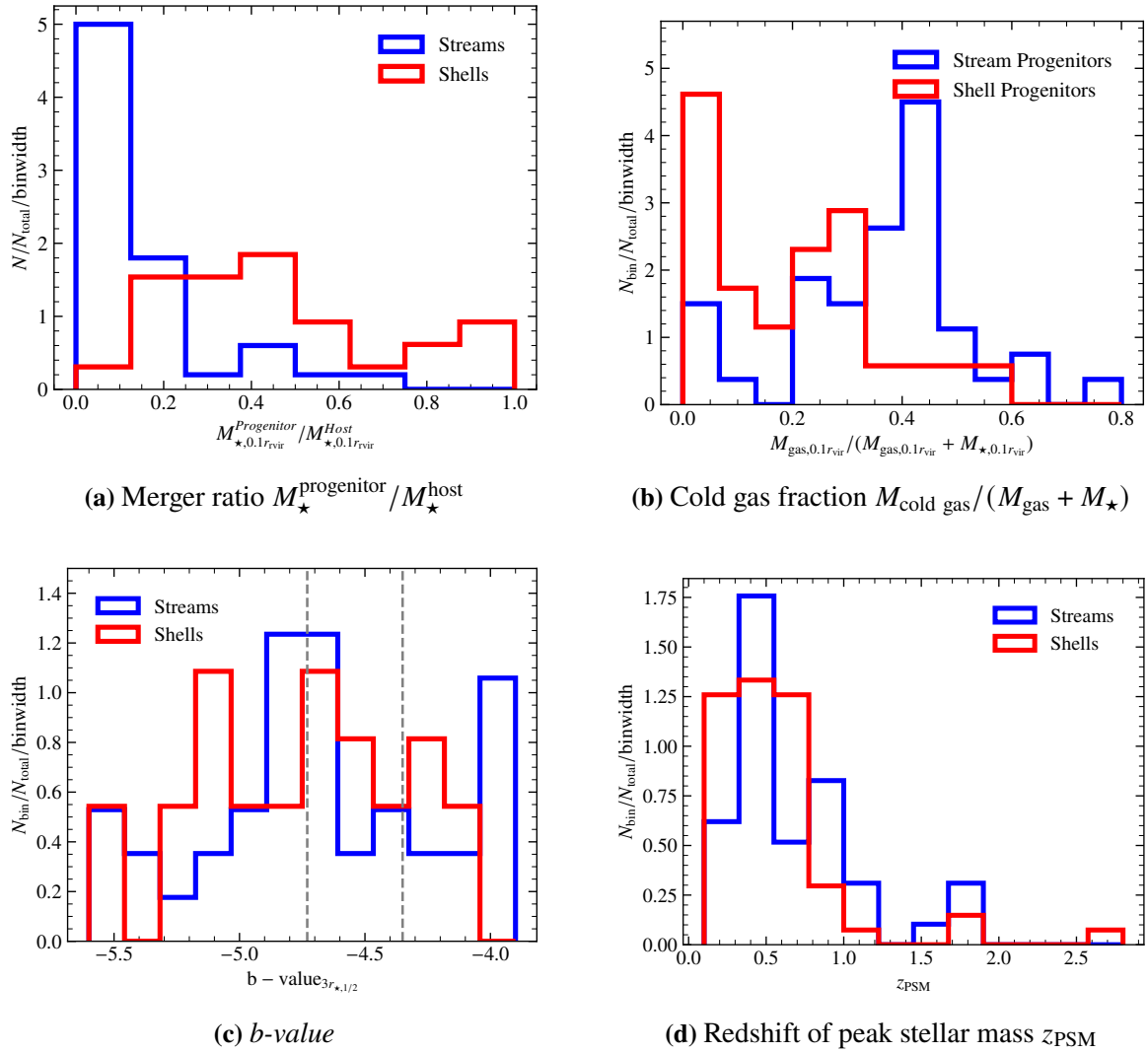


**Figure 5.22:** Distributions of the respective parameters. The blue histogram represents stream progenitors, the red one shell progenitors.

Finally, the redshift of the snapshot of peak stellar mass (PSM) for each progenitor is investigated. Figure 5.22d shows its distribution for shells (red) and streams (blue). Both distributions are concentrated around  $z \approx 0.45$ , suggesting that the progenitors of both types of features reach their highest amount of stellar mass at the same time, roughly  $\sim 5$  Gyr ago.

Finally, two galaxy scaling relations investigated in Chapter 3 for the whole galaxy sample are revisited again but for the progenitors of shells and streams. Figure 5.23a shows the stellar half-mass radius  $r_{1/2}$  for progenitors of streams (square) and shells (circles) as a function of stellar mass  $M_{\star}^{\text{progenitor}}$ , colored by their redshift of peak stellar mass  $z_{\text{PSM}}$ . As a comparison, all galaxies with stellar masses  $> 10^9 M_{\odot}$  at  $z = 0.45$  are shown as gray circles and at  $z = 0$  as solid black contour. Again, observations by Lange et al. (2015) for ETGs (dashed black line) and LTGs (solid black line) are overplotted. The  $z = 0$  contours lie on top of the  $z = 0.45$  sample and the shell and stream progenitors also lie on top of the same sample, as well as the observations. The only deviating stream progenitors lie significantly below the other samples, but have very high  $z_{\text{PSM}}$ , which explains their smaller sizes. In conclusion, the progenitors of shells and streams do not occupy a special region in the mass-size relation.

The same analysis is shown in Figure 5.23b for the mass-metallicity relation, where the mass-weighted metallicity  $\log_{10}(\langle Z/Z_{\odot} \rangle_{\text{mw}})$  is shown as a function of the stellar mass  $M_{\star}^{\text{progenitor}}$ . Again, all considered samples ( $z = 0$ ,  $z = 0.45$ , and shell/stream progenitors) lie on top of each other and are consistent with all considered observations. Therefore, the progenitors of shells and streams do not occupy a special region in the mass-metallicity relation. But in line with the mass-metallicity relation, the more massive shell progenitors are found in the top-right end of the relation, meaning they are also more metal-rich than stream progenitors.

### 5.3.6 Summary: Connecting Shells and Streams to Their Progenitors

In conclusion, in this section I identified the progenitors of shells and streams. The identification algorithm uses the stellar IDS saved within each feature, as presented in the last section, and matches them to the stellar IDs of subhalos around the progenitors of the feature’s host galaxy. The following results were obtained:

- 27 progenitors of 60/60 shells were identified and 40 progenitors of 43/57 streams. No progenitors could be identified for the group of very young streams mentioned in the last section.
- There is a large variety among the morphology of shell systems (whole galaxy with shells, double cones, “umbrella”s) and streams (straight/arc, circles/spirals, “umbrella”s), where “umbrella”-like features seem to be an intermediate class between shells and streams.
- The evolution of two exemplary progenitors illustrates the formation scenarios, where shells originate from a merger on a radial orbit and streams from mergers on an orbit with a larger angular momentum, agreeing with Karademir et al. (2019).

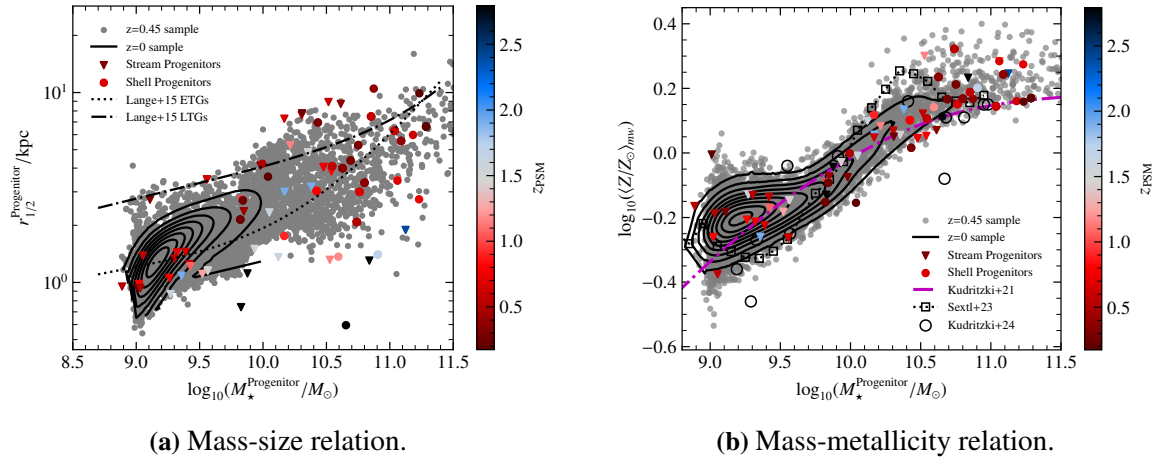


**Figure 5.23:** *Left panel:* Mass-size relation for shells (circles) and streams (upside-down triangles). It shows the stellar half-mass radius  $r_{1/2}$  as a function of the stellar mass  $M_{\star}$ . Observations by Lange et al. (2015) for ETGs (dashed black line) and LTGs (solid black line) are overplotted. *Right panel:* Mass-metallicity relation for shell (circles) and stream (diamonds) progenitors. It shows mass weighted metallicity  $\log_{10}(\langle Z/Z_{\odot} \rangle_{\text{mw}})$  as a function of the stellar mass  $M_{\star}$ . Again results from stacked galaxy spectra by Sextl et al. (2024) (open black squares and dotted line), and from individual blue supergiants (Kudritzki et al., 2016; Davies et al., 2017; Bresolin et al., 2022; Urbaneja et al., 2023) are shown as open black dots, as well as the prediction of a galaxy evolution lookback model by Kudritzki et al. (2021) (magenta dash-dotted line). In both panels, the shells and streams are colored by the redshift of peak stellar mass  $z_{\text{PSM}}$ . As a comparison, in both panels, all galaxies with stellar masses  $> 10^9 M_{\odot}$  at  $z = 0.45$  are shown as gray circles and at  $z = 0$  as solid black contour.

- Decomposing the same exemplary galaxies into the *true shell system/stream* and the host galaxy in configuration and radial velocity-radius phase space reveals that shells appear as caustics in the phase space (Pop et al., 2018; Donlon et al., 2024). Streams look similar to shells in phase space, but are more complicated. This decomposition gives additional credibility to the progenitor identification algorithm because it can clearly be seen, that removing the *true shell system/stream* from the galaxy also removes the identified feature.

Next, the properties of these progenitors are compared to the properties of the feature at  $z = 0$  and compared between shells and streams.

- The masses of all features which originate from one progenitor were summed up. The masses  $\log_{10}(M_{\star}/M_{\odot})$  of such shell systems (median  $\mu = 9.9$ ) are larger than of streams ( $\mu = 9.2$ ). Their respective progenitors are more massive but keep the difference between shell progenitors ( $\mu = 10.7$ ) and stream progenitors ( $\mu = 9.9$ ).
- The ratio of these two masses  $M_{\star}^{\text{feature}}/M_{\star}^{\text{progenitor}}$  is related to the intruder fraction  $f_{\text{intruder}} = |N_{\text{feature}} - N_{\text{match}}|/N_{\text{feature}}$ , which is due to the method of selecting the features and not related to physical reasons. Most features have a mass ratio between 0.0 and 0.2 with an intruder fraction between 0.1 and 0.8. The information within these two properties is very convoluted and difficult to interpret.
- An interesting question is whether the widths of shells and streams reflect the size of the progenitor galaxies. Most widths of shells and streams were found to be larger than the half-mass radius of their progenitor. But no clear conclusion could be drawn

because the widths of each feature was visually identified and therefore is closer to a truncation radius than a half-mass radius.

- Furthermore, the progenitors' properties are analyzed. Shells formed from mergers with a higher mass ratio than streams. Stream progenitors have, on average, a higher cold gas fraction. The median *b-value* is the same for shell and stream progenitors, but there are proportionally slightly more stream progenitors among the disks (28%) than shell progenitors (19%). The median redshift of peak stellar mass ( $z_{\text{PSM}} = 0.45$ ) is the same for shell and stream progenitors.
- Finally, shell and stream progenitors do not occupy special regions in the mass-size relation or mass-metallicity relation, but lie perfectly on top of the overall sample of galaxies at  $z = 0$  and  $z = 0.45$ . In line with the mass-metallicity relation, the more massive shell progenitors are on average also more metal-rich.

# Chapter 6

## Summary and Conclusion

In this thesis, I investigated the stellar ages and the metal content of galaxies and their tidal structures such as stellar shells and streams, and their progenitors. It also includes an analysis of a kinematically peculiar group of galaxies: Prolate rotators. The age of stars in a galaxy and their metallicity provide insights into the formation history and their star formation history. I utilized the hydrodynamical cosmological simulation Magneticum Pathfinder to study the galaxies found within the highest-resolution run Box4.

### Ages and Metallicities of Galaxies

The global age and metallicity of galaxies was analyzed by first comparing luminosity-weighted quantities to mass-weighted quantities. It was found that luminosity-weighted galactic ages are on average smaller than mass-weighted ages, while luminosity-weighted galactic metallicities are smaller for spheroidal galaxies, while many disk galaxies have higher luminosity-weighted metallicities. The simulation's agreement with observations is verified by comparing it to numerous scaling relations, including the stellar mass-size relation, the stellar mass-stellar age relation, and the stellar mass-stellar metallicity relation. While the metallicity strongly correlates with stellar mass, the age is correlated with the galaxy's morphology. The stellar mass-stellar metallicity relation is still valid if the stars are split up into an old, middle-aged and young stellar population, but old stars are metal-poor in disk galaxies compared to spheroidal galaxies. An interesting relation was recently put forward where the best predictor of a galaxy's gas-phase metallicity is a proxy for its baryonic gravitational potential  $\Phi \propto M_{\star} \times r_{1/2}^{-\alpha}$  (Sánchez-Menguiano et al., 2024). An attempt was made to reproduce this relation with the stellar metallicity, which is tightest for  $\alpha \sim 0.8$  opposed to  $\alpha \approx 0.6$  as found for the gas-phase. The ages and metallicities relation with the rotational support  $V/\sigma$  and  $\lambda_{r_{1/2}}$  revealed, that the young disk galaxies are more rotationally supported and have higher ellipticities  $\epsilon$  than the old spheroidal galaxies. The metallicity is not dependent on  $v/\sigma$  or  $\epsilon$ .

The spatially resolved analysis of ages and metals in this work focuses on radial profiles and radial metallicity gradients. The age profiles of spheroids are slightly increasing at small radii, indicating an “outside-in” progression of star formation, while disks' age decreases at small radii, representative of an “inside-out” growth. This binary scenario stands in contrast

to declining metallicity profiles for every morphology, which are typical for the “inside-out” scenario (Venturi et al., 2024). When split into a young, middle-aged and old stellar population again, differences among their metallicity distribution are revealed. Young stars are the most metal rich in disks over up to  $\sim 2.5r_{1/2}$ , while they are only the most metal rich in the innermost center among the other morphologies, and middle-aged stars take over as the most metal rich over all radii. This difference is attributed to the different formation histories, that is secular star formation vs. minor and major mergers. The steepness of their decline is also different, which leads to the investigation of metallicity gradients.

The metallicity gradients are calculated as a straight line fit to the distribution of metallicity as a function of radius within  $3r_{1/2}$ . The median metallicity gradient is most negative in spheroidal galaxies, while it is the flattest (still negative, but smaller value) for disk galaxies. There is a trend to steeper (more negative) metallicity gradients with increasing stellar mass. No conclusive trend is found with the galaxies’ age. Increasing  $V/\sigma$  for spheroidal and intermediate galaxies leads to steeper gradients, which is not the case for disks. The previously found differences regarding the metallicity distribution among the different age populations is further analyzed by comparing the metallicity gradient within young stars to the metallicity gradient within old stars. The majority of galaxies show a negative gradient within both groups. An interesting set of galaxies exhibits a positive young metallicity gradient while having an old negative metallicity gradient. It is speculated, that some of these galaxies’ star formation was quenched during their evolution and later restart it in their outskirts (Remus & Kimmig, 2023, Fortuné et al., in prep.).

These rejuvenating galaxies are part of a *star formation history classification* defined by Fortuné et al. (in prep.) for the *Magneticum galaxies*. For these classes and the *kinematic groups* defined by Schulze et al. (2017) for the *Magneticum Galaxies*, age and metallicity profiles are produced. The star formation classes who have been on the star formation main sequence (Speagle et al., 2014) for their whole evolution are younger – most pronounced in the core – than those that were quenched at some time. The age and metallicity profiles of those galaxies that later had a burst of star formation or jumped back onto the star formation main sequence compared to those who were quenched completely are flatter in the center. The age profiles of galaxies exhibiting a kinematically distinct core (KDC) have a steep decline towards the center, compatible with the scenario of young KDCs made up of newly formed stars during a major merger. All other classes are generally old over all radii. Their metallicity profiles are declining as well, with the highest metallicity in the center of KDCs.

### **Prolate Rotators**

The classes with the oldest stars are the non-rotators and prolate rotators. The prolate rotators are peculiar and rare galaxies which rotate around their long axis, opposed to normal oblate rotation around the short axis. They are a very rare group of galaxies, which might be due to the fact, that the prolate rotation is only stable for a very short amount of time. Therefore, their formation and the rotation’s stability is investigated, along with the merger which caused the rotation to become prolate. First, an isolated binary disk merger simulation is analyzed. Two

spiral galaxies of the same mass are colliding, which produces an off-axis rotation similar to prolate rotation. This is stable up to the end of the simulation, or at least 4.5 Gyr. More realistically, the first progenitors of the prolate rotators identified by (Schulze et al., 2017) in *Magneticum* are visually inspected regarding their velocity and velocity dispersion. This is done to identify the snapshot of first prolate rotation and to find the merger progenitors. Using this information, it is possible to determine the lifetime of the prolate rotation, which is  $> 3$  Gyr for most and the longest lifetime is 9 Gyr. As these are prolate rotators at  $z = 0$ , it is not surprising that for most of them the prolate rotation occurred only recently. In future work, the prolate rotators are identified at higher redshift, so that their progenitors and descendants can be investigated for prolate rotation and a true lifetime can be determined Remus et al. (in prep.). In this work, the merger ratio of these galaxies was calculated to be typically  $M_{\star}^{\text{central}}/M_{\star}^{\text{satellite}} \leq 4$ . Finally, an exemplary prolate rotator was studied in more detail, illustrating the formation scenario of a polar merger. The satellite galaxy falls into the central galaxies almost parallel to its rotation axis, elongating it along this direction while the rotation pattern survives (e.g., Hegde et al., 2022). The ages of stars spatially associated with this rotation are slightly younger than the surrounding stars.

### Stellar Shells and Streams

Exactly these prolate rotators exhibit the most tidal features in their outskirts (Valenzuela & Remus, 2024). They have the highest percentage of showing stellar shells and also exhibit a significant amount of stellar streams. Valenzuela & Remus (2024) found that shells appear as a depression in the velocity dispersion map. According to the mass-metallicity, and mass-age relation, less massive galaxies, which might be the progenitors of shells and streams, are younger and metal-poor compared to the massive galaxy the features are identified in. This would mean they are younger and have a smaller metallicity than their surroundings. Whether this is the case and if the velocity dispersion is consistently lower within these features was studied. All galaxies exhibiting shells and streams as identified by Valenzuela & Remus (2024) are used, and mock-observations produced in an edge-on, face-on, and side-on projection. Each feature's location and shape is identified, if possible. The further analysis is done for the face-on projection because most streams were identified in this projection, while 71% of shells and 55% of streams are found in 2 out of 3 projections. Velocity-dispersion, age and metallicity are analyzed via Voronoi-binned maps. Two different methods are then employed to analyze the features: Radial profiles over the shells are calculated, while streams are selected within a polygon. The basic properties of the shells' and streams' location and shape, such as their mean radius, angular position, radial width and angular width can then be analyzed. Shells can be found at  $\langle r \rangle \sim 20$  kpc and streams at  $\langle r \rangle \sim 27$  kpc with widths of  $\langle w_{\text{shells}} \rangle \sim 6$  kpc and  $\langle w_{\text{streams}} \rangle \sim 5.6$  kpc. In the face-on projection, most shells are aligned with the major axis while streams are evenly distributed. The median projected stellar masses of shells ( $\langle M_{\star}^{\text{shells}} \rangle = 4.39 \times 10^9 M_{\odot}$ ) are larger than the median projected stellar mass of streams ( $\langle M_{\star}^{\text{streams}} \rangle = 1.62 \times 10^9 M_{\odot}$ ). Both types of features have lower velocity dispersions than their surroundings at  $\Delta \langle \log \sigma \rangle_{1w} \sim -14 \text{ km s}^{-1}$  for shells and  $\sim -21 \text{ km s}^{-1}$

for streams. The age could not be identified to be significantly younger or older than their surroundings, but there is a noteworthy sample of very young streams. In agreement with Pop et al. (2017), shells are slightly more metal-rich than their surroundings. Streams, on the other hand, are metal-poor compared to their surroundings. This might be due to the effect of the mass-metallicity relation. The surrounding host galaxy is more massive than the stream’s progenitor galaxy.

Finally, the progenitors of streams and shells are identified by tracing their stellar IDs back in time and matching them with nearby subhalos. 27 progenitors were found for 60/60 shells and 40 progenitors for 43/57 streams. Multiple shells share the same progenitor, and only three streams do so. Forward tracing the stellar particles of the identified progenitor makes it possible to see the *true stream* or *true shell system*, which might have been obstructed by the host galaxy before. Doing this, a quick classification was done for the *true streams and true shell systems*: There can be strongly phase mixed shells, which appear similar to the host galaxy itself while still exhibiting shells. Then there are typical “double cone” shells, which show multiple shells within both directions of the major axis. And finally, “umbrella”-like shells appear, that look like a straight stream is attached to the concave side of a shell. These “umbrellas” are also found among the *true streams*, while the rest either look like single straight, or arc-like lines, or like spirals or multiple circles interwoven. The evolution of an exemplary shell and stream progenitor illustrates the formation scenario that shells form through a radial merger, while stream progenitors are on orbits with higher angular momentum, in agreement with Karademir et al. (2019). Decomposing the galaxies into the host galaxy and the *true feature* reveals that shells appear as caustics in the phase space (Pop et al., 2018; Donlon et al., 2024) and gives additional confidence to the identification algorithm. Finally, the properties of the  $z = 0$  shells and streams can be compared to the progenitors and among each other. The stellar masses of all features belonging to the same progenitor were summed up. The median stellar mass of shell systems is  $\langle \log_{10}(M_{\star}^{\text{shell}}/M_{\odot}) \rangle = 9.9$  and therefore larger than that of streams  $\langle \log_{10}(M_{\star}^{\text{shell}}/M_{\odot}) \rangle = 9.2$ . One motivation for this work was to find out the connection between a progenitor’s size and the width of the resulting feature. This could hint at a puffing up of the stream or that the elongation along the orbit diminishes the width perpendicular to it. It is found that, on average, the features’ width is larger than the progenitors’ half-mass radius  $r_{1/2}$ . Unfortunately, the results are not very conclusive because the measured widths are based on the visual truncation in the mock observation rather than a “half-light approach”. In a last step, the merger ratio, cold gas fraction, *b-value*, and redshift of peak stellar mass  $z_{\text{PSM}}$  is determined. Shells form from a merger with a higher merger ratio than streams, stream progenitors have on average a higher cold gas fraction, slightly more stream progenitors are disks (28%) compared to shell progenitors (19%), but for both the majority are intermediate or spheroidal galaxies. The median  $z_{\text{PSM}}$  is the same ( $\sim 0.45$ ) for both features. Finally, the shell and stream progenitors do not occupy special regions in the mass-size and mass-metallicity relations.

In the future, the identified progenitors of shells and streams can be used to infer the formation and evolution of observed shells and streams in more detail. For example, it

was not statistically analyzed how the orbit (e.g., via  $v_r(r = r_{\text{vir}})$ ) affects the formation. Other interesting cases are the “umbrella”-like streams and shells, which seem to build an intermediate class between shells and streams. Finally, the sample of very young stellar streams, which could not be matched to a progenitor galaxy, even if the gas particles IDs are matched additionally, are an intriguing anomaly. A speculation to their formation may be that they are formed from gas already within the host galaxy, after star formation was triggered by a galaxy closely passing by.

### **Concluding Remarks About the Age and Metallicity of Galaxies and Their Stellar Shells and Streams**

In summary, stellar ages and metallicities of galaxies and of their tidal shells and streams play a major role as tracers of galaxy formation history. The age and metallicity grow with the stellar mass of a galaxy, which is known as the mass-metallicity and mass-age relation. Ages have an additional primary dependence on the morphological type, where disk galaxies are younger than spheroidal galaxies. Even more insight is gained by studying the spatially resolved ages and metallicities in the form of radial profiles. Spheroids are old – with a slight decrease towards the center – whereas disks are older in the center compared to higher radii. These age gradients (positive age gradient in spheroids, negative age gradient in disks) point towards an “outside-in” and “inside-out” progression of star formation, respectively. Metallicity gradients, on the other hand, are in general negative, which suggests the “inside-out” growth. By splitting the stars into an old and a young component, the separated metallicity gradients reveal even more details about galaxy formation. Adding a second tracer of galaxy formation and their accretion history, namely stellar shells and streams, and analyzing their age and metal content, extends the picture even further. Opposed to the inference of the formation history from age gradients, the difference in age between the tidal features and their surroundings is not significant. However, their metallicity is different from their surroundings. Shells are more metal-rich, while streams are metal-poor compared to their environment. This is likely related to the mass-metallicity relation because stream progenitors are less massive than shell progenitors, and therefore also less metal-rich. Observationally, the global and spatially resolved ages and metallicities of galaxies and their tidal features can be measured by utilizing stellar population synthesis models and IFU surveys. With these new insights about the age and metallicity of galaxies and their stellar shells and streams from a cosmological simulation, the formation history of observed galaxies, shells, and streams can be further constrained. This will be useful for extending our knowledge about galaxies and their tidal features using new and exciting telescopes such as the upcoming Vera C. Rubin Observatory<sup>1</sup>, or the ESA ARRAKHIS mission<sup>2</sup>, which are set to observe low surface brightness features at an unprecedented depth.

---

<sup>1</sup><https://www.lsst.org/>

<sup>2</sup><https://www.cosmos.esa.int/web/call-for-missions-2021/selection-of-f2>

# Appendix A

## Different Options to Calculate Ages

The simulations output provides the scale factor  $a_{\text{form}}$  of the universe at which each stellar particle formed. A galaxy's age is calculated by first transforming  $a_{\text{form}}$  into the star's age (lookback time) and averaging over all stars within a sphere of radius  $3r_{1/2}$ . Averaging  $a_{\text{form}}$  first and transforming the mean formation scale factor into an age strongly correlates with the first method, presented in Figure A.1.

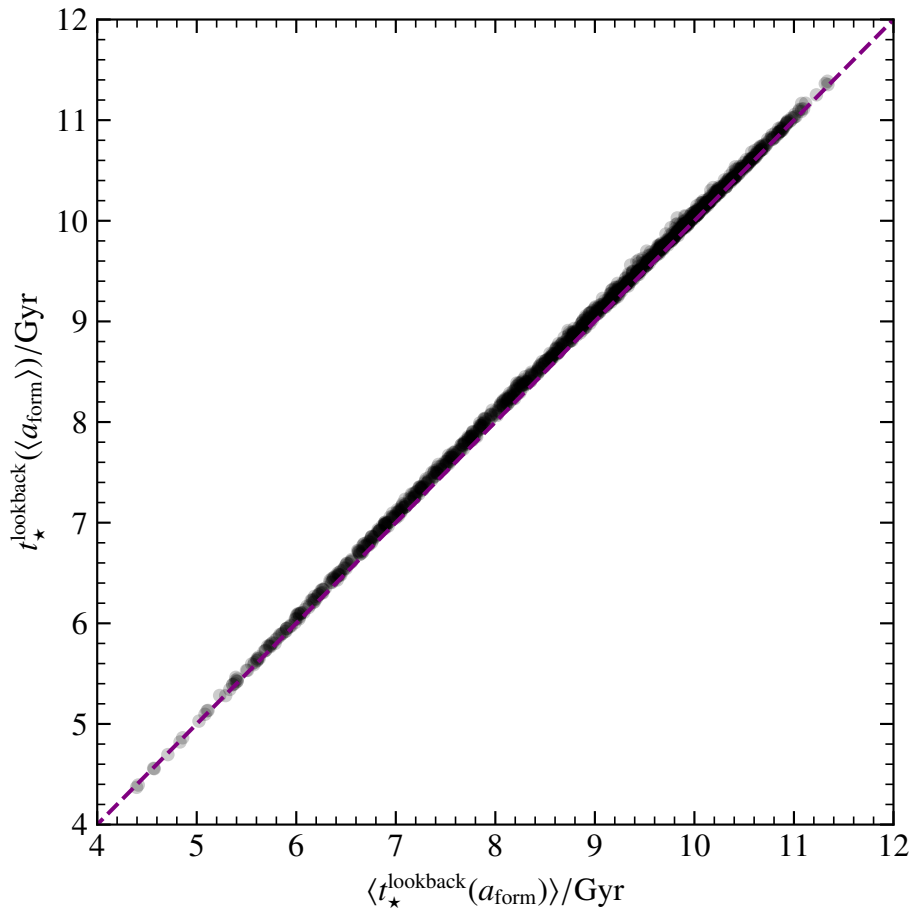


**Figure A.1:** Comparison between  $\langle t_{\star}^{\text{lookback}}(a_{\text{form}}) \rangle$  and  $t_{\star}^{\text{lookback}}(\langle a_{\text{form}} \rangle)$ .

# Appendix B

## $\Phi$ ZR

Sánchez-Menguiano et al. (2024) claim that the  $\Phi = \log_{10}(M_{\star}/M_{\odot}) - \alpha \log_{10}(r_{1/2}/\text{kpc})$  is the best predictor of the gas-phase metallicity  $Z_g$  of galaxies, where  $\alpha = 0.6$ . I tested this for the stellar mass-weighted metallicity  $\log_{10}(\langle Z/Z_{\odot} \rangle_{\text{mw}})$ . A quadratic function is fit to the relation using an orthogonal distance regression fit. The “predictability” is captured by the Pearson correlation coefficient  $p$  and the mean orthogonal distance  $\langle OD \rangle$ . Figure B.1 shows the  $\Phi$ ZR,  $\log_{10}(\langle Z/Z_{\odot} \rangle_{\text{mw}})$  as a function of  $\Phi$  for varying  $\alpha$ . The highest correlation is found for  $\alpha = 1.1$ , while the lowest scatter, as classified by the  $\langle OD \rangle$  is found for  $\alpha = 0.8$ .

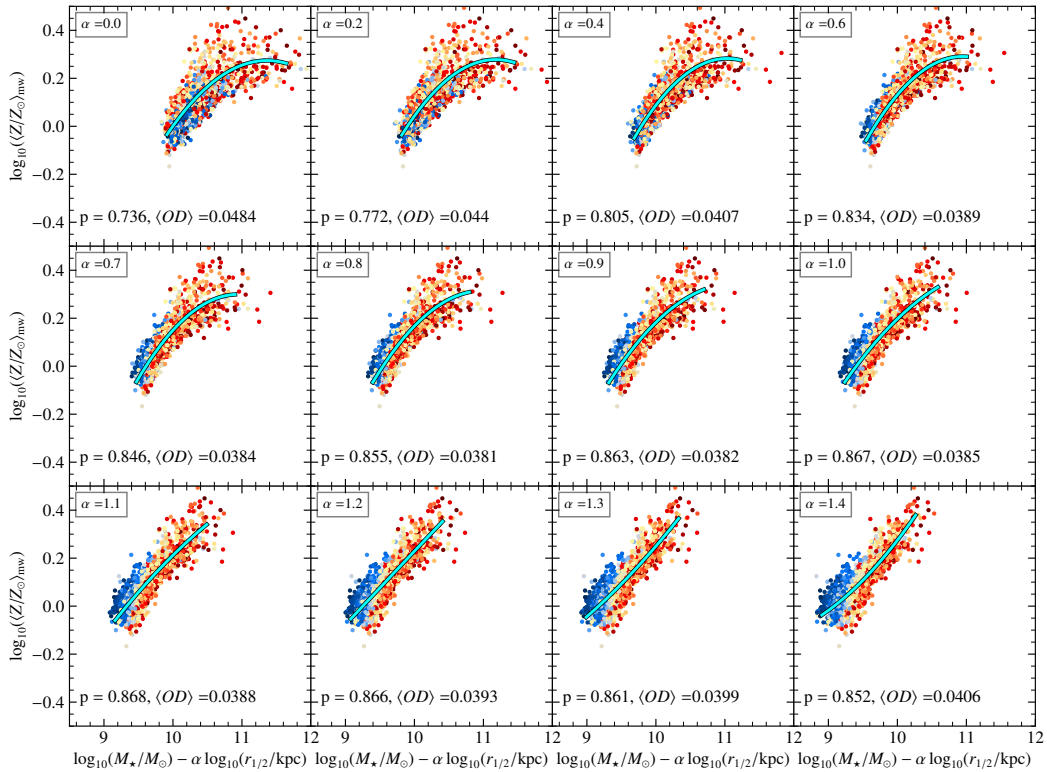


**Figure B.1:**  $\Phi$ ZR: Mass weighted mean metallicity  $\log_{10}(\langle Z/Z_{\odot} \rangle_{\text{mw}})$  as a function of  $\Phi = \log_{10}(M_{\star}/M_{\odot}) - \alpha \log_{10}(r_{1/2}/\text{kpc})$  for  $\alpha = 0.0$  to  $\alpha = 0.6$  in step of 0.2 and from there to  $\alpha = 1.4$  in steps of 0.1 (from the top left to the bottom right). The black line represents an orthogonal distance regression fit to a quadratic function. Shown in each panel is the Pearson correlation coefficient  $p$  and the mean orthogonal distance  $\langle OD \rangle$  as a measure for the scatter of the relation.

# Appendix C

## Stacked Metallicity Profiles and Resulting Gradients

The correlations of the metallicity gradient  $\nabla \log_{10}(\langle Z/Z_{\odot} \rangle_{lw})$  with global properties such as stellar mass  $M_{\star}$ , luminosity-weighted mean stellar age  $\langle t_{\star} \rangle_{lw}$ , and  $V/\sigma$ , as presented in Figure 3.21, can also be analyzed using a different approach, which holds more statistical power. It can be achieved by stacking the galaxies' particles within a certain bin within stellar mass, age or  $v/\sigma$  before calculating the metallicity gradient over all stacked particles combined. The bins of these properties were chosen so that each bin contains approximately the same number of stellar particles, not the same number of galaxies. The calculated bin edges  $e_j$  and number of galaxies per bin are presented in Table C.1. Figure C.1 to Figure C.12 show the stacked profiles in four bins. The *top row* shows disks, the *middle row* intermediates and the *bottom row* spheroids. Each panel displays the radial metallicity profile within 30 radial bins within  $3r_{1/2}$  (black line), a straight line fit to the profile (orange line), and the stacked particles as a 2D histogram. When fitting the straight line to calculate the metallicity gradient as its slope, the center needs to be excluded because of the limited spatial resolution. The radius where the fit starts is chosen to be the radius at which 50% of the galaxies'  $r_{1/2}$  is larger than 1.5 kpc. Then there are four versions of the stacked profiles for each property. ① luminosity-weighted metallicity, fit up to  $1r_{1/2}$  ② mass-weighted metallicity, fit up to  $1r_{1/2}$ , ③ luminosity-weighted metallicity, fit up to  $3r_{1/2}$  ④ mass-weighted metallicity, fit up to  $3r_{1/2}$ . Finally, Figure C.13 shows the slopes within each bin are plotted as a function of the average stellar mass (*left column*), luminosity-weighted stellar age (*middle column*), and  $V/\sigma$  (*right column*). Also shown are observed metallicity gradients from stacked spectra from MaNGA (Neumann et al., 2021). The results are strongly varying. For almost each combination of property and galaxy type, you can find a version where the gradient's absolute value is increasing and decreasing with the increasing property. For example, while the luminosity-weighted metallicity gradient measured within  $1r_{1/2}$  becomes more negative with increasing mass, the luminosity-weighted metallicity gradient measured within  $3r_{1/2}$  is increasing for low masses and almost constant at high masses. Another example is the increasing luminosity-weighted metallicity gradient within  $1r_{1/2}$  with increasing  $V/\sigma$ , while the luminosity- and

mass-weighted metallicity gradient within  $3r_{1/2}$  is decreasing. It can be concluded, that the trends of metallicity gradients with global galaxy properties are dependent on the choice of luminosity- or mass-weighting, and even stronger depends on whether gradients are measured within  $1r_{1/2}$  or  $3r_{1/2}$ . The luminosity-weighted metallicity gradients measured within  $3r_{1/2}$  are also shown in Figure 3.21.

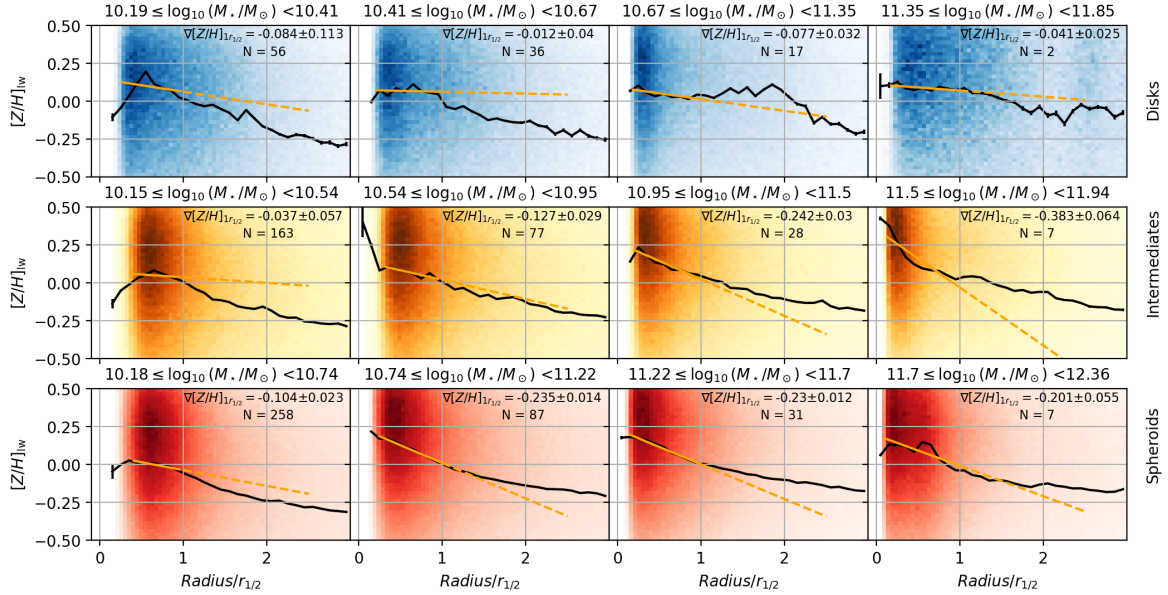


**Figure C.1:** Stacked luminosity-weighted metallicity profiles in stellar mass bins for disk (*top row*), intermediate (*middle row*), and spheroidal (*bottom row*) galaxies. The orange line shows a straight line fit to the profile within  $1r_{1/2}$ .

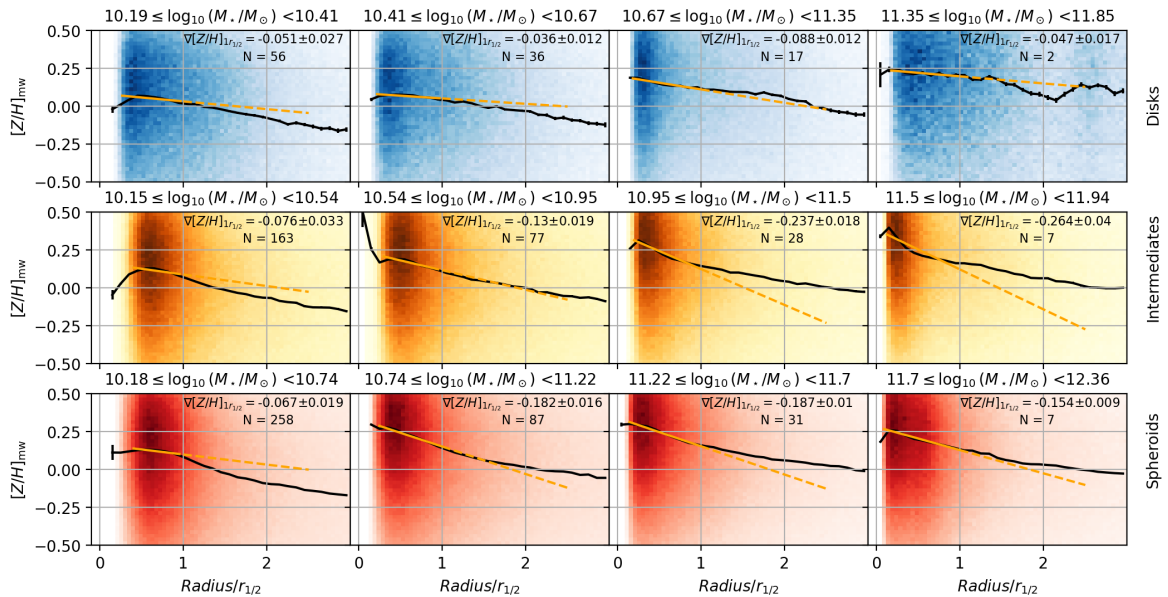


**Figure C.2:** Same as Figure C.1 using mass-weighted metallicities.

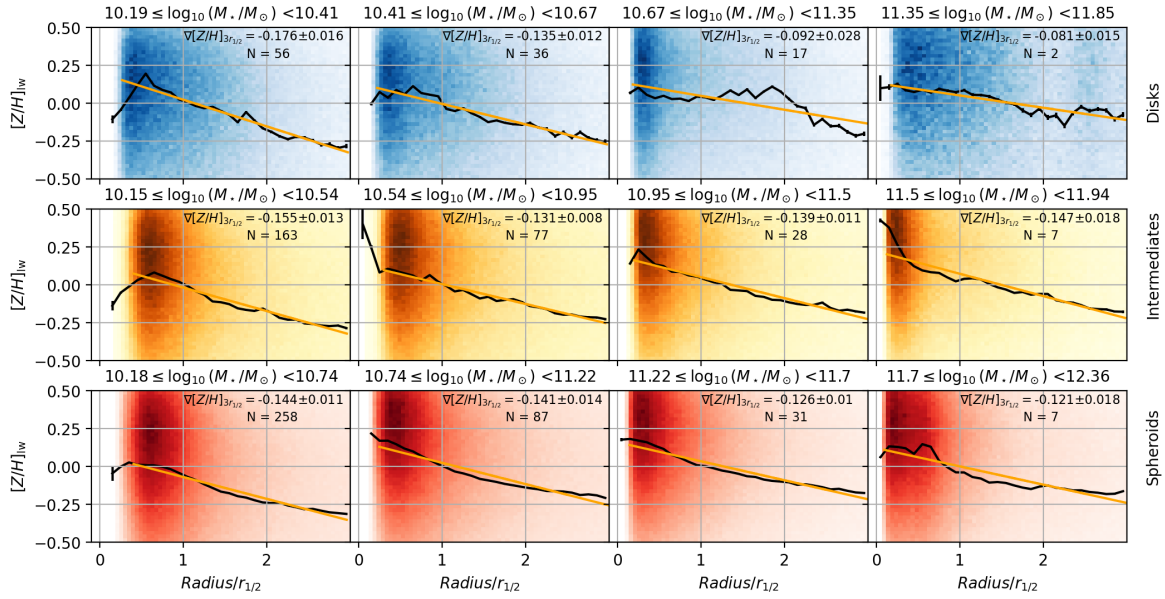


Figure C.3: Same as Figure C.1, fit to the profile within  $3r_{1/2}$ .

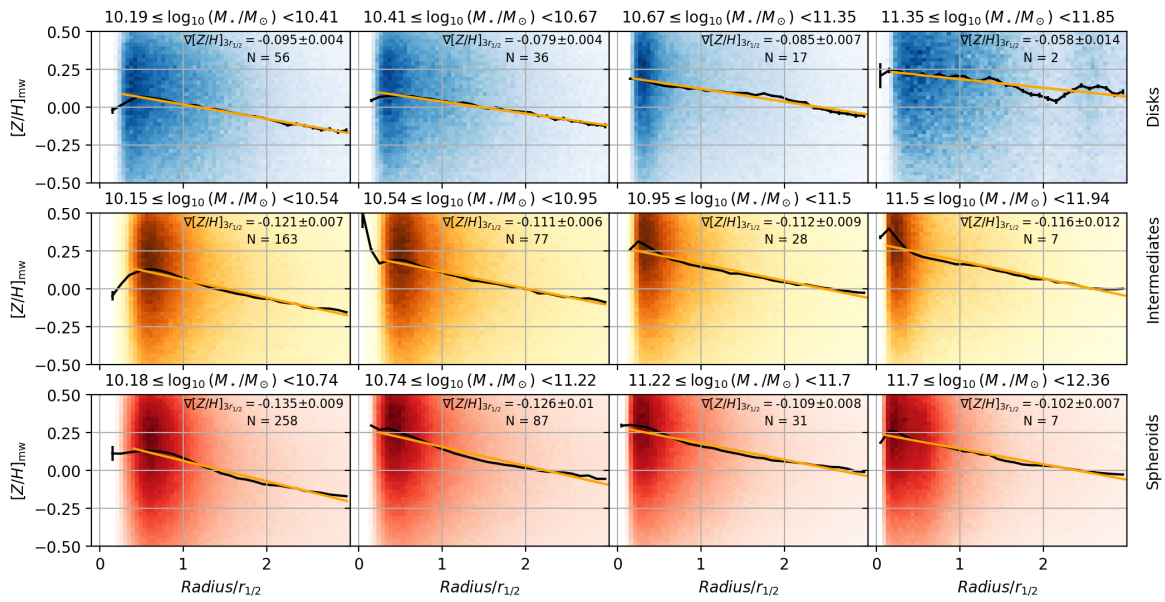
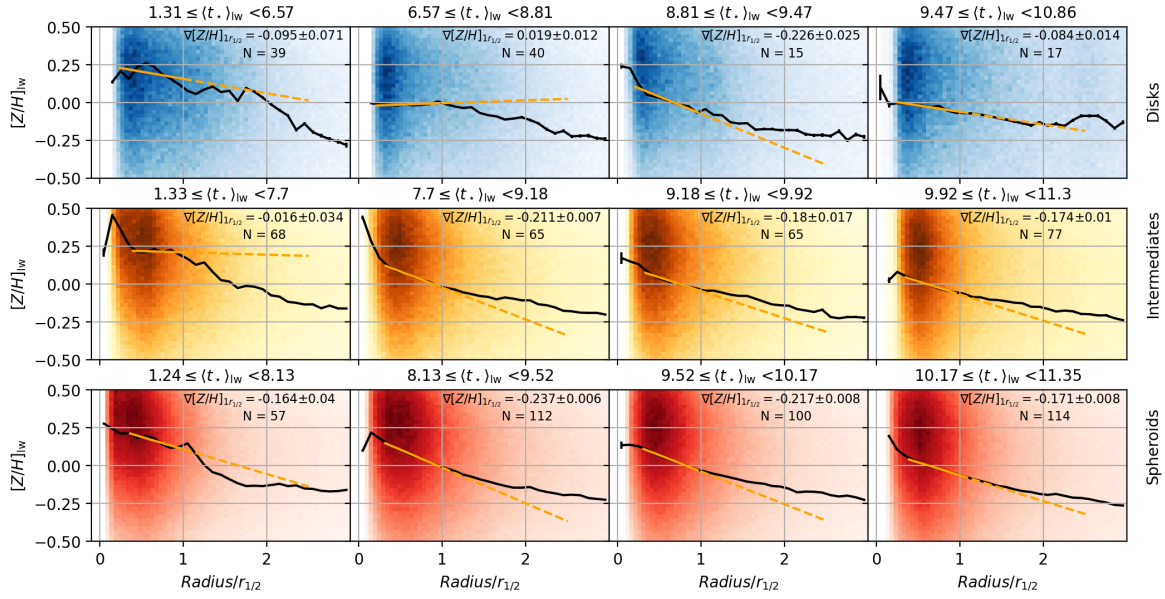


Figure C.4: Same as Figure C.1 using mass-weighted metallicities, fit to the profile within  $3r_{1/2}$ .

**Table C.1:** The calculated bin edges for  $\log_{10}(M_{\star}/M_{\odot})$ ,  $\langle t_{\star} \rangle_{\text{mw}}$ , and  $V/\sigma$  to stack galaxies together and calculate a combined metallicity gradient. The bin edges are chosen in a way so that each bin contains roughly the same number of stellar particles, which leads to a different number of galaxies per bin.

$\log_{10}(M_{\star}/M_{\odot})$				
Disks				
bin edges	[10.19,10.41]	[10.19,10.67]	[10.67,11.35]	[11.35,11.85]
$n_{\text{galaxies}}$	56	36	17	2
Intermediates				
bin edges	[10.15,10.54]	[10.54,10.95]	[10.95,11.5]	[11.5,11.94]
$n_{\text{galaxies}}$	163	77	28	7
Spheroids				
bin edges	[10.18,10.74]	[10.74,11.22]	[11.22,11.7]	[11.7,12.36]
$n_{\text{galaxies}}$	258	87	31	7
$\langle t_{\star} \rangle_{\text{lw}}/\text{Gyr}$				
Disks				
bin edges	[1.31,6.57]	[6.57,8.81]	[8.81,9.47]	[9.47,10.86]
$n_{\text{galaxies}}$	39	40	15	17
Intermediates				
bin edges	[1.33,7.7]	[7.7,9.18]	[9.18,9.92]	[9.92,11.3]
$n_{\text{galaxies}}$	68	65	65	77
Spheroids				
bin edges	[1.24,8.13]	[8.13,9.52]	[9.52,10.17]	[10.17,11.35]
$n_{\text{galaxies}}$	57	112	100	114
$v/\sigma$				
Disks				
bin edges	[0.32,0.62]	[0.62,0.86]	[0.86,1.12]	[1.12,2.07]
$n_{\text{galaxies}}$	11	36	30	34
Intermediates				
bin edges	[0.16,0.43]	[0.43,0.54]	[0.54,0.68]	[0.68,1.64]
$n_{\text{galaxies}}$	67	73	77	58
Spheroids				
bin edges	[0.09,0.16]	[0.16,0.24]	[0.24,0.43]	[0.43,1.07]
$n_{\text{galaxies}}$	115	87	120	61



**Figure C.5:** Stacked luminosity-weighted metallicity profiles in luminosity-weighted stellar age bins for disk (*top row*), intermediate (*middle row*), and spheroidal (*bottom row*) galaxies. The orange line shows a straight line fit to the profile within  $1r_{1/2}$ .

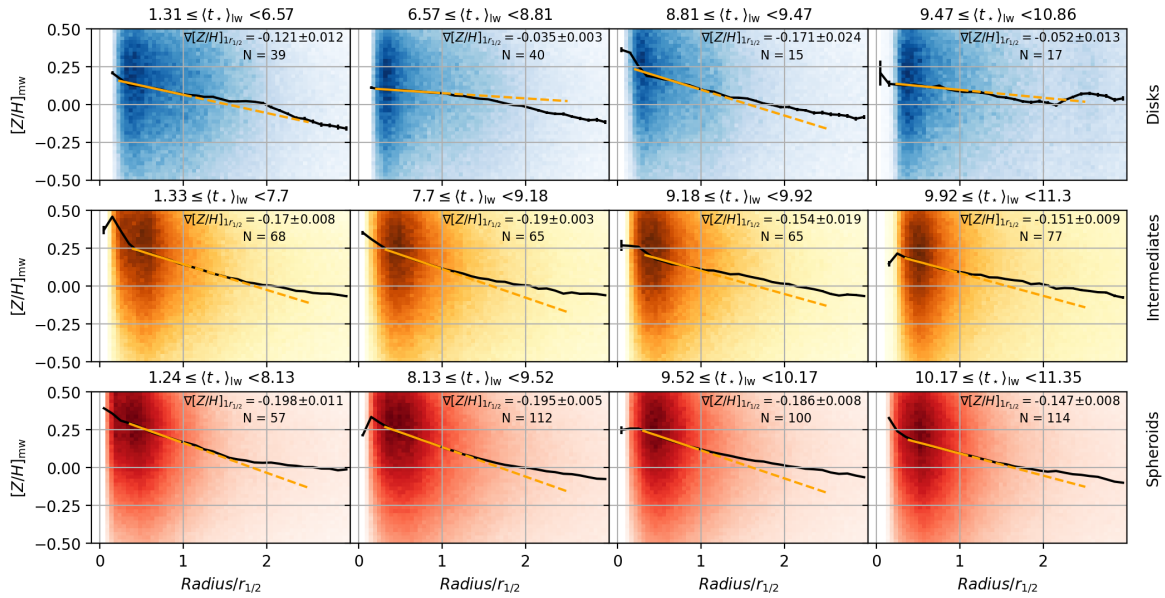


**Figure C.6:** Same as Figure C.5 using mass-weighted metallicities.

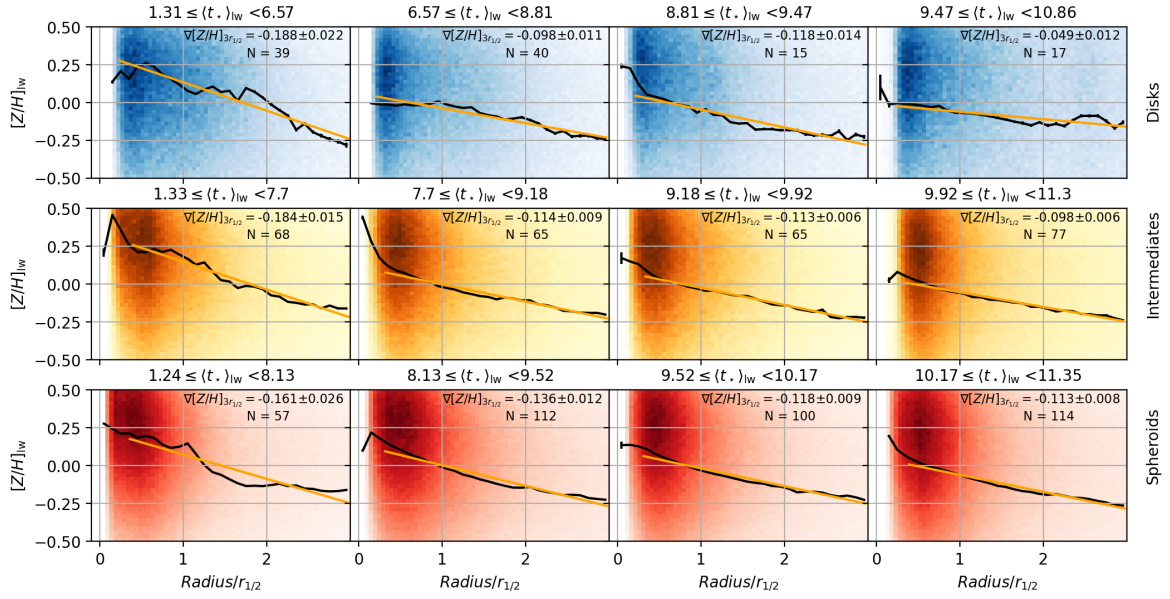


**Figure C.7:** Same as Figure C.5, fit to the profile within  $3r_{1/2}$ .

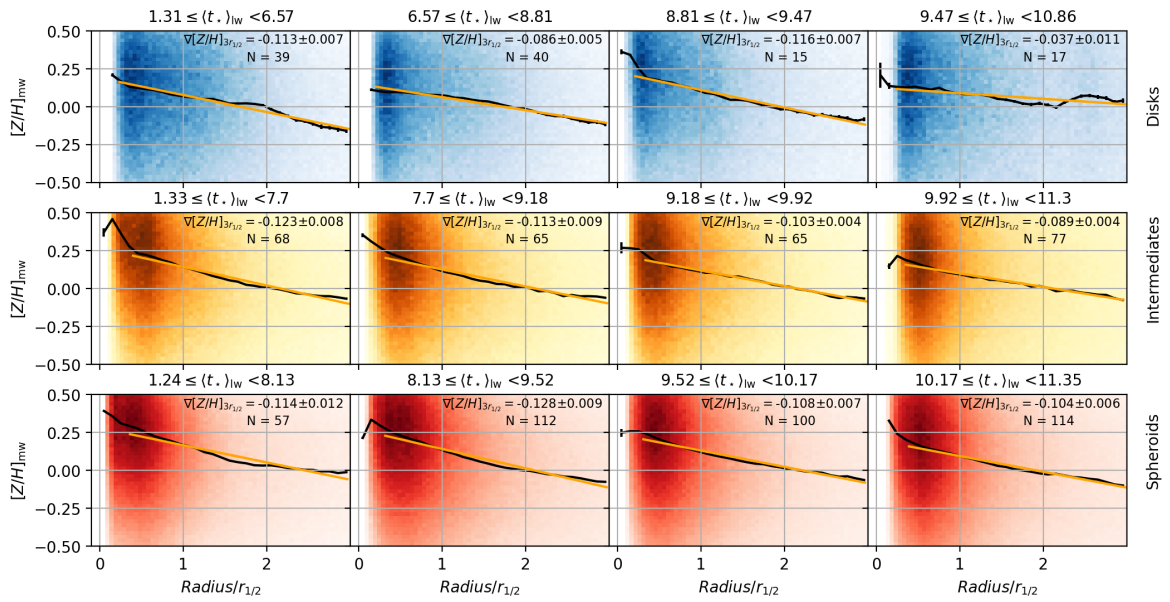


**Figure C.8:** Same as Figure C.5 using mass-weighted metallicities, fit to the profile within  $3r_{1/2}$ .

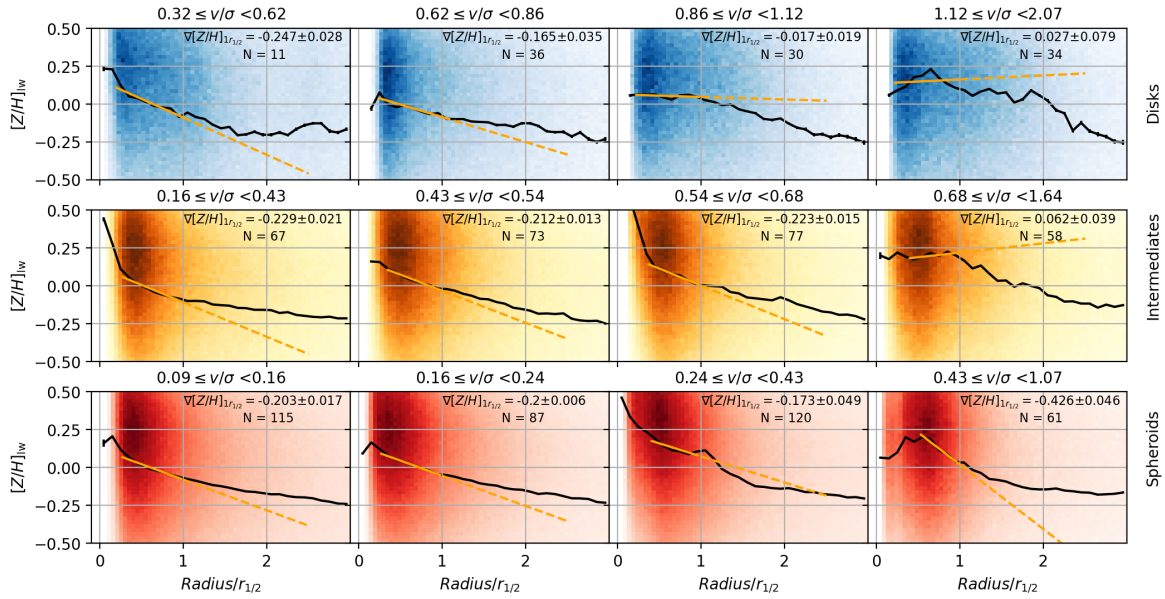


**Figure C.9:** Stacked luminosity-weighted metallicity profiles in  $V/\sigma$  bins for disk (*top row*), intermediate (*middle row*), and spheroidal (*bottom row*) galaxies. The orange line shows a straight line fit to the profile within  $1r_{1/2}$ .

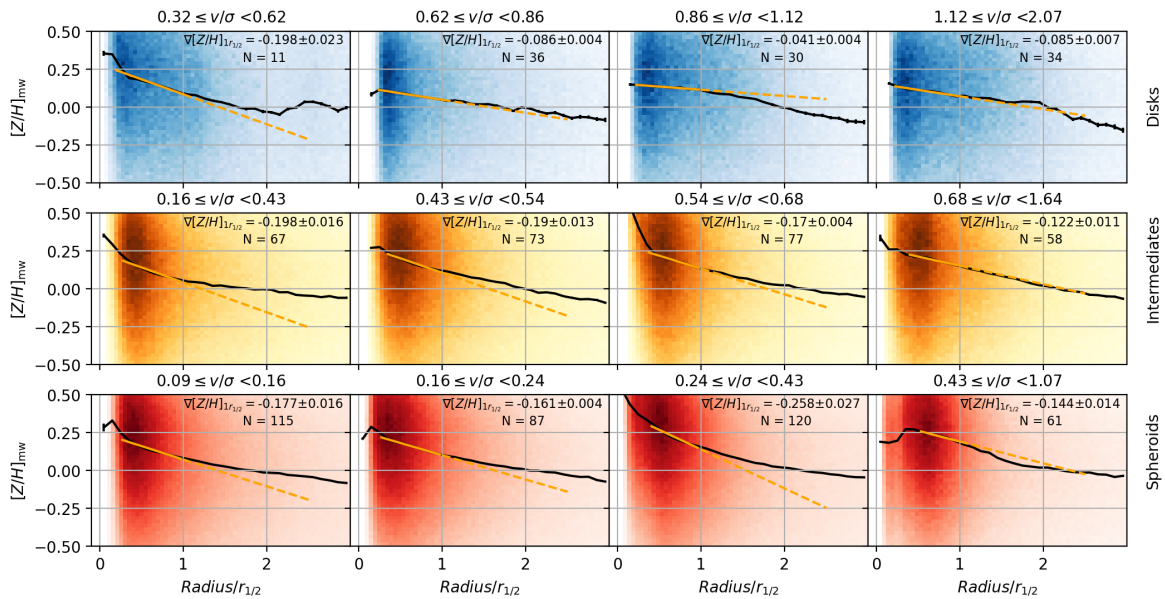


**Figure C.10:** Same as Figure C.9 using mass-weighted metallicities.

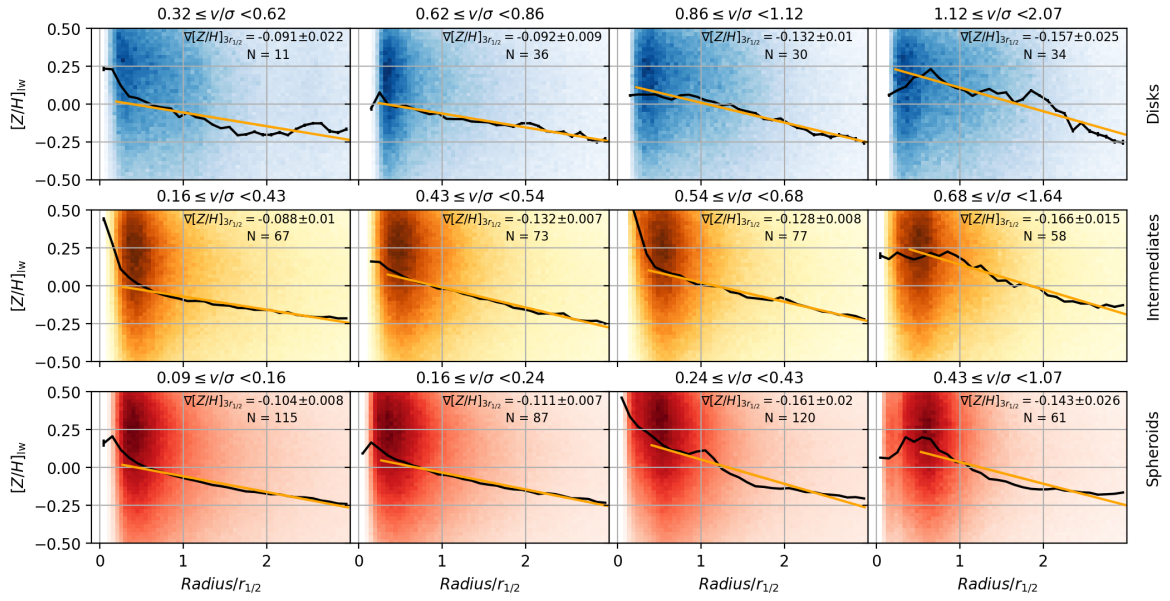


Figure C.11: Same as Figure C.5, fit to the profile within  $3r_{1/2}$ .

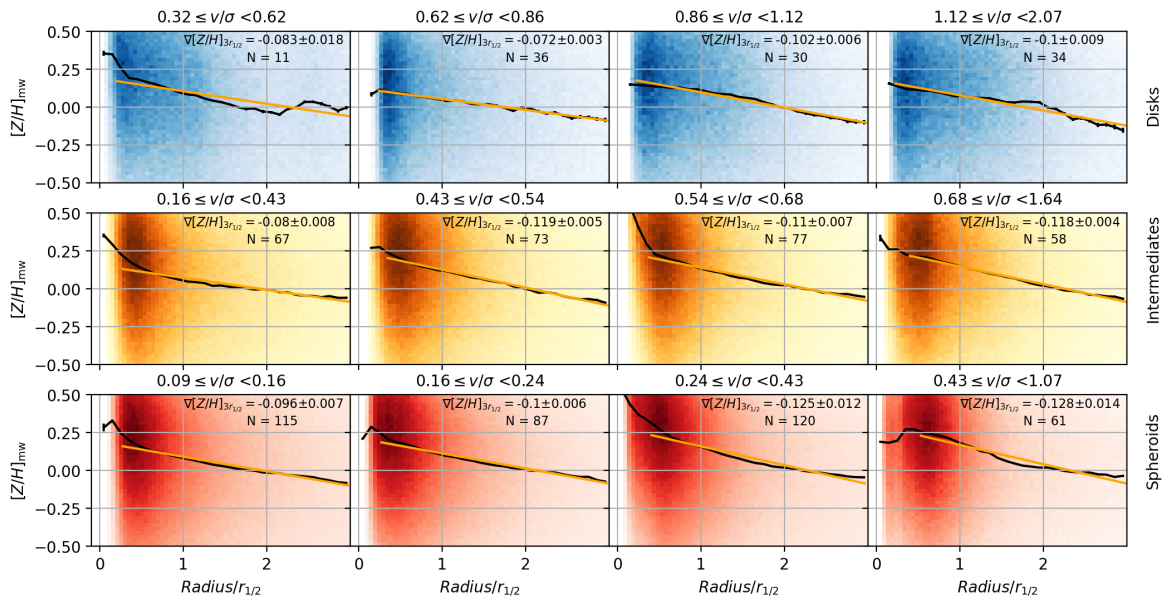
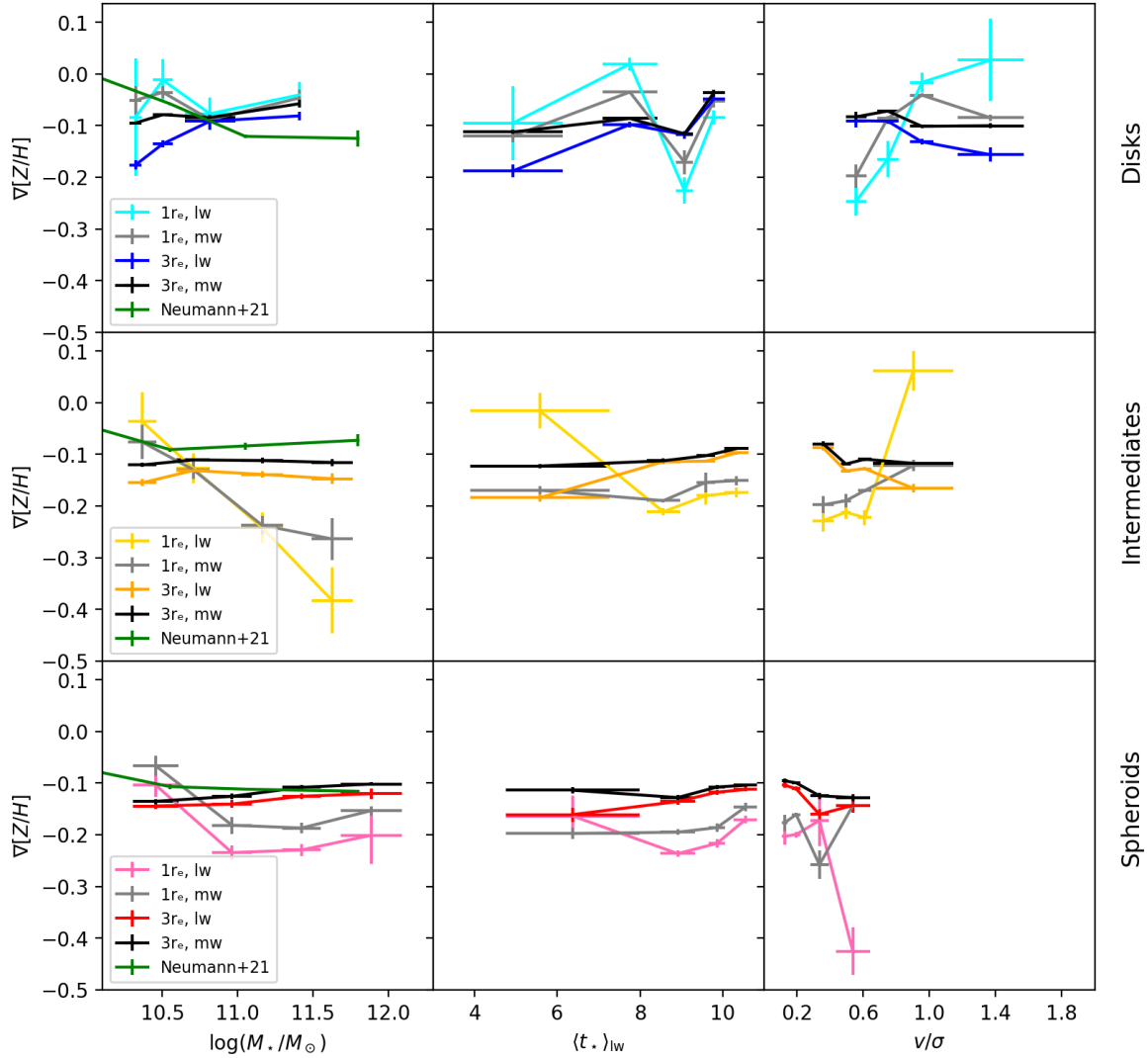


Figure C.12: Same as Figure C.9 using mass-weighted metallicities, fit to the profile within  $3r_{1/2}$ .



**Figure C.13:** Stacked metallicity gradients as a function of the average stellar mass (*left column*), luminosity-weighted stellar age (*middle column*), and  $V/\sigma$  (*right column*). Each panel depicts four different lines, which are the mass-weighted and luminosity weighted cases, where the gradient is measured within  $1r_{1/2}$  or  $3r_{1/2}$ . In the left column, observational results from Neumann et al. (2021) are overplotted.

# Appendix D

## Diagnostics Plots for Shells and Streams

This appendix includes all diagnostics plots for shells and streams. They are described in Figure 5.1 and 5.2.

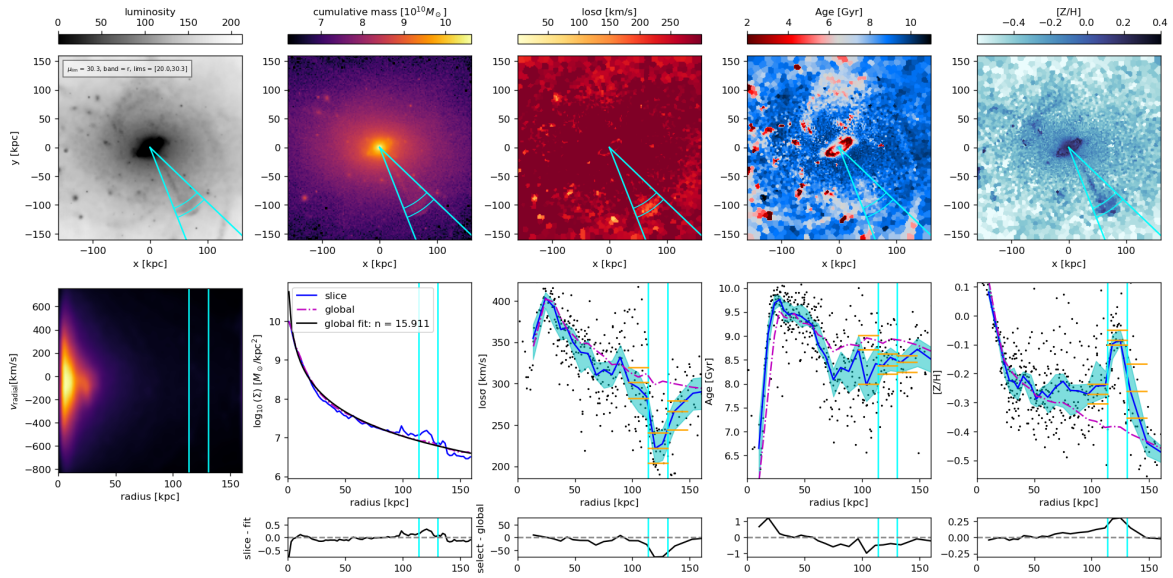


Figure D.1: UID 0, Shell 1

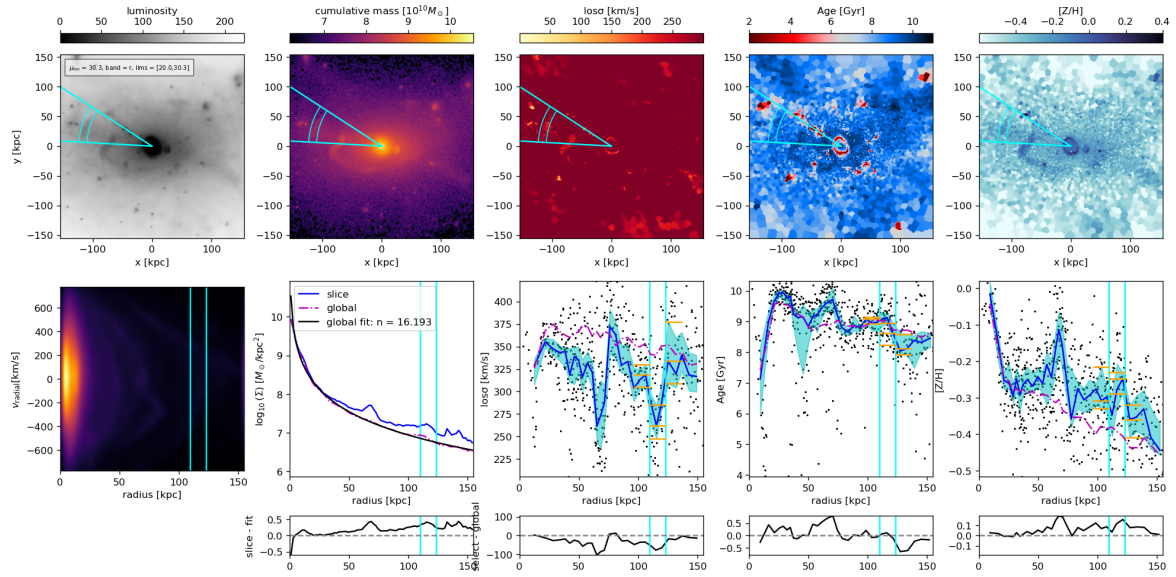


Figure D.2: UID 1414, Shell 1

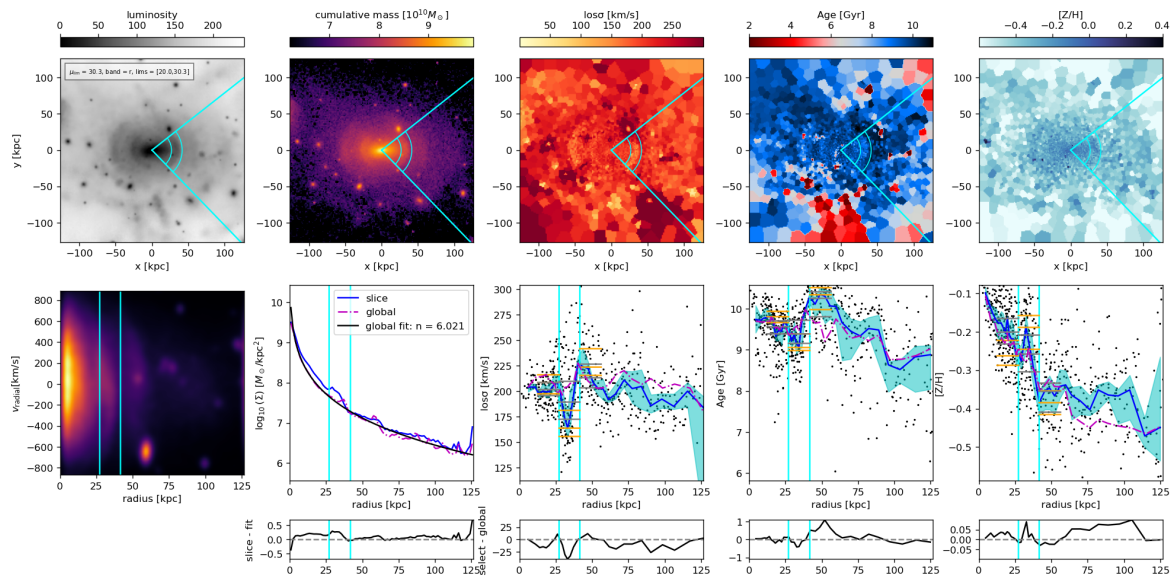


Figure D.3: UID 3968, Shell 1

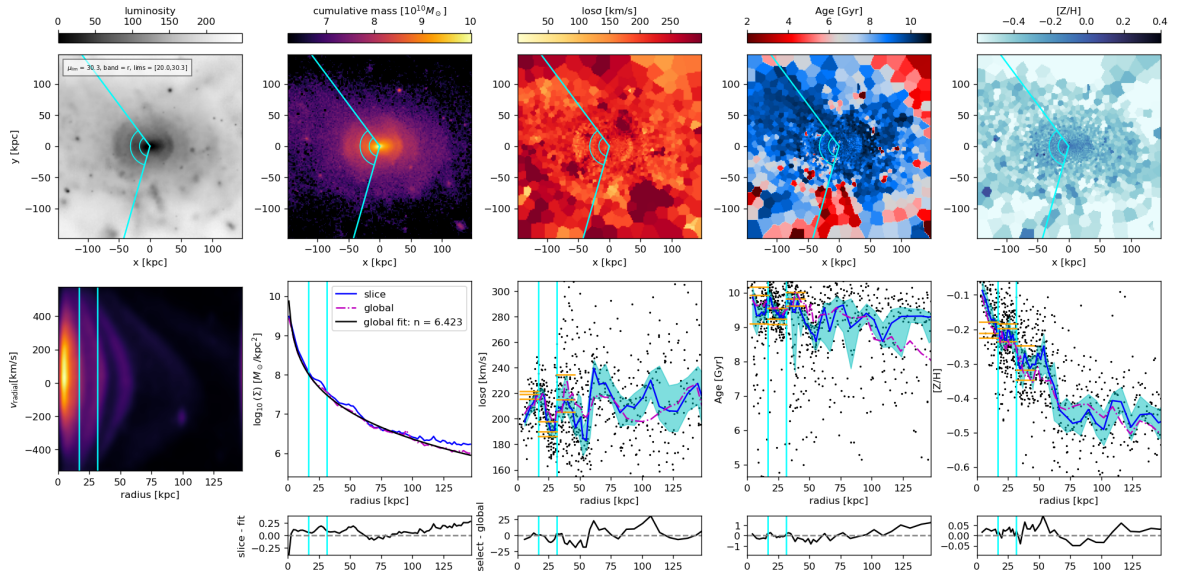


Figure D.4: UID 3968, Shell 2

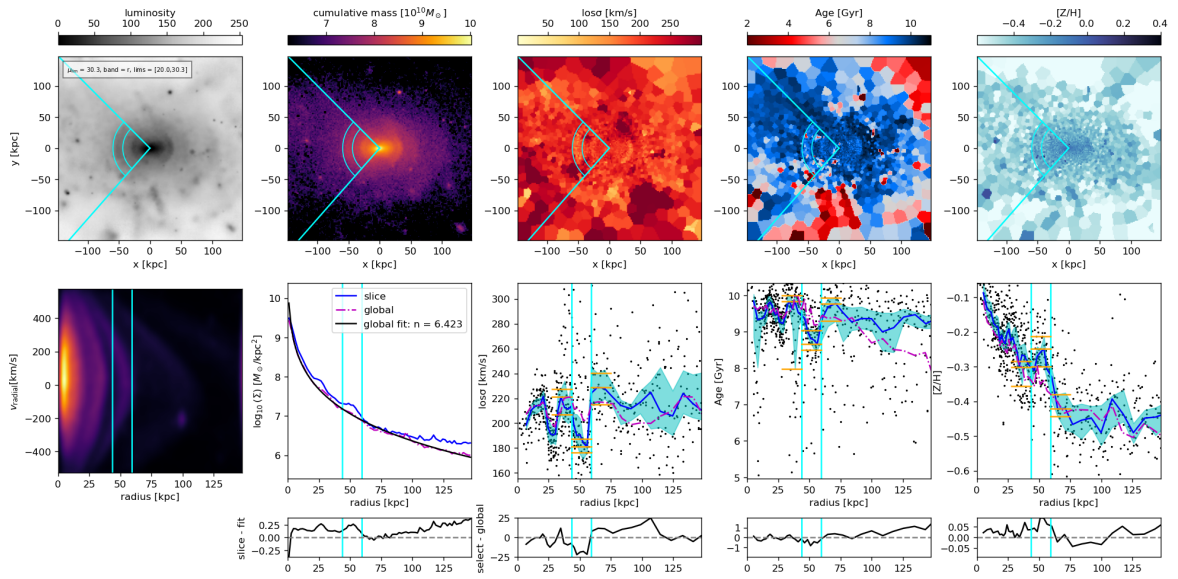


Figure D.5: UID 3968, Shell 3

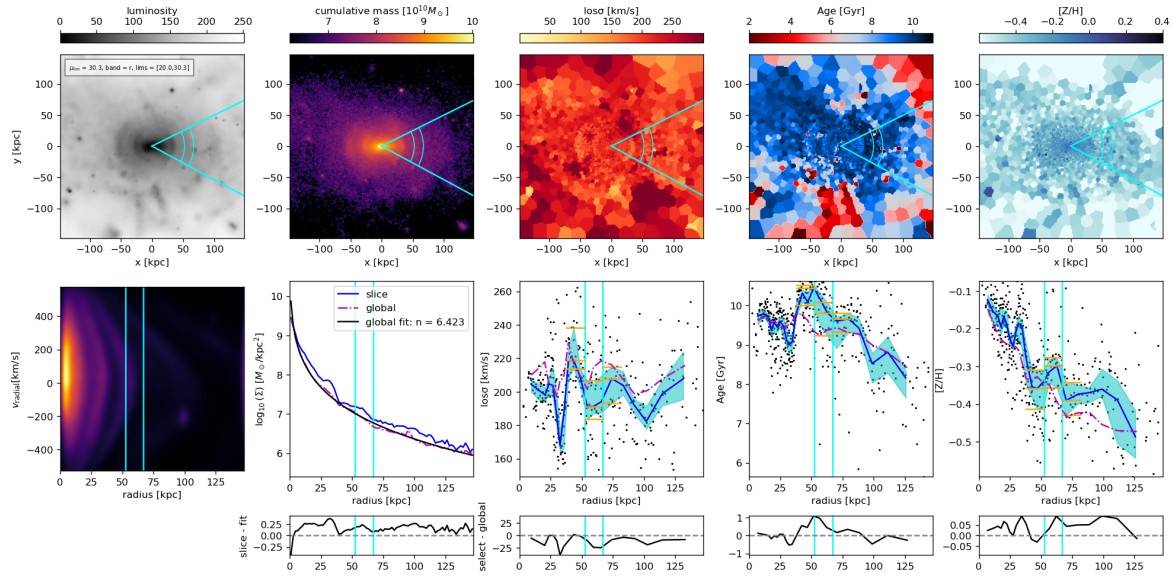


Figure D.6: UID 3968, Shell 4

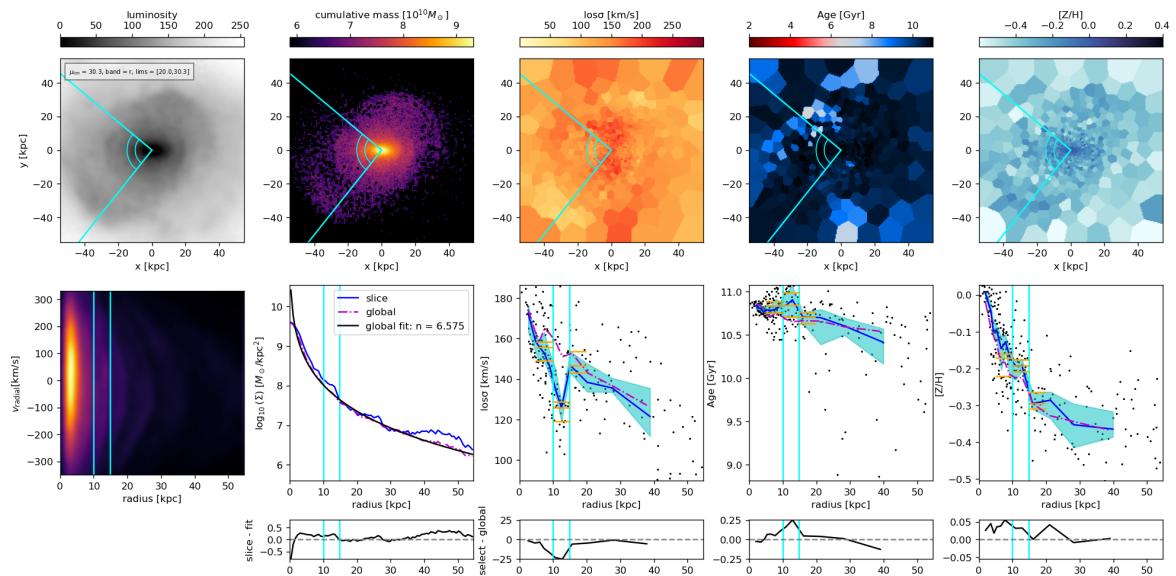


Figure D.7: UID 3970, Shell 1

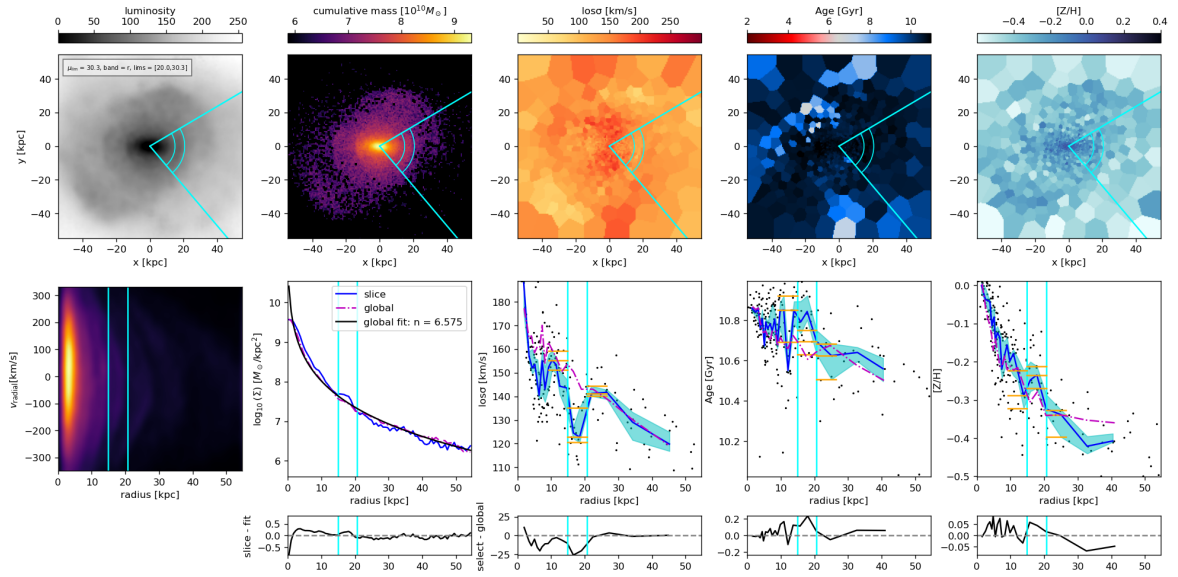


Figure D.8: UID 3970, Shell 2

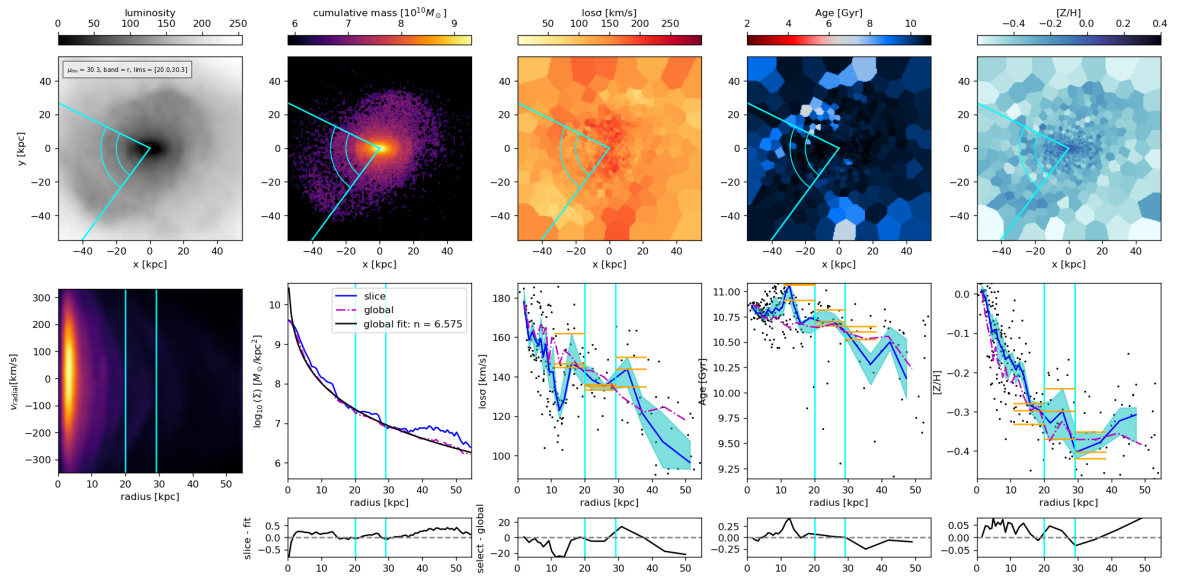


Figure D.9: UID 3970, Shell 3

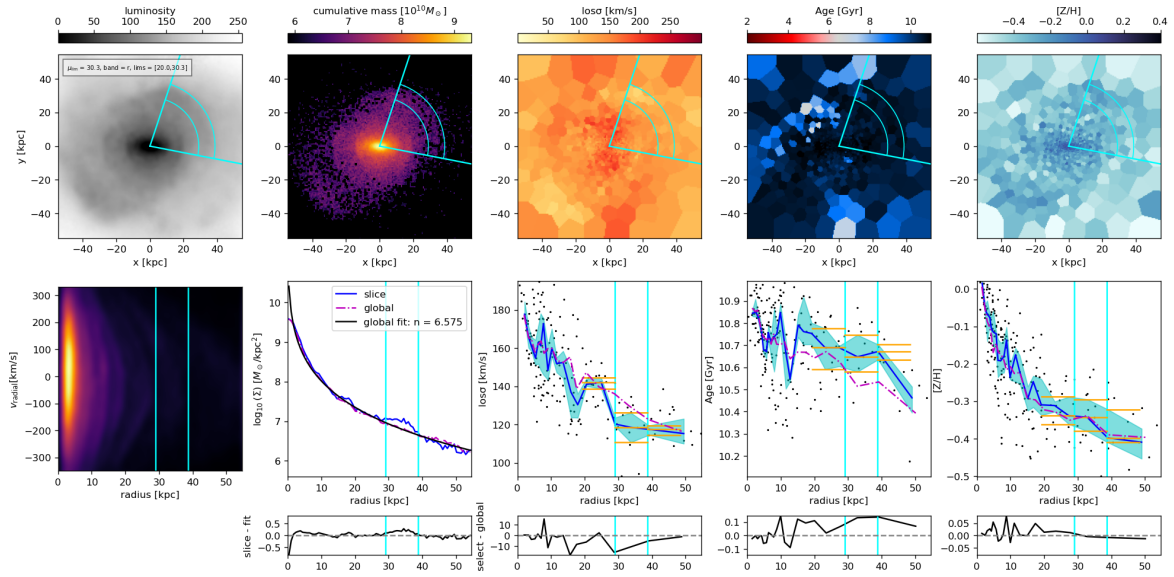


Figure D.10: UID 3970, Shell 4

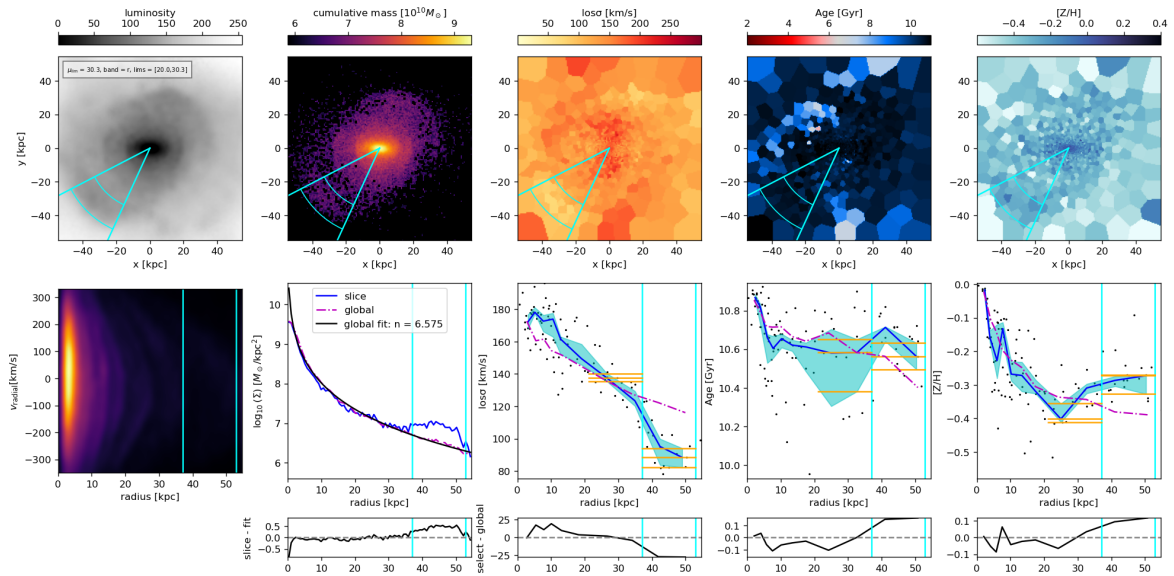


Figure D.11: UID 3970, Shell 5

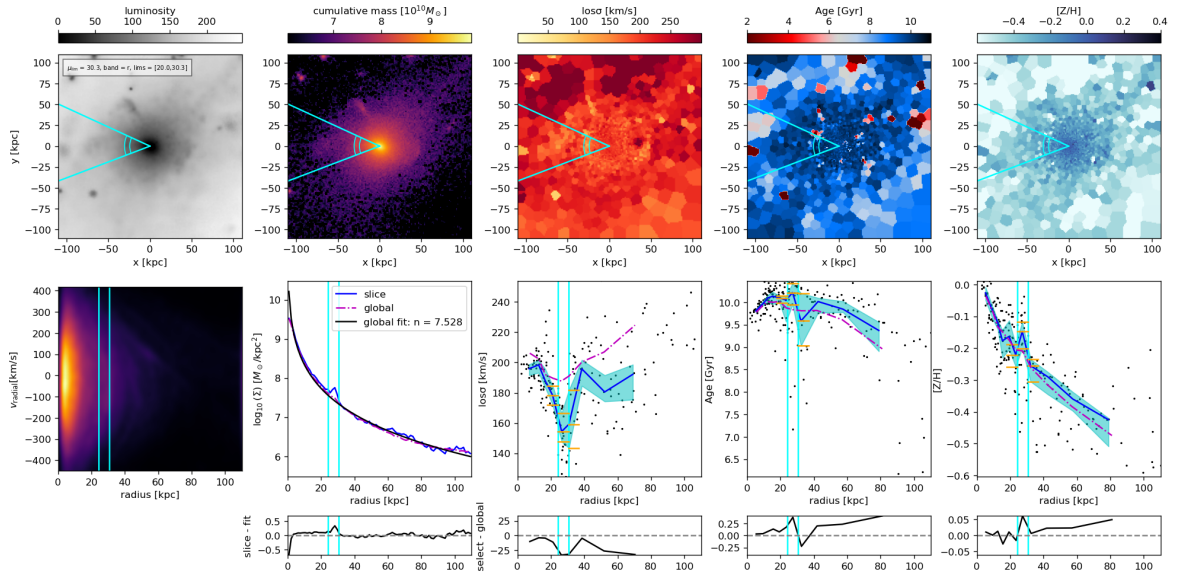


Figure D.12: UID 5416, Shell 1

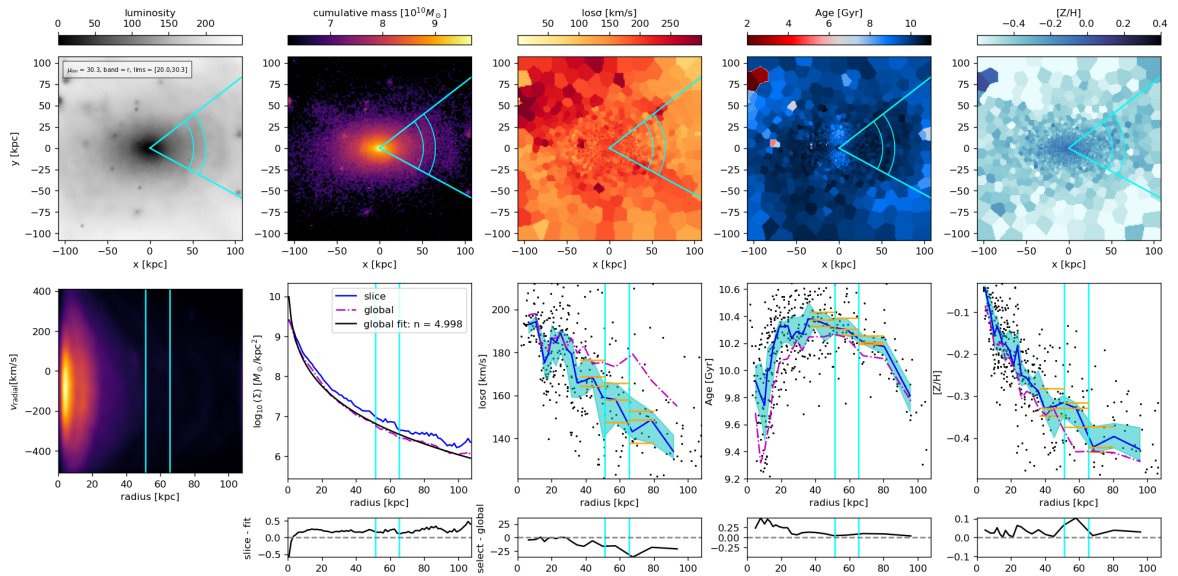


Figure D.13: UID 7186, Shell 1

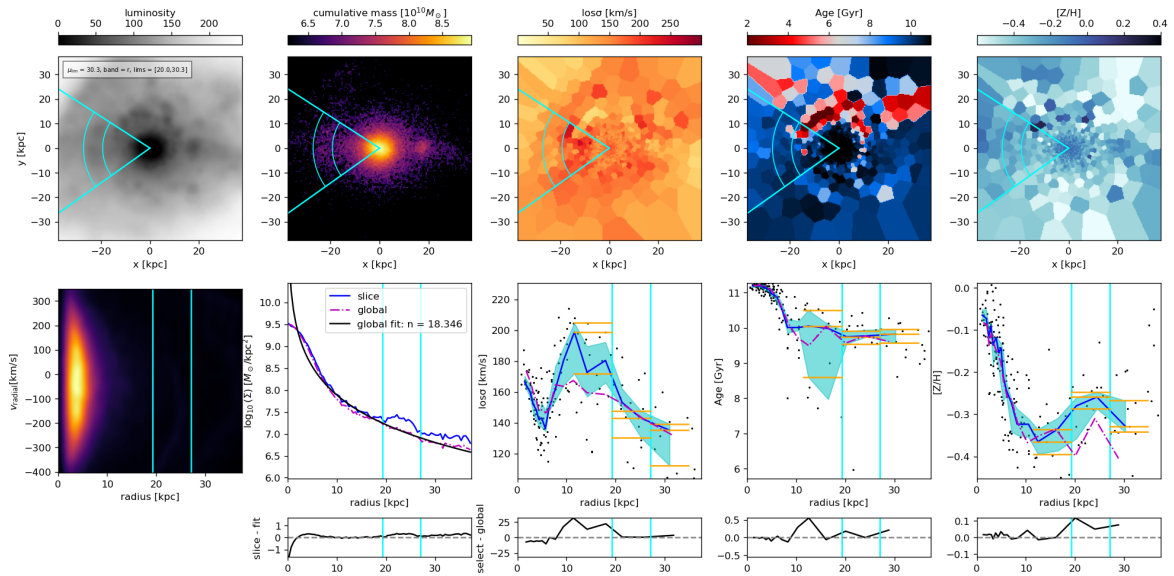


Figure D.14: UID 7903, Shell 1

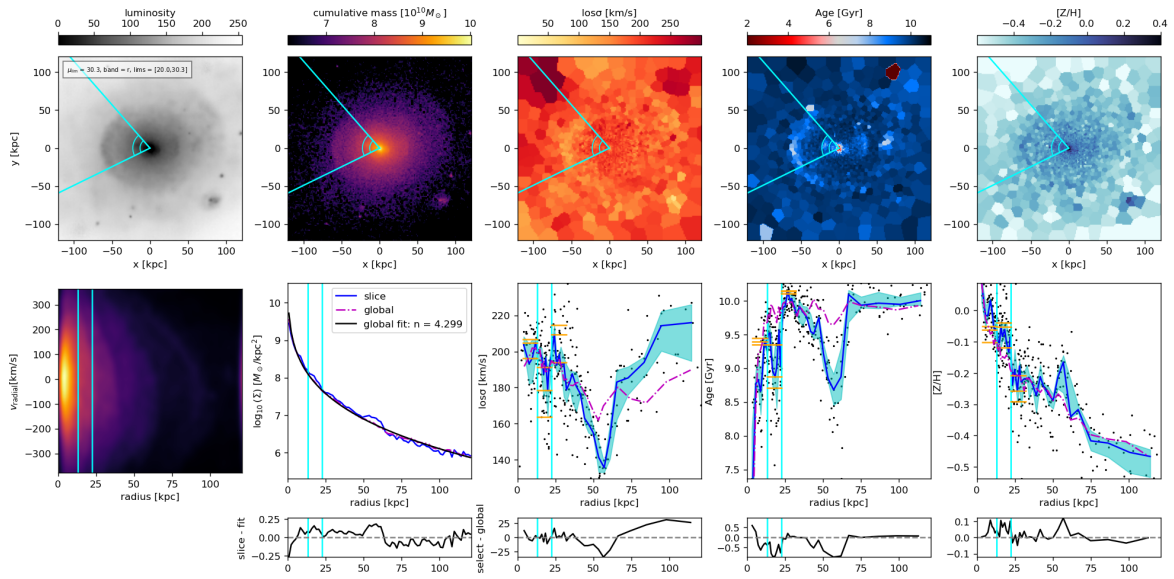


Figure D.15: UID 10053, Shell 1

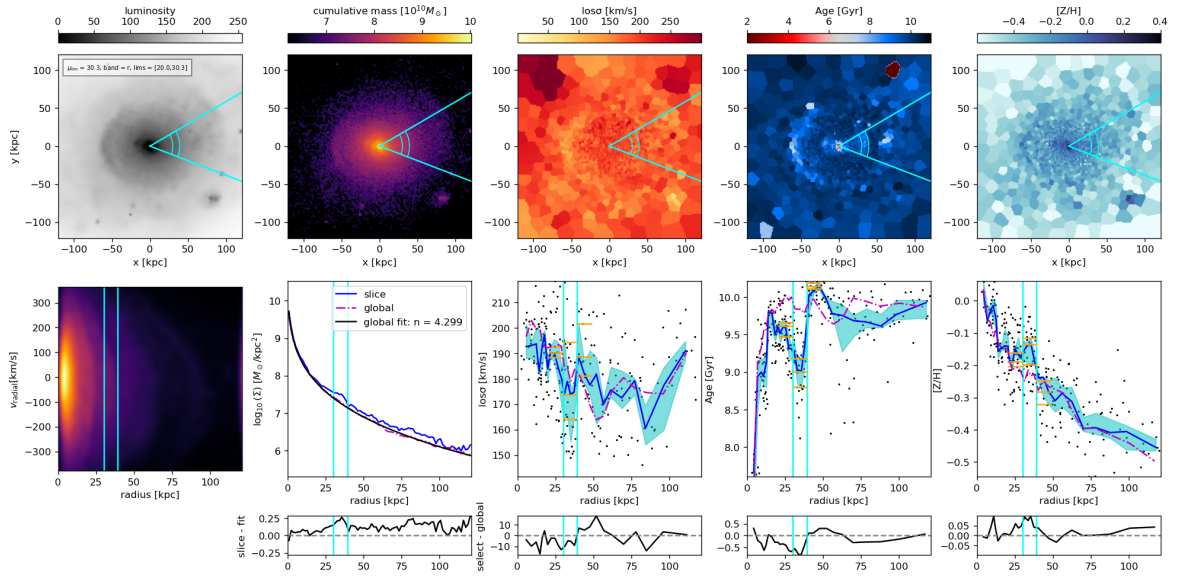


Figure D.16: UID 10053, Shell 2

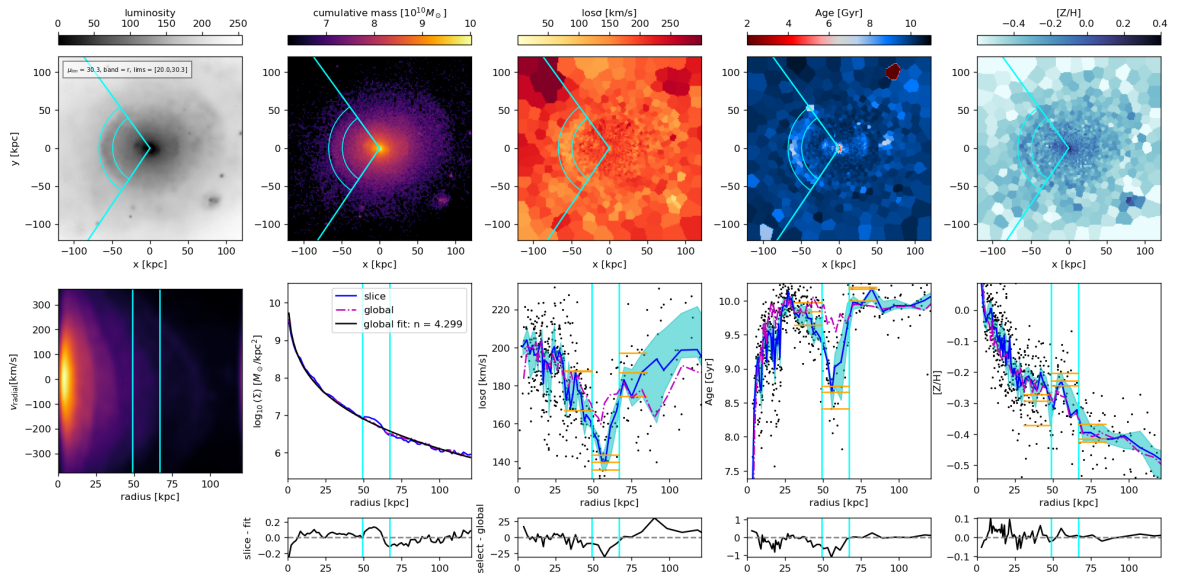


Figure D.17: UID 10053, Shell 3

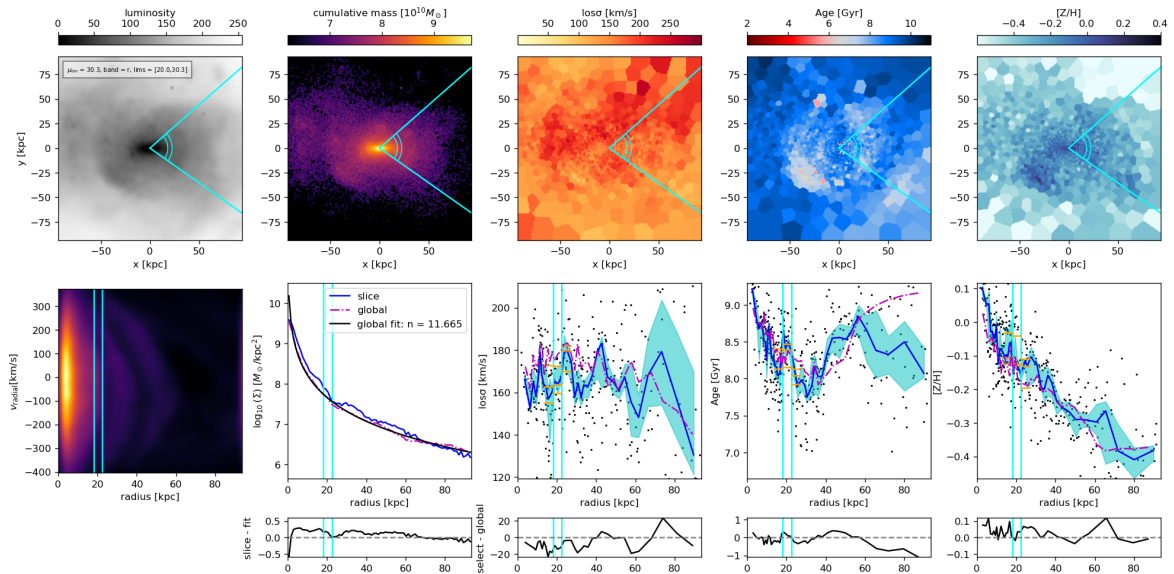


Figure D.18: UID 10541, Shell 1

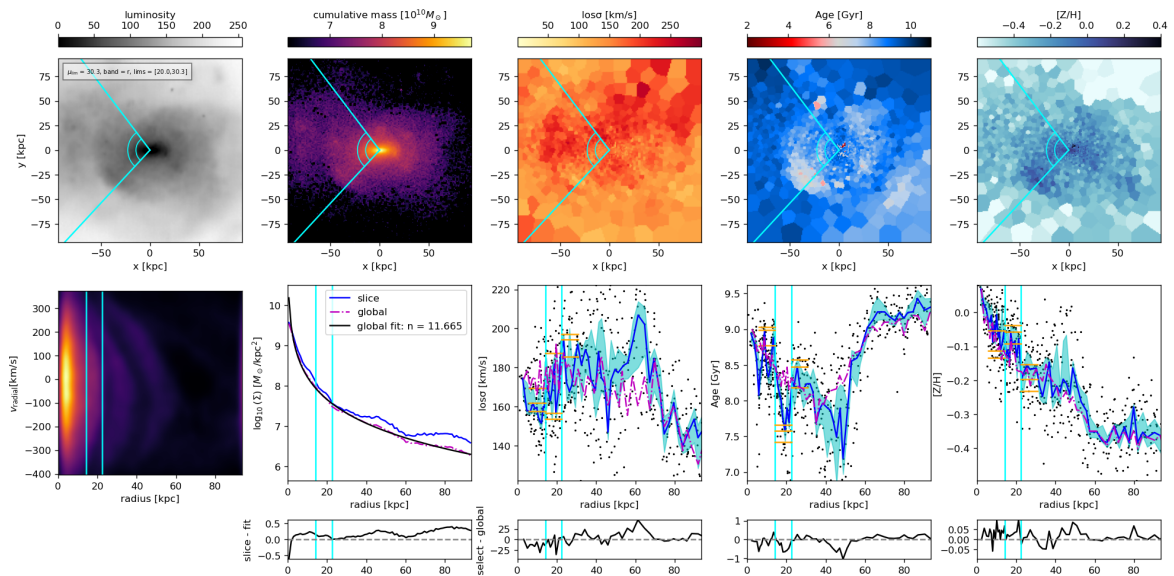


Figure D.19: UID 10541, Shell 2

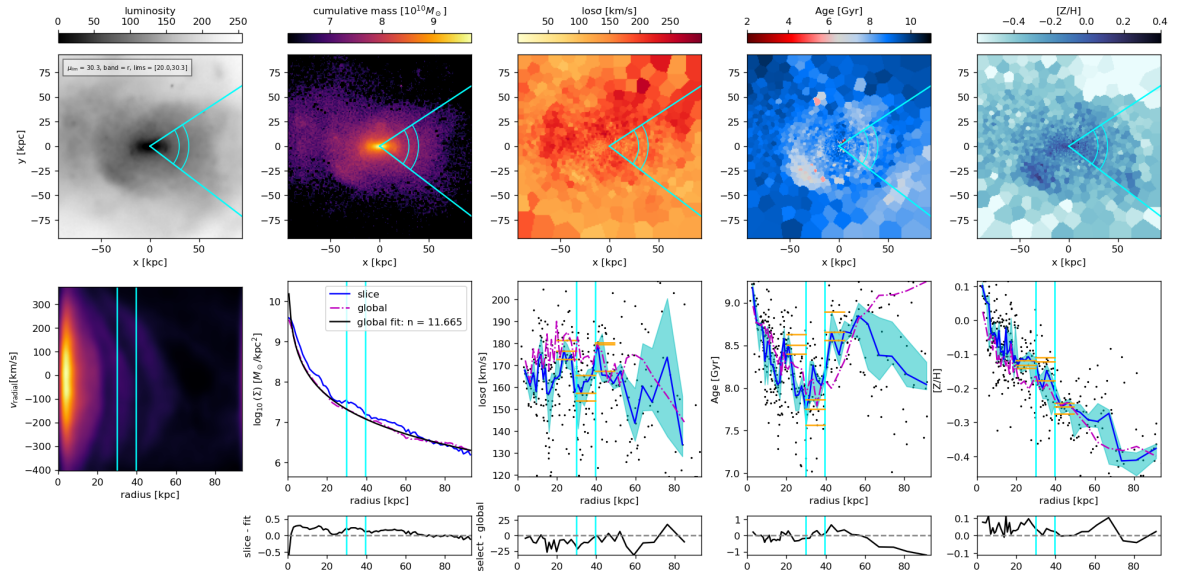


Figure D.20: UID 10541, Shell 3

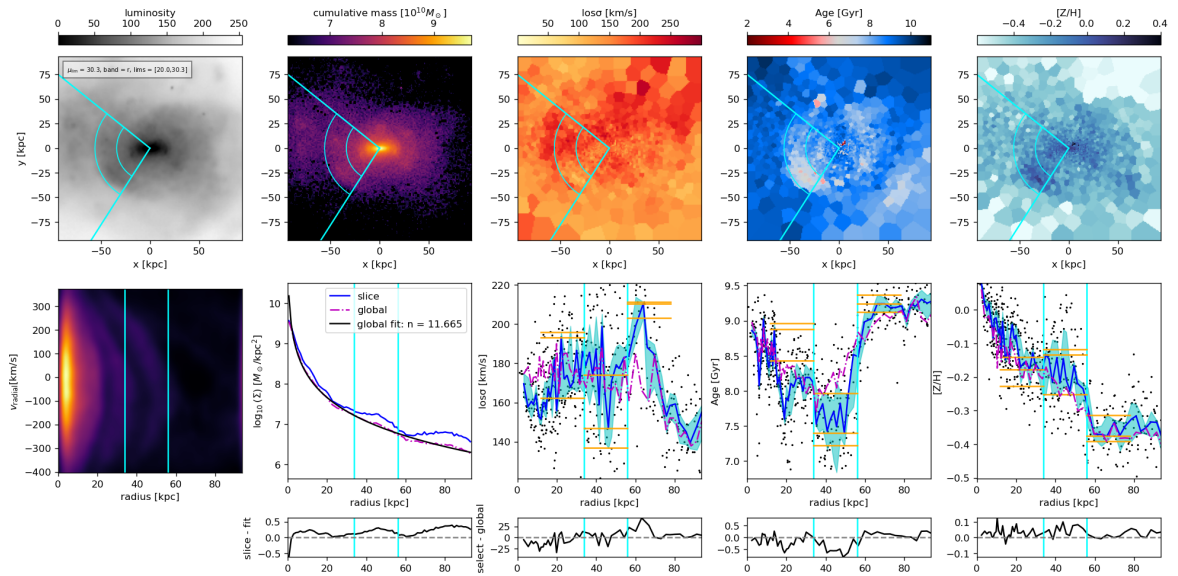


Figure D.21: UID 10541, Shell 4

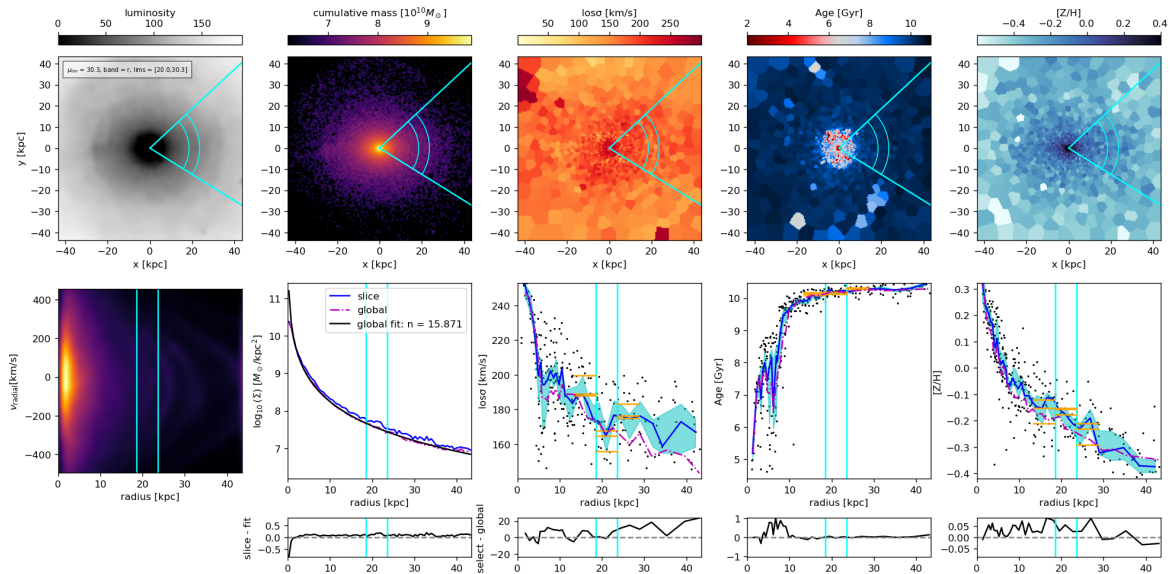


Figure D.22: UID 11651, Shell 1

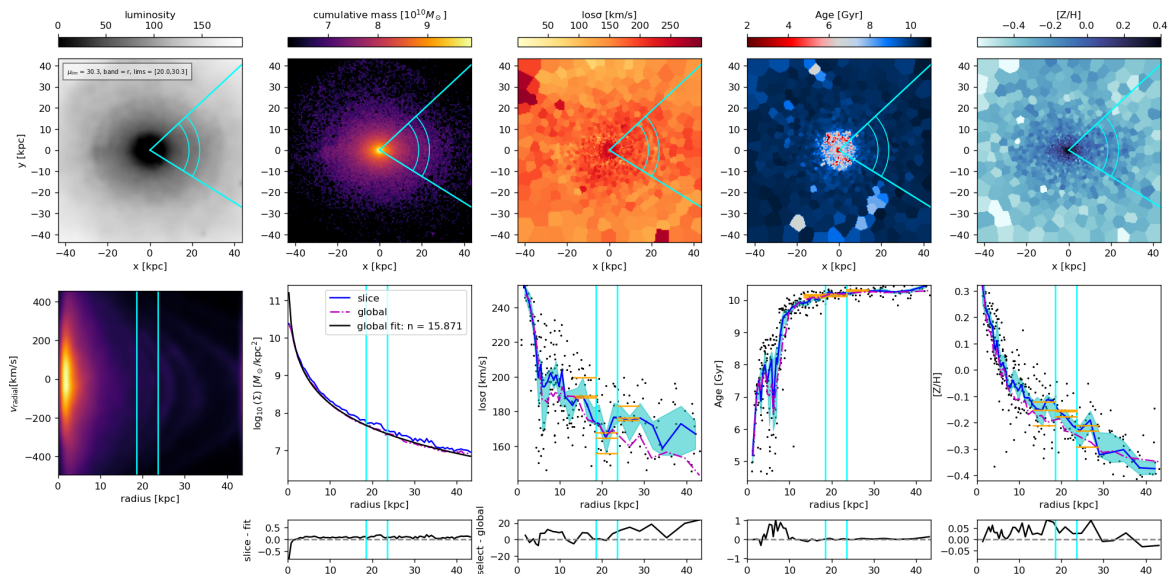


Figure D.23: UID 11651, Shell 1

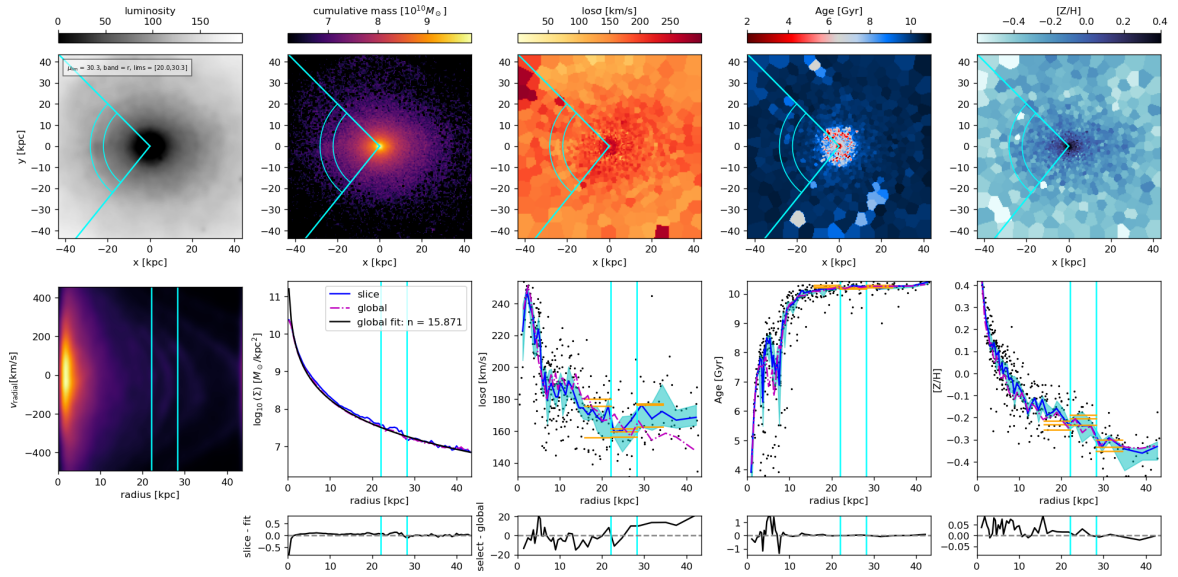


Figure D.24: UID 11651, Shell 2

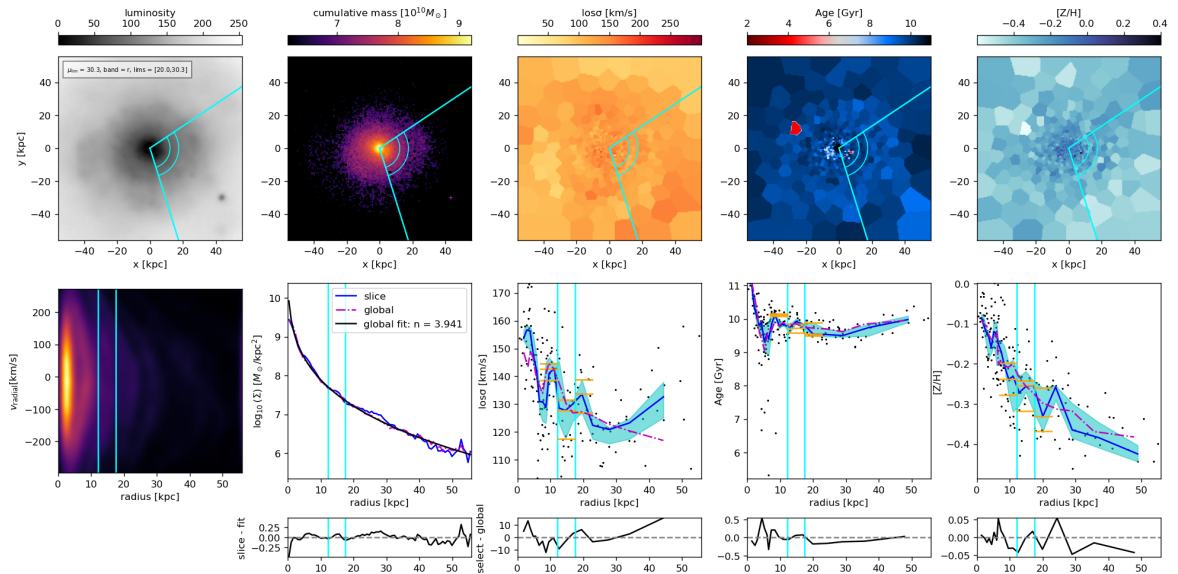


Figure D.25: UID 12433, Shell 1

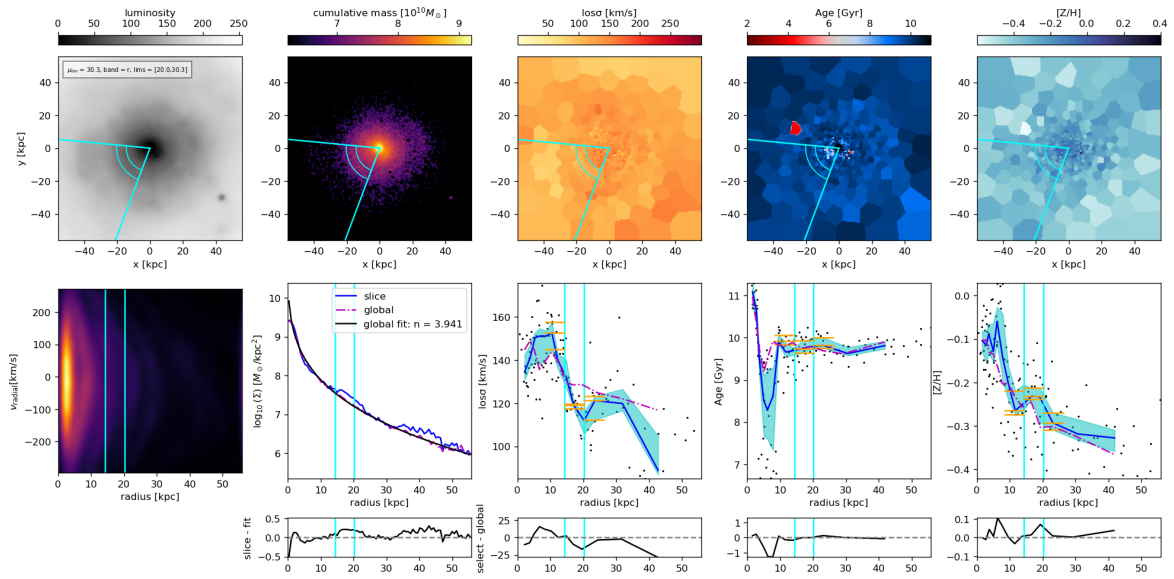


Figure D.26: UID 12433, Shell 2

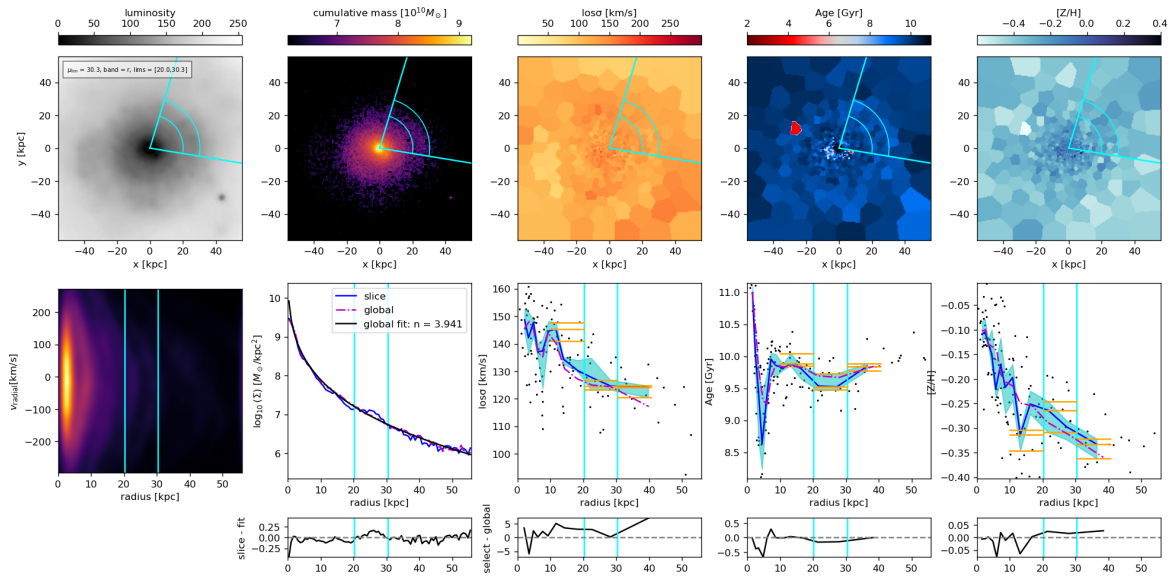


Figure D.27: UID 12433, Shell 3

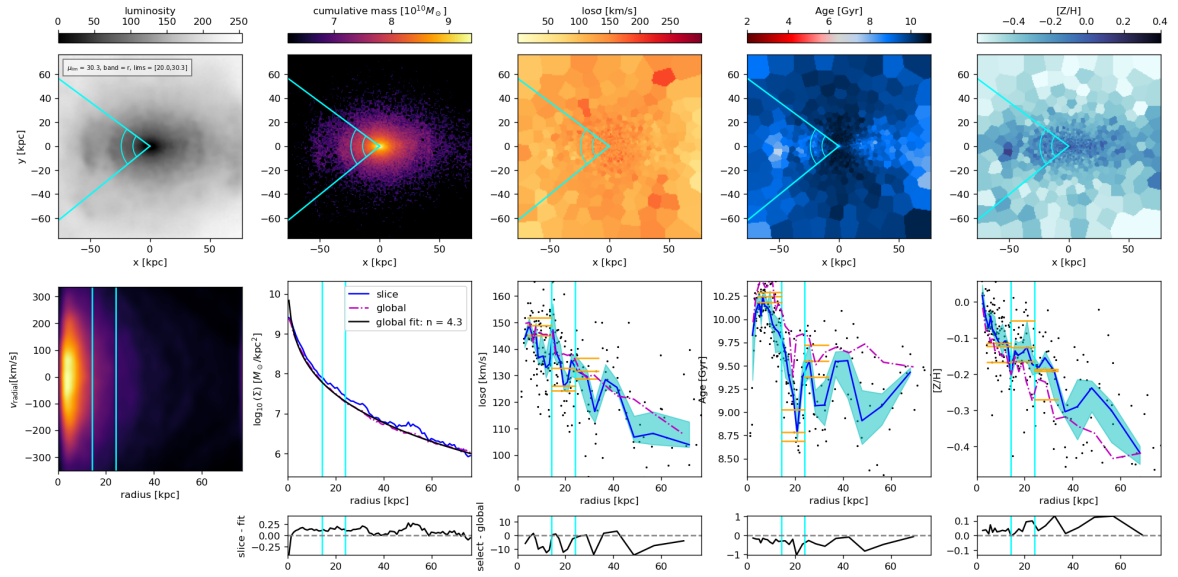


Figure D.28: UID 13500, Shell 1

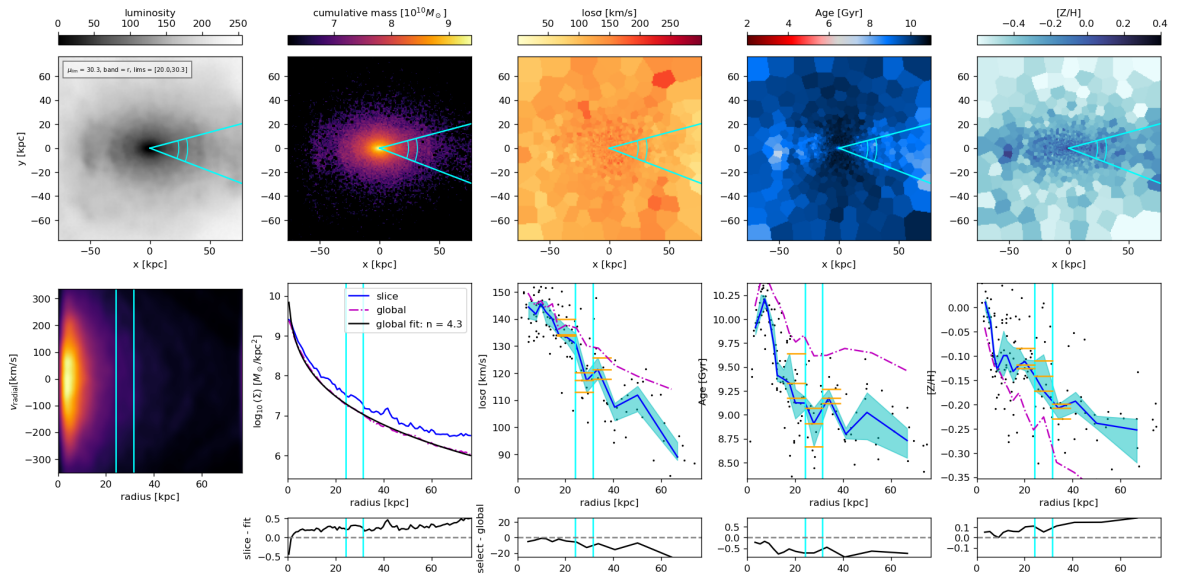


Figure D.29: UID 13500, Shell 2

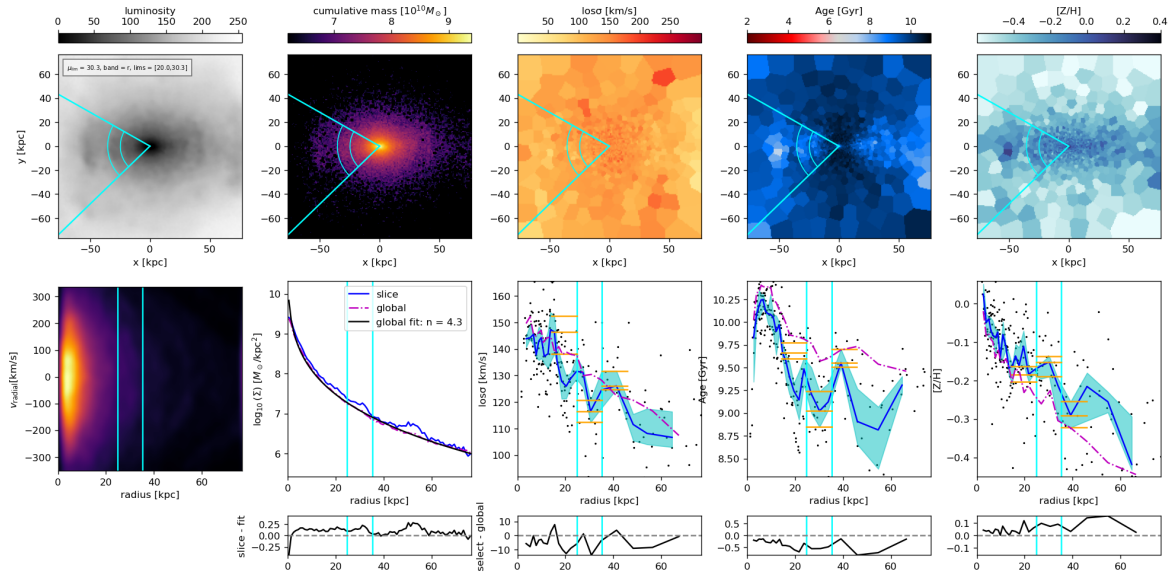


Figure D.30: UID 13500, Shell 3

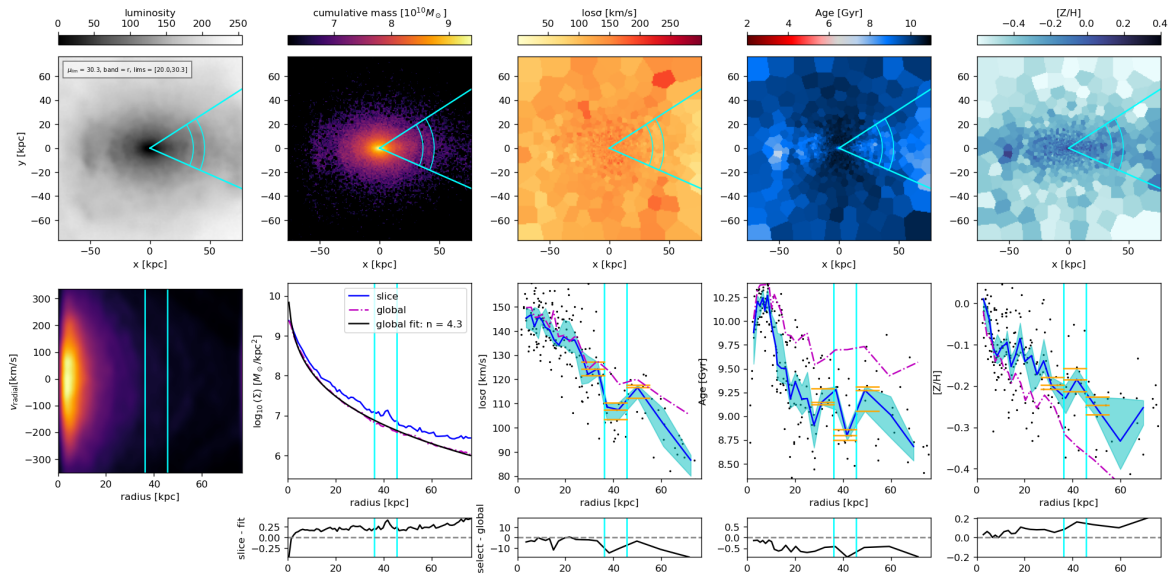


Figure D.31: UID 13500, Shell 4

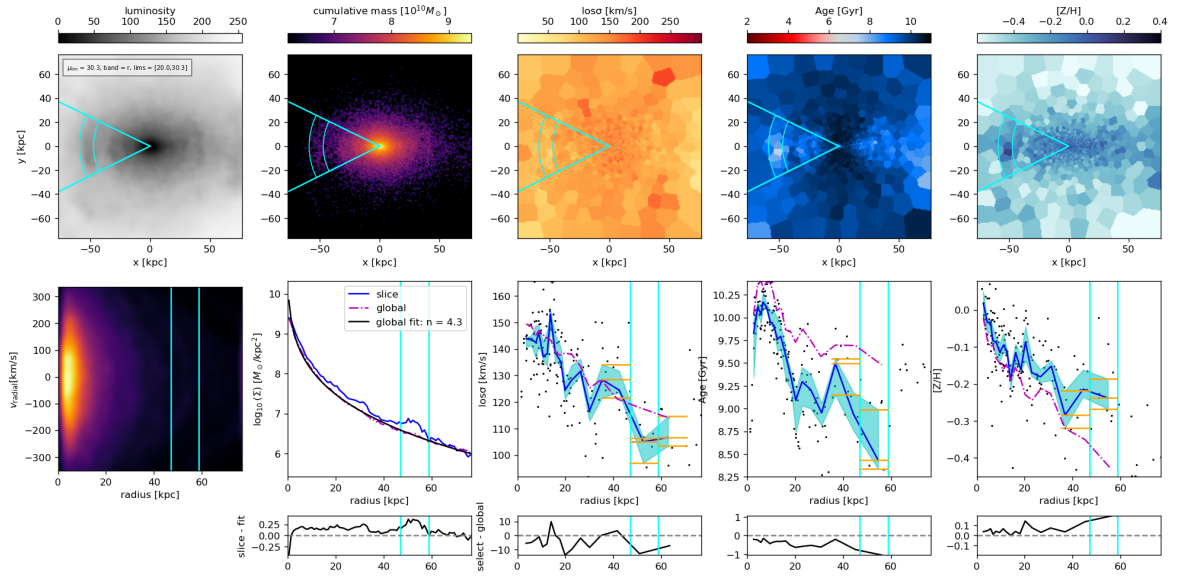


Figure D.32: UID 13500, Shell 5

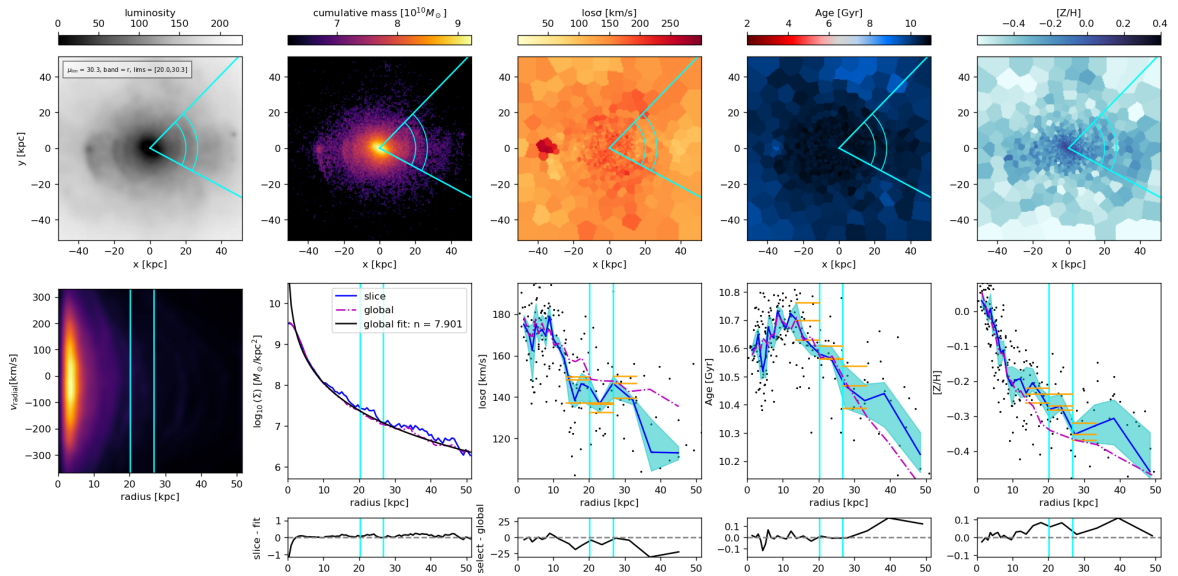


Figure D.33: UID 13844, Shell 1

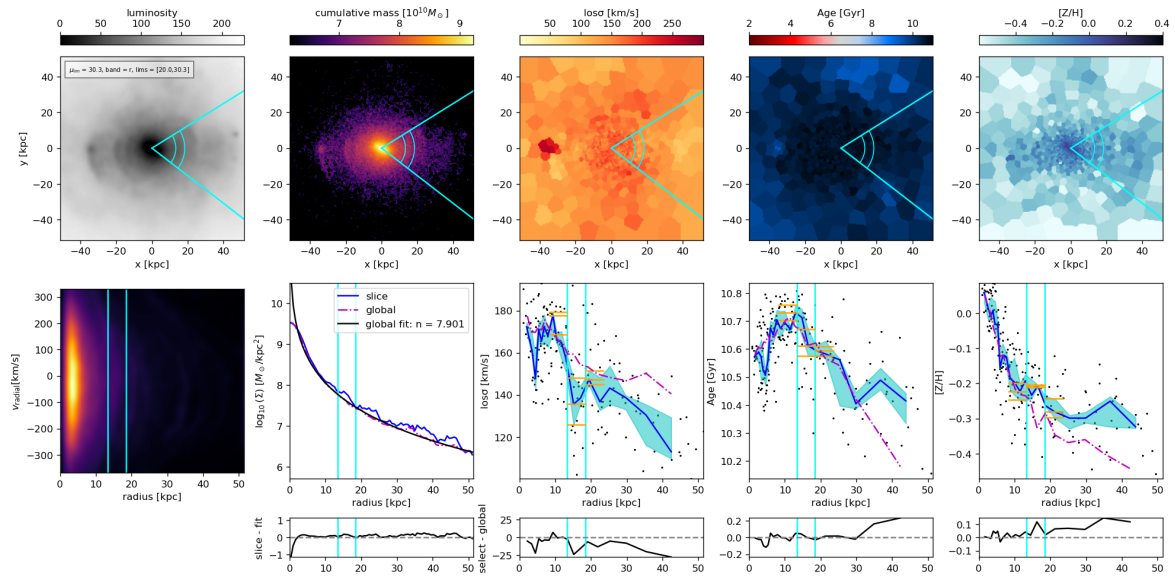


Figure D.34: UID 13844, Shell 2

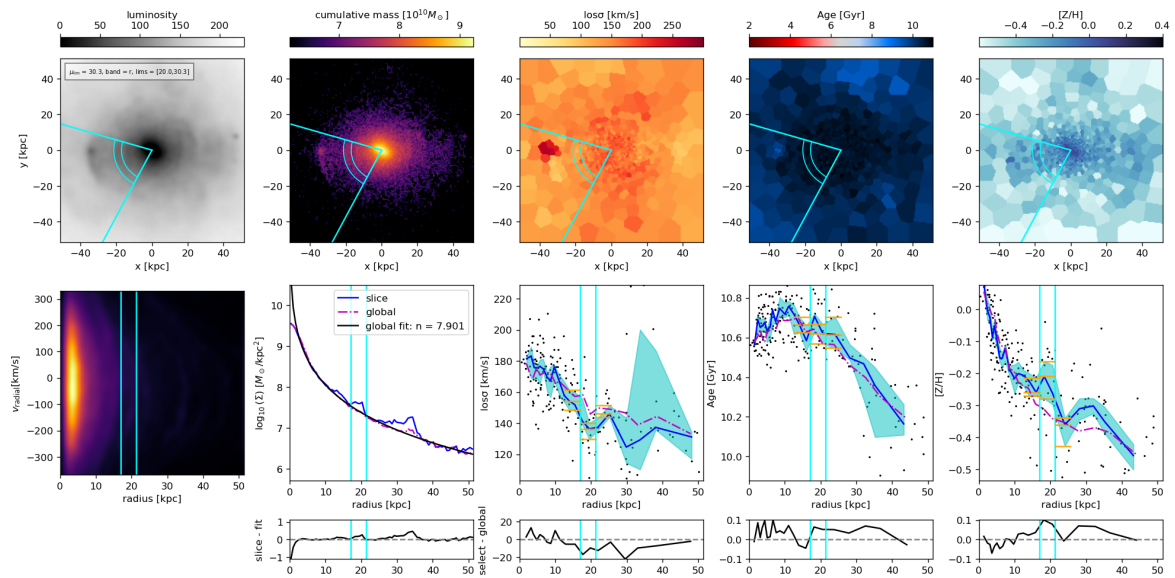


Figure D.35: UID 13844, Shell 3

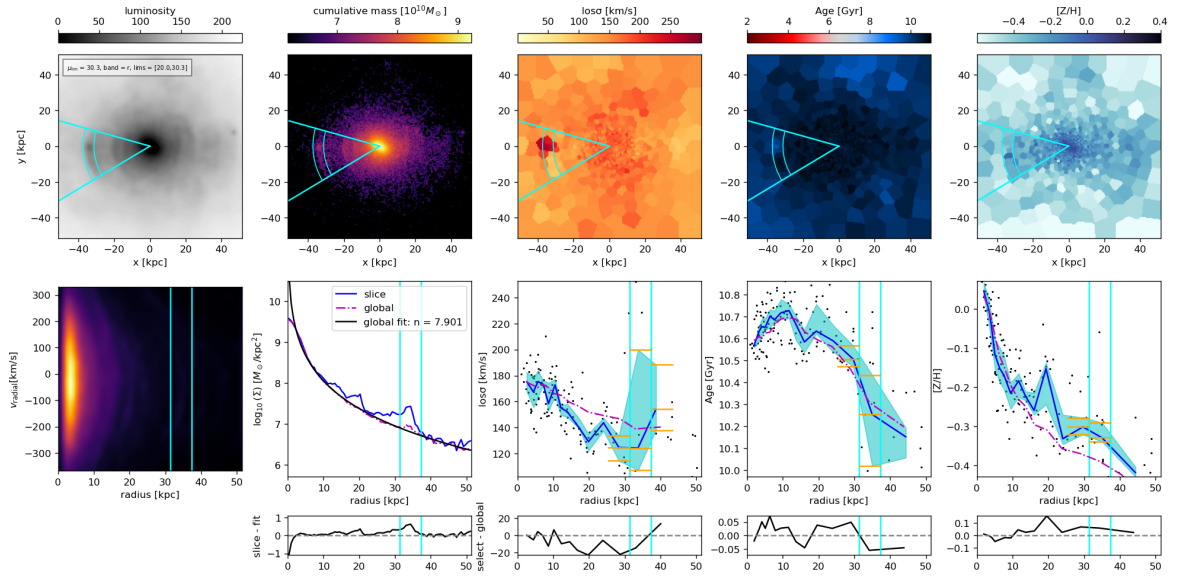


Figure D.36: UID 13844, Shell 4

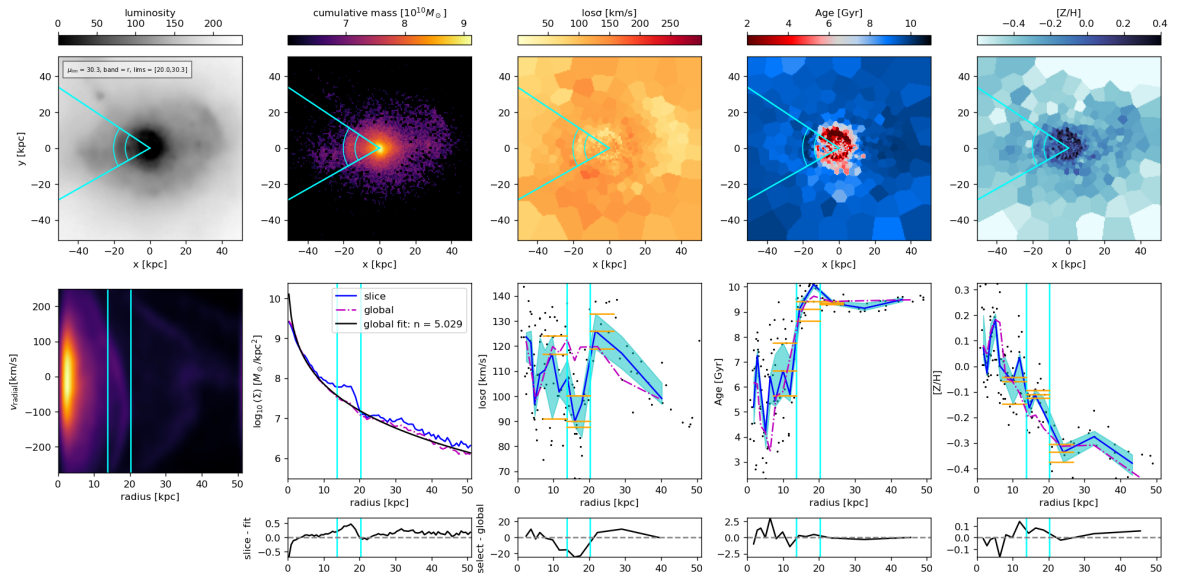


Figure D.37: UID 15741, Shell 1

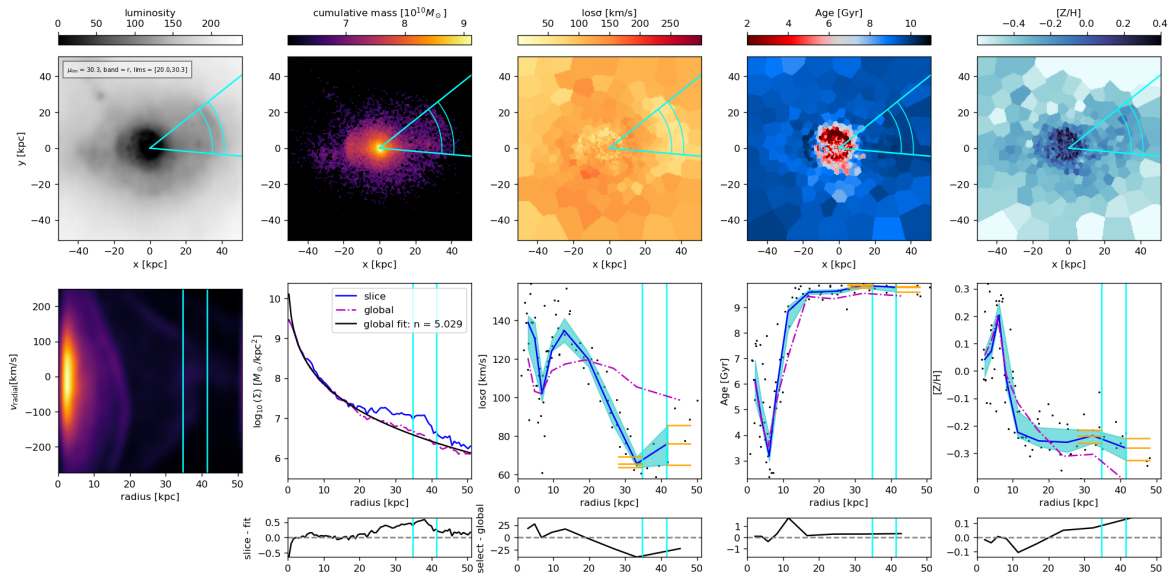


Figure D.38: UID 15741, Shell 2

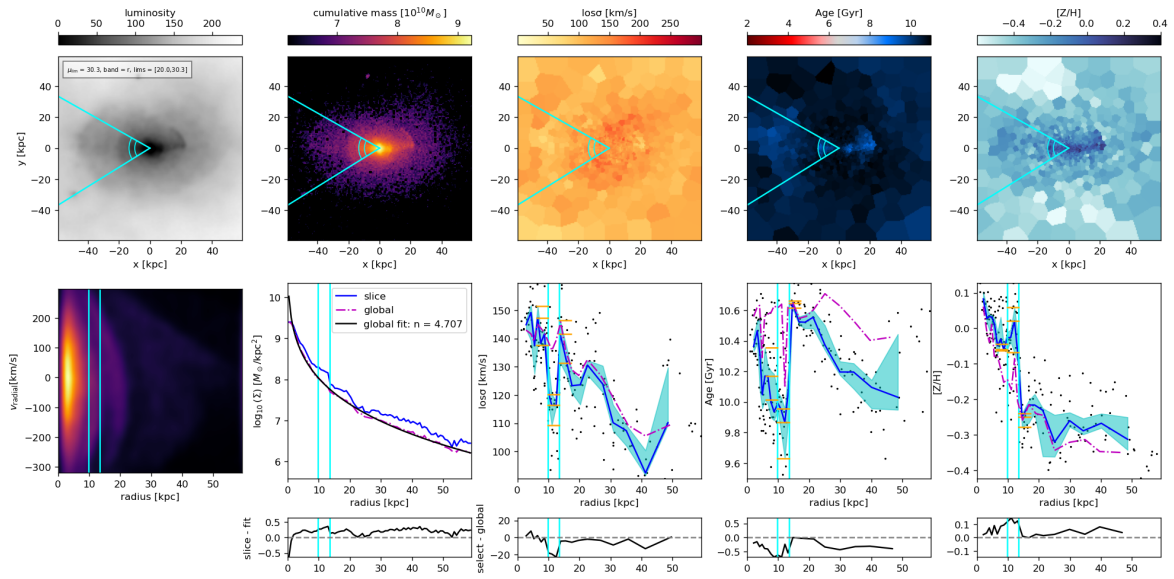


Figure D.39: UID 15880, Shell 1

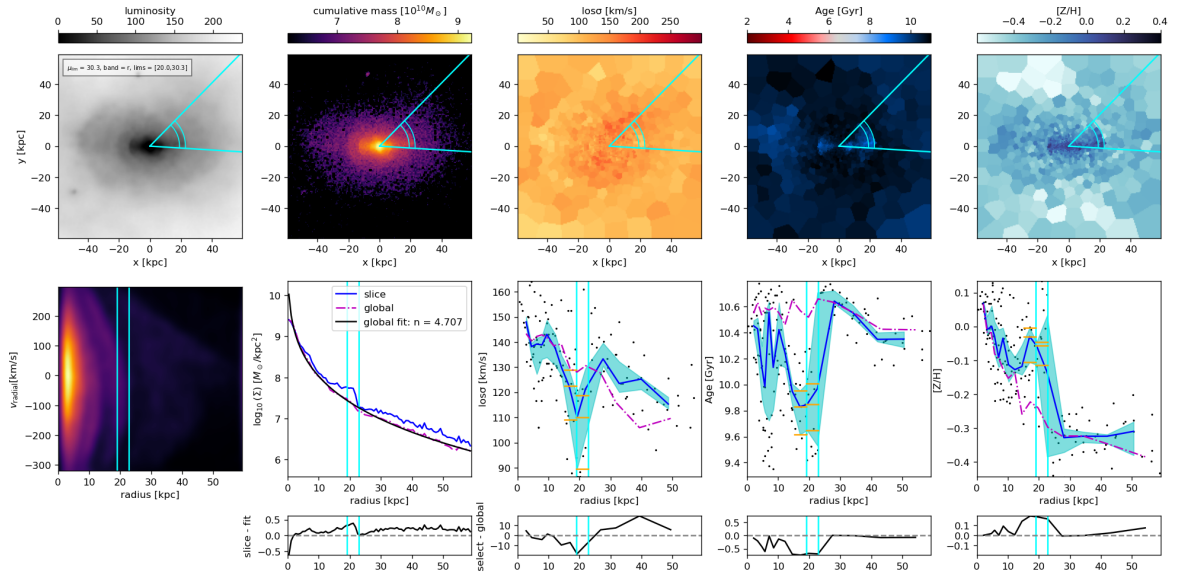


Figure D.40: UID 1580, Shell 2

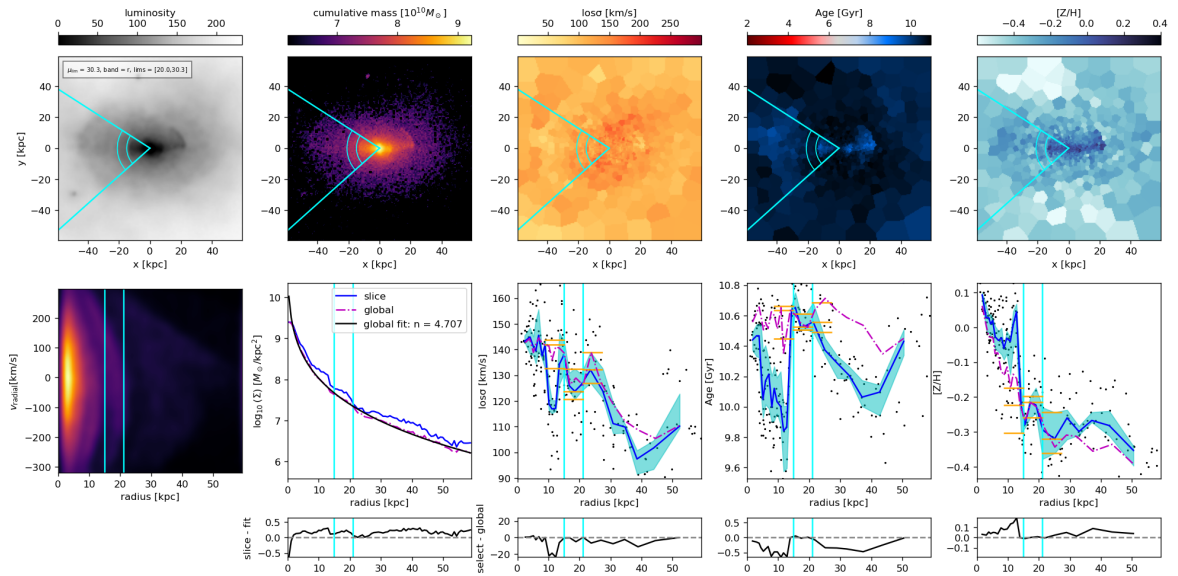


Figure D.41: UID 1580, Shell 3

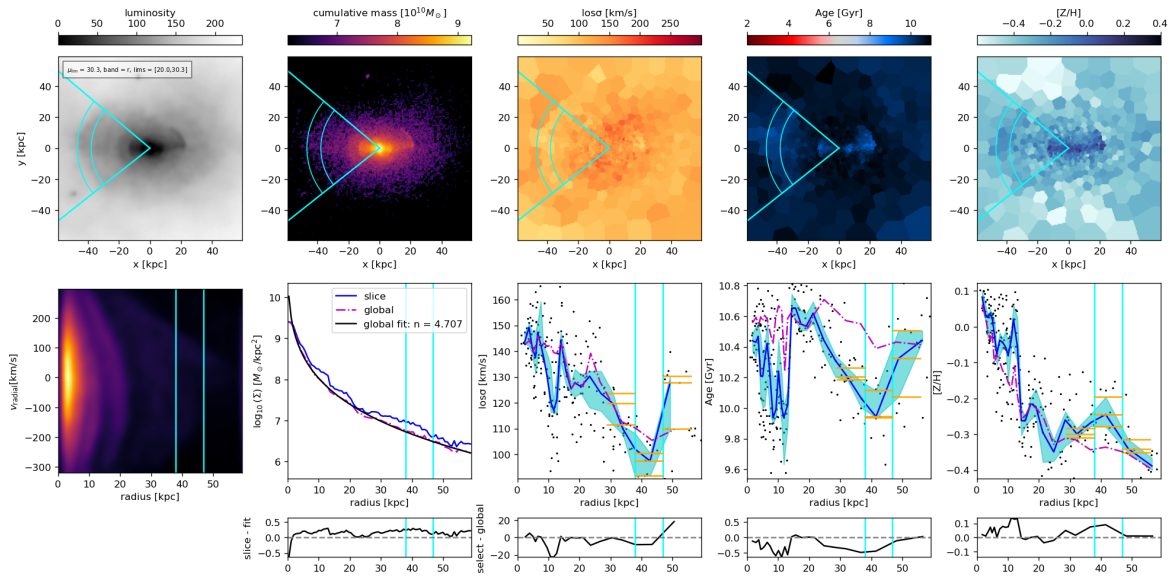


Figure D.42: UID 15880, Shell 4

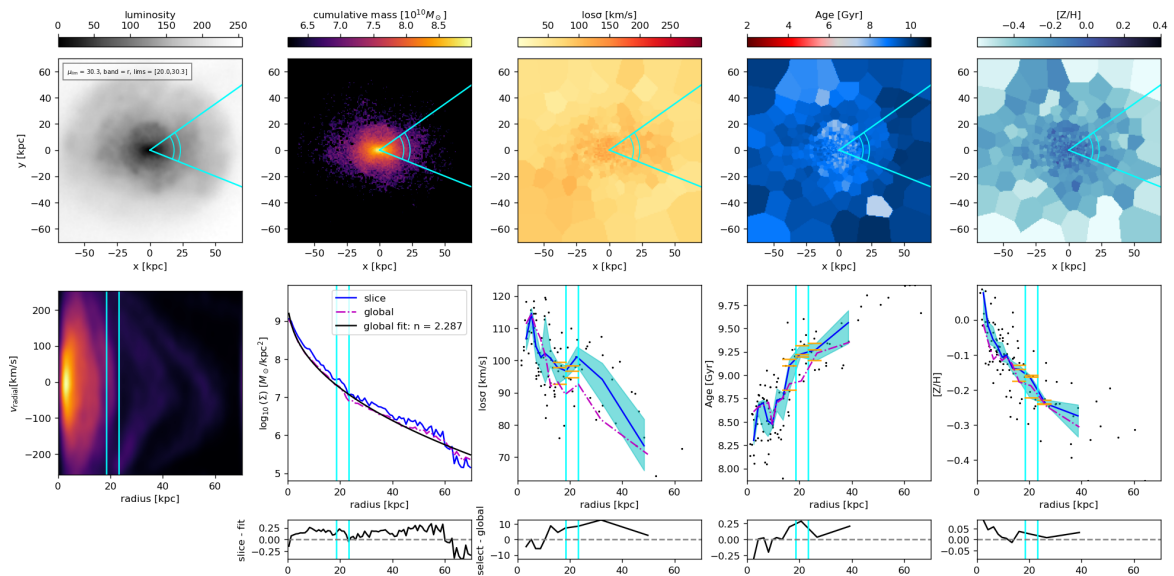


Figure D.43: UID 17268, Shell 1

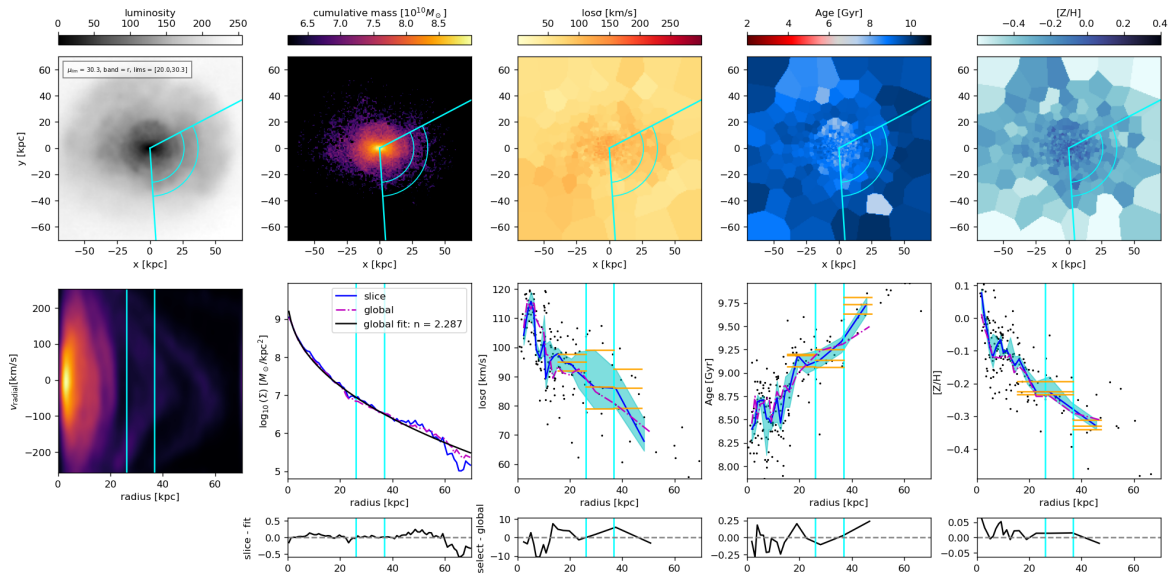


Figure D.44: UID 17268, Shell 2

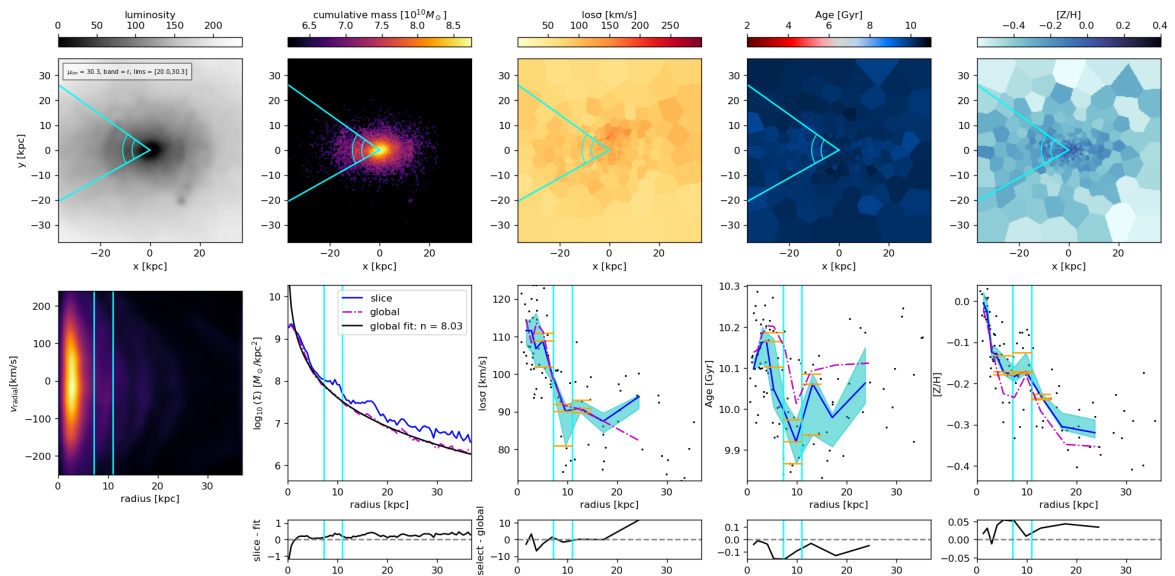


Figure D.45: UID 17986, Shell 1

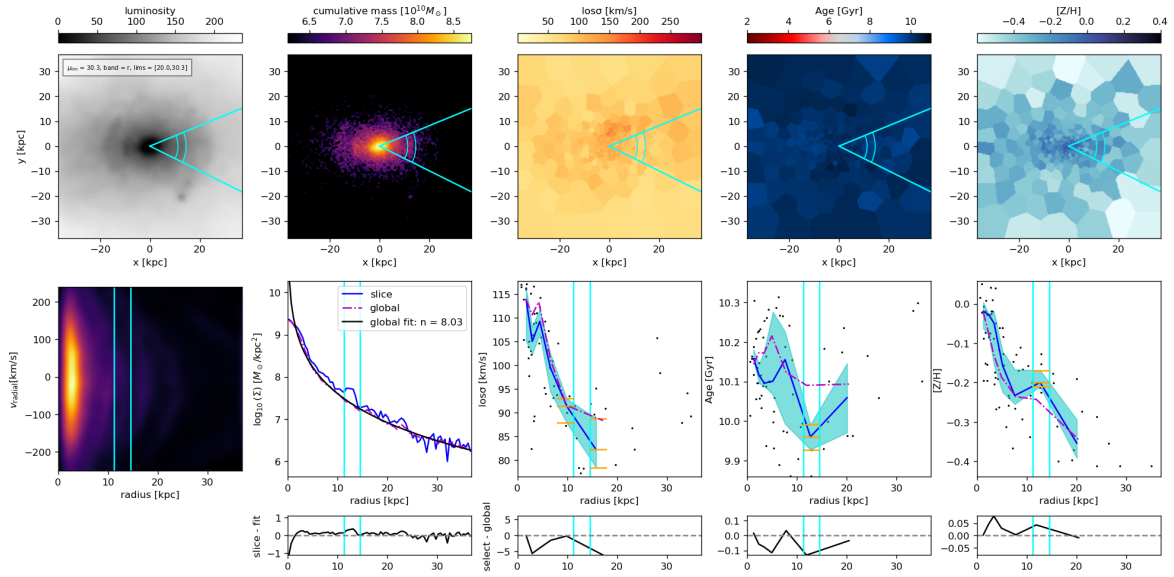


Figure D.46: UID 17986, Shell 2

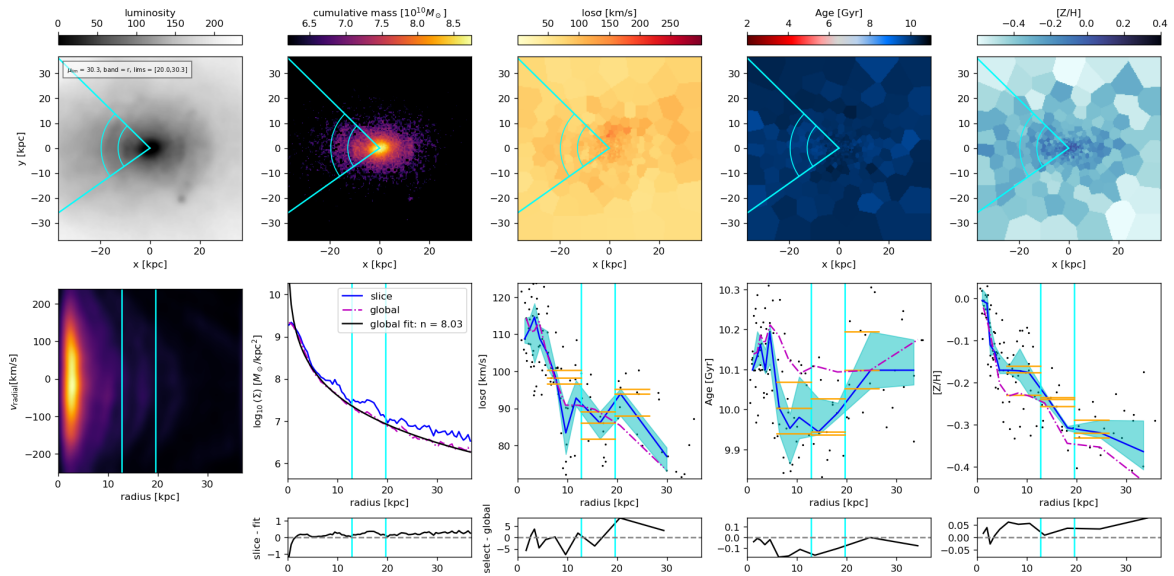


Figure D.47: UID 17986, Shell 3

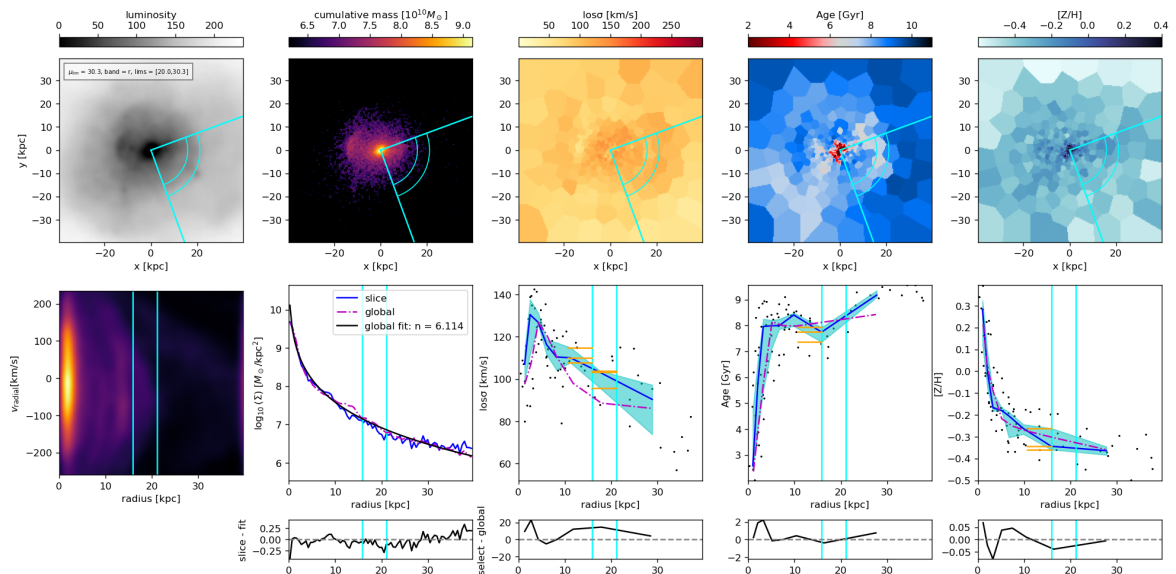


Figure D.48: UID 18231, Shell 1

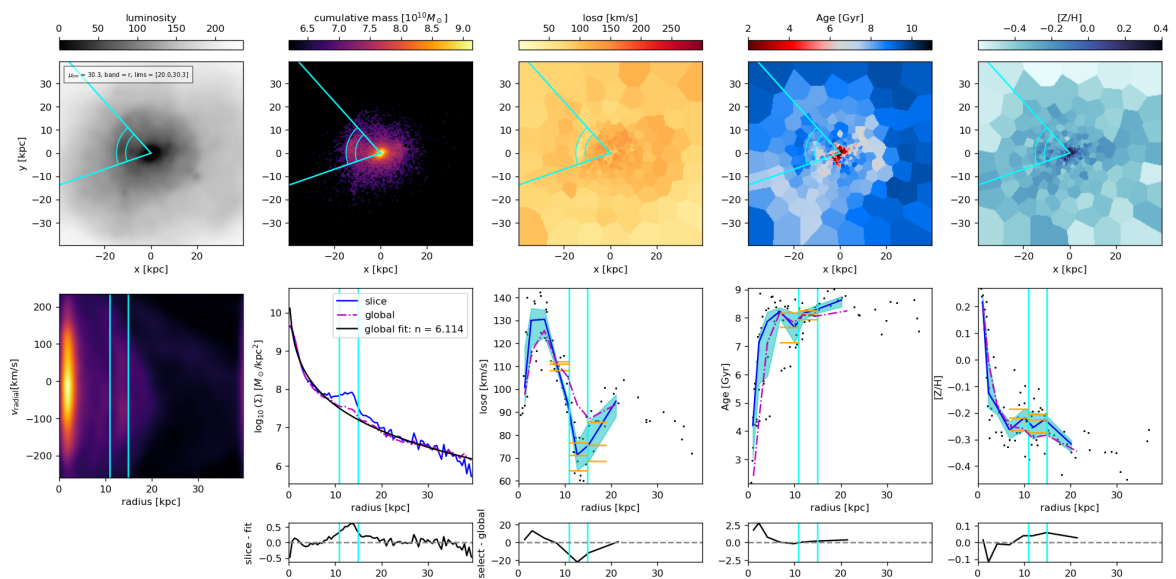


Figure D.49: UID 18231, Shell 2

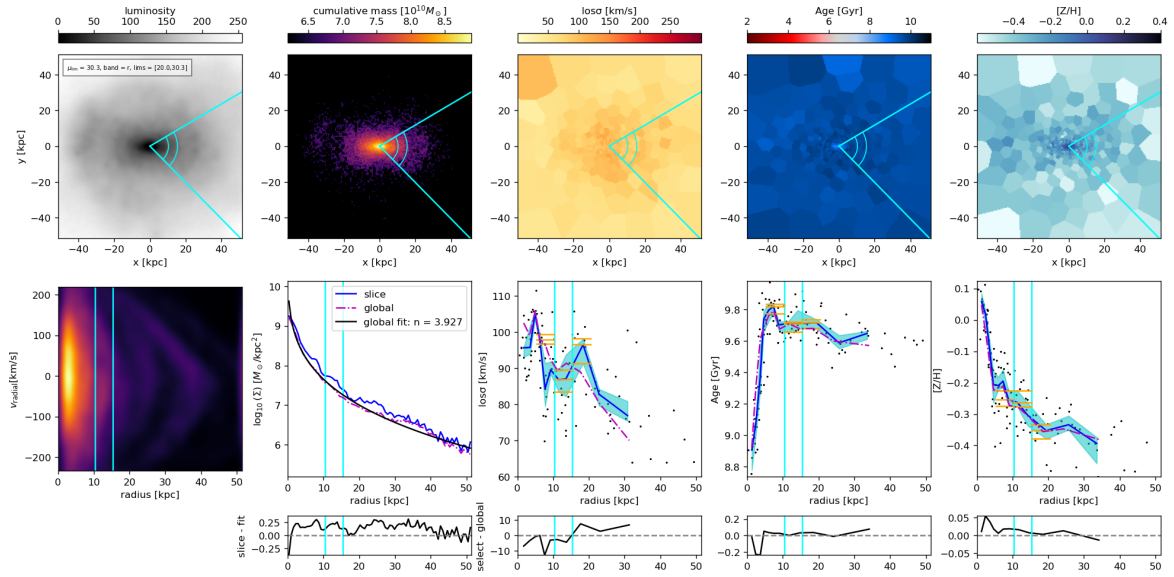


Figure D.50: UID 18335, Shell 1

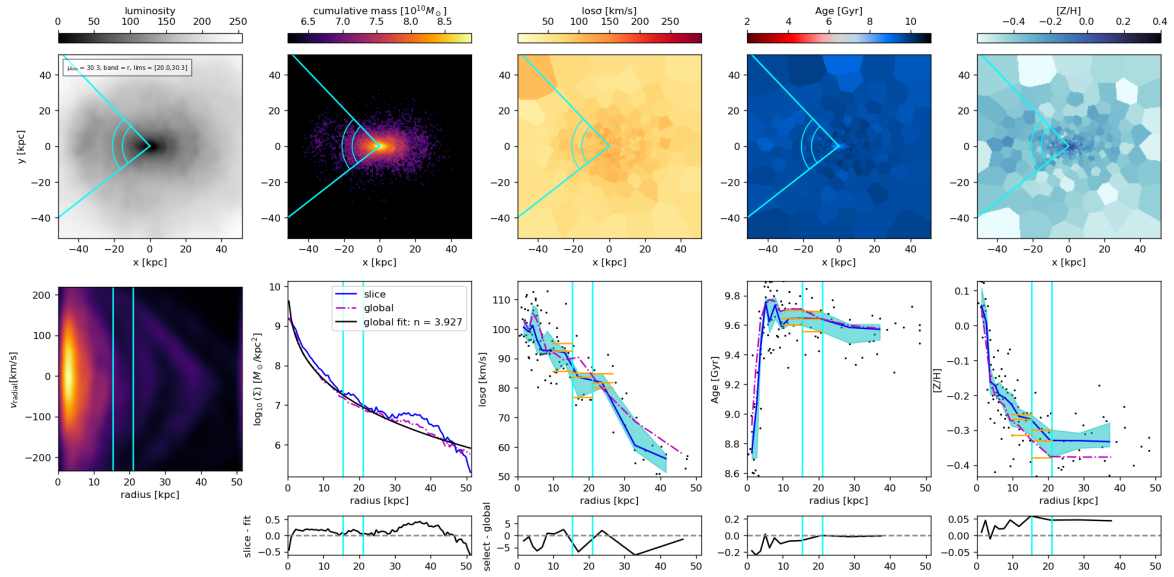


Figure D.51: UID 18335, Shell 2

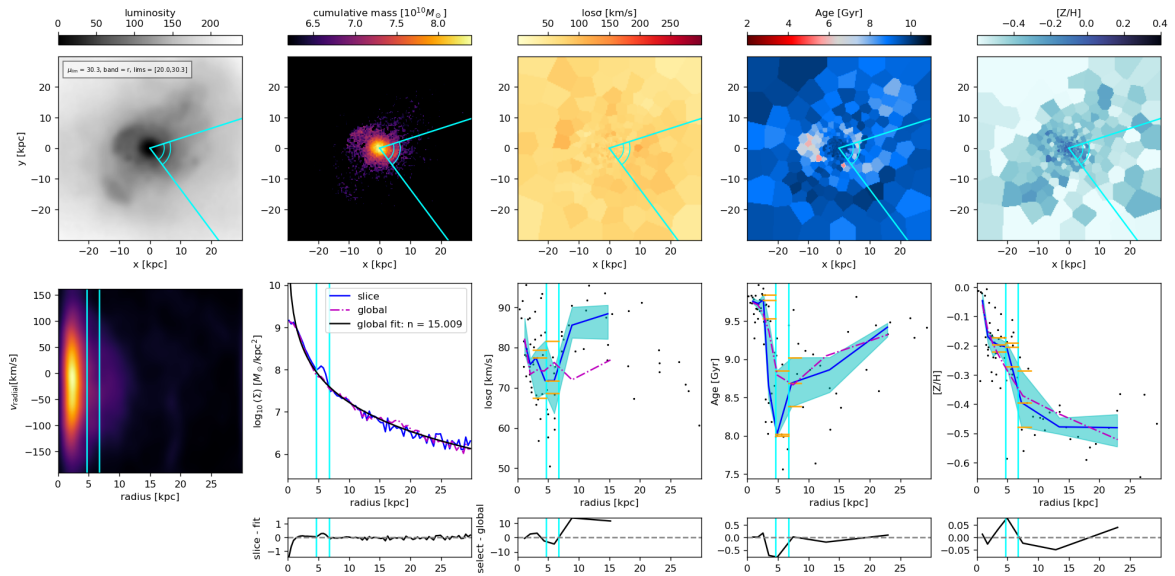


Figure D.52: UID 20194, Shell 1

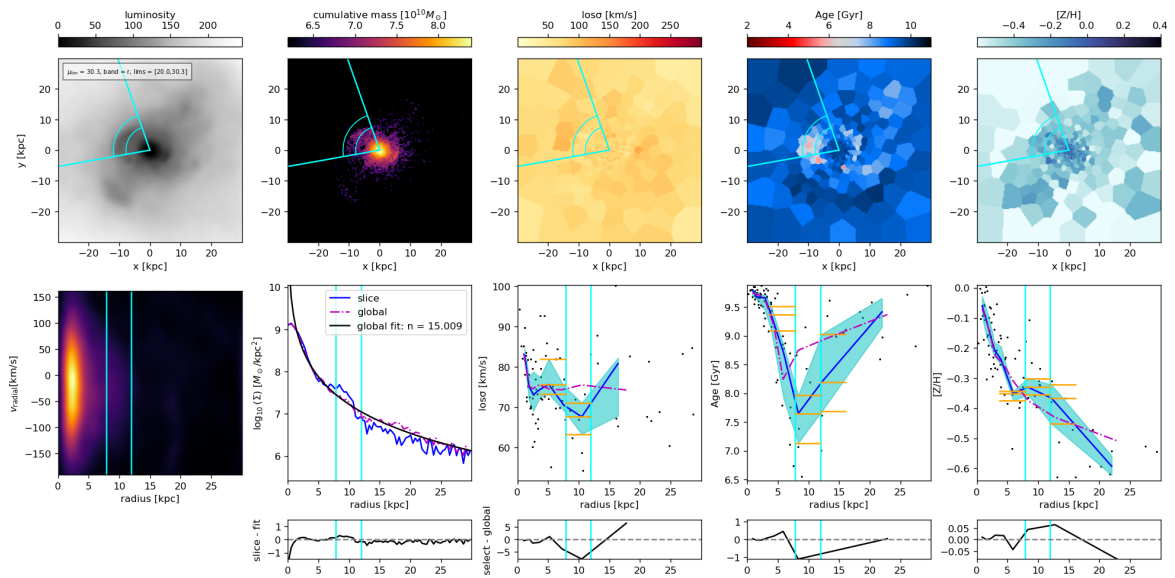


Figure D.53: UID 20194, Shell 2

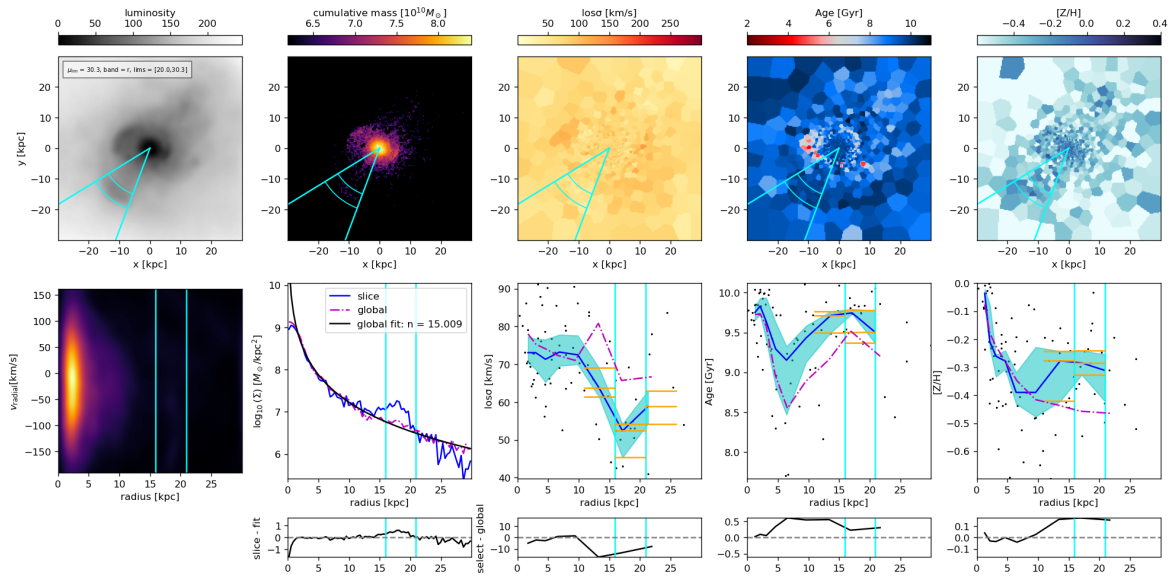


Figure D.54: UID 20194, Shell 3

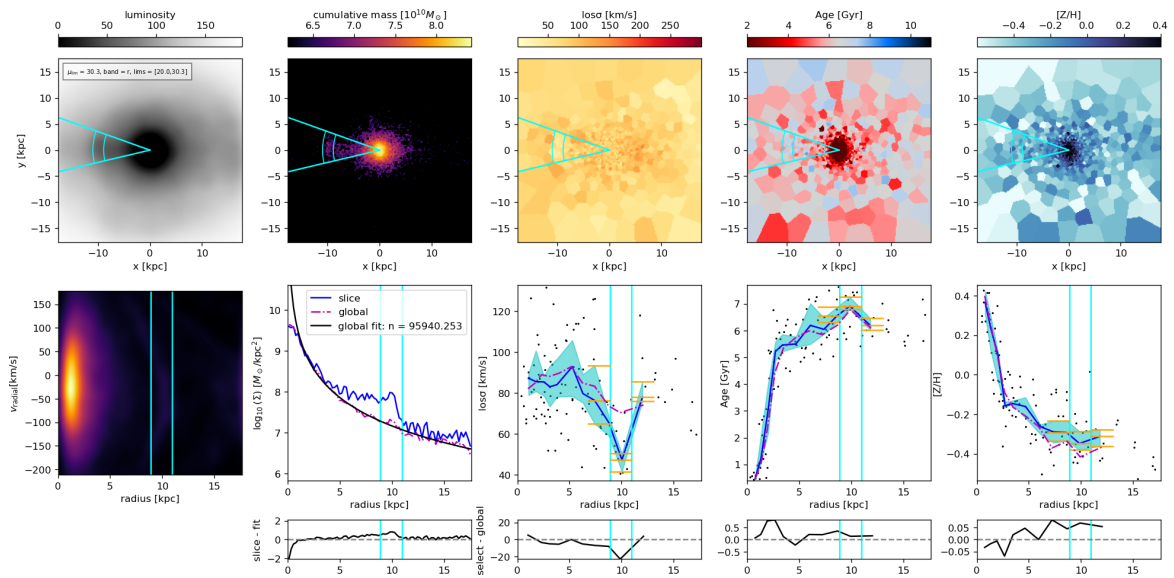


Figure D.55: UID 20577, Shell 1

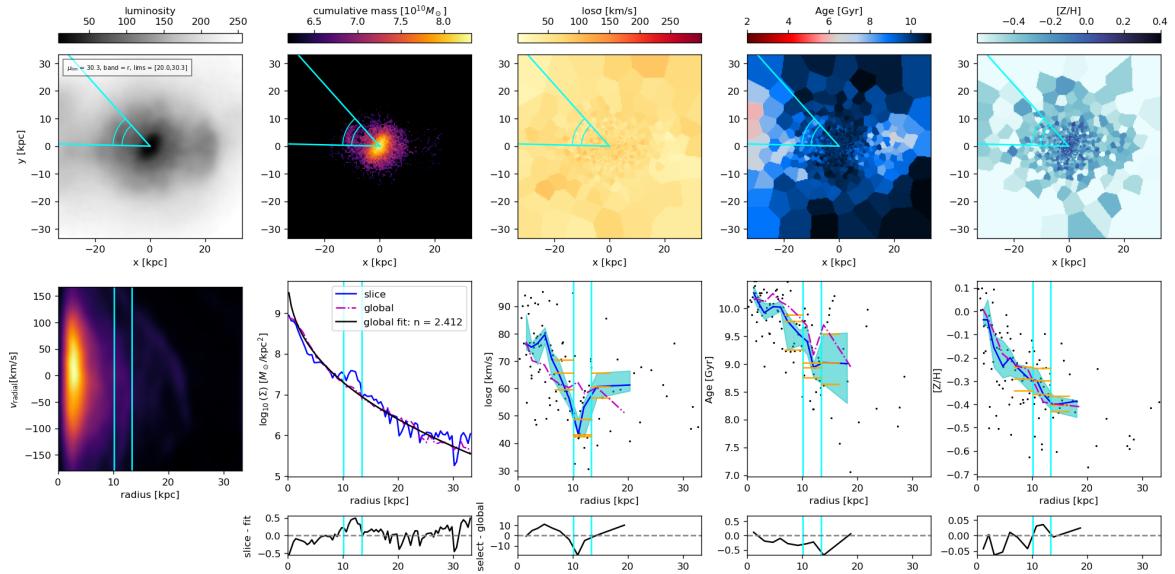


Figure D.56: UID 21477, Shell 1

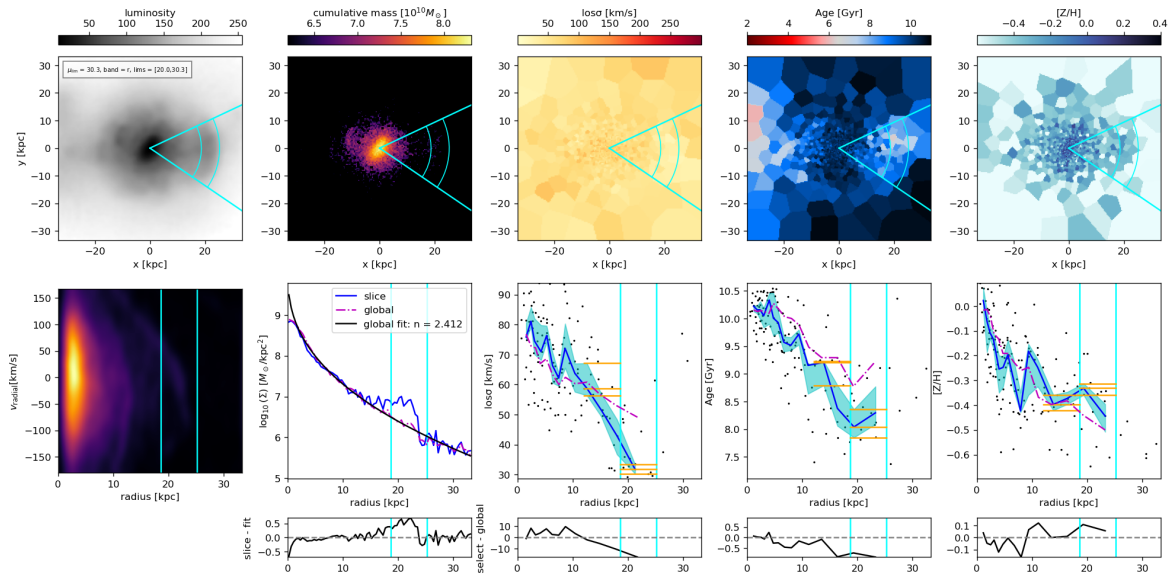


Figure D.57: UID 21477, Shell 2

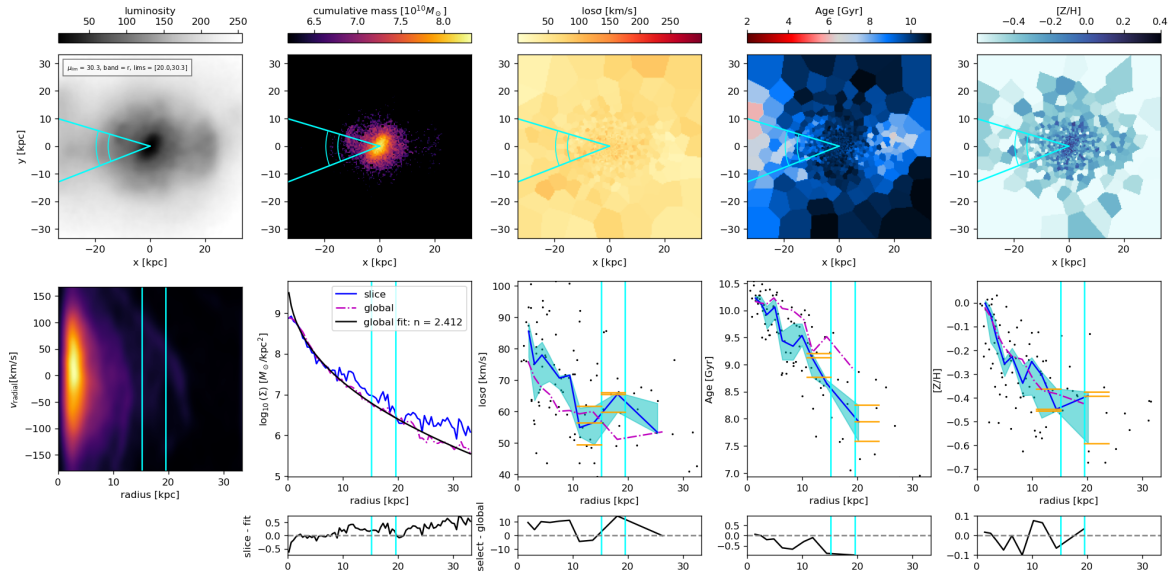


Figure D.58: UID 21477, Shell 3

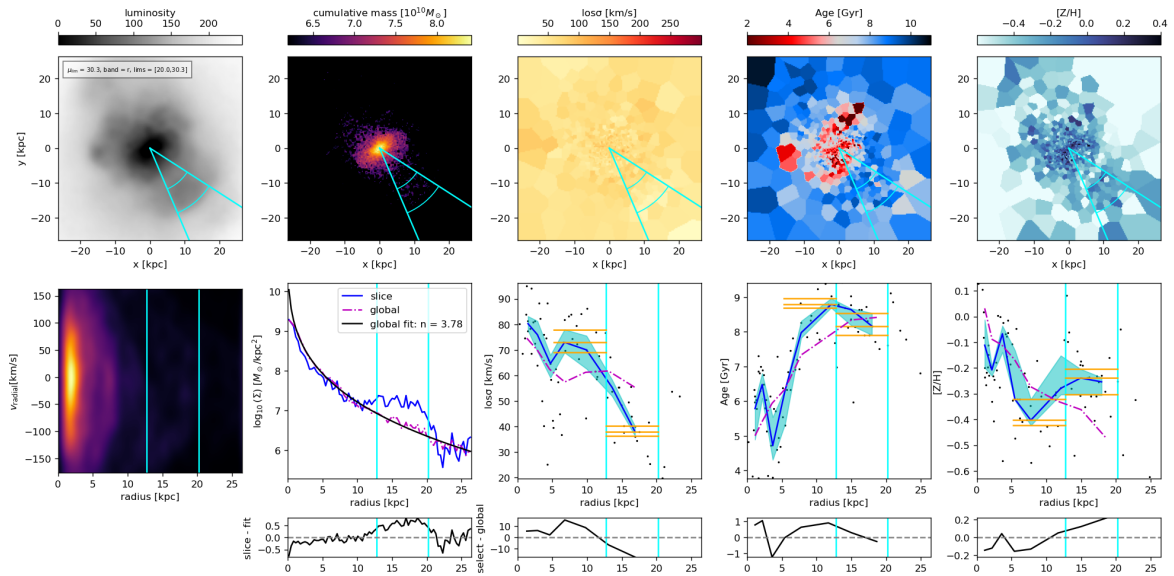


Figure D.59: UID 21654, Shell 1

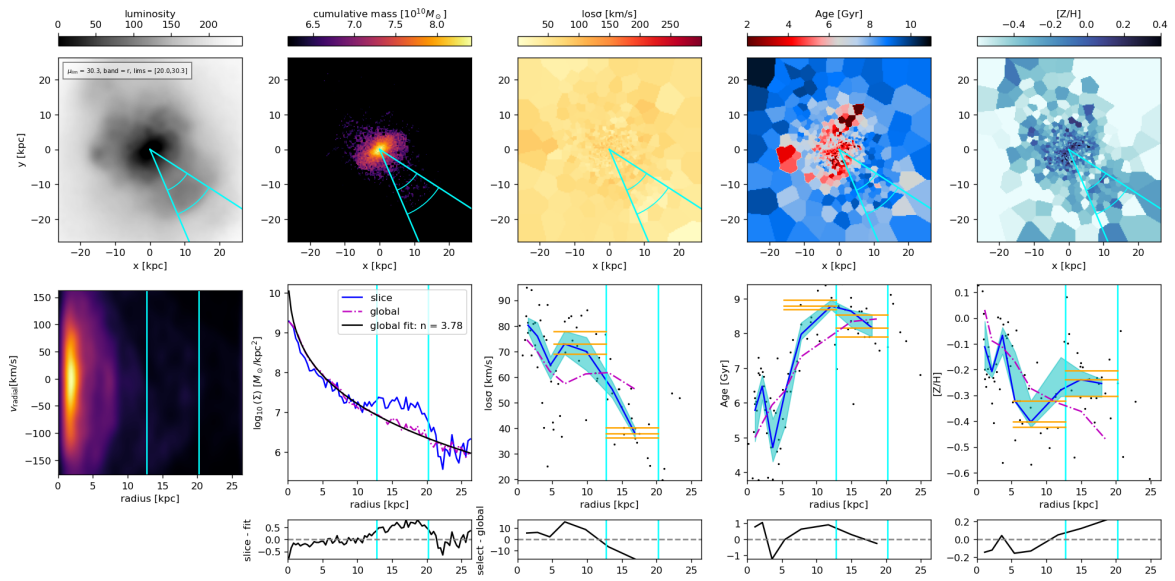


Figure D.60: UID 0, Stream 1

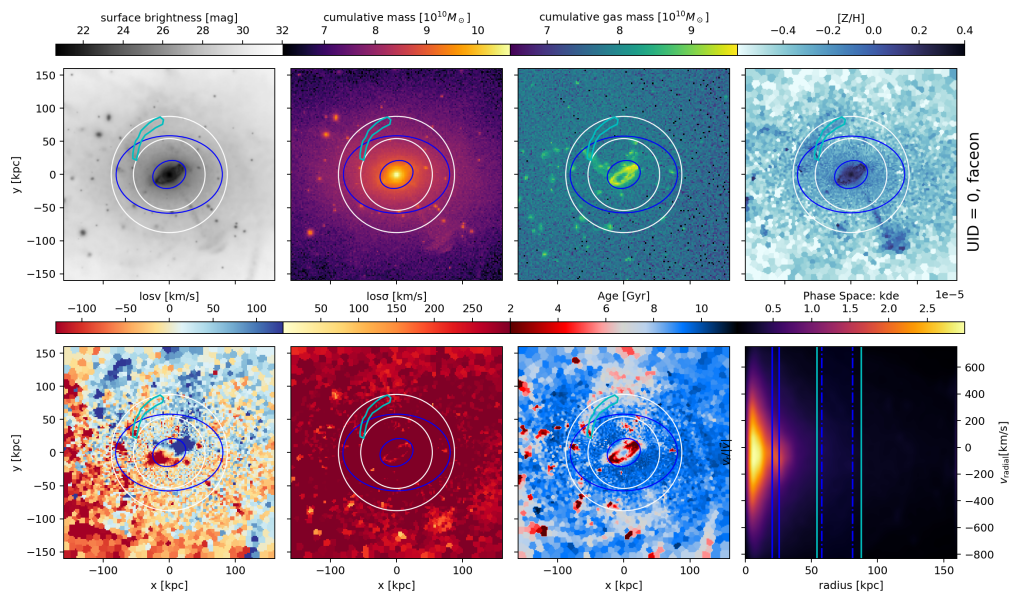


Figure D.61: UID 0, Stream 1

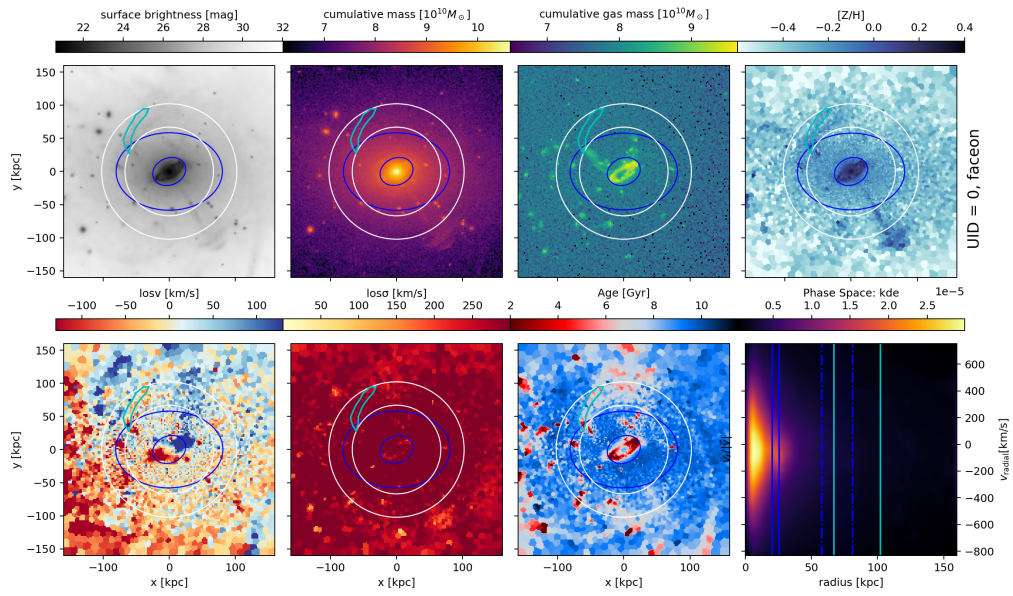


Figure D.62: UID 0, Stream 2

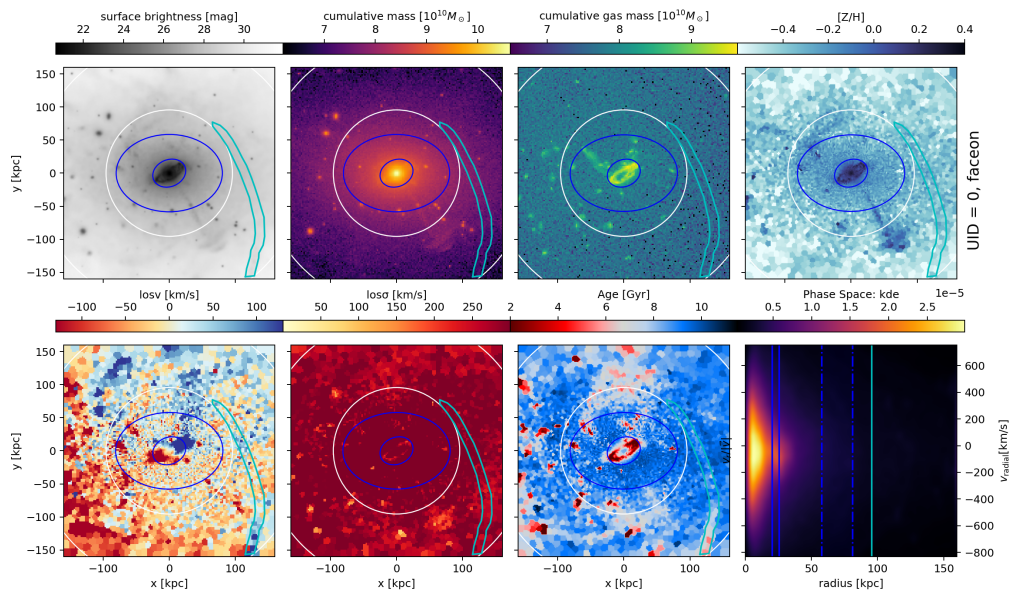


Figure D.63: UID 0, Stream 3

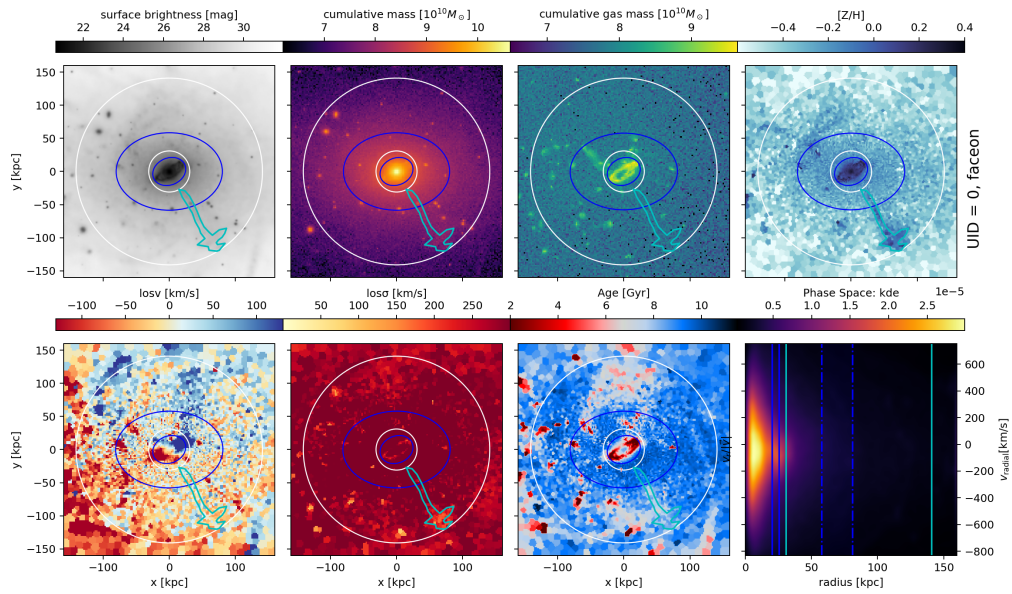


Figure D.64: UID 0, Stream 4

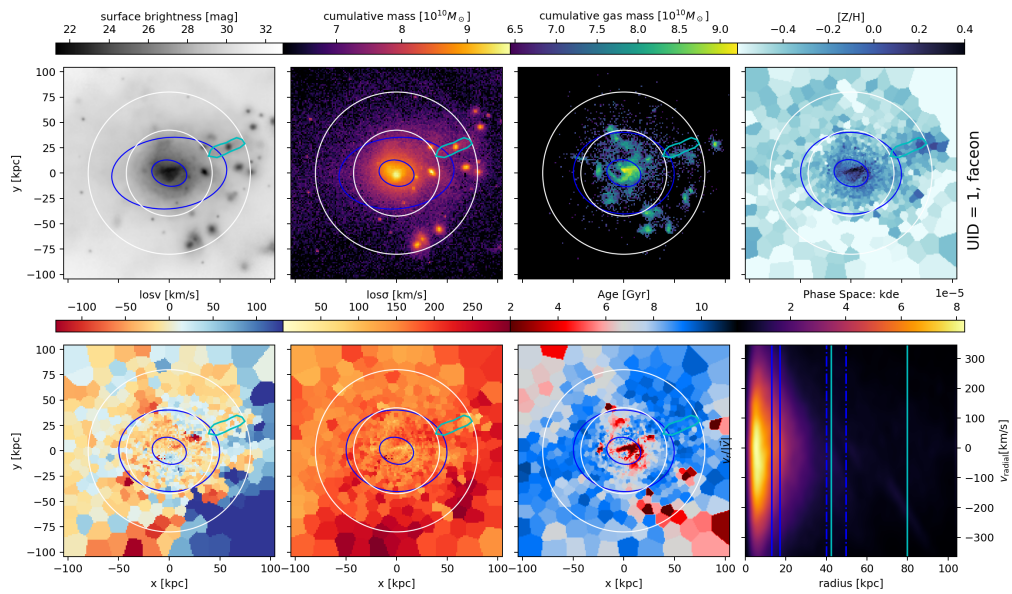


Figure D.65: UID 1, Stream 1

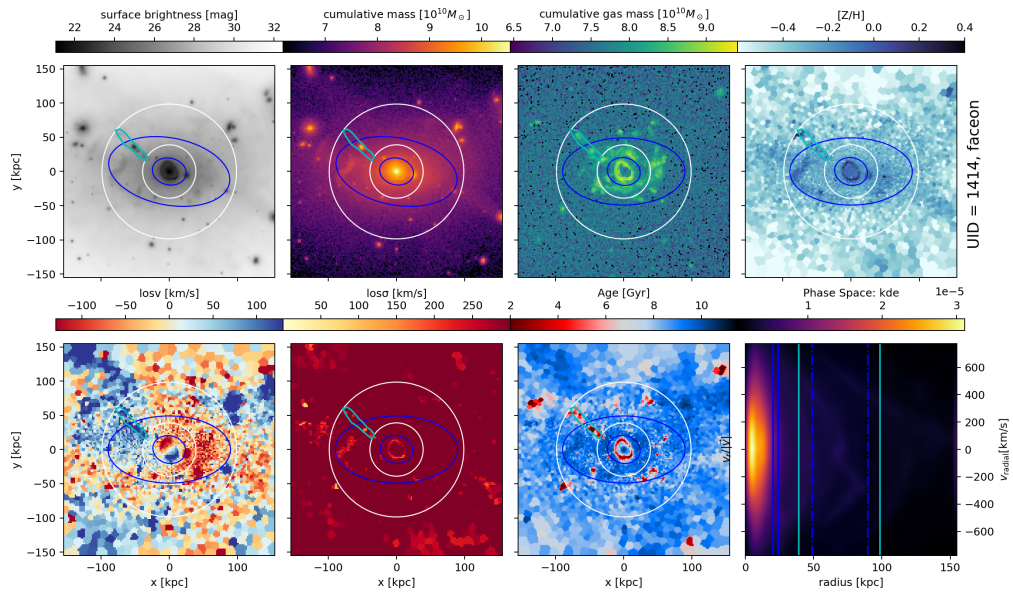


Figure D.66: UID 1414, Stream 1

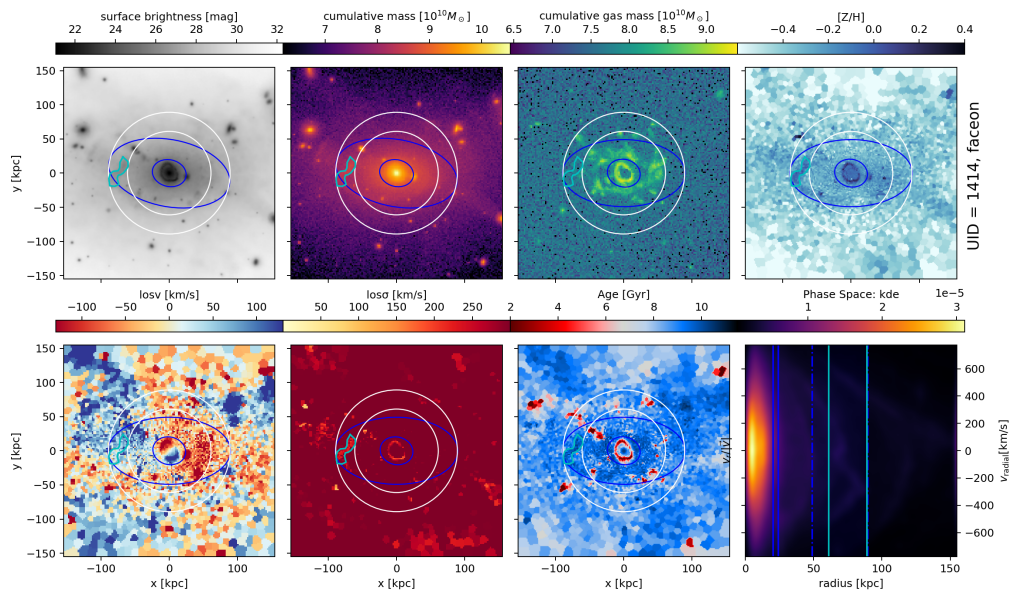


Figure D.67: UID 1414, Stream 2

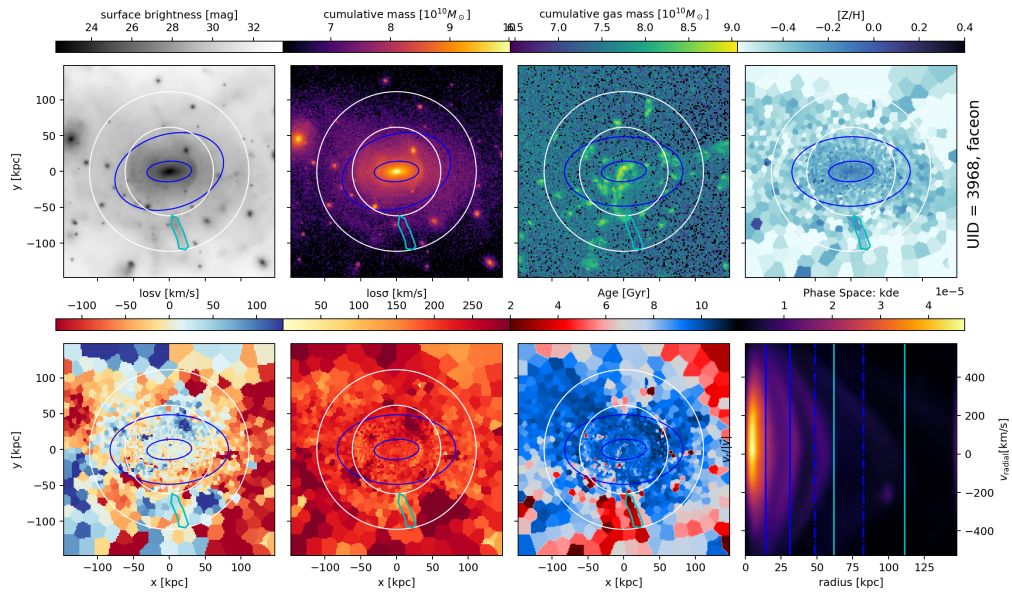


Figure D.68: UID 3968, Stream 1

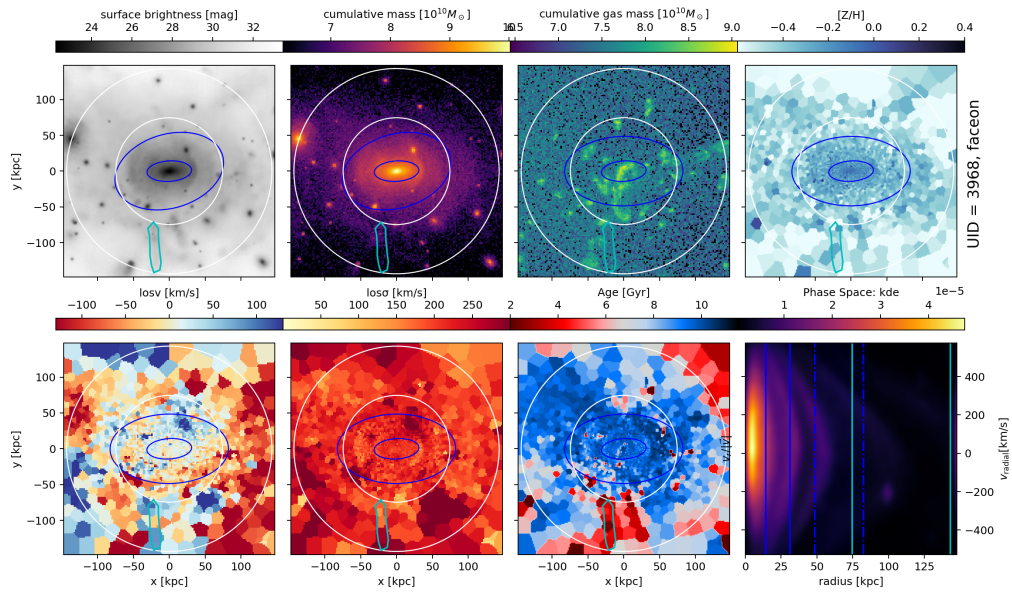


Figure D.69: UID 3968, Stream 2

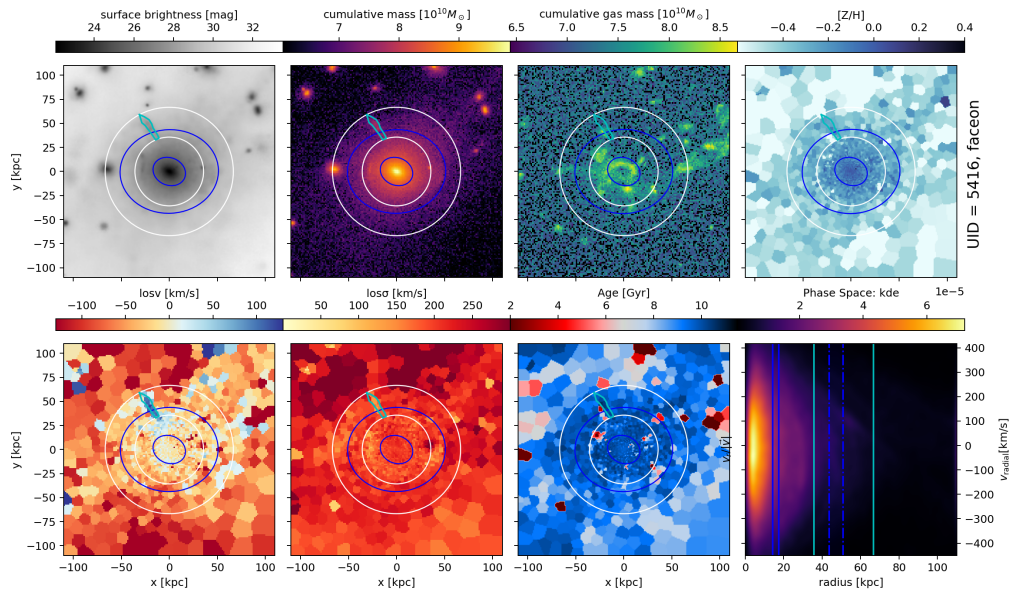


Figure D.70: UID 5416, Stream 1

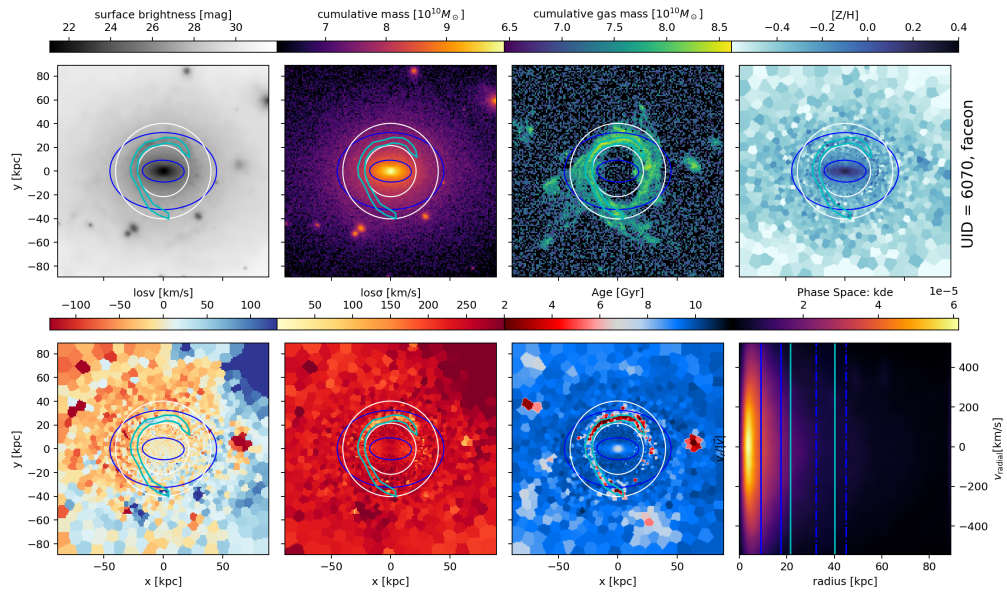


Figure D.71: UID 6070, Stream 1

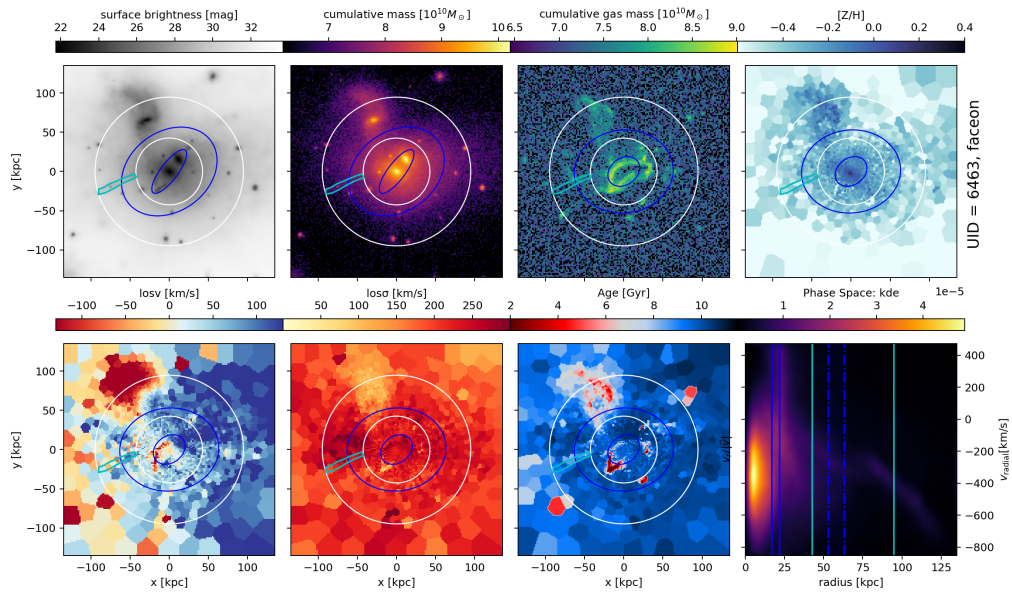


Figure D.72: UID 6463, Stream 1

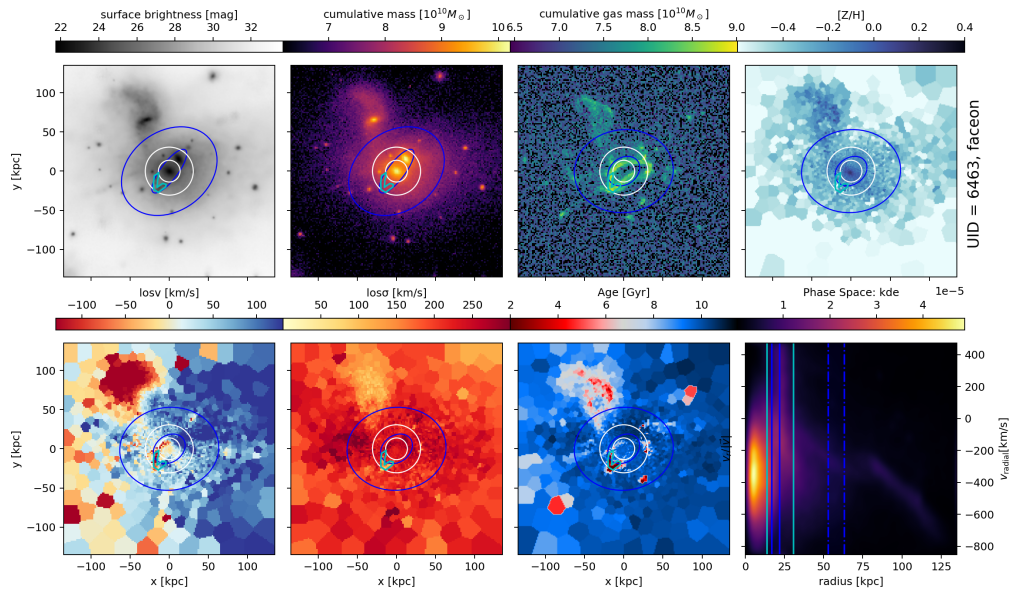


Figure D.73: UID 6463, Stream 2

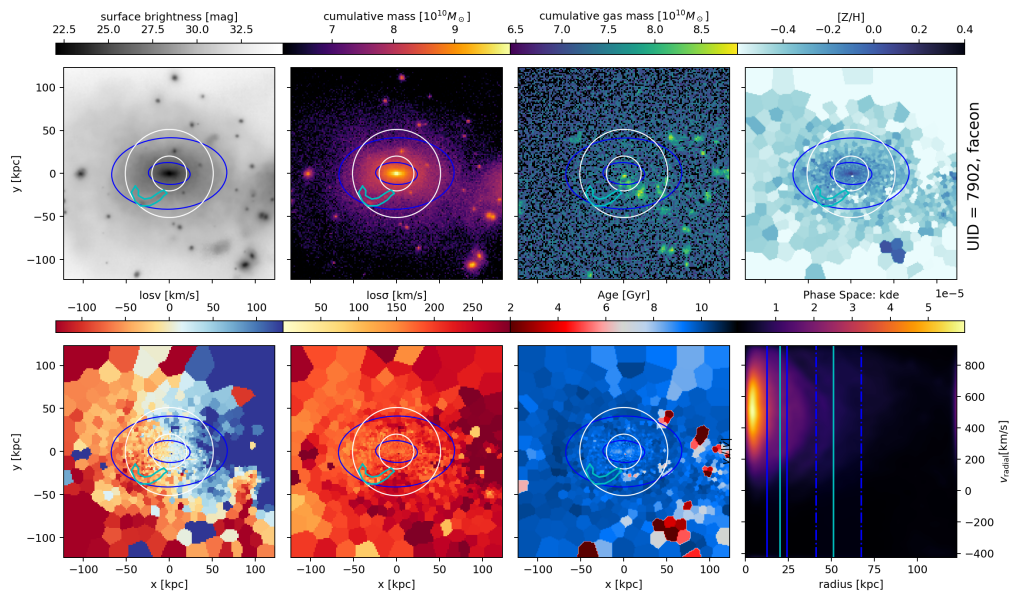


Figure D.74: UID 7902, Stream 1

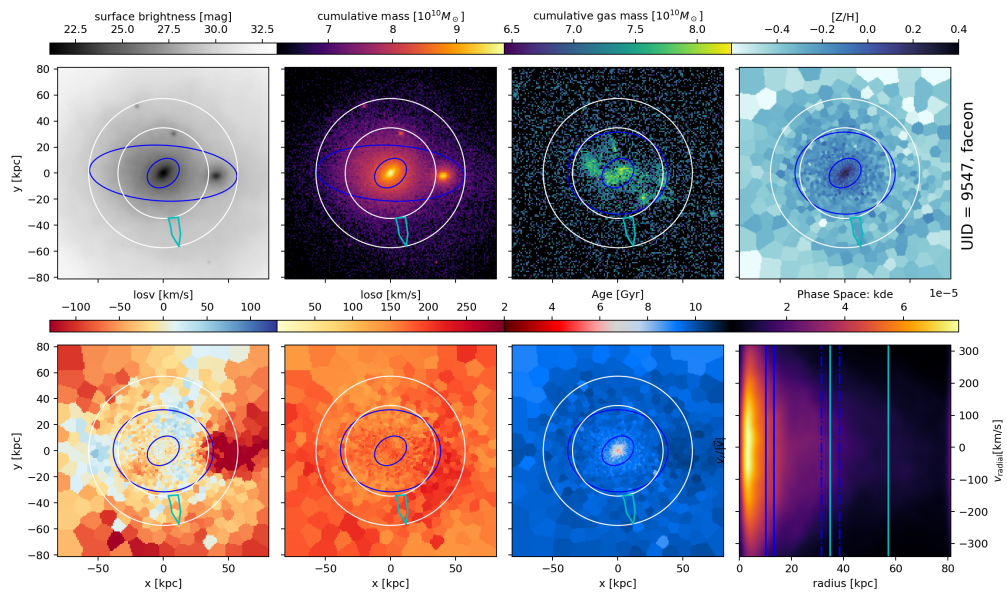


Figure D.75: UID 9547, Stream 1

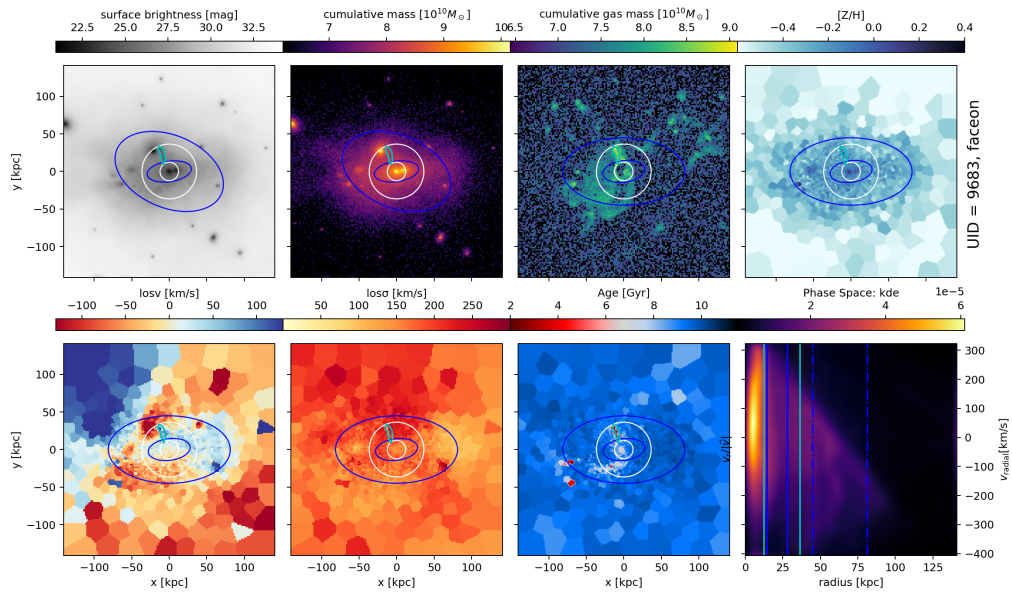


Figure D.76: UID 9683, Stream 1

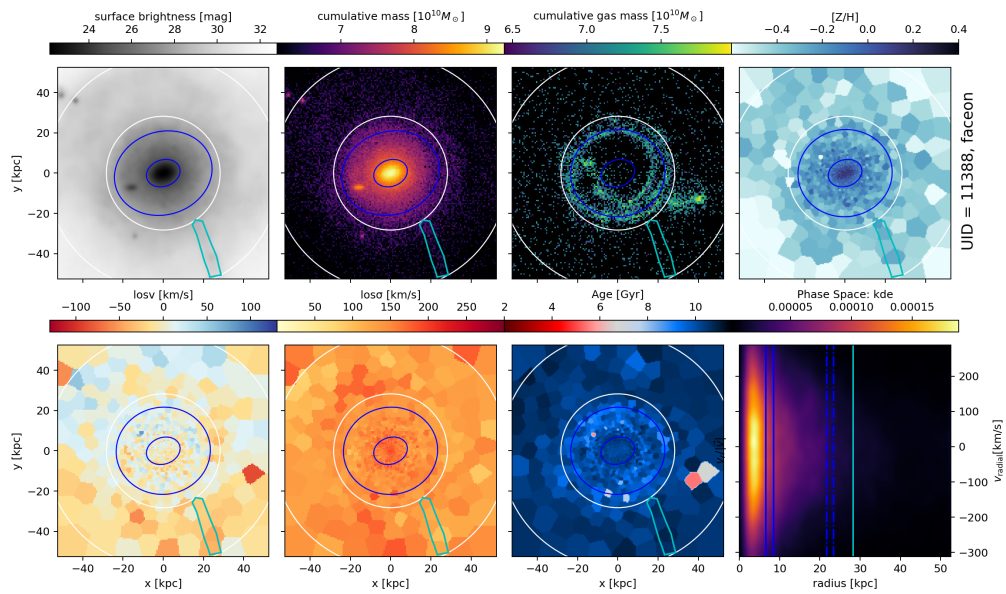


Figure D.77: UID 11388, Stream 1

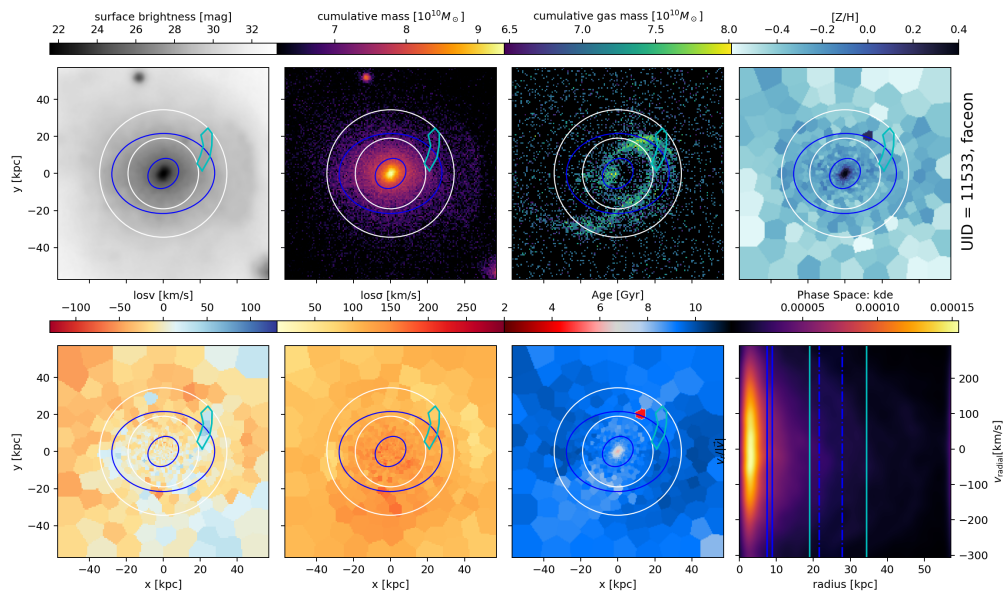


Figure D.78: UID 11533, Stream 1

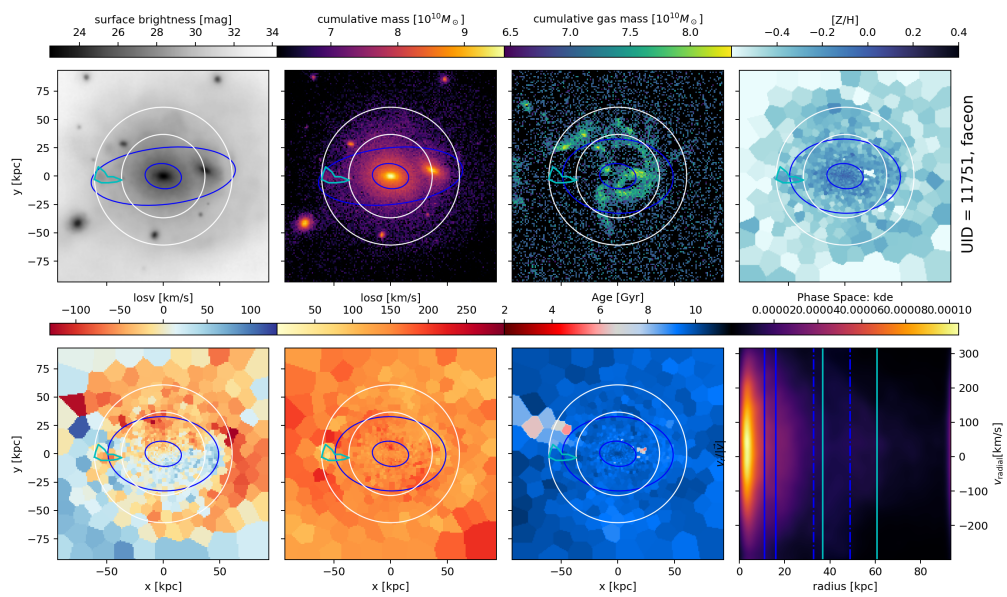


Figure D.79: UID 11751, Stream 1

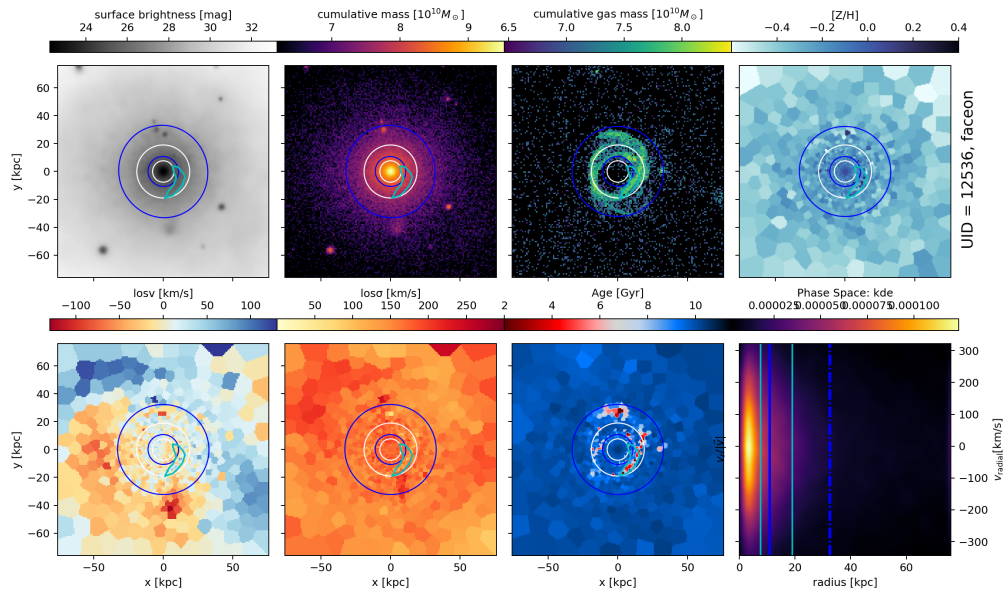


Figure D.80: UID 12536, Stream 1

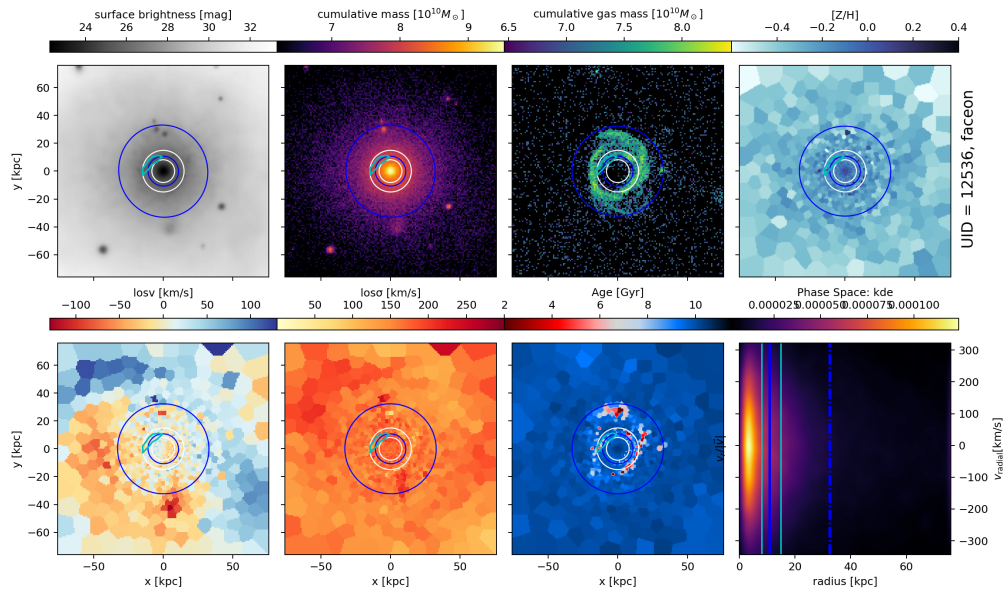


Figure D.81: UID 12536, Stream 2

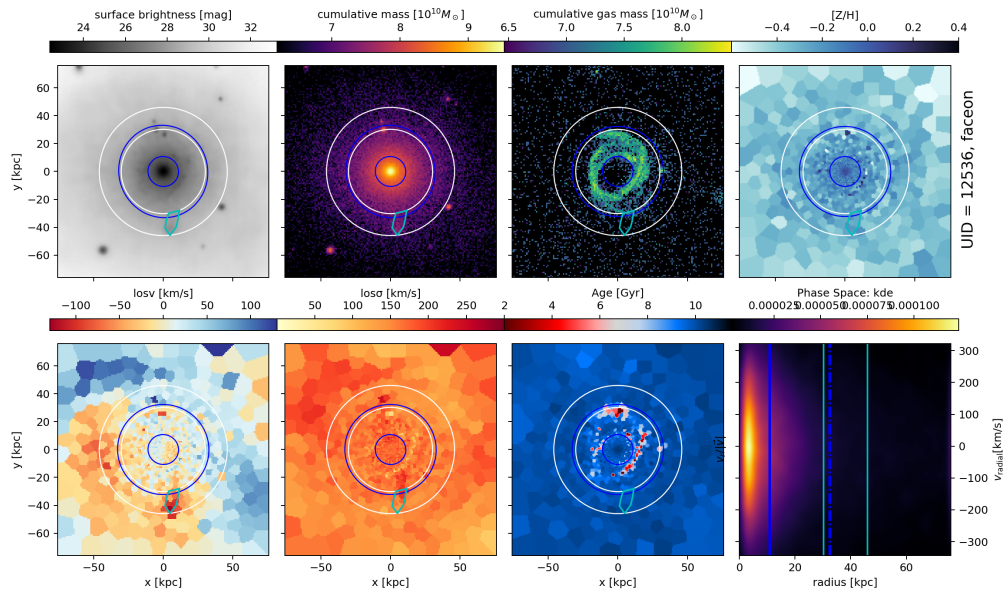


Figure D.82: UID 12536, Stream 3

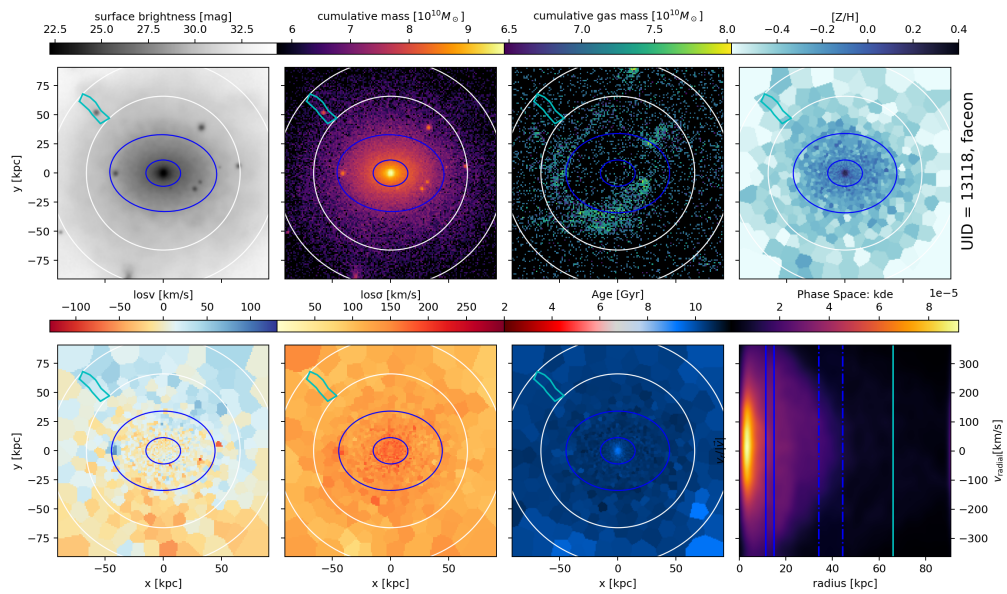


Figure D.83: UID 13118, Stream 3

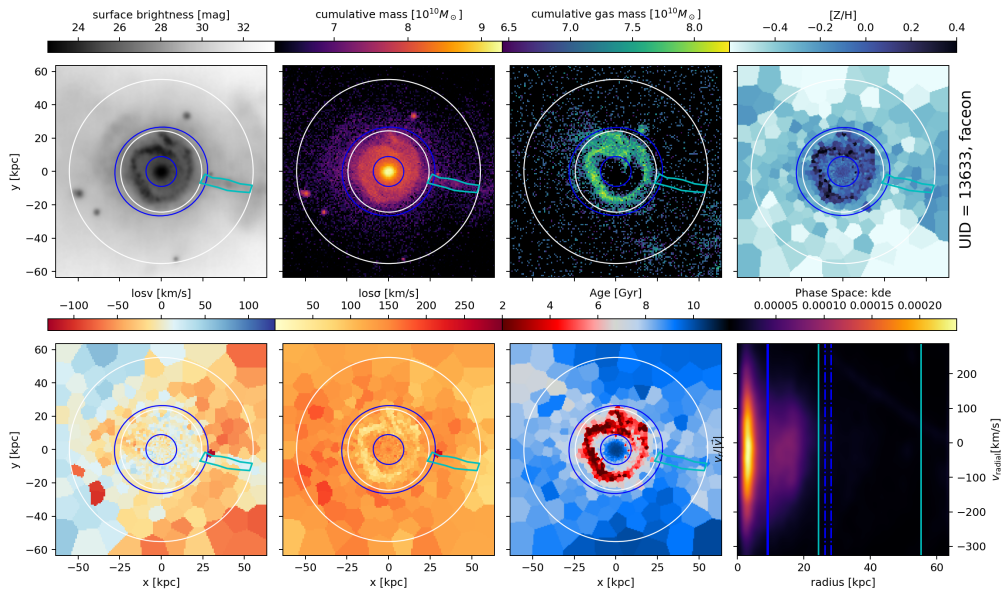


Figure D.84: UID 13633, Stream 1

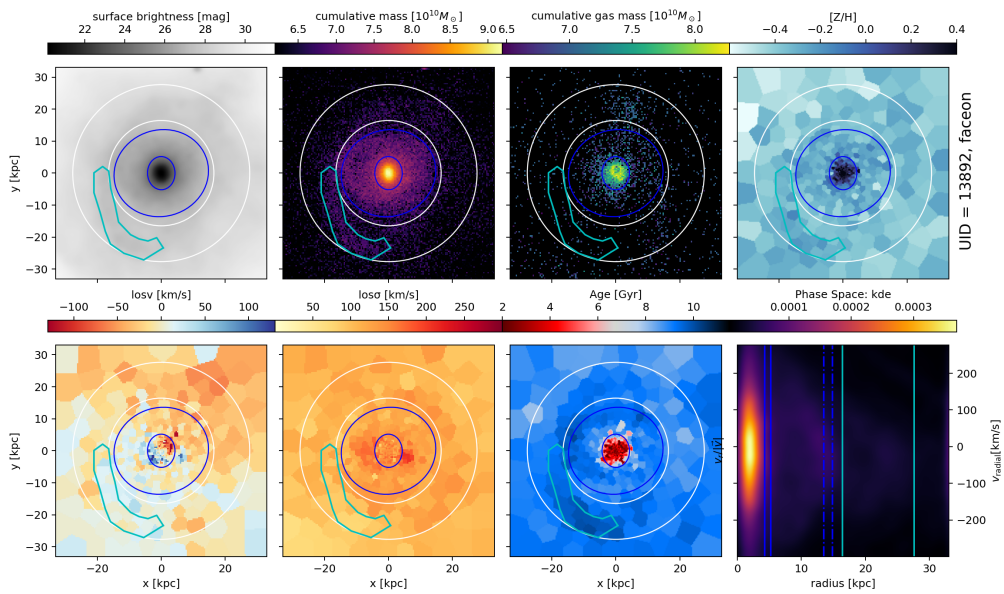


Figure D.85: UID 13892, Stream 1

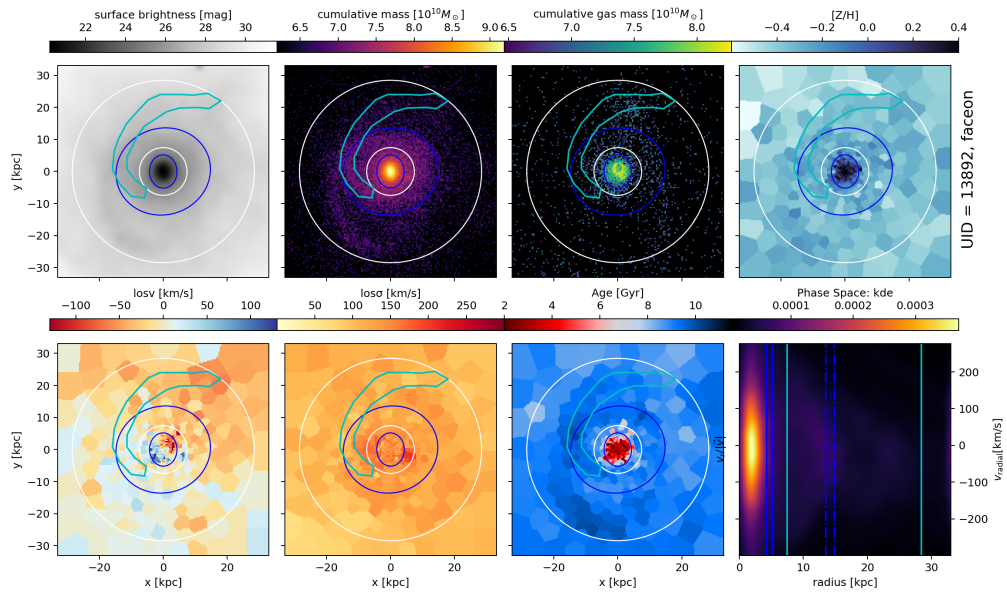


Figure D.86: UID 13892, Stream 2

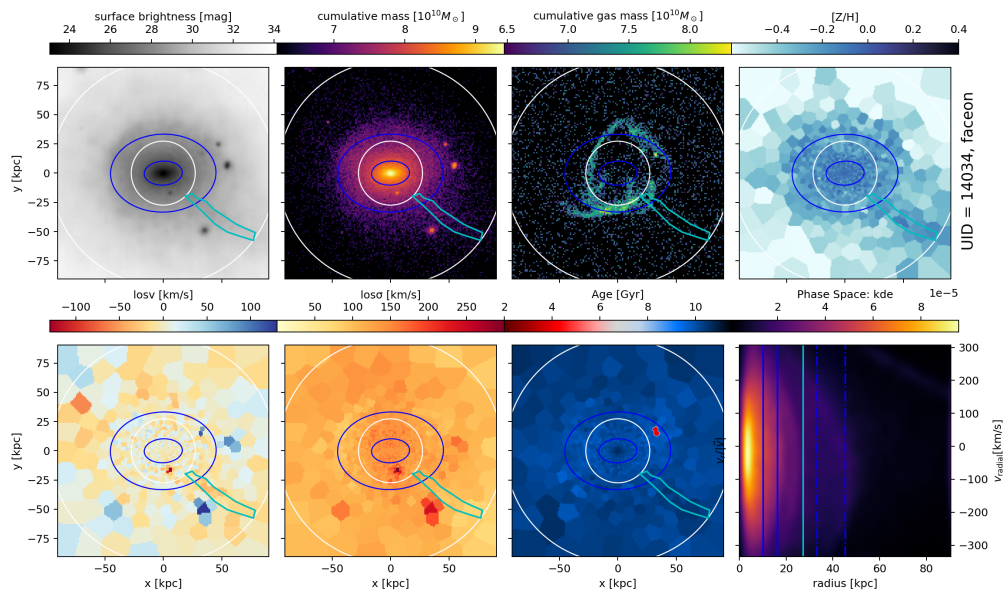


Figure D.87: UID 14034, Stream 1

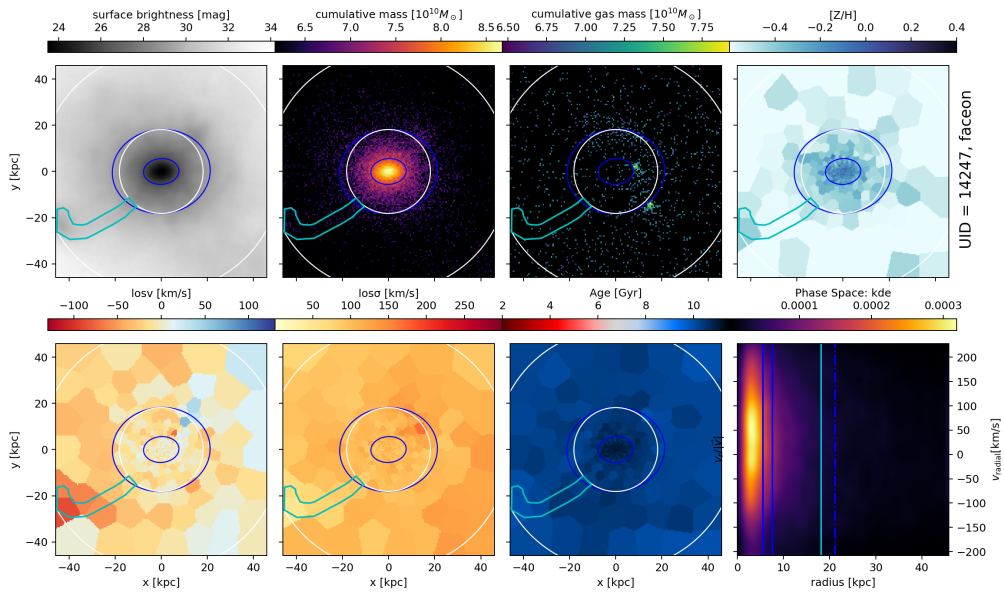


Figure D.88: UID 14247, Stream 1

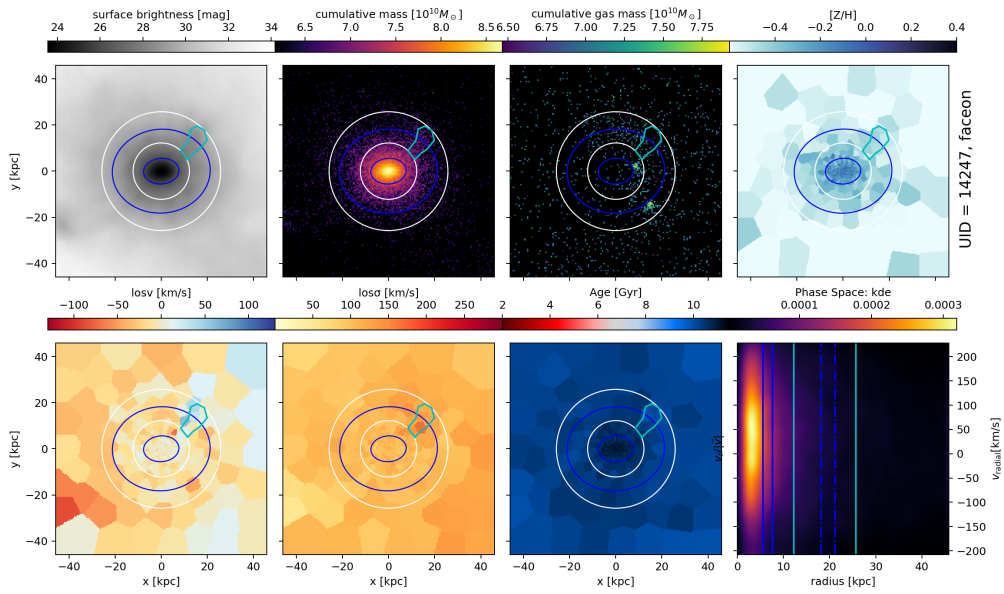


Figure D.89: UID 14247, Stream 2

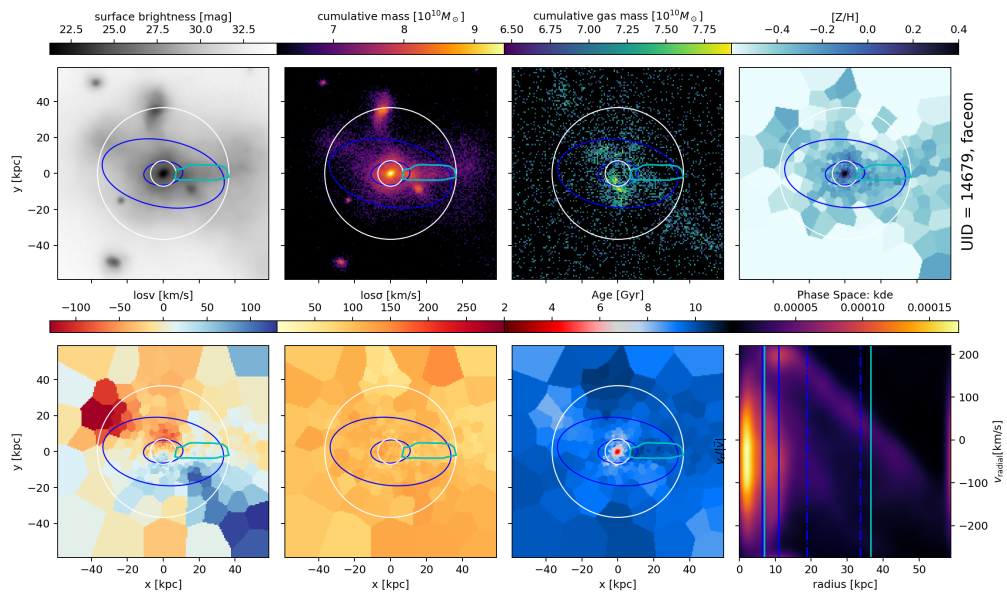


Figure D.90: UID 14679, Stream 1

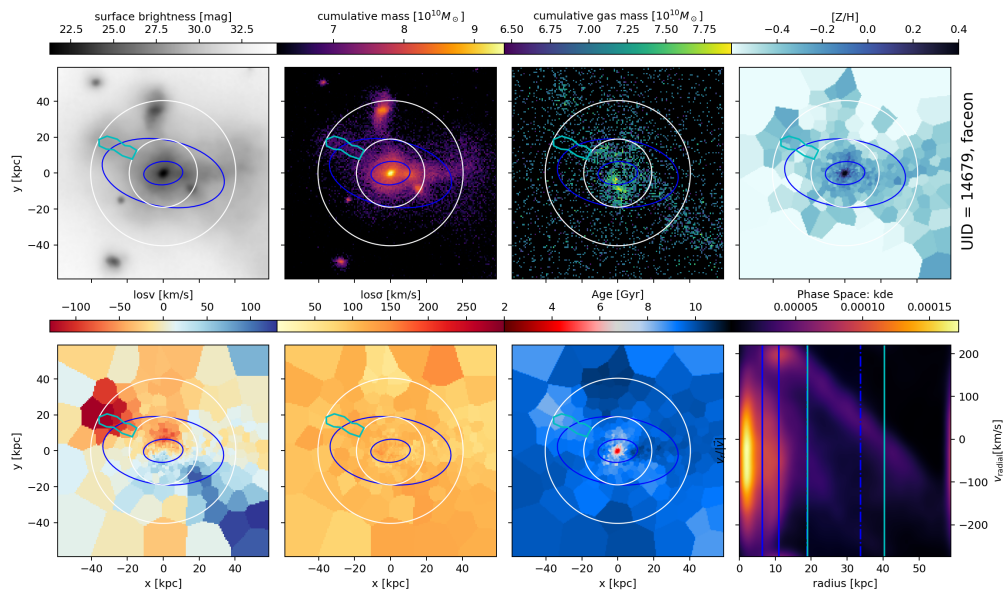


Figure D.91: UID 14679, Stream 2

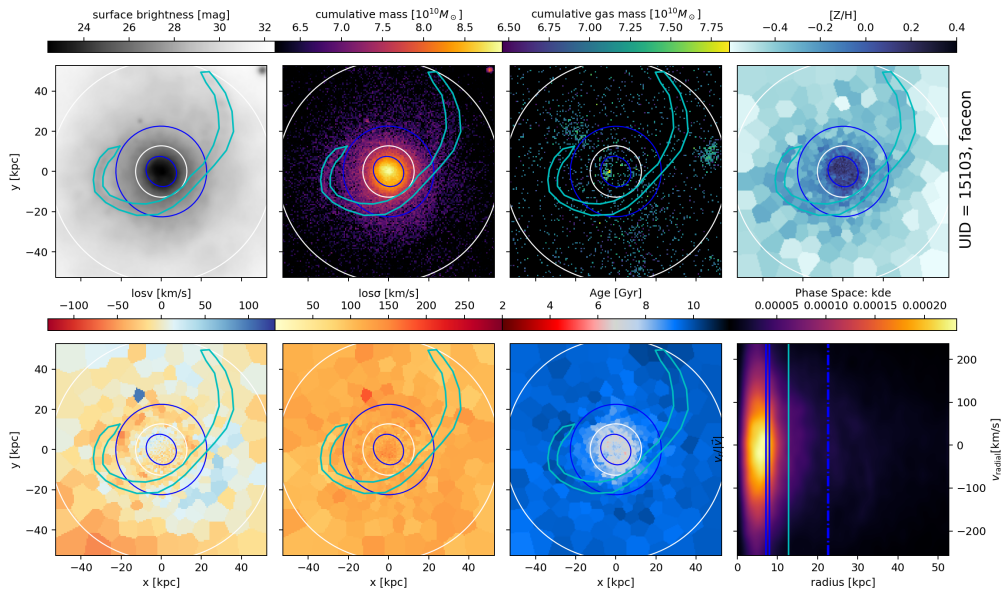


Figure D.92: UID 15301, Stream 1

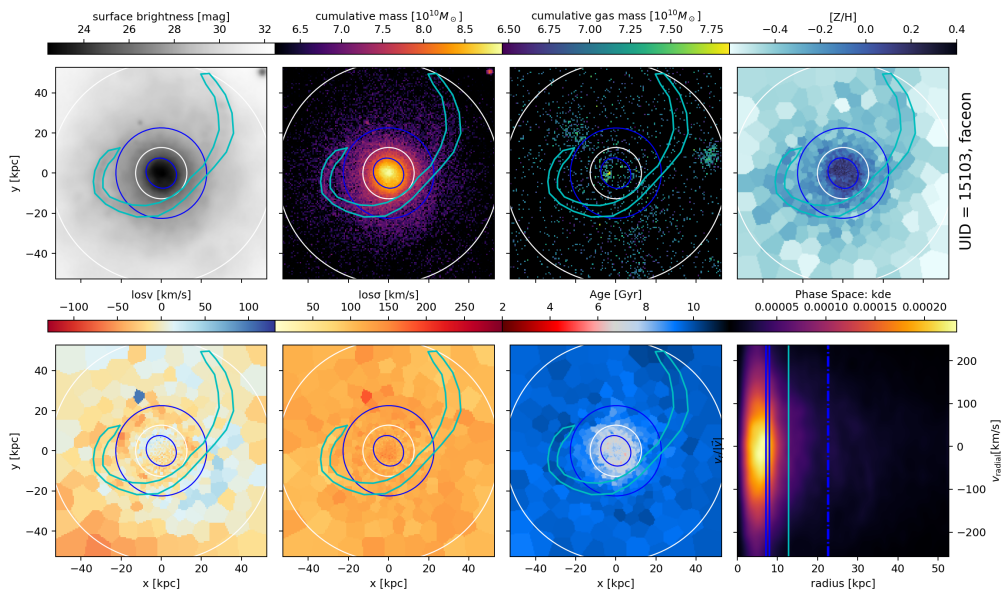


Figure D.93: UID 15103, Stream 1

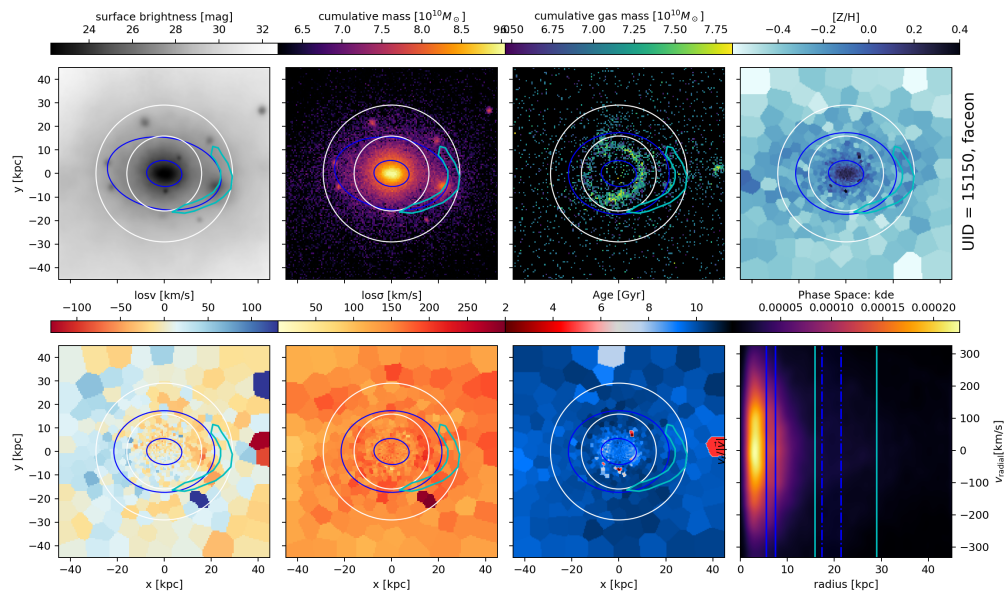


Figure D.94: UID 15150, Stream 1

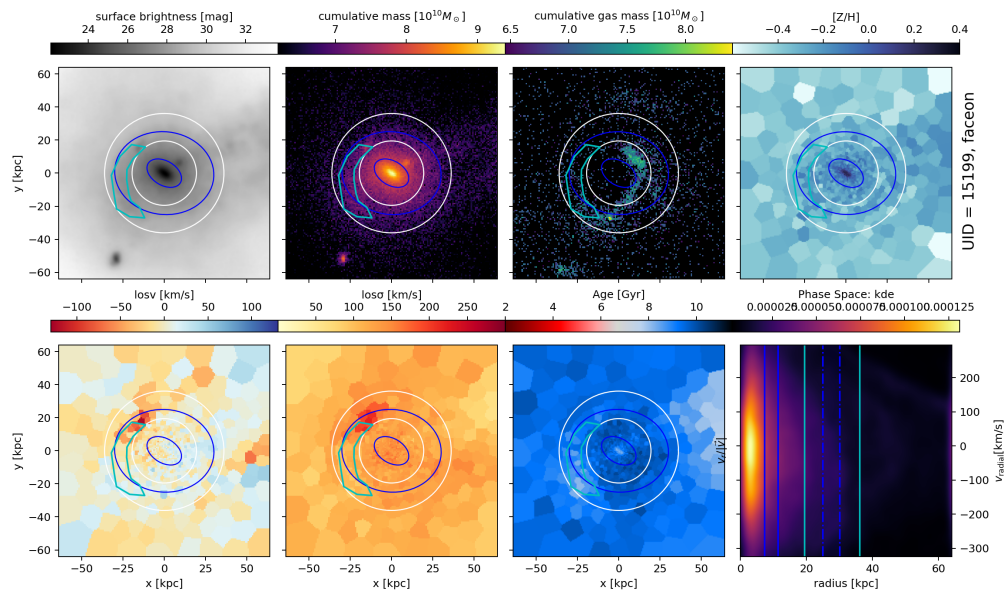


Figure D.95: UID 15199, Stream 1

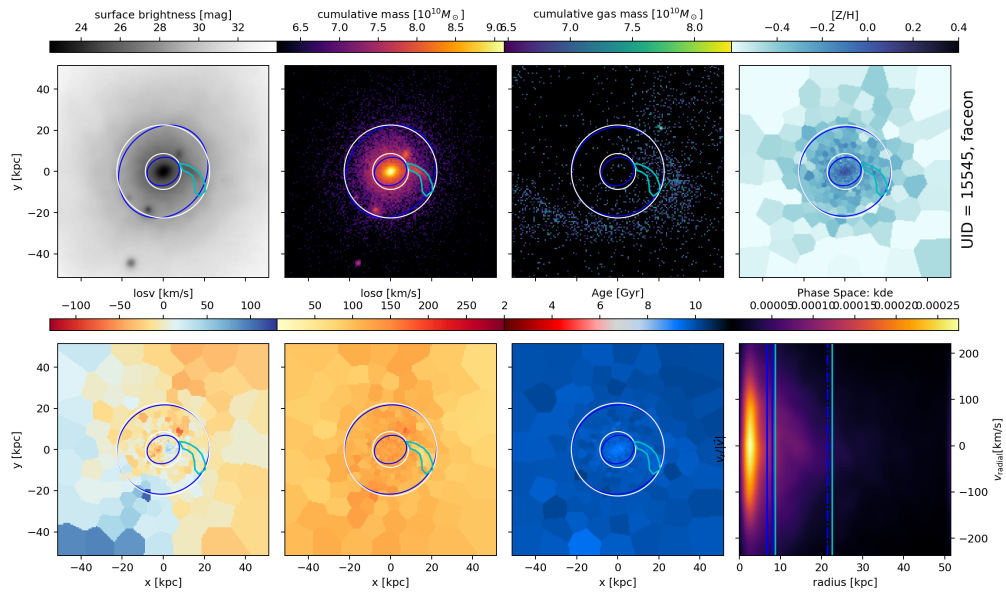


Figure D.96: UID 15545, Stream 1

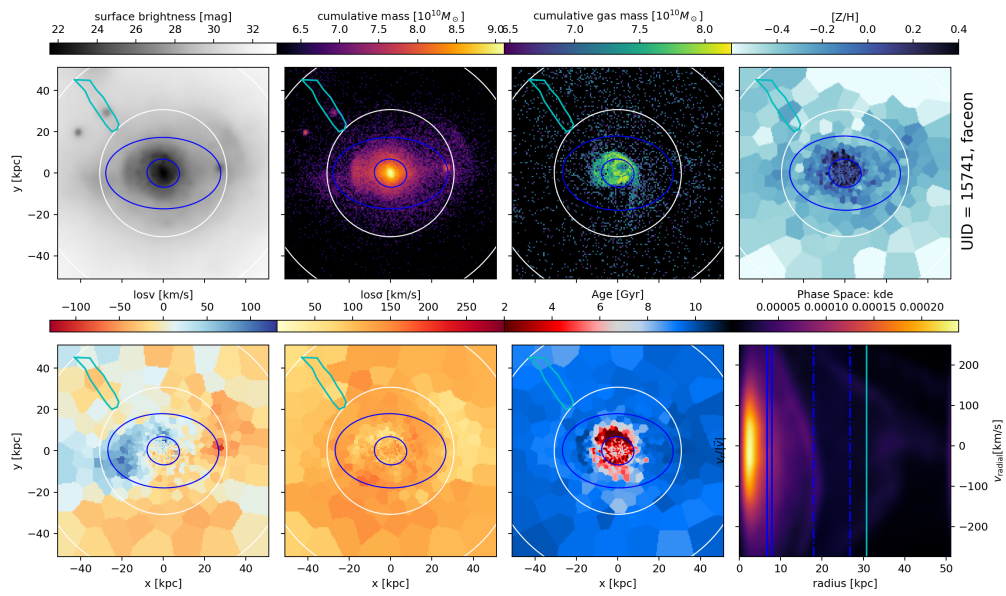


Figure D.97: UID 15741, Stream 1

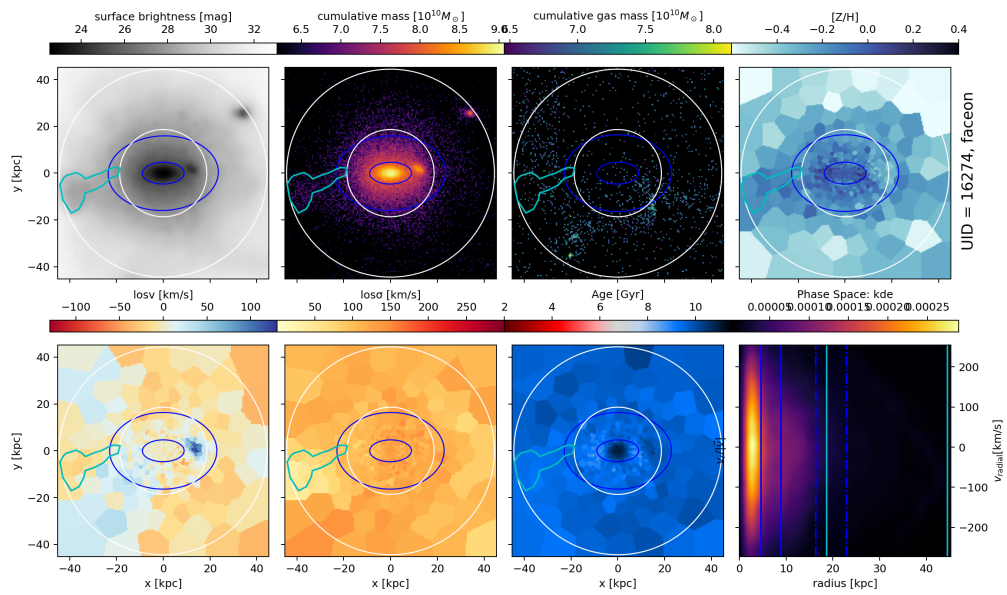


Figure D.98: UID 16274, Stream 1

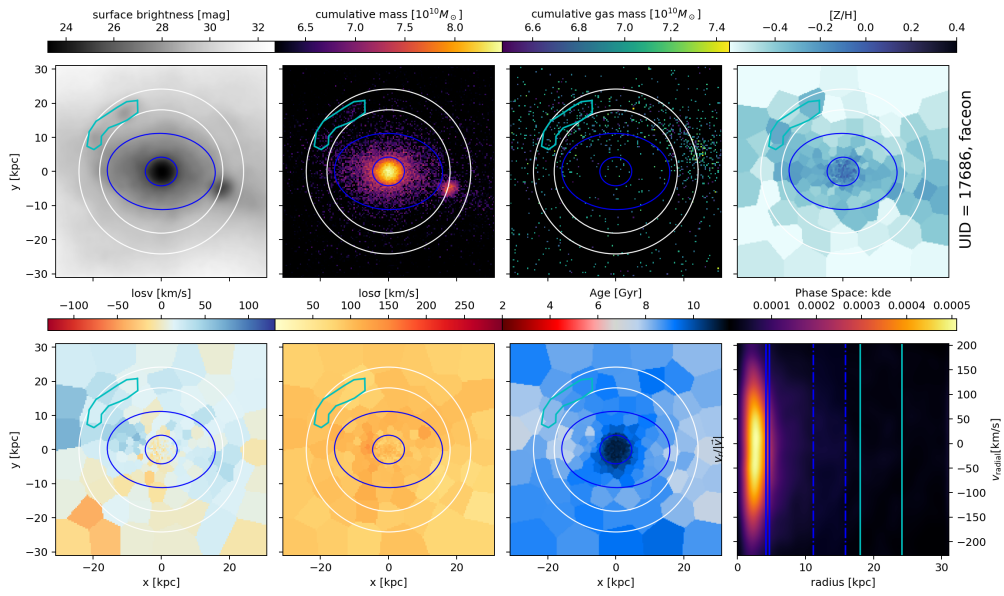


Figure D.99: UID 17686, Stream 1

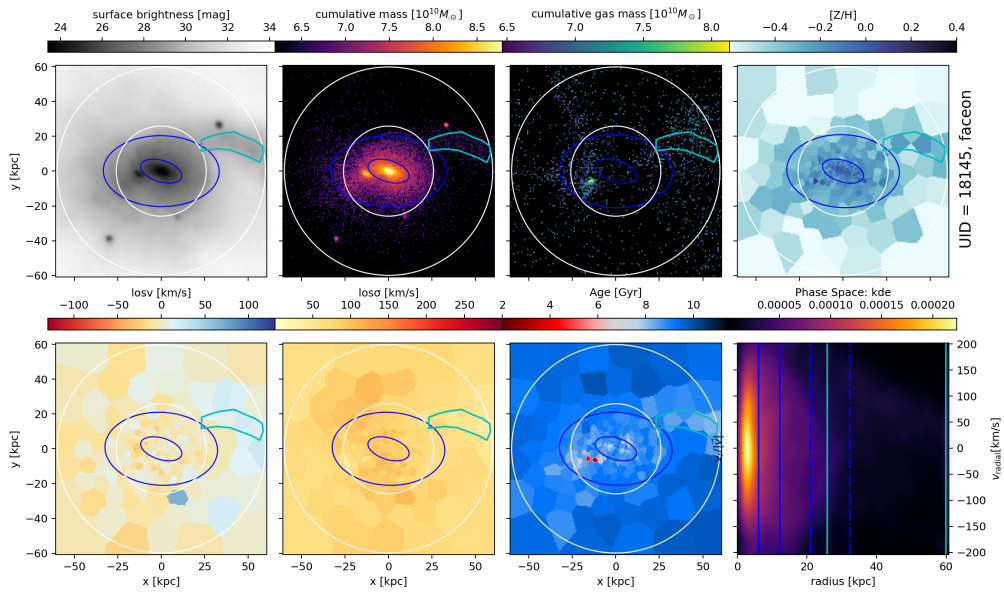


Figure D.100: UID 18145, Stream 1

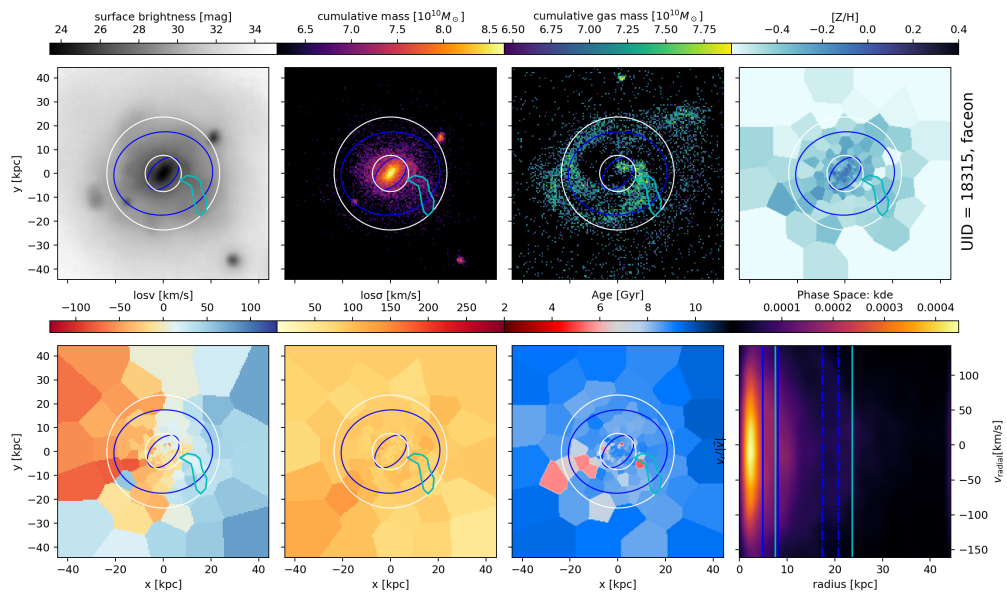


Figure D.101: UID 18315, Stream 1

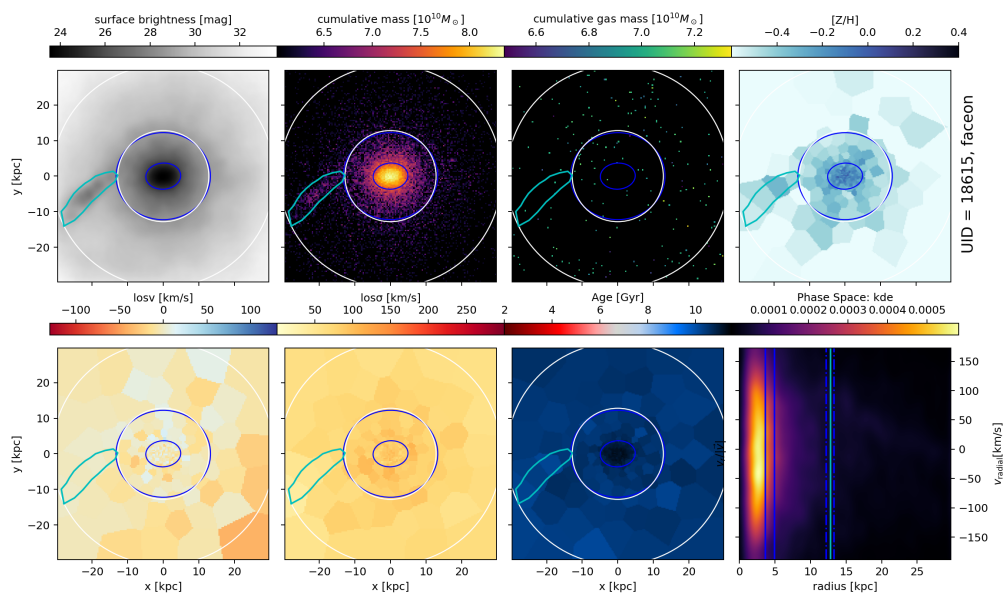


Figure D.102: UID 18615, Stream 1

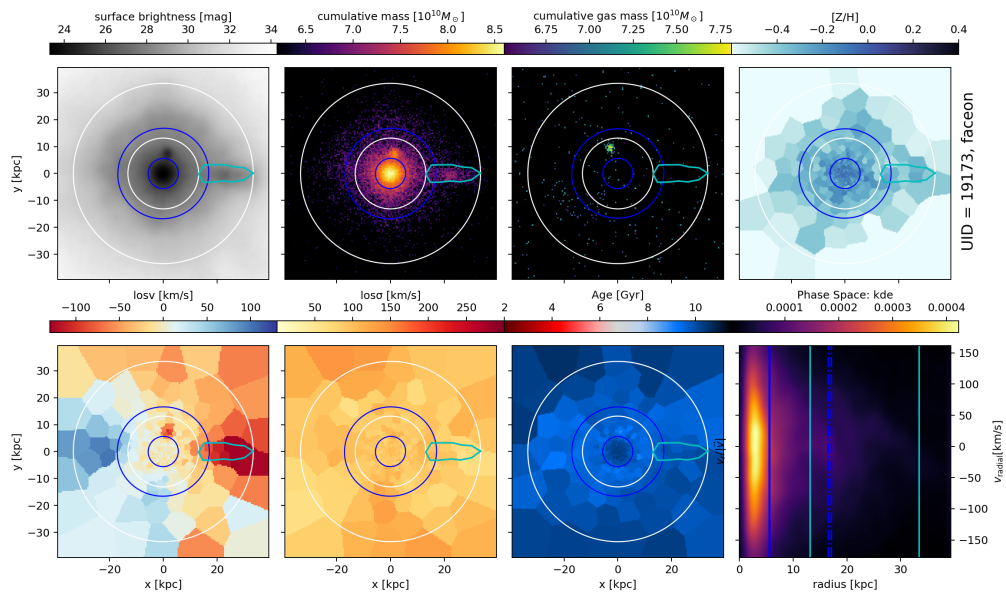


Figure D.103: UID 19173, Stream 1

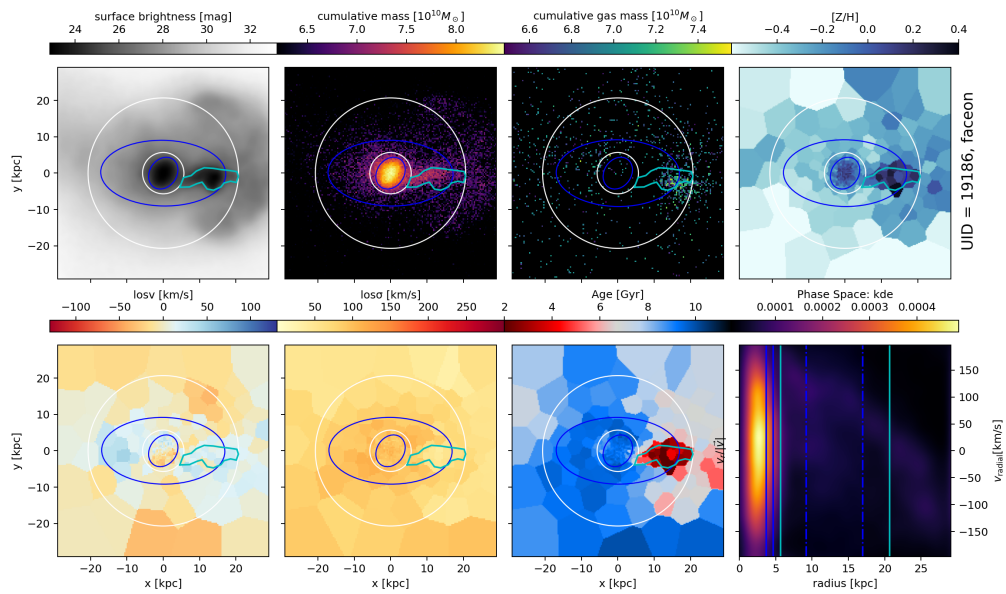


Figure D.104: UID 19186, Stream 1

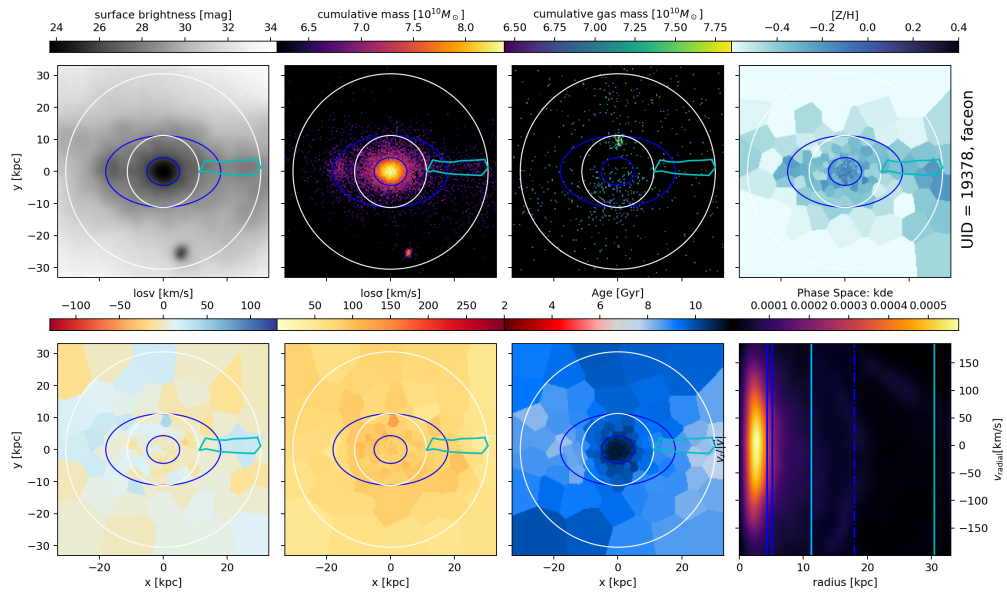


Figure D.105: UID 19378, Stream 1

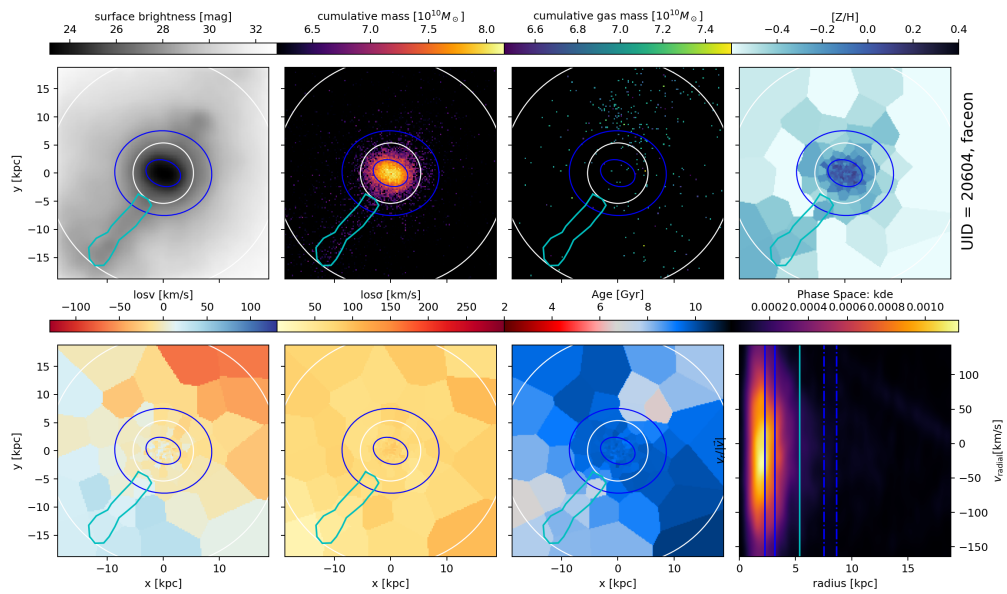


Figure D.106: UID 20604, Stream 1

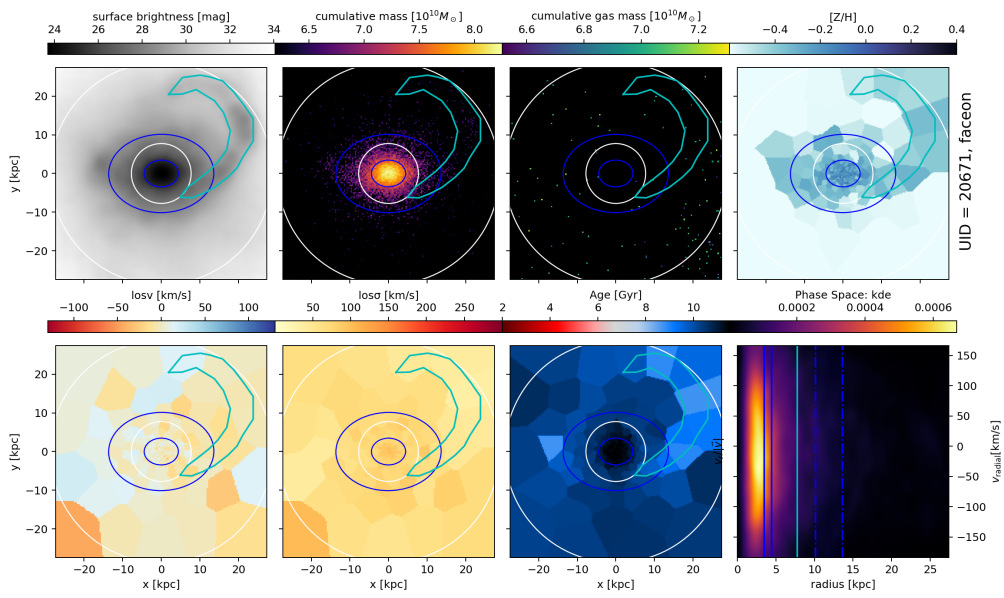


Figure D.107: UID 20671, Stream 1

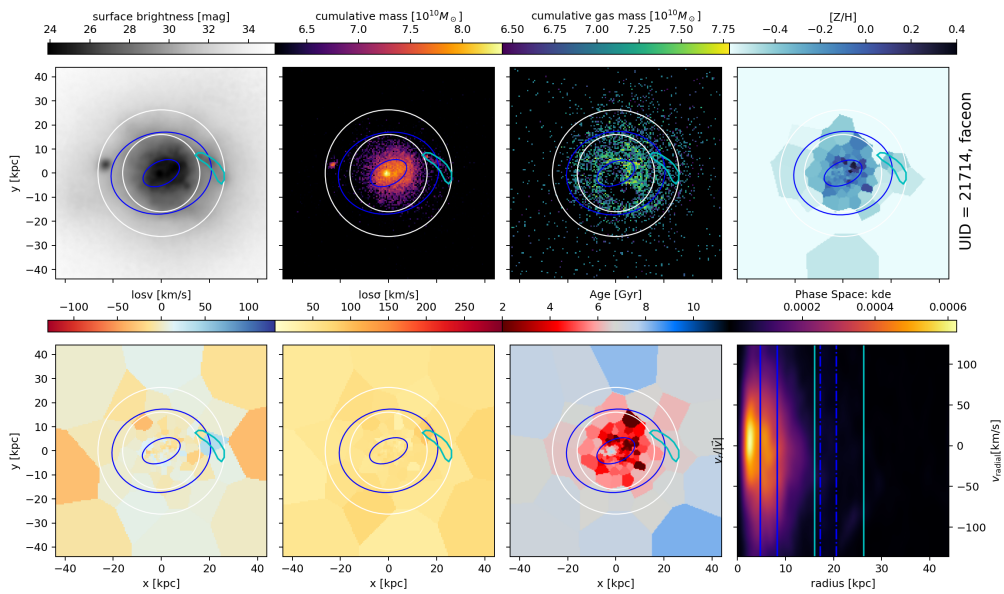


Figure D.108: UID 21714, Stream 1

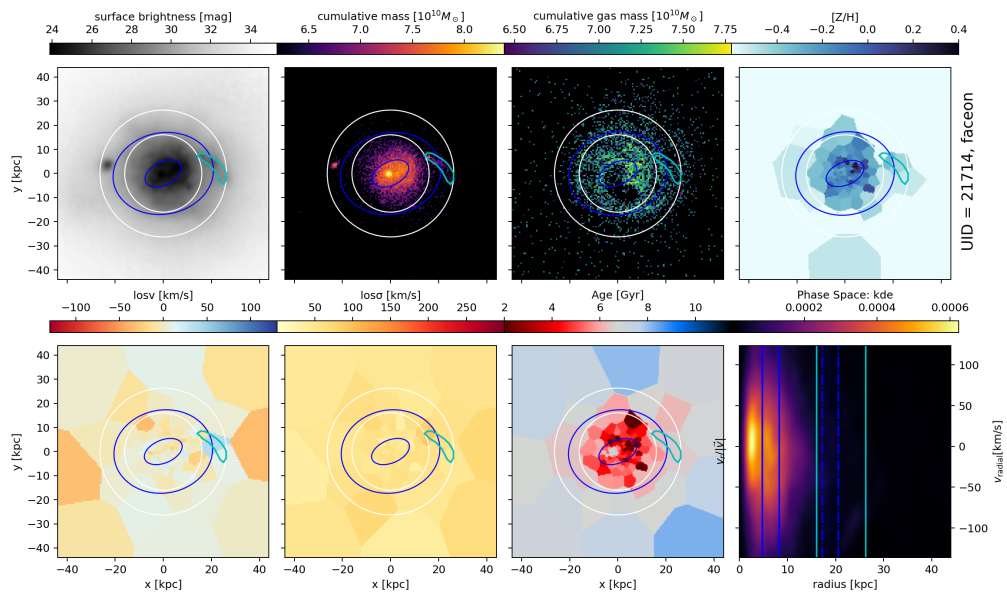


Figure D.109: UID 21714, Stream 1

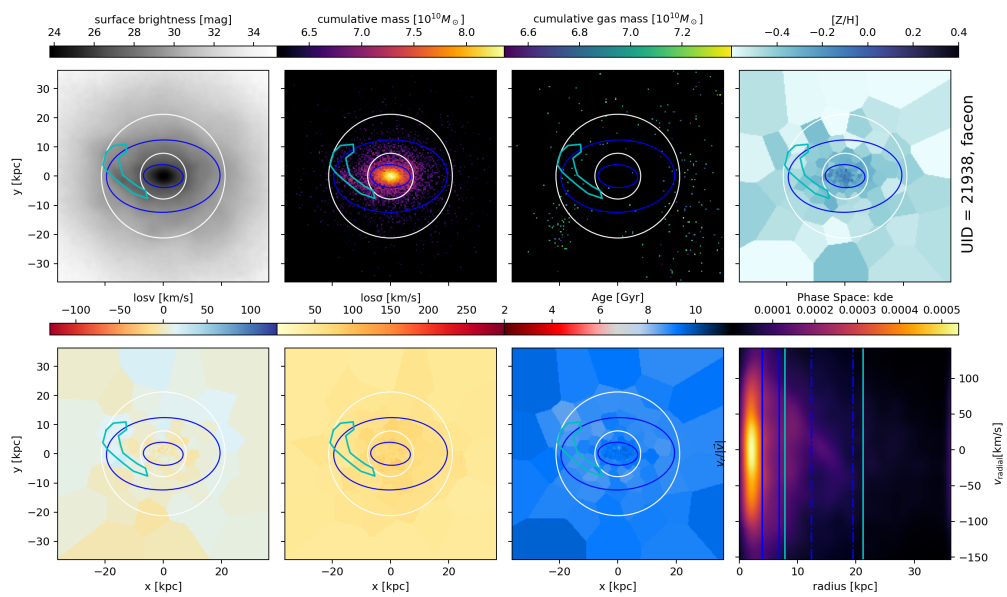


Figure D.110: UID 21938, Stream 1

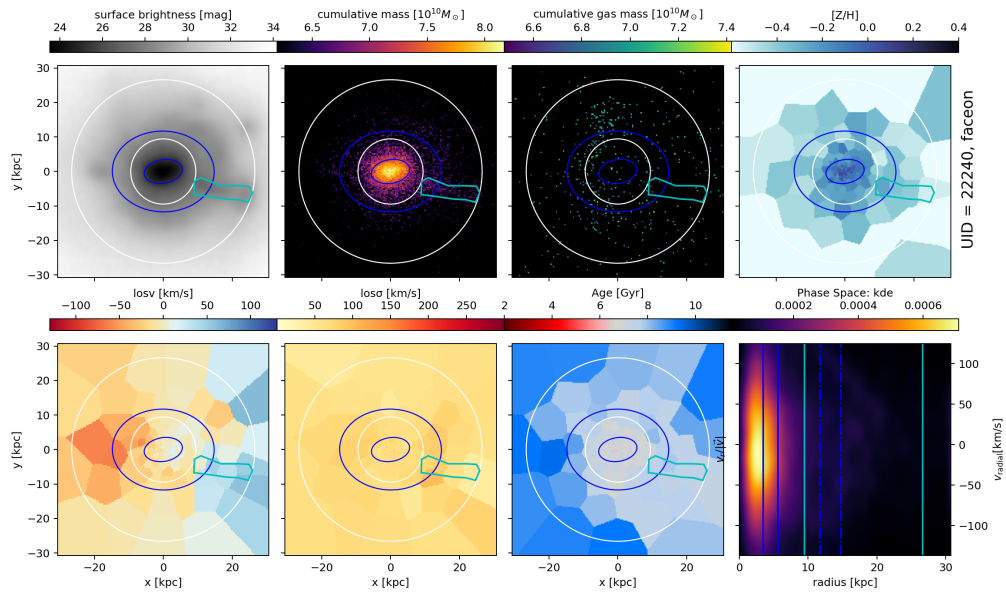


Figure D.111: UID 22240, Stream 1

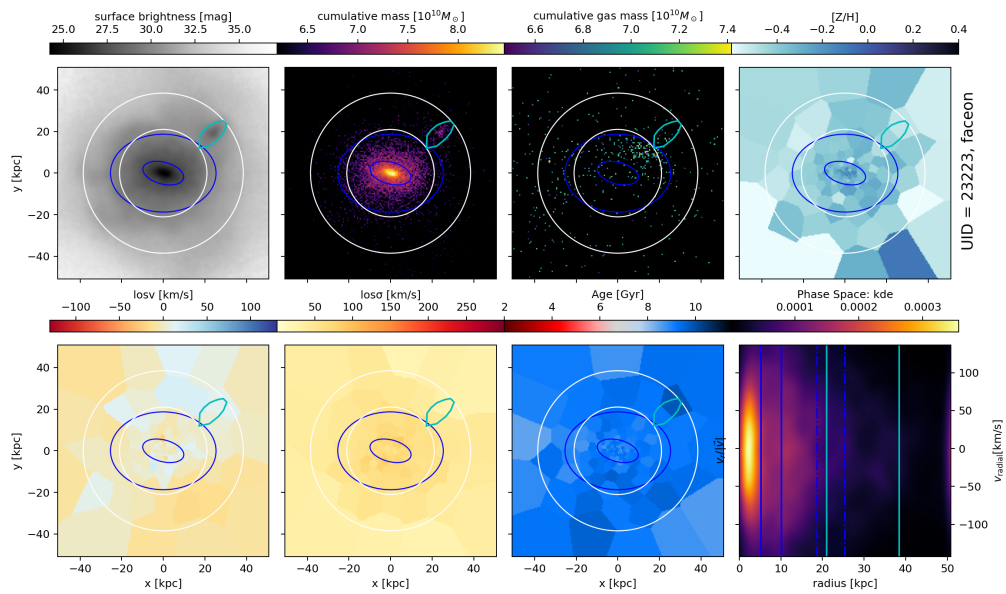


Figure D.112: UID 23223, Stream 1



# References

- Amorisco, N. C. (2015). On feathers, bifurcations and shells: The dynamics of tidal streams across the mass scale. *Monthly Notices of the Royal Astronomical Society*, 450, 575–591.
- Arp, H. (1966). Atlas of Peculiar Galaxies. *The Astrophysical Journal Supplement Series*, 14, 1.
- Asplund, M., Grevesse, N., Sauval, A. J., & Scott, P. (2009). The Chemical Composition of the Sun. *Annual Review of Astronomy and Astrophysics*, 47, 481–522.
- Aurenhammer, F. (1991). Voronoi diagrams—a survey of a fundamental geometric data structure. *ACM Comput. Surv.*, 23(3), 345–405.  
URL <https://doi.org/10.1145/116873.116880>
- Bacon, R., Copin, Y., Monnet, G., Miller, B. W., Allington-Smith, J. R., Bureau, M., Carollo, C. M., Davies, R. L., Emsellem, E., Kuntschner, H., Peletier, R. F., Verolme, E. K., & de Zeeuw, P. T. (2001). The SAURON project - I. The panoramic integral-field spectrograph. *Monthly Notices of the Royal Astronomical Society*, 326, 23–35.
- Barnes, K. L., van Zee, L., Dale, D. A., Staudaher, S., Bullock, J. S., Calzetti, D., Chandar, R., & Dalcanton, J. J. (2014). New Insights on the Formation and Assembly of M83 from Deep Near-infrared Imaging. *The Astrophysical Journal*, 789, 126.
- Beck, A. M., Murante, G., Arth, A., Remus, R. S., Teklu, A. F., Donnert, J. M. F., Planelles, S., Beck, M. C., Förster, P., Imgrund, M., Dolag, K., & Borgani, S. (2016). An improved SPH scheme for cosmological simulations. *Monthly Notices of the Royal Astronomical Society*, 455, 2110–2130.
- Bílek, M., Duc, P.-A., Cuillandre, J.-C., Gwyn, S., Cappellari, M., Bekaert, D. V., Bonfini, P., Bitsakis, T., Paudel, S., Krajnović, D., Durrell, P. R., & Marleau, F. (2020). Census and classification of low-surface-brightness structures in nearby early-type galaxies from the MATLAS survey. *Monthly Notices of the Royal Astronomical Society*, 498, 2138–2166.
- Bílek, M., Ebrova, I., Jungwiert, B., Jílkova, L., & Bartořkova, K. (2015). Shell galaxies as laboratories for testing MOND. *Canadian Journal of Physics*, 93, 203–212.
- Binney, J., & Merrifield, M. (1998). *Galactic Astronomy*.
- Binney, J., & Tremaine, S. (1987). *Galactic Dynamics*.

- Böss, L. M., & Valenzuela, L. M. (2024). LudwigBoess/GadgetIO.jl: V0.8.0. *Zenodo*.
- Bresolin, F., Kudritzki, R.-P., & Urbaneja, M. A. (2022). The Metallicity and Distance of NGC 2403 from Blue Supergiants. *The Astrophysical Journal*, *940*, 32.
- Bruzual, G., & Charlot, S. (2003). Stellar population synthesis at the resolution of 2003. *Monthly Notices of the Royal Astronomical Society*, *344*(4), 1000–1028.
- Bryant, J. J., Owers, M. S., Robotham, A. S. G., Croom, S. M., Driver, S. P., Drinkwater, M. J., Lorente, N. P. F., Cortese, L., Scott, N., Colless, M., Schaefer, A., Taylor, E. N., Konstantopoulos, I. S., Allen, J. T., Baldry, I., Barnes, L., Bauer, A. E., Bland-Hawthorn, J., Bloom, J. V., Brooks, A. M., Brough, S., Cecil, G., Couch, W., Croton, D., Davies, R., Ellis, S., Fogarty, L. M. R., Foster, C., Glazebrook, K., Goodwin, M., Green, A., Gunawardhana, M. L., Hampton, E., Ho, I. T., Hopkins, A. M., Kewley, L., Lawrence, J. S., Leon-Saval, S. G., Leslie, S., McElroy, R., Lewis, G., Liske, J., López-Sánchez, Á. R., Mahajan, S., Medling, A. M., Metcalfe, N., Meyer, M., Mould, J., Obreschkow, D., O’Toole, S., Pracy, M., Richards, S. N., Shanks, T., Sharp, R., Sweet, S. M., Thomas, A. D., Tonini, C., & Walcher, C. J. (2015). The SAMI Galaxy Survey: Instrument specification and target selection. *Monthly Notices of the Royal Astronomical Society*, *447*, 2857–2879.
- Buitrago, F., & Trujillo, I. (2024). Strong size evolution of disc galaxies since  $z = 1$ . Readdressing galaxy growth using a physically motivated size indicator. *Astronomy and Astrophysics*, *682*, A110.
- Bundy, K., Bershady, M. A., Law, D. R., Yan, R., Drory, N., MacDonald, N., Wake, D. A., Cherinka, B., Sánchez-Gallego, J. R., Weijmans, A.-M., Thomas, D., Tremonti, C., Masters, K., Coccato, L., Diamond-Stanic, A. M., Aragón-Salamanca, A., Avila-Reese, V., Badenes, C., Falcón-Barroso, J., Belfiore, F., Bizyaev, D., Blanc, G. A., Bland-Hawthorn, J., Blanton, M. R., Brownstein, J. R., Byler, N., Cappellari, M., Conroy, C., Dutton, A. A., Emsellem, E., Etherington, J., Frinchaboy, P. M., Fu, H., Gunn, J. E., Harding, P., Johnston, E. J., Kauffmann, G., Kinemuchi, K., Klaene, M. A., Knapen, J. H., Leauthaud, A., Li, C., Lin, L., Maiolino, R., Malanushenko, V., Malanushenko, E., Mao, S., Maraston, C., McDermid, R. M., Merrifield, M. R., Nichol, R. C., Oravetz, D., Pan, K., Parejko, J. K., Sanchez, S. F., Schlegel, D., Simmons, A., Steele, O., Steinmetz, M., Thanjavur, K., Thompson, B. A., Tinker, J. L., van den Bosch, R. C. E., Westfall, K. B., Wilkinson, D., Wright, S., Xiao, T., & Zhang, K. (2015). Overview of the SDSS-IV MaNGA Survey: Mapping nearby Galaxies at Apache Point Observatory. *The Astrophysical Journal*, *798*, 7.
- Caldwell, N. (1983). Structure and stellar content of dwarf elliptical galaxies. *The Astronomical Journal*, *88*, 804–812.
- Caon, N., Capaccioli, M., & D’Onofrio, M. (1993). On the shape of the light profiles of early-type galaxies. *Monthly Notices of the Royal Astronomical Society*, *265*, 1013–1021.

- Cappellari, M. (2016). Structure and Kinematics of Early-Type Galaxies from Integral Field Spectroscopy. *Annual Review of Astronomy and Astrophysics*, 54, 597–665.
- Cappellari, M., & Copin, Y. (2003). Adaptive spatial binning of integral-field spectroscopic data using Voronoi tessellations. *Monthly Notices of the Royal Astronomical Society*, 342, 345–354.
- Cappellari, M., Emsellem, E., Krajnović, D., McDermid, R. M., Scott, N., Verdoes Kleijn, G. A., Young, L. M., Alatalo, K., Bacon, R., Blitz, L., Bois, M., Bournaud, F., Bureau, M., Davies, R. L., Davis, T. A., de Zeeuw, P. T., Duc, P.-A., Khochfar, S., Kuntschner, H., Lablanche, P.-Y., Morganti, R., Naab, T., Oosterloo, T., Sarzi, M., Serra, P., & Weijmans, A.-M. (2011). The ATLAS3D project - I. A volume-limited sample of 260 nearby early-type galaxies: Science goals and selection criteria. *Monthly Notices of the Royal Astronomical Society*, 413, 813–836.
- Chabrier, G. (2003). Galactic Stellar and Substellar Initial Mass Function. *Publications of the Astronomical Society of the Pacific*, 115, 763–795.
- Cheng, Y., Gialvalisco, M., Simons, R. C., Ji, Z., Stroupe, D., & Cleri, N. J. (2024). Exploring the Gas-phase Metallicity Gradients of Star-forming Galaxies at Cosmic Noon. *The Astrophysical Journal*, 964, 94.
- Cowie, L. L., Songaila, A., Hu, E. M., & Cohen, J. G. (1996). New Insight on Galaxy Formation and Evolution From Keck Spectroscopy of the Hawaii Deep Fields. *The Astronomical Journal*, 112, 839.
- Croom, S. M., Lawrence, J. S., Bland-Hawthorn, J., Bryant, J. J., Fogarty, L., Richards, S., Goodwin, M., Farrell, T., Miziarski, S., Heald, R., Jones, D. H., Lee, S., Colless, M., Brough, S., Hopkins, A. M., Bauer, A. E., Birchall, M. N., Ellis, S., Horton, A., Leon-Saval, S., Lewis, G., López-Sánchez, Á. R., Min, S.-S., Trinh, C., & Trowland, H. (2012). The Sydney-AAO Multi-object Integral field spectrograph. *Monthly Notices of the Royal Astronomical Society*, 421, 872–893.
- Davies, B., Kudritzki, R.-P., Lardo, C., Bergemann, M., Beasor, E., Plez, B., Evans, C., Bastian, N., & Patrick, L. R. (2017). Red Supergiants as Cosmic Abundance Probes: Massive Star Clusters in M83 and the Mass-Metallicity Relation of Nearby Galaxies. *The Astrophysical Journal*, 847, 112.
- Davis, M., Efstathiou, G., Frenk, C. S., & White, S. D. M. (1985). The evolution of large-scale structure in a universe dominated by cold dark matter. *The Astrophysical Journal*, 292, 371–394.
- de Vaucouleurs, G. (1948). Recherches sur les Nebuleuses Extragalactiques. *Annales d'Astrophysique*, 11, 247.

- de Vaucouleurs, G. (1963). Revised Classification of 1500 Bright Galaxies. *The Astrophysical Journal Supplement Series*, 8, 31.
- de Zeeuw, P. T., Bureau, M., Emsellem, E., Bacon, R., Carollo, C. M., Copin, Y., Davies, R. L., Kuntschner, H., Miller, B. W., Monnet, G., Peletier, R. F., & Verolme, E. K. (2002). The SAURON project - II. Sample and early results. *Monthly Notices of the Royal Astronomical Society*, 329, 513–530.
- Dehnen, W., & Aly, H. (2012). Improving convergence in smoothed particle hydrodynamics simulations without pairing instability. *Monthly Notices of the Royal Astronomical Society*, 425, 1068–1082.
- D'Eugenio, F., Colless, M., Groves, B., Bian, F., & Barone, T. M. (2018). The gas-phase metallicities of star-forming galaxies in aperture-matched SDSS samples follow potential rather than mass or average surface density. *Monthly Notices of the Royal Astronomical Society*, 479, 1807–1821.
- Dolag, K., Borgani, S., Murante, G., & Springel, V. (2009). Substructures in hydrodynamical cluster simulations. *Monthly Notices of the Royal Astronomical Society*, 399, 497–514.
- Dolag, K., Hansen, F. K., Roncarelli, M., & Moscardini, L. (2005a). The imprints of local superclusters on the Sunyaev-Zel'dovich signals and their detectability with Planck. *Monthly Notices of the Royal Astronomical Society*, 363, 29–39.
- Dolag, K., Jubelgas, M., Springel, V., Borgani, S., & Rasia, E. (2004). Thermal Conduction in Simulated Galaxy Clusters. *The Astrophysical Journal*, 606, L97–L100.
- Dolag, K., Mevius, E., & Remus, R.-S. (2017). Distribution and Evolution of Metals in the Magneticum Simulations. *Galaxies*, 5, 35.
- Dolag, K., Vazza, F., Brunetti, G., & Tormen, G. (2005b). Turbulent gas motions in galaxy cluster simulations: The role of smoothed particle hydrodynamics viscosity. *Monthly Notices of the Royal Astronomical Society*, 364, 753–772.
- Donlon, T., Newberg, H. J., Sanderson, R., Bregou, E., Horta, D., Arora, A., & Panithanpaisal, N. (2024). The debris of the 'last major merger' is dynamically young. *Monthly Notices of the Royal Astronomical Society*, 531, 1422–1439.
- Duc, P. A., Cuillandre, J. C., Alatalo, K., Blitz, L., Bois, M., Bournaud, F., Bureau, M., Cappellari, M., Côté, P., Davies, R. L., Davis, T. A., de Zeeuw, P. T., Emsellem, E., Ferrarese, L., Ferriere, E., Gwyn, S., Khochfar, S., Krajnovic, D., Kuntschner, H., Lablanche, P. Y., McDermid, R. M., Michel-Dansac, L., Morganti, R., Naab, T., Oosterloo, T., Sarzi, M., Scott, N., Serra, P., Weijmans, A., & Young, L. M. (2013). Probing the mass assembly of massive nearby galaxies with deep imaging. 295, 358–361.

- Duc, P.-A., Cuillandre, J.-C., Karabal, E., Cappellari, M., Alatalo, K., Blitz, L., Bournaud, F., Bureau, M., Crocker, A. F., Davies, R. L., Davis, T. A., de Zeeuw, P. T., Emsellem, E., Khochfar, S., Krajnović, D., Kuntschner, H., McDermid, R. M., Michel-Dansac, L., Morganti, R., Naab, T., Oosterloo, T., Paudel, S., Sarzi, M., Scott, N., Serra, P., Weijmans, A.-M., & Young, L. M. (2015). The ATLAS3D project - XXIX. The new look of early-type galaxies and surrounding fields disclosed by extremely deep optical images. *Monthly Notices of the Royal Astronomical Society*, *446*, 120–143.
- Ebrova, I., Bilek, M., Vudragovic, A., Yildız, M. K., & Duc, P.-A. (2021). Ubiquitous signs of interactions in early-type galaxies with prolate rotation. *Astronomy and Astrophysics*, *650*, A50.
- Ebrova, I., & Łokas, E. L. (2017). Galaxies with Prolate Rotation in Illustris. *The Astrophysical Journal*, *850*, 144.
- Emsellem, E., Cappellari, M., Krajnović, D., Alatalo, K., Blitz, L., Bois, M., Bournaud, F., Bureau, M., Davies, R. L., Davis, T. A., de Zeeuw, P. T., Khochfar, S., Kuntschner, H., Lablanche, P.-Y., McDermid, R. M., Morganti, R., Naab, T., Oosterloo, T., Sarzi, M., Scott, N., Serra, P., van de Ven, G., Weijmans, A.-M., & Young, L. M. (2011). The ATLAS3D project - III. A census of the stellar angular momentum within the effective radius of early-type galaxies: Unveiling the distribution of fast and slow rotators. *Monthly Notices of the Royal Astronomical Society*, *414*, 888–912.
- Emsellem, E., Cappellari, M., Krajnović, D., van de Ven, G., Bacon, R., Bureau, M., Davies, R. L., de Zeeuw, P. T., Falcon-Barroso, J., Kuntschner, H., McDermid, R., Peletier, R. F., & Sarzi, M. (2007). The SAURON project - IX. A kinematic classification for early-type galaxies. *Monthly Notices of the Royal Astronomical Society*, *379*, 401–417.
- Fabjan, D., Borgani, S., Tornatore, L., Saro, A., Murante, G., & Dolag, K. (2010). Simulating the effect of active galactic nuclei feedback on the metal enrichment of galaxy clusters. *Monthly Notices of the Royal Astronomical Society*, *401*, 1670–1690.
- Forbes, D. A., & Remus, R.-S. (2018). Metallicity gradients in the globular cluster systems of early-type galaxies: In situ and accreted components? *Monthly Notices of the Royal Astronomical Society*, *479*, 4760–4769.
- Francis, C., & Anderson, E. (2014). Two estimates of the distance to the Galactic Centre. *Monthly Notices of the Royal Astronomical Society*, *441*, 1105–1114.
- Gallazzi, A., Charlot, S., Brinchmann, J., White, S. D. M., & Tremonti, C. A. (2005). The ages and metallicities of galaxies in the local universe. *Monthly Notices of the Royal Astronomical Society*, *362*, 41–58.
- Goddard, D., Thomas, D., Maraston, C., Westfall, K., Etherington, J., Riffel, R., Mallmann, N. D., Zheng, Z., Argudo-Fernandez, M., Lian, J., Bershadsky, M., Bundy, K., Drory, N.,

- Law, D., Yan, R., Wake, D., Weijmans, A., Bizyaev, D., Brownstein, J., Lane, R. R., Maiolino, R., Masters, K., Merrifield, M., Nitschelm, C., Pan, K., Roman-Lopes, A., Storchi-Bergmann, T., & Schneider, D. P. (2017). SDSS-IV MaNGA: Spatially resolved star formation histories in galaxies as a function of galaxy mass and type. *Monthly Notices of the Royal Astronomical Society*, 466, 4731–4758.
- González Delgado, R. M., García-Benito, R., Pérez, E., Cid Fernandes, R., de Amorim, A. L., Cortijo-Ferrero, C., Lacerda, E. A. D., López Fernández, R., Vale-Asari, N., Sánchez, S. F., Mollá, M., Ruiz-Lara, T., Sánchez-Blázquez, P., Walcher, C. J., Alves, J., Aguerri, J. A. L., Bekeraite, S., Bland-Hawthorn, J., Galbany, L., Gallazzi, A., Husemann, B., Iglesias-Páramo, J., Kalinova, V., López-Sánchez, A. R., Marino, R. A., Márquez, I., Masegosa, J., Mast, D., Méndez-Abreu, J., Mendoza, A., del Olmo, A., Pérez, I., Quirrenbach, A., & Zibetti, S. (2015). The CALIFA survey across the Hubble sequence. Spatially resolved stellar population properties in galaxies. *Astronomy and Astrophysics*, 581, A103.
- Guérou, A., Emsellem, E., McDermid, R. M., Côté, P., Ferrarese, L., Blakeslee, J. P., Durrell, P. R., MacArthur, L. A., Peng, E. W., Cuillandre, J.-C., & Gwyn, S. (2015). The Next Generation Virgo Cluster Survey. XII. Stellar Populations and Kinematics of Compact, Low-mass Early-type Galaxies from Gemini GMOS-IFU Spectroscopy. *The Astrophysical Journal*, 804, 70.
- Harris, W. E., Remus, R.-S., Harris, G. L. H., & Babyk, Iu. V. (2020). Measuring Dark Matter in Galaxies: The Mass Fraction within Five Effective Radii. *The Astrophysical Journal*, 905, 28.
- Hegde, S., Bryan, G. L., & Genel, S. (2022). Reorientation Rates of Structural and Kinematic Axes in Simulated Massive Galaxies and the Origins of Prolate Rotation. *The Astrophysical Journal*, 937, 38.
- Hemler, Z. S., Torrey, P., Qi, J., Hernquist, L., Vogelsberger, M., Ma, X., Kewley, L. J., Nelson, D., Pillepich, A., Pakmor, R., & Marinacci, F. (2021). Gas-phase metallicity gradients of TNG50 star-forming galaxies. *Monthly Notices of the Royal Astronomical Society*, 506, 3024–3048.
- Hirschmann, M., Dolag, K., Saro, A., Bachmann, L., Borgani, S., & Burkert, A. (2014). Cosmological simulations of black hole growth: AGN luminosities and downsizing. *Monthly Notices of the Royal Astronomical Society*, 442, 2304–2324.
- Hoffman, L., Cox, T. J., Dutta, S., & Hernquist, L. (2010). Orbital Structure of Merger Remnants. I. Effect of Gas Fraction in Pure Disk Mergers. *The Astrophysical Journal*, 723, 818–844.
- Hogg, D. W. (1999). Distance measures in cosmology. *arXiv e-prints*, (pp. astro-ph/9905116).
- Hubble, E. P. (1926). Extragalactic nebulae. *The Astrophysical Journal*, 64, 321–369.

- Hubble, E. P. (1936). *Realm of the Nebulae*.
- Hubble, Edwin. (1925). No. 304. N.G.C. 6822, a remote stellar system. *Contributions from the Mount Wilson Observatory / Carnegie Institution of Washington*, 304, 1–25.
- Illingworth, G. (1977). Rotation (?) in 13 elliptical galaxies. *The Astrophysical Journal*, 218, L43–L47.
- Jones, T., Ellis, R. S., Richard, J., & Jullo, E. (2013). The Origin and Evolution of Metallicity Gradients: Probing the Mode of Mass Assembly at  $z \sim 2$ . *The Astrophysical Journal*, 765, 48.
- Karademir, G. S., Remus, R.-S., Burkert, A., Dolag, K., Hoffmann, T. L., Moster, B. P., Steinwandel, U. P., & Zhang, J. (2019). The outer stellar halos of galaxies: How radial merger mass deposition, shells, and streams depend on infall-orbit configurations. *Monthly Notices of the Royal Astronomical Society*, 487, 318–332.
- Kewley, L. J., & Ellison, S. L. (2008). Metallicity Calibrations and the Mass-Metallicity Relation for Star-forming Galaxies. *The Astrophysical Journal*, 681, 1183–1204.
- Khalid, A., Brough, S., Martin, G., Kimmig, L. C., Lagos, C. D. P., Remus, R. S., & Martinez-Lombilla, C. (2024). Characterizing tidal features around galaxies in cosmological simulations. *Monthly Notices of the Royal Astronomical Society*, 530, 4422–4445.
- Komatsu, E., Smith, K. M., Dunkley, J., Bennett, C. L., Gold, B., Hinshaw, G., Jarosik, N., Larson, D., Nolta, M. R., Page, L., Spergel, D. N., Halpern, M., Hill, R. S., Kogut, A., Limon, M., Meyer, S. S., Odegard, N., Tucker, G. S., Weiland, J. L., Wollack, E., & Wright, E. L. (2011). Seven-year Wilkinson Microwave Anisotropy Probe (WMAP) Observations: Cosmological Interpretation. *The Astrophysical Journal Supplement Series*, 192, 18.
- Krajnović, D., Emsellem, E., Cappellari, M., Alatalo, K., Blitz, L., Bois, M., Bournaud, F., Bureau, M., Davies, R. L., Davis, T. A., de Zeeuw, P. T., Khochfar, S., Kuntschner, H., Lablanche, P.-Y., McDermid, R. M., Morganti, R., Naab, T., Oosterloo, T., Sarzi, M., Scott, N., Serra, P., Weijmans, A.-M., & Young, L. M. (2011). The ATLAS3D project - II. Morphologies, kinematic features and alignment between photometric and kinematic axes of early-type galaxies. *Monthly Notices of the Royal Astronomical Society*, 414, 2923–2949.
- Kudritzki, R. P., Castro, N., Urbaneja, M. A., Ho, I. T., Bresolin, F., Gieren, W., Pietrzyński, G., & Przybilla, N. (2016). A Spectroscopic Study of Blue Supergiant Stars in the Sculptor Galaxy NGC 55: Chemical Evolution and Distance. *The Astrophysical Journal*, 829, 70.
- Kudritzki, R.-P., Teklu, A. F., Schulze, F., Remus, R.-S., Dolag, K., Burkert, A., & Zahid, H. J. (2021). Galaxy Look-back Evolution Models: A Comparison with Magnesium Cosmological Simulations and Observations. *The Astrophysical Journal*, 910, 87.

- Lange, R., Driver, S. P., Robotham, A. S. G., Kelvin, L. S., Graham, A. W., Alpaslan, M., Andrews, S. K., Baldry, I. K., Bamford, S., Bland-Hawthorn, J., Brough, S., Cluver, M. E., Conselice, C. J., Davies, L. J. M., Haeussler, B., Konstantopoulos, I. S., Loveday, J., Moffett, A. J., Norberg, P., Phillipps, S., Taylor, E. N., López-Sánchez, Á. R., & Wilkins, S. M. (2015). Galaxy And Mass Assembly (GAMA): Mass-size relations of  $z < 0.1$  galaxies subdivided by Sérsic index, colour and morphology. *Monthly Notices of the Royal Astronomical Society*, *447*, 2603–2630.
- Lequeux, J., Peimbert, M., Rayo, J. F., Serrano, A., & Torres-Peimbert, S. (1979). Chemical Composition and Evolution of Irregular and Blue Compact Galaxies. *Astronomy and Astrophysics*, *80*, 155.
- Maiolino, R., Nagao, T., Grazian, A., Cocchia, F., Marconi, A., Mannucci, F., Cimatti, A., Pipino, A., Ballero, S., Calura, F., Chiappini, C., Fontana, A., Granato, G. L., Matteucci, F., Pastorini, G., Pentericci, L., Risaliti, G., Salvati, M., & Silva, L. (2008). AMAZE. I. The evolution of the mass-metallicity relation at  $z > 3$ . *Astronomy and Astrophysics*, *488*, 463–479.
- Martin, G., Bazkiaei, A. E., Spavone, M., Iodice, E., Mihos, J. C., Montes, M., Benavides, J. A., Brough, S., Carlin, J. L., Collins, C. A., Duc, P. A., Gómez, F. A., Galaz, G., Hernández-Toledo, H. M., Jackson, R. A., Kaviraj, S., Knapen, J. H., Martínez-Lombilla, C., McGee, S., O’Ryan, D., Prole, D. J., Rich, R. M., Román, J., Shah, E. A., Starkenburg, T. K., Watkins, A. E., Zaritsky, D., Pichon, C., Armus, L., Bianconi, M., Buitrago, F., Busá, I., Davis, F., Demarco, R., Desmons, A., García, P., Graham, A. W., Holwerda, B., Hon, D. S. H., Khalid, A., Klehammer, J., Klutse, D. Y., Lazar, I., Nair, P., Noakes-Kettel, E. A., Rutkowski, M., Saha, K., Sahu, N., Sola, E., Vázquez-Mata, J. A., Vera-Casanova, A., & Yoon, I. (2022). Preparing for low surface brightness science with the Vera C. Rubin Observatory: Characterization of tidal features from mock images. *Monthly Notices of the Royal Astronomical Society*, *513*, 1459–1487.
- Martínez-Delgado, D., Cooper, A. P., Román, J., Pillepich, A., Erkal, D., Pearson, S., Moustakas, J., Laporte, C. F. P., Laine, S., Akhlaghi, M., Lang, D., Makarov, D., Borlaff, A. S., Donatiello, G., Pearson, W. J., Miró-Carretero, J., Cuillandre, J.-C., Domínguez, H., Roca-Fàbrega, S., Frenk, C. S., Schmidt, J., Gómez-Flechoso, M. A., Guzman, R., Libeskind, N. I., Dey, A., Weaver, B. A., Schlegel, D., Myers, A. D., & Valdes, F. G. (2023a). Hidden depths in the local Universe: The Stellar Stream Legacy Survey. *Astronomy and Astrophysics*, *671*, A141.
- Martínez-Delgado, D., Roca-Fàbrega, S., Miró-Carretero, J., Gómez-Flechoso, M. A., Román, J., Donatiello, G., Schmidt, J., Lang, D., Akhlaghi, M., & Hanson, M. (2023b). A giant umbrella-like stellar stream around the tidal ring galaxy NGC 922. *Astronomy and Astrophysics*, *669*, A103.

- McDermid, R. M., Bacon, R., Kuntschner, H., Emsellem, E., Shapiro, K. L., Bureau, M., Cappellari, M., Davies, R. L., Falcón-Barroso, J., Krajnović, D., Peletier, R. F., Sarzi, M., & de Zeeuw, T. (2006). Stellar kinematics and populations of early-type galaxies with the SAURON and OASIS integral-field spectrographs. *New Astronomy Reviews*, *49*, 521–535.
- Mercado, F. J., Bullock, J. S., Boylan-Kolchin, M., Moreno, J., Wetzel, A., El-Badry, K., Graus, A. S., Fitts, A., Hopkins, P. F., Faucher-Giguère, C.-A., & Gurvich, A. B. (2021). A relationship between stellar metallicity gradients and galaxy age in dwarf galaxies. *Monthly Notices of the Royal Astronomical Society*, *501*, 5121–5134.
- Miro-Carretero, J., Gomez-Flechoso, M. A., Martinez-Delgado, D., Cooper, A. P., Roca-Fabrega, S., Akhlaghi, M., Pillepich, A., Kuijken, K., Erkal, D., Buck, T., Hellwing, W. A., & Bose, S. (2024). Extragalactic Stellar Tidal Streams: Observations meet Simulation.
- Moody, C. E., Romanowsky, A. J., Cox, T. J., Novak, G. S., & Primack, J. R. (2014). Simulating multiple merger pathways to the central kinematics of early-type galaxies. *Monthly Notices of the Royal Astronomical Society*, *444*, 1475–1485.
- Nanni, L., Neumann, J., Thomas, D., Maraston, C., Trayford, J., Lovell, C. C., Law, D. R., Yan, R., & Chen, Y. (2024). iMaNGA: Mock MaNGA galaxies based on IllustrisTNG and MaStar SSPs. - III. Stellar metallicity drivers in MaNGA and TNG50. *Monthly Notices of the Royal Astronomical Society*, *527*, 6419–6438.
- Nelson, D., Pillepich, A., Springel, V., Weinberger, R., Hernquist, L., Pakmor, R., Genel, S., Torrey, P., Vogelsberger, M., Kauffmann, G., Marinacci, F., & Naiman, J. (2018). First results from the IllustrisTNG simulations: The galaxy colour bimodality. *Monthly Notices of the Royal Astronomical Society*, *475*, 624–647.
- Neumann, J., Thomas, D., Maraston, C., Goddard, D., Lian, J., Hill, L., Domínguez Sánchez, H., Bernardi, M., Margalef-Bentabol, B., Barrera-Ballesteros, J. K., Bizyaev, D., Boardman, N. F., Drory, N., Fernández-Trincado, J. G., & Lane, R. (2021). SDSS-IV MaNGA: Drivers of stellar metallicity in nearby galaxies. *Monthly Notices of the Royal Astronomical Society*, *508*, 4844–4857.
- Oort, J. H. (1940). Some Problems Concerning the Structure and Dynamics of the Galactic System and the Elliptical Nebulae NGC 3115 and 4494. *The Astrophysical Journal*, *91*, 273.
- Pearson, W. J., Wang, L., Hurley, P. D., Małek, K., Buat, V., Burgarella, D., Farrah, D., Oliver, S. J., Smith, D. J. B., & van der Tak, F. F. S. (2018). Main sequence of star forming galaxies beyond the Herschel confusion limit. *Astronomy and Astrophysics*, *615*, A146.
- Peña, M., & Flores-Durán, S. N. (2019). Metallicity Gradients in M 31, M 33, NGC 300 and the Milky Way Using Abundances of Different Elements. *Revista Mexicana de Astronomía y Astrofísica*, *55*, 255–271.

- Pettini, M., & Pagel, B. E. J. (2004). [OIII]/[NII] as an abundance indicator at high redshift. *Monthly Notices of the Royal Astronomical Society*, 348, L59–L63.
- Pillepich, A., Nelson, D., Springel, V., Pakmor, R., Torrey, P., Weinberger, R., Vogelsberger, M., Marinacci, F., Genel, S., van der Wel, A., & Hernquist, L. (2019). First results from the TNG50 simulation: The evolution of stellar and gaseous discs across cosmic time. *Monthly Notices of the Royal Astronomical Society*, 490, 3196–3233.
- Pilyugin, L. S., & Thuan, T. X. (2005). Oxygen Abundance Determination in H II Regions: The Strong Line Intensities-Abundance Calibration Revisited. *The Astrophysical Journal*, 631, 231–243.
- Pippert, J.-N., Kluge, M., & Bender, R. (2024). *Extragalactic Stream Models Based on 1D Gaussian Slices*.
- Pop, A.-R., Pillepich, A., Amorisco, N. C., & Hernquist, L. (2017). Galaxies with Shells in the Illustris Simulation: Metallicity Signatures. *Galaxies*, 5, 34.
- Pop, A.-R., Pillepich, A., Amorisco, N. C., & Hernquist, L. (2018). Formation and incidence of shell galaxies in the Illustris simulation. *Monthly Notices of the Royal Astronomical Society*, 480, 1715–1739.
- Power, C., Navarro, J. F., Jenkins, A., Frenk, C. S., White, S. D. M., Springel, V., Stadel, J., & Quinn, T. (2003). The inner structure of  $\Lambda$ CDM haloes - I. A numerical convergence study. *Monthly Notices of the Royal Astronomical Society*, 338, 14–34.
- Ragagnin, A., Dolag, K., Biffi, V., Cadolle Bel, M., Hammer, N. J., Krukau, A., Petkova, M., & Steinborn, D. (2017). A web portal for hydrodynamical, cosmological simulations. *Astronomy and Computing*, 20, 52–67.
- Remus, R.-S. (2015). *The Outer Halos of Elliptical Galaxies: Implications for Their Formation Histories*. Ph.D. thesis.
- Remus, R.-S., Dolag, K., Naab, T., Burkert, A., Hirschmann, M., Hoffmann, T. L., & Johansson, P. H. (2017). The co-evolution of total density profiles and central dark matter fractions in simulated early-type galaxies. *Monthly Notices of the Royal Astronomical Society*, 464, 3742–3756.
- Remus, R.-S., & Forbes, D. A. (2022). Accreted or Not Accreted? The Fraction of Accreted Mass in Galaxies from the Magneticum Simulations and Observations. *The Astrophysical Journal*, 935, 37.
- Remus, R.-S., & Kimmig, L. C. (2023). Relight the Candle: What happens to High Redshift Massive Quenched Galaxies.
- Romanowsky, A. J., & Fall, S. M. (2012). Angular Momentum and Galaxy Formation Revisited. *The Astrophysical Journal Supplement Series*, 203, 17.

- Roškar, R., Debattista, V. P., Quinn, T. R., Stinson, G. S., & Wadsley, J. (2008). Riding the Spiral Waves: Implications of Stellar Migration for the Properties of Galactic Disks. *The Astrophysical Journal*, 684, L79.
- Rubin, V. C., Burbidge, E. M., Burbidge, G. R., Crampin, D. J., & Prendergast, K. H. (1965). The Rotation and Mass of NGC 7331. *The Astrophysical Journal*, 141, 759.
- Rubin, V. C., & Ford, W. K., Jr. (1970). Rotation of the Andromeda Nebula from a Spectroscopic Survey of Emission Regions. *The Astrophysical Journal*, 159, 379.
- Rubin, V. C., Ford, W. K., Jr., & Thonnard, N. (1978). Extended rotation curves of high-luminosity spiral galaxies. IV. Systematic dynamical properties, Sa -> Sc. *The Astrophysical Journal*, 225, L107–L111.
- Rubin, V. C., Ford, W. K., Jr., & Thonnard, N. (1980). Rotational properties of 21 SC galaxies with a large range of luminosities and radii, from NGC 4605 (R=4kpc) to UGC 2885 (R=122kpc). *The Astrophysical Journal*, 238, 471–487.
- Rutherford, T. H., van de Sande, J., Croom, S. M., Valenzuela, L. M., Remus, R.-S., D'Eugenio, F., Vaughan, S. P., Zovaro, H. R. M., Casura, S., Barsanti, S., Bland-Hawthorn, J., Brough, S., Bryant, J. J., Goodwin, M., Lorente, N., Oh, S., & Ristea, A. (2024). The SAMI Galaxy Survey: Using tidal streams and shells to trace the dynamical evolution of massive galaxies. *Monthly Notices of the Royal Astronomical Society*, 529, 810–830.
- San Roman, I., Cenarro, A. J., Díaz-García, L. A., López-Sanjuan, C., Varela, J., González Delgado, R. M., Sánchez-Blázquez, P., Alfaro, E. J., Ascaso, B., Bonoli, S., Borlaff, A., Castander, F. J., Cerviño, M., Fernández-Soto, A., Márquez, I., Masegosa, J., Muniesa, D., Pović, M., Viironen, K., Aguerri, J. A. L., Benítez, N., Broadhurst, T., Cabrera-Caño, J., Cepa, J., Cristóbal-Hornillos, D., Infante, L., Martínez, V. J., Moles, M., del Olmo, A., Perea, J., Prada, F., & Quintana, J. M. (2018). The ALHAMBRA survey: 2D analysis of the stellar populations in massive early-type galaxies at  $z < 0.3$ . *Astronomy and Astrophysics*, 609, A20.
- Sánchez, S. F., Barrera-Ballesteros, J. K., López-Cobá, C., Brough, S., Bryant, J. J., Bland-Hawthorn, J., Croom, S. M., van de Sande, J., Cortese, L., Goodwin, M., Lawrence, J. S., López-Sánchez, A. R., Sweet, S. M., Owers, M. S., Richards, S. N., & Walcher, C. J. (2019). The SAMI galaxy survey: Exploring the gas-phase mass-metallicity relation. *Monthly Notices of the Royal Astronomical Society*, 484, 3042–3070.
- Sánchez, S. F., Kennicutt, R. C., Gil de Paz, A., van de Ven, G., Vílchez, J. M., Wisotzki, L., Walcher, C. J., Mast, D., Aguerri, J. A. L., Albiol-Pérez, S., Alonso-Herrero, A., Alves, J., Bakos, J., Bartáková, T., Bland-Hawthorn, J., Boselli, A., Bomans, D. J., Castillo-Morales, A., Cortijo-Ferrero, C., de Lorenzo-Cáceres, A., Del Olmo, A., Dettmar, R. J., Díaz, A., Ellis, S., Falcón-Barroso, J., Flores, H., Gallazzi, A., García-Lorenzo, B., González Delgado, R., Gruel, N., Haines, T., Hao, C., Husemann, B., Iglésias-Páramo, J., Jahnke, K.,

- Johnson, B., Jungwiert, B., Kalinova, V., Kehrig, C., Kupko, D., López-Sánchez, Á. R., Lyubenova, M., Marino, R. A., Mármol-Queraltó, E., Márquez, I., Masegosa, J., Meidt, S., Mendez-Abreu, J., Monreal-Ibero, A., Montijo, C., Mourão, A. M., Palacios-Navarro, G., Papaderos, P., Pasquali, A., Peletier, R., Pérez, E., Pérez, I., Quirrenbach, A., Relaño, M., Rosales-Ortega, F. F., Roth, M. M., Ruiz-Lara, T., Sánchez-Blázquez, P., Sengupta, C., Singh, R., Stanishev, V., Trager, S. C., Vazdekis, A., Viironen, K., Wild, V., Zibetti, S., & Ziegler, B. (2012). CALIFA, the Calar Alto Legacy Integral Field Area survey. I. Survey presentation. *Astronomy and Astrophysics*, 538, A8.
- Sánchez-Menguiano, L., Sánchez Almeida, J., Sánchez, S. F., & Muñoz-Tuñón, C. (2024). Stellar mass is not the best predictor of galaxy metallicity. The gravitational potential-metallicity relation  $\Phi ZR$ . *Astronomy and Astrophysics*, 681, A121.
- Sandage, A. (1961). *The Hubble Atlas of Galaxies*.
- Schauer, A. T. P., Remus, R.-S., Burkert, A., & Johansson, P. H. (2014). The Mystery of the  $\sigma$ -Bump—A New Signature for Major Mergers in Early-type Galaxies? *The Astrophysical Journal*, 783, L32.
- Schawinski, K., Urry, C. M., Simmons, B. D., Fortson, L., Kaviraj, S., Keel, W. C., Lintott, C. J., Masters, K. L., Nichol, R. C., Sarzi, M., Skibba, R., Treister, E., Willett, K. W., Wong, O. I., & Yi, S. K. (2014). The green valley is a red herring: Galaxy Zoo reveals two evolutionary pathways towards quenching of star formation in early- and late-type galaxies. *Monthly Notices of the Royal Astronomical Society*, 440, 889–907.
- Schulze, F., Remus, R.-S., & Dolag, K. (2017). On the Kinematics, Stability and Lifetime of Kinematically Distinct Cores: A Case Study. *Galaxies*, 5, 41.
- Schulze, F., Remus, R.-S., Dolag, K., Bellstedt, S., Burkert, A., & Forbes, D. A. (2020). Kinematics of simulated galaxies II: Probing the stellar kinematics of galaxies out to large radii. *Monthly Notices of the Royal Astronomical Society*, 493, 3778–3799.
- Schulze, F., Remus, R.-S., Dolag, K., Burkert, A., Emsellem, E., & van de Ven, G. (2018). Kinematics of simulated galaxies - I. Connecting dynamical and morphological properties of early-type galaxies at different redshifts. *Monthly Notices of the Royal Astronomical Society*, 480, 4636–4658.
- Scott, N., Brough, S., Croom, S. M., Davies, R. L., van de Sande, J., Allen, J. T., Bland-Hawthorn, J., Bryant, J. J., Cortese, L., D'Eugenio, F., Federrath, C., Ferreras, I., Goodwin, M., Groves, B., Konstantopoulos, I., Lawrence, J. S., Medling, A. M., Moffett, A. J., Owers, M. S., Richards, S., Robotham, A. S. G., Tonini, C., & Yi, S. K. (2017). The SAMI Galaxy Survey: Global stellar populations on the size-mass plane. *Monthly Notices of the Royal Astronomical Society*, 472, 2833–2855.

- Sérsic, J. L. (1963). Influence of the atmospheric and instrumental dispersion on the brightness distribution in a galaxy. *Boletín de la Asociación Argentina de Astronomía La Plata Argentina*, 6, 41–43.
- Sextl, E., Kudritzki, R.-P., Burkert, A., Ho, I. T., Zahid, H. J., Seibert, M., Battisti, A. J., Madore, B. F., & Rich, J. A. (2024). The TYPHOON Stellar Population Synthesis Survey. I. The Young Stellar Population of the Great Barred Spiral NGC 1365. *The Astrophysical Journal*, 960, 83.
- Sextl, E., Kudritzki, R.-P., Zahid, H. J., & Ho, I. T. (2023). Mass-Metallicity Relationship of SDSS Star-forming Galaxies: Population Synthesis Analysis and Effects of Star Burst Length, Extinction Law, Initial Mass Function, and Star Formation Rate. *The Astrophysical Journal*, 949, 60.
- Sharda, P., Wisnioski, E., Krumholz, M. R., & Federrath, C. (2021). The role of gas kinematics in setting metallicity gradients at high redshift. *Monthly Notices of the Royal Astronomical Society*, 506, 1295–1308.
- Shen, S., Mo, H. J., White, S. D. M., Blanton, M. R., Kauffmann, G., Voges, W., Brinkmann, J., & Csabai, I. (2003). The size distribution of galaxies in the Sloan Digital Sky Survey. *Monthly Notices of the Royal Astronomical Society*, 343, 978–994.
- Sola, E., Duc, P.-A., Richards, F., Paiement, A., Urbano, M., Klehammer, J., Bílek, M., Cuillandre, J.-C., Gwyn, S., & McConnachie, A. (2022). Characterization of low surface brightness structures in annotated deep images. *Astronomy and Astrophysics*, 662, A124.
- Speagle, J. S., Steinhardt, C. L., Capak, P. L., & Silverman, J. D. (2014). A Highly Consistent Framework for the Evolution of the Star-Forming "Main Sequence" from  $z \sim 0-6$ . *The Astrophysical Journal Supplement Series*, 214, 15.
- Spitzer, L. (1962). *Physics of Fully Ionized Gases*.
- Springel, V. (2005). The cosmological simulation code GADGET-2. *Monthly Notices of the Royal Astronomical Society*, 364, 1105–1134.
- Springel, V., Di Matteo, T., & Hernquist, L. (2005). Modelling feedback from stars and black holes in galaxy mergers. *Monthly Notices of the Royal Astronomical Society*, 361, 776–794.
- Springel, V., & Hernquist, L. (2003). Cosmological smoothed particle hydrodynamics simulations: A hybrid multiphase model for star formation. *Monthly Notices of the Royal Astronomical Society*, 339, 289–311.
- Springel, V., White, S. D. M., Tormen, G., & Kauffmann, G. (2001a). Populating a cluster of galaxies - I. Results at  $z=0$ . *Monthly Notices of the Royal Astronomical Society*, 328, 726–750.

- Springel, V., Yoshida, N., & White, S. D. M. (2001b). GADGET: A code for collisionless and gasdynamical cosmological simulations. *New Astronomy*, 6, 79–117.
- Teklu, A. F., Remus, R.-S., Dolag, K., Beck, A. M., Burkert, A., Schmidt, A. S., Schulze, F., & Steinborn, L. K. (2015). Connecting Angular Momentum and Galactic Dynamics: The Complex Interplay between Spin, Mass, and Morphology. *The Astrophysical Journal*, 812, 29.
- Teklu, A. F., Remus, R.-S., Dolag, K., & Burkert, A. (2017). The morphology-density relation: Impact on the satellite fraction. *Monthly Notices of the Royal Astronomical Society*, 472, 4769–4785.
- Tornatore, L., Borgani, S., Dolag, K., & Matteucci, F. (2007). Chemical enrichment of galaxy clusters from hydrodynamical simulations. *Monthly Notices of the Royal Astronomical Society*, 382, 1050–1072.
- Tornatore, L., Borgani, S., Matteucci, F., Recchi, S., & Tozzi, P. (2004). Simulating the metal enrichment of the intracluster medium. *Monthly Notices of the Royal Astronomical Society*, 349, L19–L24.
- Tremonti, C. A., Heckman, T. M., Kauffmann, G., Brinchmann, J., Charlot, S., White, S. D. M., Seibert, M., Peng, E. W., Schlegel, D. J., Uomoto, A., Fukugita, M., & Brinkmann, J. (2004). The Origin of the Mass-Metallicity Relation: Insights from 53,000 Star-forming Galaxies in the Sloan Digital Sky Survey. *The Astrophysical Journal*, 613, 898–913.
- Tsatsi, A., Lyubenova, M., van de Ven, G., Chang, J., Aguerri, J. A. L., Falcón-Barroso, J., & Macciò, A. V. (2017). CALIFA reveals prolate rotation in massive early-type galaxies: A polar galaxy merger origin? *Astronomy and Astrophysics*, 606, A62.
- Urbaneja, M. A., Bresolin, F., & Kudritzki, R.-P. (2023). The Metallicity and Distance of Leo A from Blue Supergiants. *The Astrophysical Journal*, 959, 52.
- Valenzuela, L. M., & Remus, R.-S. (2024). A stream come true: Connecting tidal tails, shells, streams, and planes with galaxy kinematics and formation history. *Astronomy and Astrophysics*, 686, A182.
- Valenzuela, L. M., Remus, R.-S., Dolag, K., & Seidel, B. A. (2024). Galaxy shapes in Magneticum. I. Connecting stellar and dark matter shapes to dynamical and morphological galaxy properties and the large-scale structure.
- van de Sande, J., Lagos, C. D. P., Welker, C., Bland-Hawthorn, J., Schulze, F., Remus, R.-S., Bahé, Y., Brough, S., Bryant, J. J., Cortese, L., Croom, S. M., Devriendt, J., Dubois, Y., Goodwin, M., Konstantopoulos, I. S., Lawrence, J. S., Medling, A. M., Pichon, C., Richards, S. N., Sanchez, S. F., Scott, N., & Sweet, S. M. (2019). The SAMI Galaxy Survey: Comparing 3D spectroscopic observations with galaxies from

- cosmological hydrodynamical simulations. *Monthly Notices of the Royal Astronomical Society*, 484, 869–891.
- van de Sande, J., Vaughan, S. P., Cortese, L., Scott, N., Bland-Hawthorn, J., Croom, S. M., Lagos, C. D. P., Brough, S., Bryant, J. J., Devriendt, J., Dubois, Y., D'Eugenio, F., Foster, C., Fraser-McKelvie, A., Harborne, K. E., Lawrence, J. S., Oh, S., Owers, M. S., Poci, A., Remus, R.-S., Richards, S. N., Schulze, F., Sweet, S. M., Varidel, M. R., & Welker, C. (2021). The SAMI Galaxy Survey: A statistical approach to an optimal classification of stellar kinematics in galaxy surveys. *Monthly Notices of the Royal Astronomical Society*, 505, 3078–3106.
- Vaughan, S. P., Barone, T. M., Croom, S. M., Cortese, L., D'Eugenio, F., Brough, S., Colless, M., McDermid, R. M., van de Sande, J., Scott, N., Bland-Hawthorn, J., Bryant, J. J., Lawrence, J. S., López-Sánchez, Á. R., Lorente, N. P. F., Owers, M. S., & Richards, S. N. (2022). The SAMI galaxy survey: Galaxy size can explain the offset between star-forming and passive galaxies in the mass-metallicity relationship. *Monthly Notices of the Royal Astronomical Society*, 516, 2971–2987.
- Venturi, G., Carniani, S., Parlanti, E., Kohandel, M., Curti, M., Pallottini, A., Vallini, L., Arribas, S., Bunker, A. J., Cameron, A. J., Castellano, M., Ferrara, A., Fontana, A., Gallerani, S., Gelli, V., Maiolino, R., Ntormousi, E., Pacifici, C., Pentericci, L., Salvadori, S., & Vanzella, E. (2024). Gas-phase metallicity gradients in galaxies at  $z \sim 6-8$ .
- Zahid, H. J., Kudritzki, R.-P., Conroy, C., Andrews, B., & Ho, I. T. (2017). Stellar Absorption Line Analysis of Local Star-forming Galaxies: The Relation between Stellar Mass, Metallicity, Dust Attenuation, and Star Formation Rate. *The Astrophysical Journal*, 847, 18.
- Zemp, M., Gnedin, O. Y., Gnedin, N. Y., & Kravtsov, A. V. (2011). On Determining the Shape of Matter Distributions. *The Astrophysical Journal Supplement Series*, 197, 30.
- Zhuang, Y., Leaman, R., van de Ven, G., Zibetti, S., Gallazzi, A., Zhu, L., Falcón-Barroso, J., & Lyubenova, M. (2019). A dynamical view on stellar metallicity gradient diversity across the Hubble sequence with CALIFA. *Monthly Notices of the Royal Astronomical Society*, 483, 1862–1880.
- Zwicky, F. (1937). On the Masses of Nebulae and of Clusters of Nebulae. *The Astrophysical Journal*, 86, 217.



# Acknowledgments

At the end of this thesis and at the end of my studies to obtain a Master's degree, I want to thank all the people who made it possible for me to get this far. First, I want to thank [Prof. Dr. Klaus Dolag](#) for his advice and help during the work on the Master's thesis. He already supervised my Bachelor's thesis and played a crucial role during my studies in the last two years, as a lecturer, as the supervisor of my research assistant position, and he made it possible for me to attend research conferences this early in my scientific career. I am also grateful for the possibility to work with him as a PhD student during the coming years. Next, I want to thank [Dr. Rhea-Silvia Remus](#), who inspired my interest in galaxies with her fantastic lecture about elliptical galaxies during my first semester. She has been a great supervisor who was always open to discussing scientific and organizational questions regarding my master project and helped me with questions about the scientific community even beyond that. I am grateful for her low-hierarchy supervision style, which really benefitted me. I also want to thank her for all the great tutorials during the "Essentials of Advanced Astrophysics" lecture, the "Gravitational Dynamics" lecture, and for her own great lecture about "Chaos and Dynamics in Astrophysics". Rhea kindly introduced me to her research group, the DRAGONS Team. I want to thank every member of the group that I got to know, [Lucas Valenzuela](#), [Lucas Kimmig](#), [Benjamin Seidel](#), [Silvio Fortuné](#), [Anna Ivleva](#), and [Anita Schiller](#), who made this last year not just great scientifically, but it was also fun to joke with you during our breaks, game nights, and on conference travels. I want to thank every member for the help they all provided, but I want to specifically thank Lucas Valenzuela and Lucas Kimmig. [Lucas Valenzuela](#) was always the first person I could go to with any problem. He answered all my programming questions regarding [Julia](#)<sup>1</sup>, and his very helpful JuliaCosmoSims package, without which this thesis would not have been possible. I want to thank him for the extensive feedback and proofreading of my Master's thesis. I want to thank [Lucas Kimmig](#) for his help in understanding the physical processes and his new ideas regarding the first part of my thesis about the metallicity and metallicity gradient of galaxies. Thanks are due to [Tadziu Hoffmann](#) for all the quick technical support and great tutorials, to [Eva SEXTL](#) and [Rolf-Peter Kudritzki](#), for discussions about the metallicity of galaxies, to [Elisabeth Sola](#), for providing her dataset of observed shells and streams, and to all the people I forgot and who helped me during the last year. For the team work and help during the lecture period, I thank [Eric Muir](#), whom I wish great success in his PhD program in Gent, [Xiomara Runge](#), [Tapan Mayuk](#), [Helena Lamprecht](#), [Laura Schöller](#), [Ben Röcken](#), and [Fabian Solfronk](#). Finally, I

---

<sup>1</sup>[www.julialang.org](http://www.julialang.org)

want to thank [my parents](#) and [my girlfriend](#) for their emotional and financial support ever since I started to study physics.

# Selbstständigkeitserklärung

Hiermit erkläre ich, die vorliegende Arbeit selbstständig verfasst zu haben und keine anderen als die in der Arbeit angegebenen Quellen und Hilfsmittel benutzt zu haben.

München, 27.11.2024

---

Johannes Stoiber